ADVANCED PRESSURE SWING ADSORPTION SYSTEM WITH FIBER SORBENTS FOR HYDROGEN RECOVERY

A Dissertation
Presented to
The Academic Faculty

By

Naoki Bessho

In Partial Fulfillment
of the Requirements for the Degree
Doctor of Philosophy in the
School of Chemical & Biomolecular Engineering

Georgia Institute of Technology

December 2010

ADVANCED PRESSURE SWING ADSORPTION SYSTEM WITH FIBER SORBENTS FOR HYDROGEN RECOVERY

Approved by:

Dr. William J. Koros, Advisor
School of Chemical & Biomolecular Engineering
Georgia Institute of Technology

Dr. Anselm C. Griffin
School of Materials Science and Engineering
Georgia Institute of Technology

Dr. Ronald W. Rousseau
School of Chemical & Biomolecular Engineering
Georgia Institute of Technology

Dr. James F. Stevens
Catchlight Energy LLC

Dr. Pradeep K. Agrawal
School of Chemical & Biomolecular Engineering
Georgia Institute of Technology

Date Approved: October 25, 2010

ACKNOWLEDGEMENTS

I would like to acknowledge Dr. Koros for guiding my research for the last four years. His approach was impressive and different from my past school academic and business supervisors. His passion for the research was so strong and it kept me stay in the laboratory. This opportunity was a unique experience for me since I came here after I quit a secure job. The challenge is complete thanks to Dr. Koros' sincere advice.

I would like to thank my committee members, Dr. Rousseau, Dr. Agrawal, Dr. Griffin and Dr. Stevens for the time and effort you spent on my proposal and this final defense.

I also would like to thank Chevron Technologies Ventures for funding this research.

I appreciate Dr. Yoshiaki Kawajiri, ChBE, to give me the permission to use gPROMS®.

I must give my appreciation to Dr. Yasushi Maeda, Dow Chemical Japan Limited. Without his support before and after I joined GT, I could not achieve my goals. Unfortunately we cannot work together at this time, but I'm looking forward to working together again someday.

I would also like to thank all of Koros research members, especially for Dhaval Bhandari in the collaboration in the same Chevron-funded project, and Junqiang Liu, Jongsuk Lee and Ryan Lively in the same batch. The Koros group is very professional in my view.

Lastly I would like to thank my wife, Miyuki Bessho, for her support and patience to me all the time since I was not at home almost all the time. I'm very glad that my daughter, Kyoto Bessho,

was grown up with proper common sense in the different culture and my son, Ryuki Bessho, was born and makes me more energetic.

TABLE OF CONTENTS

LIST OF TABLES

LIST OF FIGURES

SUMMARY

A new concept of a “fiber sorbent” has been investigated. The fiber sorbent is produced as a pseudo-monolithic material comprising polymer (cellulose acetate, CA) and zeolite (NaY) by applying hollow fiber spinning technology. Phase separation of the polymer solution provides an appropriately porous structure throughout the fiber matrix. In addition, the zeolite crystals are homogeneously dispersed in the polymer matrix with high loading. The zeolite is the main contributor to sorption capacity of the fiber sorbent. Mass transfer processes in the fiber sorbent module are analyzed for hydrogen recovery and compared with results for an equivalent size packed bed with identical diameter and length. The model indicates advantageous cases for application of fiber sorbent module over packed bed technology that allows system downsizing and energy saving by changing the outer and bore diameters to maintain or even reduce the pressure drop. The CA-NaY fiber sorbent was spun successfully with highly porous structure and high CO_2 sorption capacity. The fiber sorbent enables the shell-side void space for thermal moderation to heat of adsorption, while this cannot be applied to the packed bed. The poly(vinyl alcohol) coated CA-NaY demonstrated the thermal moderation with paraffin wax, which was carefully selected and melt at slightly above operating temperature, in the shell-side in a rapidly cycled pressure swing adsorption. So this new approach is attractive for some hydrogen recovery applications as an alternative to traditional zeolite pellets.

CHAPTER 1 INTRODUCTION

1.1. Demanding Clean Fuels

The energy policy of each country is affected by several environmental, economic and political factors; global warming, air pollution, high energy demand in developing countries, alternative energy resources to limited fossil fuels, and geopolitical risk on crude oil sourcing significantly from the Middle East region. Global warming, which has been reported as temperature increasing tendency (Figure 1-1) at Intergovernmental Panel on Climate Change (IPCC) [1], is currently a serious concern all over the world, and is believed to be largely due to increased carbon dioxide (CO_2) emission originating from fossil fuels (coal, oil and natural gas). In addition, emission of air pollutants (nitrogen/sulfur oxides, unreacted hydrocarbons and suspended particle matters), which are released mainly from power plants and vehicles, is another serious concern possibly causing acid precipitation, photochemical smog, and human health problems. Development and implementation of environmentally benign fuels to replace the conventional fossil fuels for power generators and engines are high priorities. For elimination of the emissions of CO_2 and air pollutants, renewable energies (hydraulic, wind, solar, geothermal and tidal) are ideal, but limited meteorologically and geographically. Nuclear energy can also be used for base-load power generation without the CO_2 emission, but the nuclear systems are more costly and have safety and security issues, and require more political discussion than conventional fossil power systems. Fuel and power produced from biomass have potential to offset the CO_2 emission.

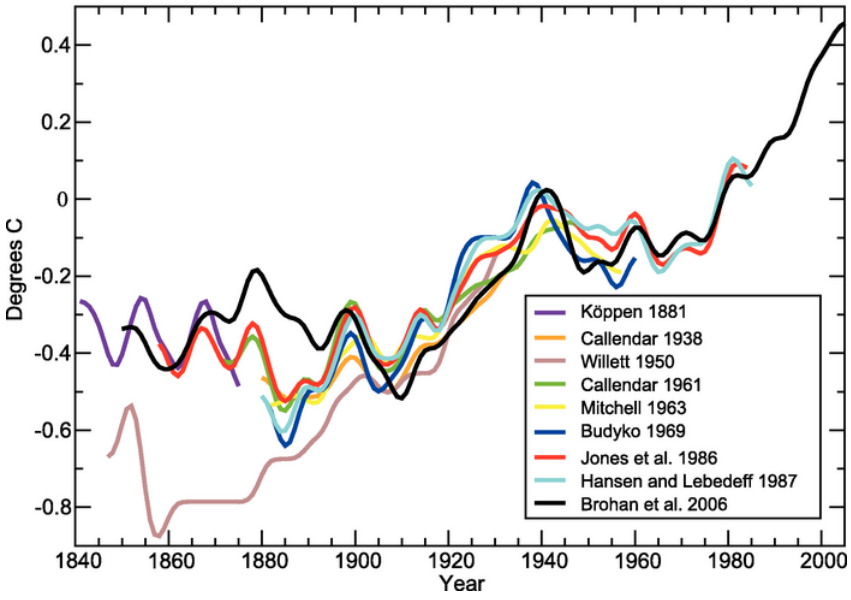

Figure 1-1 Published Records of Surface Temperature Change over Large Regions [1]

Hydrogen is attractive as a clean energy carrier since it only generates water when it combusts. However, hydrogen gas is not generally available in nature and most of the hydrogen is in the form of chemical compounds such as water and hydrocarbons. Therefore, hydrogen is industrially produced through electrolysis of water or chemical processing of hydrocarbons (reforming and gasification). Fuel cell technology can utilize hydrogen efficiently to provide both electricity and heat with only water emission. The U.S. Department of Energy (DOE) sponsors the "Fuel Cell Technologies Program" to support the development of a "hydrogen economy" featuring hydrogen fuels and fuel cells [2]. Currently centralized production of hydrogen gas (more than 750 metric tons per day) from renewable or nuclear energies without CO_2 production as a long-term goal (2030~), and distributed production from hydrocarbons with CO_2 capture as a near-term goal (2015~) have been researched for vehicle application [2-3]. Hydrogen production cost estimates with the current technologies range between $2 and $10 per gallon of gasoline equivalent (gge) (Figure 1-2) [4]. The DOE has established cost goal of $2.00-$3.00/gge (delivered, untaxed, by

2015). The cost goal was determined based on equivalent cents per mile to the conventional vehicles (Figure 1-3) [5]. In addition to the technological innovation on the hydrogen production, increased oil price today (Figure 1-4) [6] may justify relatively higher cost for the new technologies and accelerate their implementation.

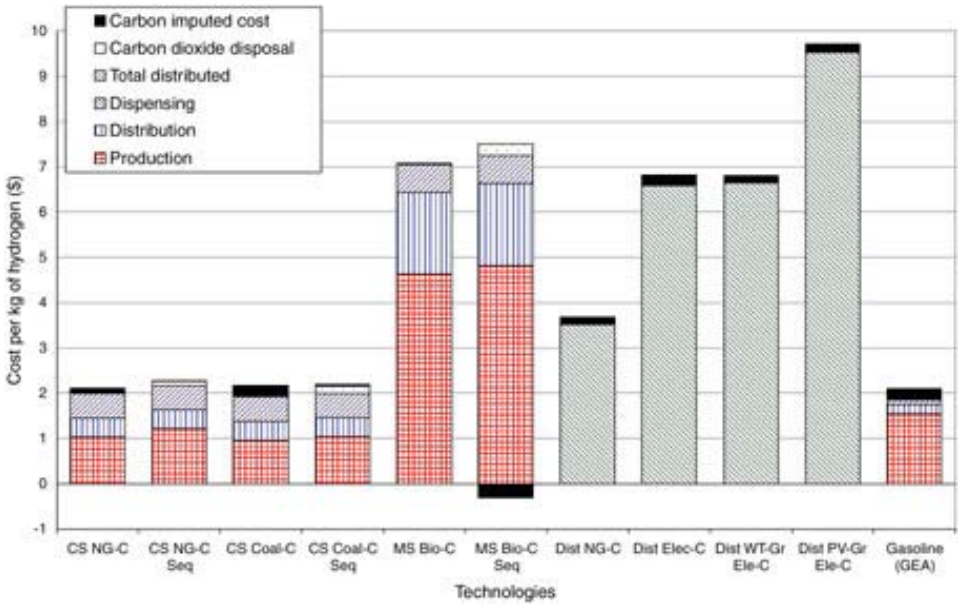

Abbrebiations:
CS: centralizd production, Dist: distributed Production, -C: current technology, Seq: sequestration, NG: natural gas, Bio: biomass, Elec: grid-based electricity, WT-Gr Elec: wind based electricity, PV-Gr Elec: photovoltaics based electricity, GEA: gasoline efficiecy adjusted

The energy content of a gallon of gasoline and a kilogram of hydrogen are approximately equal on a lower heating value basis; a kilogram of hydrogen is approximately equal to a gallon of gasoline equivalent (gge) on an energy content basis [3].

Figure 1-2 Hydrogen Production Cost [4]

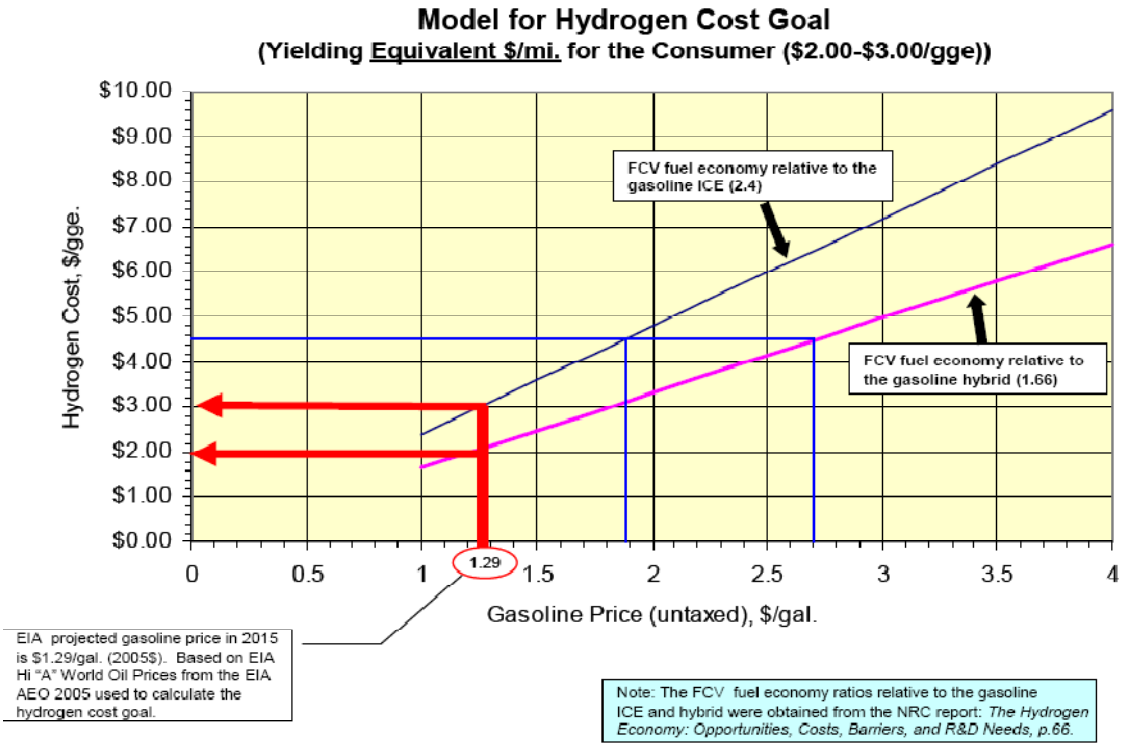

Figure 1-3 Hydrogen Cost Competitive on a Cents per Mile Basis [5]

Figure 1-4 Historical WTI Crude Oil Spot Price [6]

1.2. Fuel Cell Vehicles and Hydrogen Fueling Stations

Several types of fuel cell have been researched as summarized in Table 1-1 [2]. The principle of proton exchange membrane (or polymer electrolyte membrane) (PEM) fuel cell is illustrated in Figure 1-5. Hydrogen is fed continuously to the anode (negative electrode) and split into electrons and protons on the catalyst surface such as platinum. On the other hand, oxidant (generally O_2 from air) is fed continuously to the cathode (positive electrode) and combines with protons that travel through the electrolyte, and result in water. Transportation application has been examined, and fuel cell vehicles (**FCVs**) may be ready for commercialization with the PEM technology by automobile manufacturers [7]. Compressed hydrogen is fueled directly into the FCVs as shown in Figure 1-6 [8-9]. The hydrogen fuel quality guidelines for the FCVs was proposed based on the Society of Automotive Engineers' (SAE) specification as shown in Table 1-2.

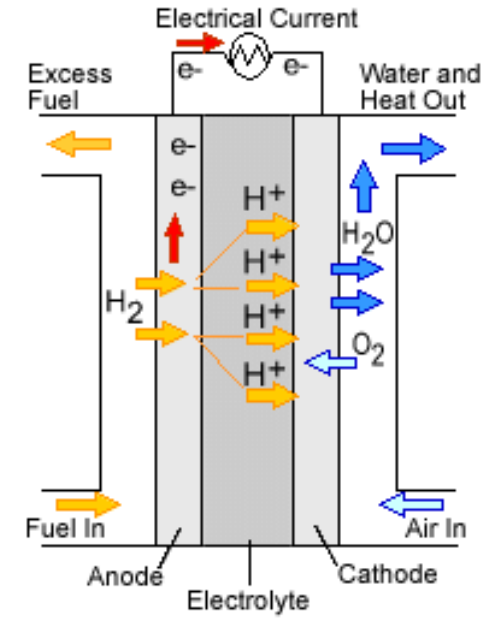

Figure 1-5 Schematic of Individual Fuel Cell (Proton Exchange Membrane Type) [2]

Table 1-1 Comparison of Fuel Cell Technologies [2]

Fuel Cell Type	Common Electrolyte	Operating Temperature [˚C]	System Output [kW]	Electrical Efficiency [%]	Combined Heat & Power (CHP) Efficiency [%]	Applications	Advantages
Proton Exchange Membrane [*or* Polymer Electrolyte Membrane] (PEM)	Solid organic polymer Polyperfluoro-sulfonic acid	50 – 100	< 1 – 250	53 – 58 (transportation) 25 – 35 (stationary)	70 – 90 (low-grade waste heat)	• Backup power • Portable power • Small distributed generation • Transportation • Specialty vehicles	• Solid electrolyte reduces corrosion & electrolyte management problems • Low temperature • Quick start-up
Alkaline (AFC)	Aqueous solution of potassium hydroxide soaked in a matrix	90 – 100	10 – 100	60	> 80 (low-grade waste heat)	• Military • Space	• Cathode reaction faster in alkaline electrolyte, leads to higher performance • Can use a variety of catalysts
Phosphoric Acid (PAFC)**	Liquid phosphoric acid soaked in a matrix	150 – 200	50 – 1,000	> 40	> 85	• Distributed generation	• Higher overall efficiency with CHP • Increased tolerance to impurities in hydrogen
Molten Carbonate (MCFC)**	Liquid solution of lithium, sodium, and/or potassium carbonates, soaked in a matrix	600 – 700	< 1 – 1,000	45 – 47	> 80	• Electric utility • Large distributed generation	• High efficiency • Fuel flexibility • Can use a variety of catalysts • Suitable for CHP
Solid Oxide (SOFC)*	Yttria stabilized zirconia	600 – 1,000	< 1 – 3,000	35 – 43	< 90	• Auxiliary power • Electric utility • Large distributed generation	• High efficiency • Fuel flexibility • Can use a variety of catalysts • Solid electrolyte reduces electrolyte management problems • Suitable for CHP • Hybrid/GT cycle

This table was slightly modified from the original table.
* 250kW module typical

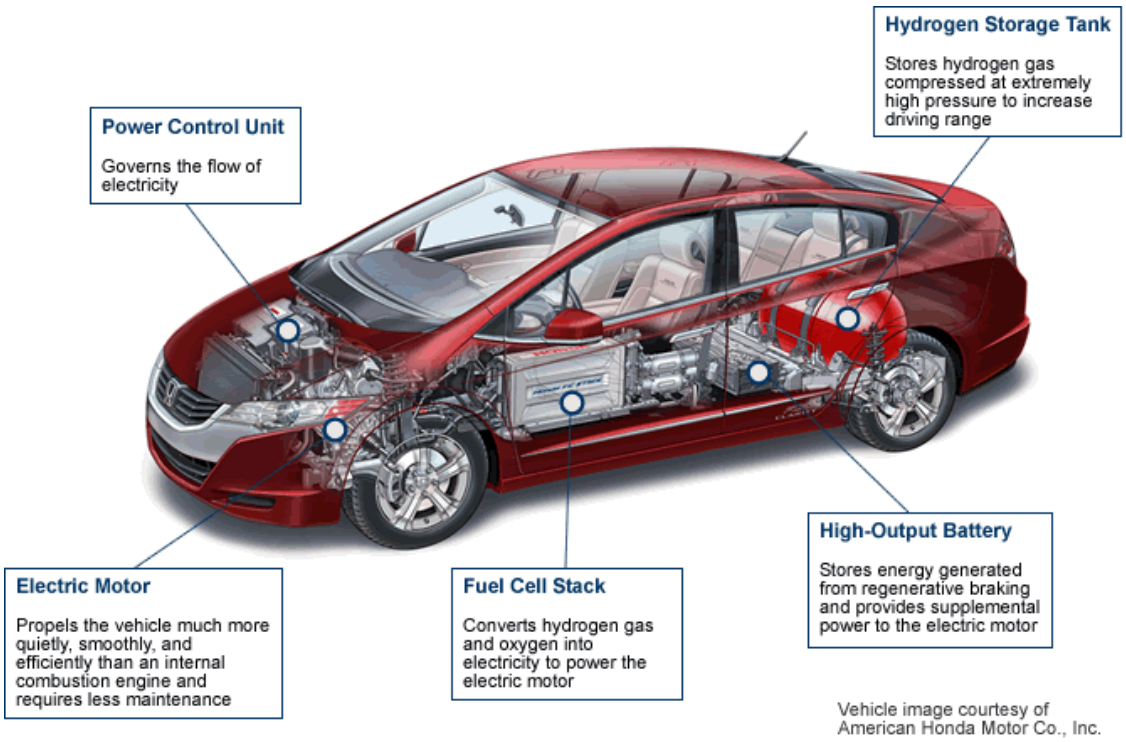

Figure 1-6 Fuel Cell Vehicle (Honda FCX Clarity) [8-9]

As a near-term solution, natural gas is a practical source to provide hydrogen fuel using existing technologies and infrastructure to facilitate "on-site" hydrogen fueling station with steam-methane reforming (SMR) as shown in Figure 1-7. The main component of natural gas is methane (Table 1-3) [10]. Distributed natural gas is pretreated to remove sulfur gases (residual H_2S and mercaptans as odorants (Table 1-4 [11]), which poison catalysts used in the reformer, and converted into hydrogen. The reformate typically contains CO_2, carbon monoxide (CO), methane and water as major impurities and hydrogen is recovered through separation processes. On-site reforming of natural gas for the distributed production requires downsizing of large scale SMR systems, including the separation units. To meet with the requirements on the hydrogen quality, efficient separation process with downsizing is a critical factor for successful distributed systems.

Table 1-2 Hydrogen Fuel Quality Guideline for Fuel Cell Vehicles [2]

Item	**Unit**	**Amount**
H_2	vol%	> 99.99%
Total Non-Particulates	ppm [a]	100
H_2O [b]	ppm	5
Total Hydrocarbons [c] (C_1 basis)	ppm	2
O_2	ppm	5
He, N_2, Ar	ppm	100
CO_2	ppm	1
CO	ppm	0.2
Total Sulfur [d]	ppm	0.004
Formaldehyde (HCHO)	ppm	0.01
Formic Acid (HCOOH)	ppm	0.2
NH_3	ppm	0.1
Total Halogenates [e]	ppm	0.05
Max. Particulate Size	μm	< 10
Particulate Concentration	μg/L-H_2	1

This table was slightly modified from the original table.

a same as μmol/mol

b A result of water threshold level, the following constituents should not be found; however, should be tested if there is a question on water content:
Na^+ @ < 0.05 μmol/mol-H_2 or < 0.05 μg/liter
K^+ @ <0.05 μmol/mol-H_2 or < 0.08 μg/liter
KOH @ < 0.05 μmol/mol-H_2 or < 0.12 μg/liter

c Includes, for example, ethylene, propylene, acetylene, benzene, phenol (paraffins, olefins, aromatic compounds, alcohols, aldehydes). Total hydrocarbons may exceed 2 ppm due only to CH_4 if the total does not exceed 100 ppm.

d Includes, for example, H_2S, carbonyl sulfide (COS), carbon disulfide (CS_2) and mercaptans.

e Includes, for example, HBr, HCl, Cl_2 and organic halides (RX).

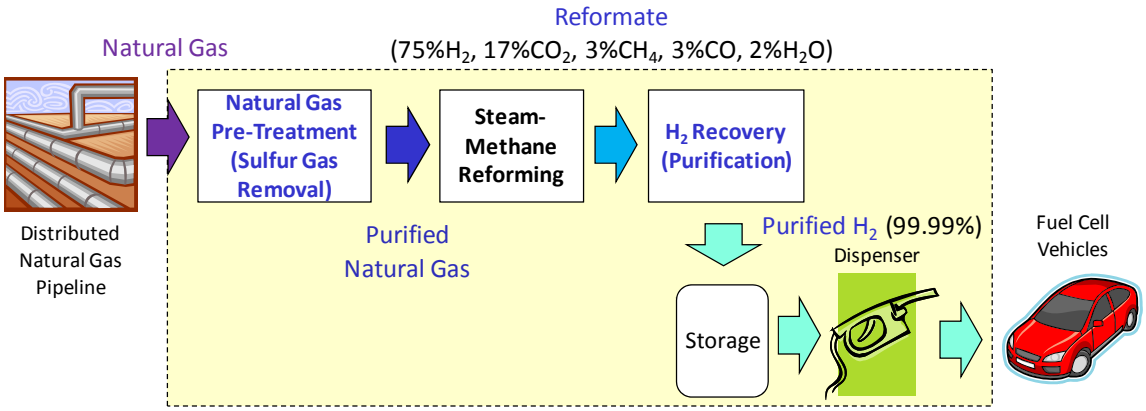

Figure 1-7 Schematic Flow Diagram of On-Site Hydrogen Fueling Station

Table 1-3 Composition Specifications for Natural Gas Delivery to the U.S. National Pipeline Grid [10]

Component	**Specification**	**U.S. Well Composition**	**% of Total U.S. Gas**
Methane	-	75 – 90%	-
CO_2	< 2 %	< 1 % 1 – 3 % 3 – 10 % > 10 %	72 % 18 % 7 % 3 %
H_2O	< 120 ppm	800 – 1,200 ppm	-
H_2S	< 4 ppm	< 4 ppm 4 – 1,000 ppm 1,000 – 10,000 ppm > 10,000 ppm	76 % 11 % 4 % 8 %
C_{3+} Content	950 – 1,050 Btu/scf Dew Point: < -20 °C	-	-
Inert Gas (He, N_2)	< 4 %	> 4 %	14 %

This table was slightly modified from the original table.

Table 1-4 Odorant Composition in the U.S. Pipeline Natural Gas [11]

Component	**Concentration [ppmv]**
Hydrogen Sulfide	0.4
Carbonyl Sulfide	1.0
Total Mercaptans	6 – 8
(Methyl Mercaptan; Ethyl Mercaptan; Isopropyl Mercaptan; N-Propyl Mercaptan; Tertiary Butyl Mercaptan)	
Dimethyl Sulfide	1 – 2
Tetrahydro Thiophene	1 – 2
Carbon Disulfide	< 1

This table was extracted from the original table.

A passenger FCV consumes 0.7 kg of hydrogen per day (kg-H_2/day) by assuming a fuel economy of 50 – 60 miles per kg of hydrogen (miles/kg-H_2) [12]. A fuel cell bus (or ZeBus) consumes 30 kg-H_2/day to provide 200 – 250 miles per day. A DOE case study for a distributed production based on natural gas provides 1,500 kg per day [13], which is equivalent to a capacity for approximately 2,500 passenger FCVs per day (based on 0.6 kg-H_2/day). The Chevron hydrogen fueling station shown in Figure 1-8 [14] can provide 150 kg/day purified hydrogen to serve three FC buses and ten passenger FCVs daily according to their analysis with a fuel economy of 20 – 30 miles/kg-H_2 [15], and approximately 200 passenger FCVs daily (based on 0.7 kg-H_2/day above).

Figure 1-8 Chevron On-Site Hydrogen Fueling Station (Oakland, California) [14]

1.3. Hydrogen Production

Current and future hydrogen production technologies are summarized in Table 1-5 [2]. As mentioned in Section 1.1 above, hydrogen gas is produced from water or hydrocarbon feedstocks. Industrial hydrogen production is roughly 50 million metric tons per year worldwide at present [16] and nearly half of the hydrogen is produced from natural gas (Table 1-6) [17]. Roughly 50% of the hydrogen is consumed in processes to generate hydrocarbons, ammonia and methanol (Table 1-7) [18]. The amount of gas to be sold outside including fuels for FCVs is still not large. Currently electrolysis is not well-implemented to produce hydrogen on purpose regardless of primary energy (fossil, renewable or nuclear) and requires long-term research for cost effective commercial production.

Table 1-5 Hydrogen Production Technologies [2]

Technology	Feedstock	Energy
Reforming	Natural Gas Oil/Bio-Liquid	Heat (Feedstock)
Gasification	Coal/Biomass	Heat (Feedstock)
Thermochemical	Water	Heat (Solar, Nuclear)
Water Electrolysis	Water	Electricity (Grid, Wind, Solar, Nuclear)
Photolysis	Water	Solar
Photolytic Biological	Water	Solar

Table 1-6 Hydrogen Production by Source [17]

Source	Share
Natural Gas	48%
Oil	30%
Coal	18%
Electrolysis	4%
Total	100%

Table 1-7 Hydrogen Production Capacity by Type [18]

Type	**Share**	
On-Purpose Captive	49%	
Oil Refinery		25%
Ammonia		21%
Methanol		2%
Other		~ 0%
On-Purpose Merchant	15%	
Off-Site Refinery		12%
Cylinder/Bulk		~ 0%
Pipeline		3%
Liquid H_2		1%
Small Reformer/Electrolizer		~ 0%
By-Products	36%	
Catalytic Reforming at Oil Refineries		28%
Other Off-Gas Recovery		4%
Chlor-Alkali Processes		4%
Total	100%	100%

The share in this table was calculated based on 2006 capacity.

Natural gas is converted into hydrogen typically with the following technologies; steam-methane reforming (SMR), partial oxidation (POX) and autothermal reforming (ATR) [2, 19-20]. The SMR is a well-developed technology at the industrial scale and contributes about 95% of the hydrogen production in the U. S. There is a two-step reaction with separate reactors in the SMR process;

1) Steam Reforming Reaction

$$CH_4 + H_2O \rightarrow CO + 3H_2 \text{ (endothermic, } \Delta H^\circ_{298K} = 206.2 \text{ kJ/mol)} \quad \text{.....(1.1)}$$

2) Water-Gas Shift (WGS) Reaction

$$CO + H_2O \rightarrow CO_2 + H_2 \text{ (exothermic, } \Delta H°_{298K} = -41.2 \text{ kJ/mol)} \quad (1.2)$$

The reaction temperature for the first reaction is at 700 – 1000 °C. The second reaction reduces CO level and increases the amount of hydrogen. High and low temperature water-gas shift (WGS) are performed at 350 – 500 °C with an iron/chrome oxide catalyst and 180 – 250 °C with a copper/zinc oxide catalyst, respectively. Depending on the application, low temperature WGS is eliminated. Typical conditions of produced reformates from the steam-methane reforming (SMR) are summarized in Table 1-8. For on-site hydrogen fueling stations, a highly integrated advanced steam methane reformer has been developed with significant downsizing to be installed in such a small area [21].

Table 1-8 Typical Reformate Conditions from SMR

Reference		[19]	[22]		[23]	[24]	[25]
Component							
H_2	%	74	70 – 80	77.1	70 – 75	74	73
CO_2	%	16	15 – 25	22.5	20 – 25	22.5	8.5
CH_4	%	7	3 – 6	0.013	4	Trace	5.5
CO	%	3	1 – 3	0.35	1	Trace	13
N_2	%	–	trace	–	–	Trace	–
H_2O	%	–	saturated	–	–	Trace	–
Temperature	°C	20 – 50	21 – 38	21	15 – 50	27	850
Pressure	atm	10 – 50	8 – 28	20.7	14 – 27	1	25

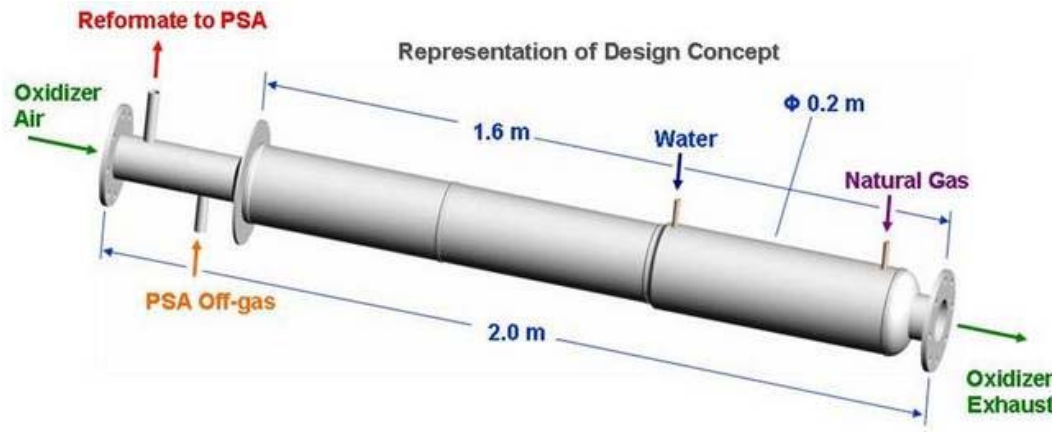

Figure 1-9 Advanced Steam Methane Reformer for On-Site Hydrogen Fueling Stations [21]

Catalytic partial oxidation (POX) is an exothermic reaction as follows and proceeds faster than the steam-methane reforming (SMR);

$$CH_4 + \tfrac{1}{2}O_2 \rightarrow CO + 2H_2 \text{ (endothermic, } \Delta H^\circ_{298K} = -35.6 \text{ kJ/mol)} \quad (1.3)$$

Smaller reactors can be built using this technology, but the yield of produced hydrogen is less than for SMR. The combination of reactions (1.1) and (1.3) is referred to as autothermal reforming (ATR). POX and ATR are more effective for handling heavy hydrocarbons such as naphtha. Oxygen availability from air separation units is also a critical factor to apply the POX and ATR instead of the SMR.

As long as hydrocarbon feedstocks or electricity produced from fossil fuels are used for hydrogen production, CO_2 is generated as a by-product and needs to be captured for reducing CO_2 emissions. Sequestration is storage of CO_2 under the ground permanently (Figure 1-10) [26]. This process is attractive to remove CO_2 from the atmosphere, but long-term impacts on the geological and ecological systems are unknown. Recycle of CO_2 as a raw material can also be beneficial for

sustainable carbon-based economy. It is widely accepted that CO_2 is thermodynamically stable, but CO_2 has a strong affinity toward nucleophiles and electron-donating reagents due to the electron deficiency of the carbonyl carbons [27]. Synthesis of polycarbonate from CO_2 without phosgene is an example of the material recycle and safer process (Figure 1-11).

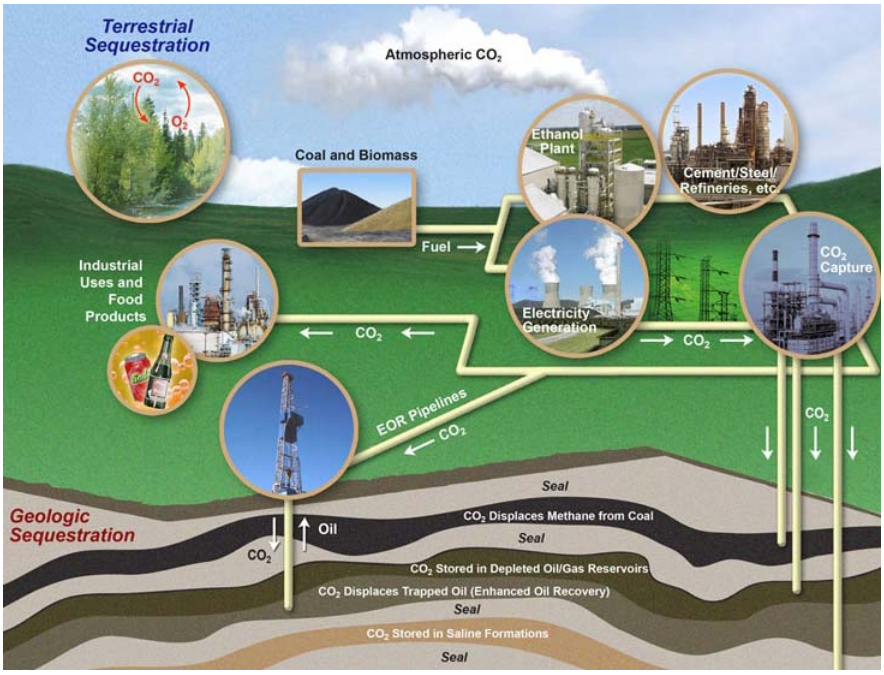

Figure 1-10 Schematic Diagram of Carbon Capture and Storage [26]

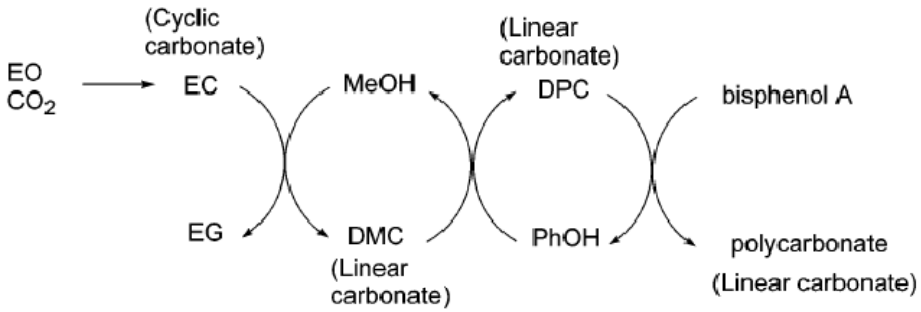

Figure 1-11 Non-Phosgene Process for Manufacturing Polycarbonate [27]

1.4. Separation Processes for Hydrogen Recovery and Purification

The separation process accounts for at least 50% of the capital investment for large scale production [28]. The DOE case study for a distributed production mentioned in Section 1.2 assumed that pressure swing adsorption (PSA) unit for hydrogen recovery occupies about 11% of the total capital cost (Table 1-9) [13]. In addition to capital and operational costs, productivity (production flow rate per separation media such as adsorbent amount or membrane area), recovery and purity are important performances to characterize the separation processes.

Table 1-9 Capital Cost for Distributed Production [13]

Major Systems	**Share**
Water Purification/Feed System	6.5%
NG Feed/Desulfurization System	3.6%
Air Feed/Burner/Boiler/Superheater	7.2%
Reformer	33.1%
Water Gas Shift Reactor	27.5%
Reformate Cooler	5.6%
Condenser	5.8%
Pressure Swing Adsorption Unit	10.9%
Total	100%

The items in this table were re-categorized from the original table.

There are four current technologies for hydrogen recovery: cryogenic distillation, PSA, membrane processes and gas-liquid contacting [29-30]. Cryogenic distillation employs volatility difference between hydrogen and impurities. Feed gas is cooled down to low enough temperature to condense impurities by applying Joule-Thomson refrigeration derived from a throttling process. Cryogenic distillation is advantageous only for large scale hydrogen production due to economy

of scale. For medium and small scales, PSA and membrane processes are candidates for hydrogen recovery based on the cost analysis for air separation (Figure 1-12) [31]. Counter-current gas absorption system cannot achieve high purity of product hydrogen gas competitively to PSA or membrane systems [30].

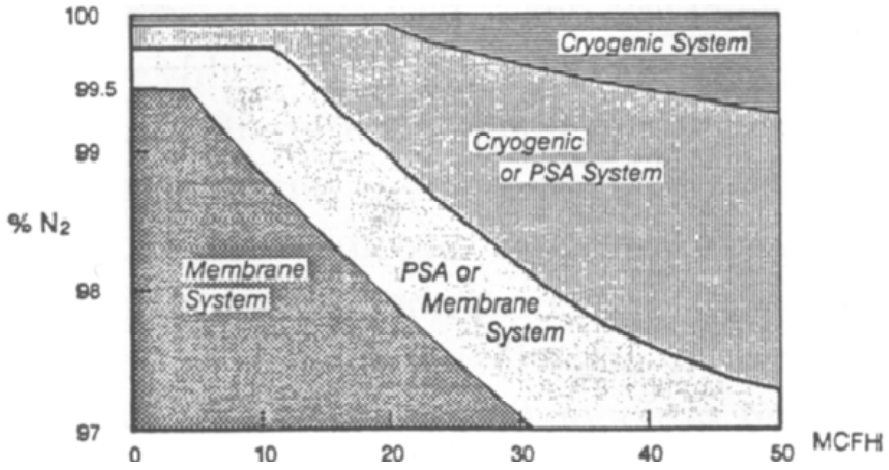

Figure 1-12 Cost Effectiveness Comparisons for Nitrogen Systems [31]

Hollow fiber polymeric membranes are popularly used for gas separations. Attaining high selectivity (or purity) and high permeability (or productivity) simultaneously is difficult for polymeric membranes [32]. The "upper-bound" curve is shown in Figure 1-13. Other types of membranes made of zeolite, carbon molecular sieve (CMS) and metals are also candidates, but face technical and economical challenges related to membrane formation, mechanical strength and cost [33]. Several membrane classes are summarized in Table 1-10.

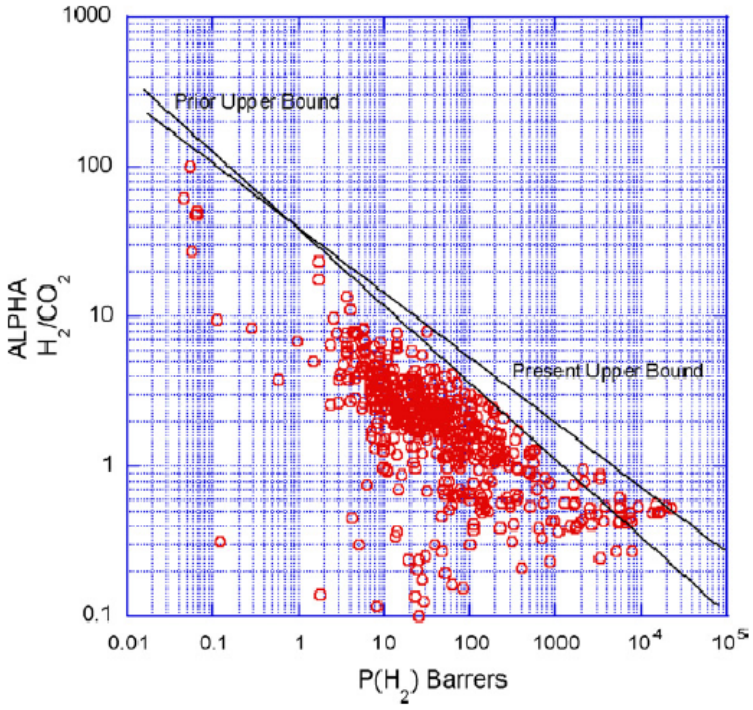

Figure 1-13 Upper Bound Curve for H_2/CO_2 Separation [32]

Table 1-10 Comparison of Membrane Classes for H_2 Separation

Class	**Dense Polymer**	**Dense Metallic**	**Dense Ceramic**	**Microporous Ceramic**	**Porous Carbon**
Materials	Polyester, Polyether Polyimide, Polyurethane, etc.	Pd, Ta, V, Nb, Alloy	Proton Conducting Ceramics ($SrCeO_{3-\delta}$, $BaCeO_{3-\delta}$)	Silica, Alumina Zirconia, Titania Zeolites	Carbon Molecular Sieve, Single-Wall Carbon Nanotube
Temperature Range [°C]	< 100	500 – 900	600 – 900	200 – 600	300 – 600
H_2 Selectivity	Low	4 – 20	> 1,000	5 – 139	> 1,000
H_2 Flux	Low	10 – 200	6 – 80	60 – 300	60 – 300
Stability Issue	Swelling, Compaction, Mechanical Strength	Phase Transition	Brittle, Stability in CO_2	Stability in H_2O	Very Brittle, Oxidizing
Poisoning Issue	HCl, SOx, (CO_2)	H_2S, HCl, CO	H_2S	-	Strong Absorbing Vapors, Organics
Transport Mechanism	Solution-Diffusion	Solution-Diffusion	Solution-Diffusion (Proton Conduction)	Molecular Sieving	Solution-Diffusion/ Molecular Sieving

This table was re-formatted from [33] and [34].

On the other hand, PSA with multiple packed bed columns is reliably operated at the industrial scale and can deliver high purity (99.99%) with high recovery (> 80%) [29]. Zeolite pellets are commonly used, which comprise small-size crystals (typically 1 – 10 μm) [35] and inorganic binder materials such as clay having appropriate porosity and mechanical strength for the packed beds. For bulk gas separation, which contains strongly adsorbed pieces more than 10% by weight, PSA is preferred compared with temperature swing adsorption (TSA) [36-37]. The packed bed, however, can potentially be improved in terms of the trade-off between mass transfer resistance and pressure drop [38]. Different configurations for radial diffusion (gas feed into a tube [39-40] or hollow fibers [41-42] embedded in packed beds) and different structures of adsorbents (sheet [38] and monolith [43-44]) have been proposed to overcome the above mentioned trade-off (Figure 1-14). Rotary valve-based fast cycle PSA units are installed at some on-site hydrogen fueling stations [45], but conclusions on the best method of gas separation are still under consideration. Another issue in packed beds can be attrition of the pellets which generate fine particles and cause clogging, capacity loss and other mechanical troubles by carryover from the columns.

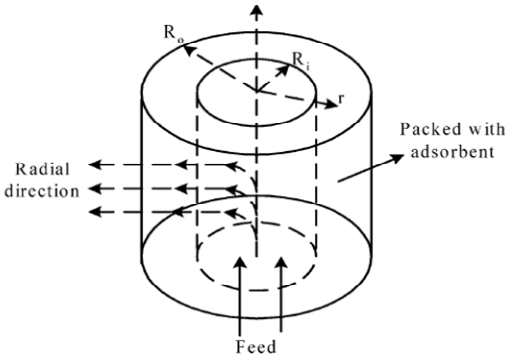

(a) Packed Bed with a Radial Flow [40]

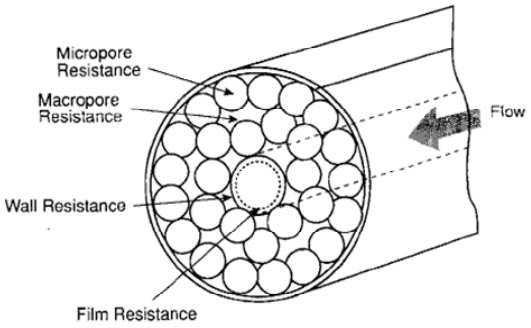

(b) Hollow Fibers in a Packed Bed [41]

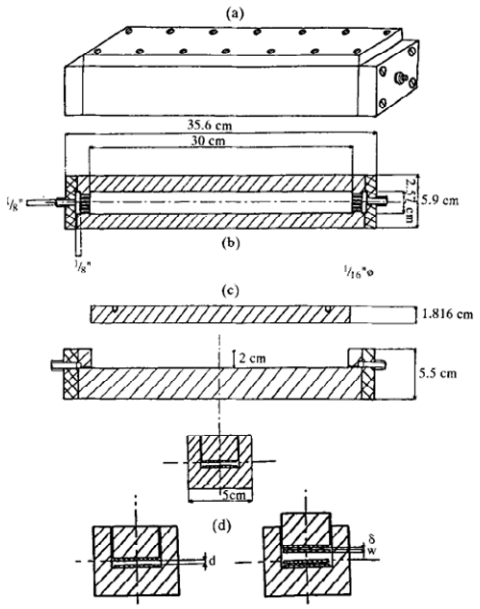

Figure 1 Details of the parallel passage adsorber. (a) Outside view of the cell. (b) Top view of the open cell. (c) Side view of the open cell. (d) Cross-section view of the parallel-sided duct coated with two or more layers of ACF adsorbent

(c) Sheet-Type Adsorbent [38]

	Mono1	Mono2	MonoC	SP7-9181
cpsi	100	200	400	–
D (cm)	1–3	1–3	1–3	–
s (mm)	0.8	0.5	0.3	–
ε_B	0.44	0.50	0.59	0.4
ϱ (g/cm^3)	1.15	1.15	1.15	1.13
R_m (N/mm^2)	≈30	≈30	≈30	≈30
FR	0.7–0.8	0.7–0.8	0.7–0.8	0.7–0.8

(d) Monolith-Type Adsorbent [44]

Figure 1-14 Modifications on Packed Bed for Better Mass Transfer

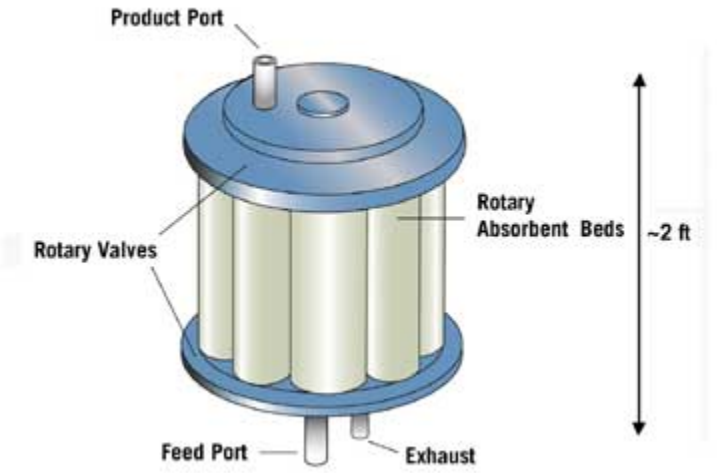

The elements of a rotary fast-cycle hydrogen PSA consist of set of structured adsorbent beds arranged between two rotary valves. The beds rotate around a central shaft. Feed gas enters the PSA module at one end and product gas is withdrawn from the opposite end of the module.

Figure 1-15 Rotary Valve-Based Fast-Cycle PSA Unit [45]

1.5. Research Objectives

A new concept, which will be referred to simply as "fiber sorbents," has arisen to provide a new format for gas separation. The ultimate goal of this research is to develop both fiber sorbents and a rapidly cycled pressure swing adsorption (RCPSA) process for the fiber sorbent module used in the hydrogen recovery application. In order to achieve this goal, the following objectives are investigated;

Objective 1: Assess the feasibility of the fiber sorbent concept for the hydrogen recovery application

Objective 2: Produce fiber sorbents with high sorption capacity by spinning polymer solution with high loading of zeolite and by manipulating internal morphology to create a highly porous structure

1) Select appropriate polymer and zeolite for the fiber sorbents
2) Optimize dope composition and spinning conditions for the fiber sorbents

Objective 3: Characterize the fiber sorbents in terms of porous structure and transport properties

1) Evaluate porous structure of the fiber sorbents
2) Determine gas transport properties of the fiber sorbents for single and mixed gases

Objective 4: Develop a rapidly cycled PSA (RCPSA) process for the fiber sorbent module by building a laboratory scale system and validating results by comparing with computer simulated results

1) Determine breakthrough characteristics
2) Demonstrate an RCPSA process for module operation with/without thermal moderation
3) Simulate dynamic modeling and evaluate the results comparing with experimental data

1.6. Dissertation Overview

This dissertation is divided into seven chapters including this chapter. The description of each of the chapters is as follows: Chapter 2 explains the concept of "fiber sorbents" and modeling of

theoretical calculations to assess feasibility of the fiber sorbent and the module operation. Chapter 3 describes materials and experimental methods used throughout this research. Chapter 4 describes results of bare fiber sorbent spinning and characterization of the spun fibers. Chapter 5 describes additional efforts to develop impermeable layer development by spinning and post-treatment with characterization. Chapter 6 describes dynamic behavior of fiber sorbent module in PSA process with a newly constructed laboratory scale system and comparison with simulation. Chapter 7 summarizes the accomplishments of this research and recommendations for the future works.

1.7. References

1. Le Treut, H. and R. Somerville, *Chapter 1 Historical Overview of Climate Change Science*, in *Contribution of Working Group I to the Fourth Assessment Report of the Intergovernmental Panel on Climate Change*, S. Solomon, et al., Editors. 2007, Cambridge University Press,: Cambridge, UK; New York, NY, USA. p. 93-127.

2. U.S. Department of Energy. *Fuel Cell Technologies Program*. 2010 [cited 2010 August, 10]; Available from: http://www1.eere.energy.gov/hydrogenandfuelcells

3. FreedomCAR and Fuel Partnership, *Hydrogen Production Roadmap: Technology Pathways to the Future*. 2009.

4. National Research Council (U.S.). Committee on Alternatives and Strategies for Future Hydrogen Production and Use, National Academy of Engineering, and National Academy of Sciences (U.S.), *The Hydrogen Economy : Opportunities, Costs, Barriers, and R&D Needs*. 2004, Washington, D.C.: National Academies Press.

5. U.S. Department of Energy, *Hydrogen Cost Competitive on a Cents per Mile Basis*, U.S. Department of Energy, Editor. 2006.

6. U.S. Energy Information Administration. *Petroleum Navigator - Spot Prices*. 2010 [cited 2010 August 10]; Available from: http://www.eia.gov/.

7. Fuel Cell 2000. *Fuel Cell Reference Charts*. 2010 [cited 2010 August 10]; Available from: http://www.fuelcells.org/info/charts.html.

8. U.S. Department of Energy and U.S. Environmental Protection Agency. *www.fueleconomy.gov the Official U.S. Government Source for Fuel Economy Information*. 2010; Available from: http://www.fueleconomy.gov/.

9. Honda Motor Co. Ltd. *Honda FCX Clarity Overview - Fuel Cell Electric Vehicle*. 2010 [cited 2010 August 10]; Available from: http://automobiles.honda.com/fcx-clarity/.

10. Baker, R.W. and K. Lokhandwala, *Natural Gas Processing with Membranes: An Overview.* Industrial & Engineering Chemistry Research, 2008. **47**(7): p. 2109-2121.

11. Katikaneni, S., et al., *The Direct Carbonate Fuel Cell Technology: Advances in Multi-Fuel Processing and Internal Reforming.* Catalysis Today, 2002. **77**(1-2): p. 99-106.

12. California Fuel Cell Partnership, *Vision for Rollout of Fuel Cell Vehicles and Hydrogen Fuel Stations*. 2008.

13. U.S. Department of Energy. *DOE H2A Analysis*. 2008 [cited 2010 August 10]; Available from: http://www.hydrogen.energy.gov/h2a_analysis.html.

14. Coates, M. *Chevron Hydrogen Boss Explores the Future of Fueling*. [cited 2010 August 10]; Available from: http://www.hydrogenforecast.com/ArticleDetails.php?articleID=300.

15. Chevron Technology Ventures LLC, *Questions & Answers Chevron Hydrogen Energy Station AC Transit Operations Center – Oakland, California*. 2006.

16. Ogden, J. *Hydrogen as an Energy Carrier: Outlook for 2010, 2030 and 2050*. in *The 10-50 Solution: Technologies and Policies for a Low-Carbon Future*. 2004.

17. U.S. Department of Energy. *Hydrogen, Fuel Cells, and Infrastructure Technologies - Commonly Used Data*. 2003; Available from: https://apps3.eere.energy.gov/ba/pba/analysis_database/docs/excel/hydrogen.xls.

18. U.S. Energy Information Administration. *The Impact of Increased Use of Hydrogen on Petroleum Consumption and Carbon Dioxide Emissions*. 2008 [cited 2010 August 10]; Available from: http://www.eia.doe.gov/oiaf/servicerpt/hydro/index.html.

19. Ritter, J.A. and A.D. Ebner, *State-of-the-Art Adsorption and Membrane Separation Processes for Hydrogen Production in the Chemical and Petrochemical Industries.* Separation Science and Technology, 2007. **42**(6): p. 1123-1193.

20. Navarro, R.M., M.A. Pen˜a, and J.L.G. Fierro, *Hydrogen Production Reactions from Carbon Feedstocks: Fossil Fuels and Biomass.* Chemical Review, 2007. **107**(10): p. 3952-3991.

21. Green Car Congress. *On-Site Steam Methane Reforming Unit for Hydrogen Refueling Station*. 2006 [cited 2010 August 10]; Available from: http://www.greencarcongress.com/2006/08/onsite_steam_me.html.

22. Sircar, S. and T.C. Golden, *Purification of Hydrogen by Pressure Swing Adsorption.* Separation Science and Technology, 2000. **35**(5): p. 667-687.

23. Anand, M. and M.B. Rao, *Hydrogen Recovery by Adsorbent Membranes*, in *U.S. Patent No.5,435,836*. 1995.

24. Safdar, M., A. Baksh, and F. Nataro, *PSA Process and System*, in *U.S. Patent No.6,007,606*. 1999.

25. Hufton, J.R., et al., *Integrated Steam Methane Reforming Process for Producing Carbon Monoxide and Hydrogen*, in *U.S. Patent No.6,312,658*. 2001.

26. U.S. Department of Energy. *Carbon Capture and Storage R&D Overview*. 2010 [cited 2010 August 10].

27. Sakakura, T., J.-C. Choi, and H. Yasuda, *Transformation of Carbon Dioxide.* Chemical Reviews, 2007. **107**(6): p. 2365-2387.

28. Nenoff, T.M., R.J. Spontak, and C.M. Aberg, *Membranes for Hydrogen Purification: An Important Step toward a Hydrogen-Based Economy.* MRS Bulletin, 2006. **31**(10): p. 735-741.

29. Miller, G.Q. and J. Stöcker, *Selection of a Hydrogen Separation Process*, in *National Petrochemical and Refiners Association Annual Meeting, San Francisco*. 1989, UOP Report 3111, January 1999.

30. Peramanu, S., B.G. Cox, and B.B. Pruden, *Economics of Hydrogen Recovery Processes for the Purification of Hydroprocessor Purge and Off-Gases.* International Journal of Hydrogen Energy, 1999. **24**(5): p. 405-424.

31. Koros, W.J. and G.K. Fleming, *Membrane-Based Gas Separation.* Journal of Membrane Science, 1993. **83**(1): p. 1-80.

32. Robeson, L.M., *The Upper Bound Revisited.* Journal of Membrane Science, 2008. **320**(1-2): p. 390-400.

33. Ockwig, N.W. and T.M. Nenoff, *Membranes for Hydrogen Separation.* Chemical Reviews, 2007. **107**(10): p. 4078-4110.

34. Kluiters, S.C.A., *Status Review on Membrane Systems for Hydrogen Separation*, Energy Research CEntre of the Netherlands, Editor. 2004.

35. Ruthven, D.M., *Principles of Adsorption and Adsorption Processes*. 1984, New York: Wiley-Interscience Publication.

36. Keller, G.E., II, and R.L. Jones, *A New Process for Adsorption Separation of Gas Stream*, in *Adsorption and Ion Exchange with Synthetic Zeolites: Principles and Practice*, W.H. Flank, Editor. 1980, American Chemical Society: Washington, D.C. p. 275-286.

37. Yang, R.T., *Chapter 6 Cyclic Gas Separation Processes*, in *Gas Separation by Adsorption Processes*. 1997, World Scientific: Singapore ; River Edge, N.J. p. 201-235.

38. Ruthven, D.M. and C. Thaeron, *Performance of a Parallel Passage Adsorbent Contactor.* Gas Separation & Purification, 1996. **10**(1): p. 63-73.

39. Chiang, A.S.T. and M.C. Hong, *Radial Flow Rapid Pressure Swing Adsorption.* Adsorption, 1995. **1**(2): p. 153-164.

40. Huang, W.C. and C.T. Chou, *Comparison of Radial- and Axial-Flow Rapid Pressure Swing Adsorption Processes.* Industrial & Engineering Chemistry Research, 2003. **42**(9): p. 1998-2006.

41. Gilleskie, G.L., J.L. Parker, and E.L. Cussler, *Gas Separations in Hollow-Fiber Adsorbers.* Aiche Journal, 1995. **41**(6): p. 1413-1425.

42. Feng, X., et al., *Hollow-Fiber-Based Adsorbers for Gas Separation by Pressure-Swing Adsorption.* AIChE Journal, 1998. **44**(7): p. 1555-1562.

43. Patton, A., B.D. Crittenden, and S.P. Perera, *Use of the Linear Driving Force Approximation to Guide the Design of Monolithic Adsorbents.* Chemical Engineering Research & Design, 2004. **82**(A8): p. 999-1009.

44. Gorbach, A., *Compact Rapid Pressure Swing Adsorption Processes - Impact of Novel Adsorbent Monoliths*, in *Ph.D. Thesis*. 2006, Stuttgart University, Germany.

45. Babicki, M. and A. Hall. *PSA Technology Hits the Fast Lane*. 2003 [cited 2010 August 10]; Available from: http://www.chemicalprocessing.com/articles/2003/322.html?page=full.

CHAPTER 2 BACKGROUD AND THEORY

2.1. Concept of a "Fiber Sorbent"

Fiber sorbents enable one to realize pseudo-monolithic structures comprising polymer and adsorbent as shown in Figure 2-1. Such materials are produced as hollow (or solid) fibers using spinning technology, which has been developed for polymeric hollow fiber membranes [1-2]. Different polymers and adsorbents can be selected for specific applications. In this research, a spinning process extrudes a zeolite dispersed in a polymer solution ("dope") from a spinneret (die), and phase separation is induced in an aqueous quenching media to create a porous structure throughout the fiber matrix. The fiber sorbents, with uniformly dispersed zeolite crystals can be bundled into convenient modules using technology like that to form membrane modules [3]. Feed gas can then be introduced from either bore side (inside of hollow fibers) or shell side (outside) depending upon the specific application (Figure 2-2).

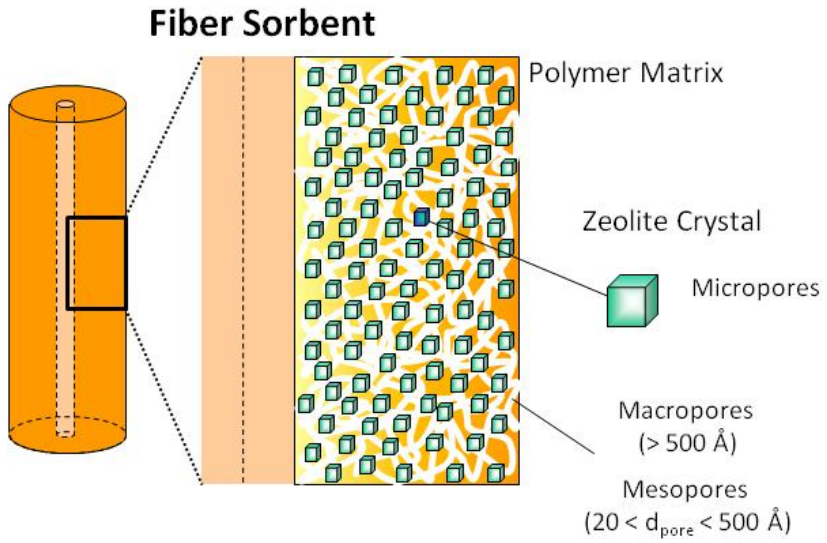

Figure 2-1 Schematic of Fiber Sorbent

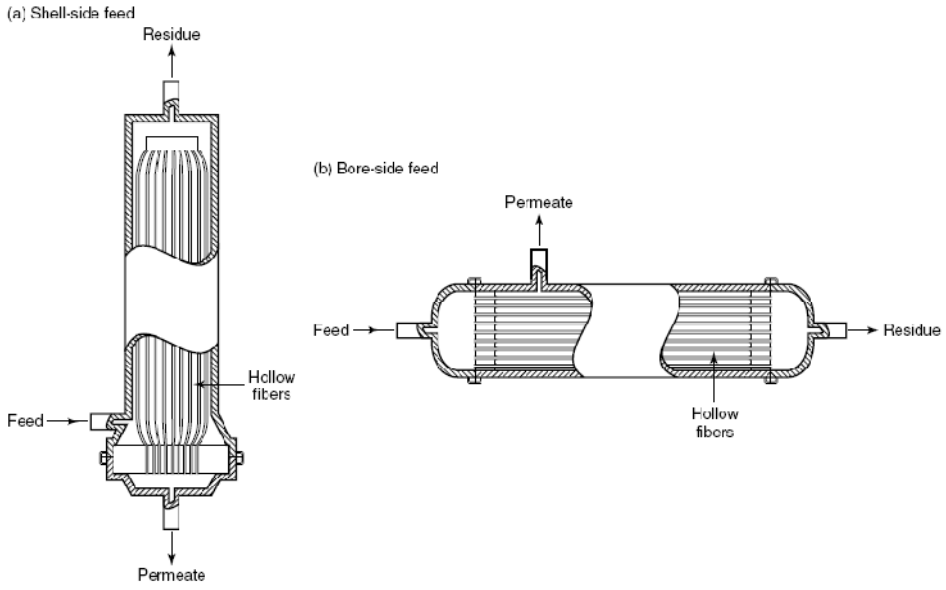

Figure 2-2 Hollow Fiber Membrane Modules [3]

The zeolite is loaded at a high enough level to give high sorption capacity for capturing impurities. Zeolite-dispersed polymer solutions are also applied for mixed matrix membranes (MMMs) for gas separation. In most of the MMM cases, however, the solutions form an additional layer at the external surface of the hollow fiber to impart the selectivity and the loading level is typically less than 40 wt% [4]. Typical zeolite pellets contain 10 – 20 wt% of the binder material [5]. For fiber sorbents, it is desired to use similar zeolite loading level; however, the zeolite is dispersed throughout the entire fiber wall, which presents technical challenges to disperse large amount of the zeolite crystals homogeneously in polymer solutions and to spin the high zeolite loading dope. The term "sorption" usually stands for a combinational effect of "absorption" by a swellable body and "adsorption" into or onto a rigid porous body. Since the fiber sorbent is highly loaded with zeolite, adsorption capacity of the zeolite contributes most of the total sorption capacity of the fiber sorbent and the sorption capacity of the polymer tends to be relatively small. The polymer acts as a binder primarily for the zeolite crystals and gives adequate mechanical strength with an

interconnected porous structure. The morphology of the porous structure is mainly manipulated through the phase separation in the spinning process. Another feature, the "sieve-in-a-cage" morphology, is typified by an incomplete adhesion between polymer and zeolite surfaces [6-7]. Defective morphologies for the membrane performance related to the mixed matrix membrane formation were reported as shown Figure 2-3. The sieve-in-a-cage morphology is disadvantageous for membranes to reduce selectivity with increasing permeability, but is advantageous for fiber sorbents to allow fast diffusion through the matrix and avoid polymer obstruction of the zeolitic pores.

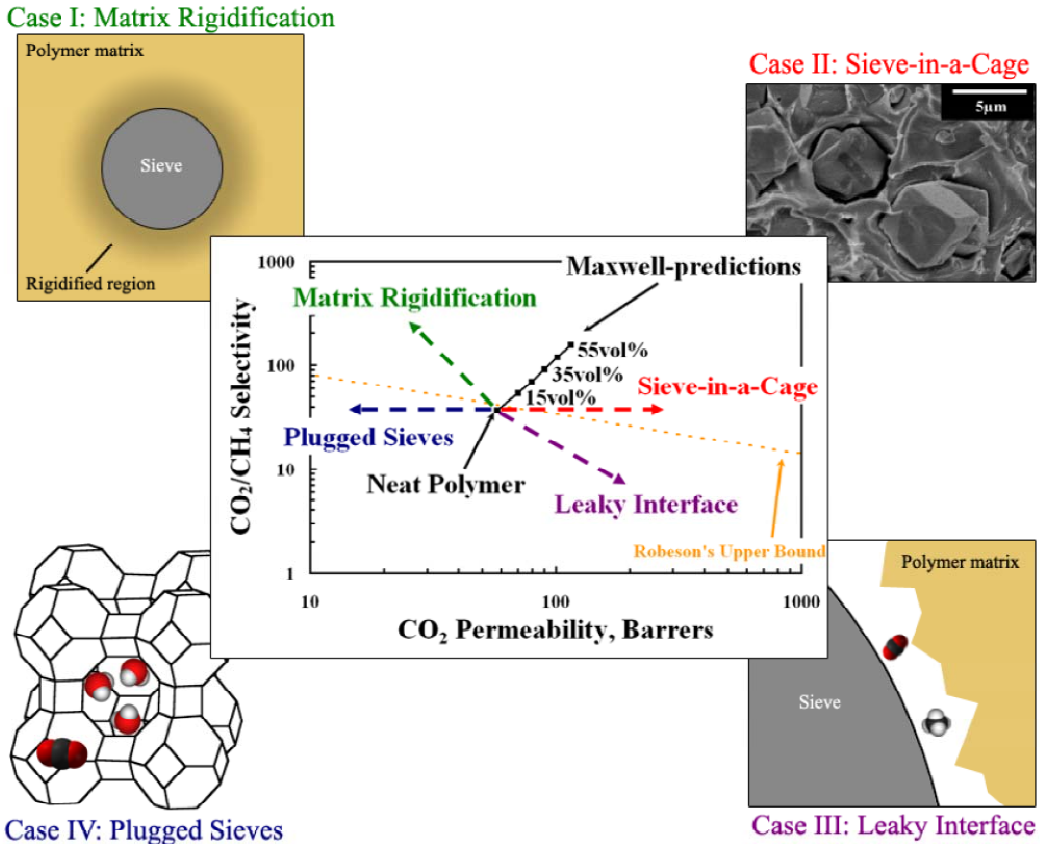

Figure 2-3 Common Interfacial Morphologies and Their Respective Effects on Membrane Transport Properties [7]

Hollow fiber membranes dispersed with ion exchange resin powders were reported for liquid application [8-9]. The loading level of adsorbent/ion exchange resins was still less than 50 wt%. Similar zeolite-based fiber sorbents for gas separation were reported [10-11], but the materials were used in a different process with electric heating regeneration by applying carbon-based electric conductive materials inside. Since the polymer composites have higher electric resistance and possibly become brittle due to degradation, there is a risk of explosion for flammable gases due to short circuit. Energy efficiency is also questionable compared with other heating approaches. Other applications of the fiber sorbents such as carbon dioxide removal from flue gas [12-13] and sulfur gas removal from natural gas [14] are under development in the Koros research group and rely upon a temperature swing adsorption (TSA) process. Impermeable layers inside or outside of the hollow fiber sorbent are necessary to isolate the fiber sorbent from a stream of heating media used in a TSA regeneration step.

A pressure swing adsorption (PSA) process is preferable for bulk gas separation such as hydrogen recovery from reformate gas [15-16] and also benefits from an impermeable layer to hinder mass transfer at the external surface of the fiber sorbent for bore-side feed operation. The highly porous structure without impermeable layer allows by-pass of feed gas into the shell side. To form the impermeable layer, spinning with a specially designed spinneret to create dual layer hollow fibers, or post-treatment coating can be applied. In this research, development of fiber sorbents with high loading of zeolite in polymers and application to hydrogen recovery at hydrogen fueling station with PSA processes were explored.

2.2. Hollow Fiber Sorbent Spinning

Phase separation behavior of polymer solutions is a key role in the polymeric hollow fiber membrane spinning process [17], and this technology is applied to spin hollow fiber sorbents. A selected polymer is dissolved in a solvent(s) and mixed with a non-solvent (coagulant). A pore former is also added if necessary, which helps to increase porosity in the final fiber. A ternary phase diagram for the polymer-solvent-non solvent system as shown in Figure 2-4 is prepared to identify a boundary between one-phase and two phase regions, the so called "binodal" curve. The binodal curve can be defined as "cloud points" in experiments, which delineate the boundary between thermodynamically stable and metastable regions. On the other hand, another boundary between unstable and metastable regions is called "spinodal" curve, which is calculated thermodynamically. There are different phase separation mechanisms in metastable and unstable regions. In the metastable regions, a "nucleation and growth" mechanism is observed. Bubbles are created in polymer-rich phase with closed cell structure above the critical point, while polymer beads are created in polymer-lean phase below critical point. In the unstable region, a "spinodal decomposition" mechanism is observed, and spontaneous phase separation occurs so that a bi-continuous porous structure is created. Theoretical calculation to predict binodal and spinodal curves are discussed for cellulose acetate-NMP-water system in Appendix A.

The procedure of dispersing zeolite in a dope with high loading is a critical step for fiber sorbents. Ultrasonic irradiation with a horn is effective to disperse zeolite particles in a liquid, but the detailed method should be different from that developed for mixed matrix membranes by previous researchers [18] since the amount of the dope and loading level of zeolite are very different (> 50% vs. < 40%). The maximum loading limit of zeolite that allows maintaining fluidity is typically used to spin the dope as a solution. Zeolite particles are an additional

component in the dope that may impact on the phase diagram of a pure polymer solution, but its effect is not well understood. Zeolite which is pre-saturated with water vapor can be considered to be an inert filler with minimal mass exchange with the surrounding phase separating matrix. Phase separation phenomena are discussed based on pure polymer solution.

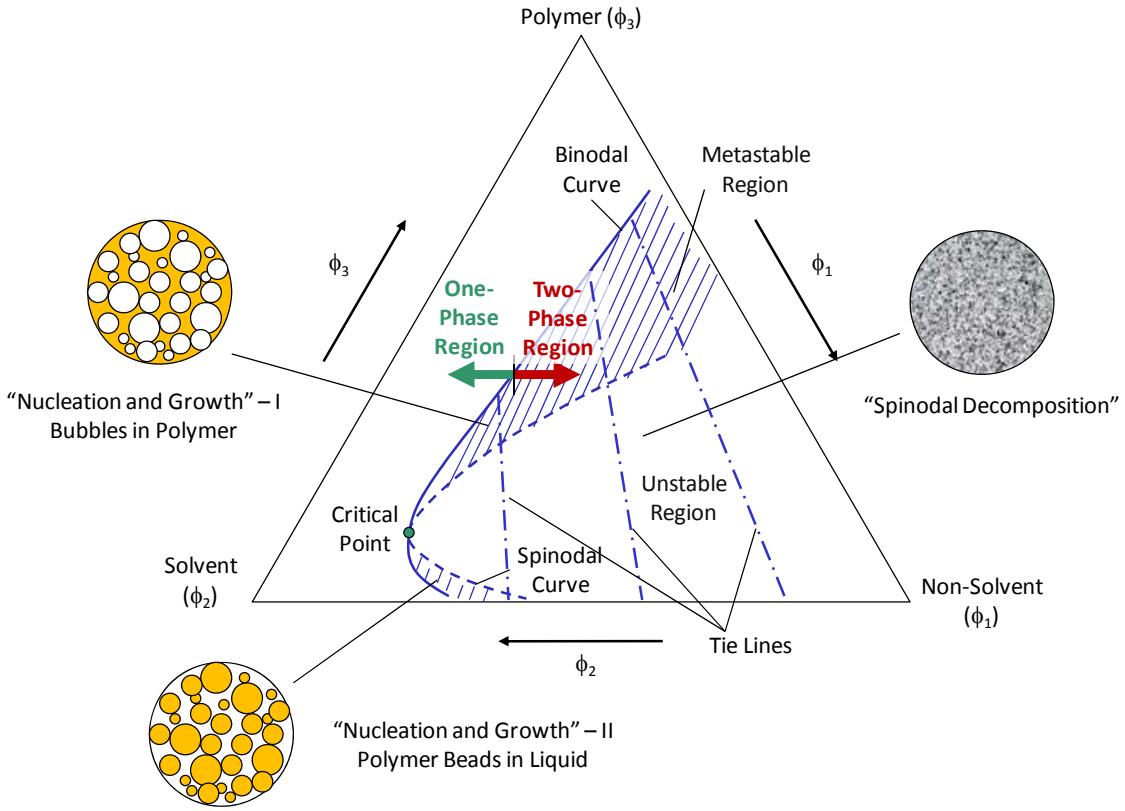

Figure 2-4 Ternary Phase Diagram

A composition is selected for preparing a "dope," which corresponds to a polymer-zeolite solution to be spun with the apparatus shown in Figure 2-5. Many factors in the spinning conditions summarized in Table 2-1 affect geometrical, structural and mechanical properties of the spun fiber [1]. The composition close to the binodal curve gives fast phase separation. By

changing the path over the ternary phase diagram, various porous structures can be formed during the spinning process. For the fiber sorbent, a truly porous structure is desired to allow gas molecules to contact an interior volume of zeolite crystals efficiently. As mentioned above, rapid diffusion rate of non-solvent from the quenching bath during the spinning process is desired to shift the dope composition into the unstable region to create the porous structure. Universally "best spinning conditions" do not exist, since the desired conditions depend on desired properties of the fiber and the purpose (application). The best material selection and spinning conditions are explored in this research specifically for fiber sorbents used in hydrogen recovery applications.

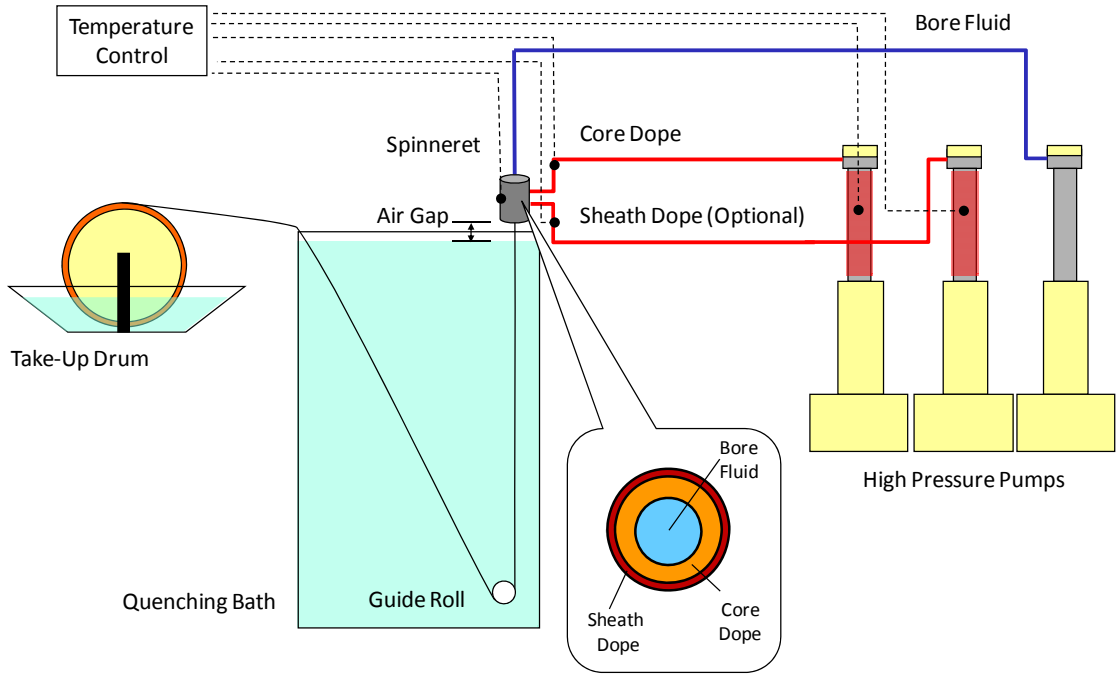

Figure 2-5 Schematic Diagram of Hollow Fiber Sorbent Spinning Apparatus

Table 2-1 Spinning Conditions for Fiber Sorbents

Dope (Core and Sheath)	Composition Temperature Flow Rate
Bore Fluid	Composition Temperature Flow Rate
Spinneret	Type Temperature
Air Gap	Distance Temperature Humidity Air Flow
Quenching Bath	Media Depth Temperature
Collection	Take-Up Rate Media Temperature
Solvent Exchange	Non-Solvent Time
Drying	Temperature Pressure (Atmospheric/Vacuum) Time

2.3. Sorption Capacity

Sorption capacity for target gases is a crucial property to characterize fiber sorbents. Ideally the maximum sorption capacity is desired to be equivalent to that determined by weight fraction and sorption capacity of pure zeolite which is mixed in the polymer matrix. Several types of sorption capacity curve (isotherm) are classified for different adsorbents [19]. A Langmuir-type isotherm

is normally observed for zeolite when micropore size is not much larger than the molecular diameter of the impurity gases, so that an approximate single site physisorption description applies with adequate accuracy for engineering purposes. The dual sorption mechanism is expected for glassy polymers [20-21]. Sorption capacities of zeolite crystal, q_c [mol/kg], and polymer, q_{pm} [mol/kg], are described;

$$q_c = \frac{q_{c,s} b_c p_2}{1 + b_c p_2} \quad \text{.....(2.1)}$$

$$q_{pm} = k_{pm} p_2 + \frac{q_{pm,s} b_{pm} p_2}{1 + b_{pm} p_2} \quad \text{.....(2.2)}$$

where,

subscript c; for zeolite crystal

subscript pm; for polymer

k; Henry's law constant [mol/kg/Pa]

q_s; saturation capacity (Langmuir capacity parameter) [mol/kg]

b; Langmuir constant (Langmuir affinity parameter) [Pa^{-1}]

p_2; partial pressure of Component 2 (CO_2) [Pa]

All of parameters used in Equations (2.1) and (2.2) are supposed to be temperature-dependent [20];

$$q_{c,s} = q_{c,s0} \exp\left(\frac{-\Delta H_{q,c}}{R_g T} \right) \quad \text{.....(2.3)}$$

$$b_c = b_{c0} \exp\left(\frac{-\Delta H_{ads,c}}{R_g T} \right) \quad \text{.....(2.4)}$$

$$k_{pm} = k_{pm0} \exp\left(\frac{-\Delta H_{dis,pm}}{R_g T} \right) \quad \text{.....(2.5)}$$

$$q_{pm,s} = q_{pm,s0} \exp\left(\frac{-\Delta H_{q,pm}}{R_g T} \right) \quad \text{.....(2.6)}$$

$$b_{pm} = b_{pm0} \exp\left(\frac{-\Delta H_{ads,pm}}{R_g T} \right) \quad \text{.....(2.7)}$$

where,

subscript 0; pre-exponential factor

$-\Delta H$; apparent enthalpy change charactering temperature dependence [J/mol]

R_g; gas constant (= 8.314472 J/mol/K)

T; temperature [K]

The enthalpy changes which are appeared in Equations (2.3) – (2.7) characterize the temperature dependence of the parameters k, q_s and b. The enthalpy change for Henry constant, $-\Delta H_{dis}$, is corresponding to the heat of dissolution from gas phase into solid phase [20]. The enthalpy change for saturation capacity, $-\Delta H_q$, may not have a simple physical meaning [20], but correlated to distribution of surface adsorption potential [22]. The enthalpy change for Langmuir constant, $-\Delta H_{ads}$, is corresponding to the heat of adsorption. The parameters calculated from literature data are summarized in used in Table 2-2. An empirical isotherm equation with temperature dependence, Toth equation, for the NaY was proposed [23] below and the parameters are summarized in Table 2-3.

Table 2-2 Sorption Parameters for CO_2 to Zeolite NaY and Cellulose Acetate

			$q_{c,s0}$	$-\Delta H_{q,c}$	b_{c0}	$-\Delta H_{ads,c}$
			[mol/kg]	[kJ/mol]	[Pa^{-1}]	[kJ/mol]
Choudhary [24] *1			3.791	1.792	2.647×10^{-9}	22.86
			$q_{c,s}$		b_c	
			[mol/kg]		[Pa^{-1}]	
35 °C			7.640		1.988×10^{-5}	
60 °C			7.273		1.018×10^{-5}	
	k_{pm0}	$-\Delta H_{dis,pm}$	$q_{pm,s0}$	$-\Delta H_{q,pm}$	b_{pm0}	$-\Delta H_{ads,pm}$
	[mol/kg/Pa]	[kJ/mol]	[mol/kg]	[kJ/mol]	[1/Pa]	[kJ/mol]
Stern and De Meringo [25] *2	4.896×10^{-11}	22.86	0.1580	4.953	1.889×10^{-10}	23.34
	k_{pm}		$q_{pm,s}$		b_{pm}	
	[mol/kg/Pa]		[mol/kg]		[1/Pa]	
35 °C	3.666×10^{-7}		1.092		1.707×10^{-6}	
60 °C	1.877×10^{-7}		0.9447		8.617×10^{-7}	
Puleo et al [21] (35°C) *3						
Cycle 1	5.279×10^{-7}		0.4575		2.990×10^{-6}	
Cycle 2	4.574×10^{-7}		0.7684		2.448×10^{-6}	

*1 The parameters were derived from the data at less than 200 kPa.
*2 The parameters were calculated from the data on Figure 5 in the reference.
*3 The parameters were derived from the data at 35 °C and less than 2.5 MPa, and converted for the units used in this table.

$$q_c = q_{c,T}\left(\frac{b_{c,T}}{p_2^t}+1\right)^{-\frac{1}{t}} \quad \text{.....(2.8)}$$

$$b_{c,T} = b_{c,T0}\exp\left(\frac{-t\Delta H_{ads,T}}{R_g T}\right) \quad \text{.....(2.9)}$$

where,

t; Toth parameter [-]

$b_{c,T}$; Toth parameter [-]

$-\Delta H_{ads,T}$; (isosteric) heat of adsorption [J/mol]

R_g; gas constant (= 8.314472 J/mol/K)

T; temperature [K]

Table 2-3 Sorption Parameters for CO_2 to Zeolite NaY (Toth Equation)

	t [-]	$b_{c,T0}$ [-]	$q_{c,T}$ [mol/kg]	$-\Delta H_{ads,T}$ [kJ/mol]
Walton and LeVan [23]	0.727	4.675×10^4	7.128	28.74

The unit for p_2 is in kPa.

Dimensionless sorption equilibrium constants of zeolite and polymer (volume of adsorbed gas per volume of zeolite or polymer), K_c [m^3-gas/m^3-zeolite crystal] and K_{pm} [m^3-gas/m^3-polymer], are described as;

$$K_c = \frac{\rho_c q_c}{C_2} \quad \text{.....(2.10)}$$

$$K_{pm} = \frac{\rho_{pm} q_{pm}}{C_2} \quad \text{.....(2.11)}$$

where,

ρ; (true) density [kg/m^3]

q; (mass) sorption capacity [mol/kg]

C_2; concentration of Component 2 (CO_2) [mol/m^3]

Volumetric sorption capacity and dimensionless sorption equilibrium constant of a fiber sorbent, $q_{V2,f}$ [mol/m^3] and K_f [m^3-gas/m^3-fiber sorbent] are described as;

$$q_{V2,f} = K_f C_2 \quad \text{.....(2.12)}$$

$$K_f = \varepsilon_f + \phi_c K_c + \phi_{pm} K_{pm} \quad \text{.....(2.13)}$$

where,

ε_f; porosity of a fiber sorbent [-]

ϕ_c; volume faction of zeolite crystals in a fiber sorbent [-]

ϕ_{pm}; volume faction of polymer in a fiber sorbent [-]

By applying the parameters in Table 2-2, the dimensionless sorption equilibrium constants for NaY and CA at the feed conditions of the reformate (Table C-1, p_{fd} = 100 psig, T_{fd} = 60 °C and y_{2fd} = 25 mol%) became K_c = 95.3 and K_{pm} = 3.2, respectively. The porosity is significantly smaller than the second and the third terms. Equations (2.10) and (2.11) are approximated as;

$$q_{V2,f} \simeq \phi_c \rho_c q_c + \phi_{pm} \rho_{pm} q_{pm} \quad \text{.....(2.14)}$$

$$K_f \simeq \phi_c K_c + \phi_{pm} K_{pm} = \left\{ \phi_c \rho_c \frac{q_{c,s} b_c}{1 + b_c p_2} + \phi_{pm} \rho_{pm} \left(k_D + \frac{q_{pm,s} b_{pm}}{1 + b_{pm} p_2} \right) \right\} R_g T \quad \text{.....(2.15)}$$

2.4. Pressure Swing Adsorption

Essential steps for a PSA process are described below and shown in Figure 2-6 [26-27];

Step I Pressurization

Step II Adsorption

Step III Depressurization (Blowdown) (counter-currently)

Step IV Desorption (Purge) (with raffinate product counter-currently)

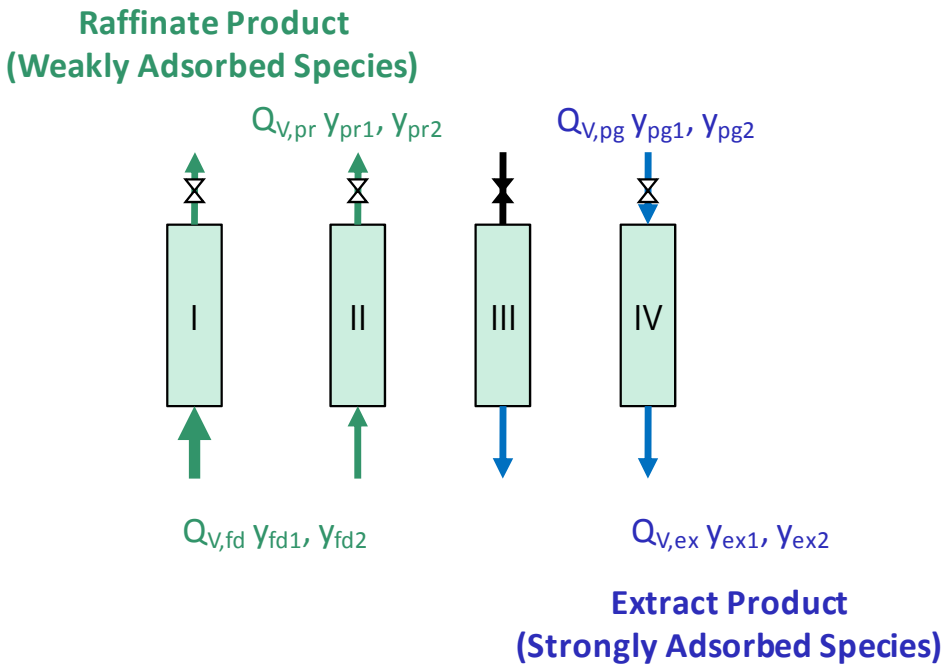

Figure 2-6 General PSA Sequential Operation

Substantially, adsorption occurs in Steps I and II at high pressure, and desorption (regeneration) in Steps III and IV at low pressure. Prior to breakthrough of the bed, Step III starts for regeneration. When two product gases are produced, weakly adsorbed species are obtained as a "raffinate" product in the adsorption step and strongly adsorbed species are obtained as an "extract" product in the desorption step. In this research, hydrogen is only recovered as a raffinate product. The extract, which is mainly CO_2, is discharged as an exhaust, but is fed to a burner as a part of fuels for steam-fuel reformer in the industrial cases since it contains hydrogen as the purge gas. The product gas (raffinate) flow is discontinued in the Steps III and IV. Therefore, the system consists of two beds to work complementarily with each other in order to produce the product gas continuously as a system, which was developed by Skarstrom. While Bed A is working, Bed B is regenerated (Figure 2-7).

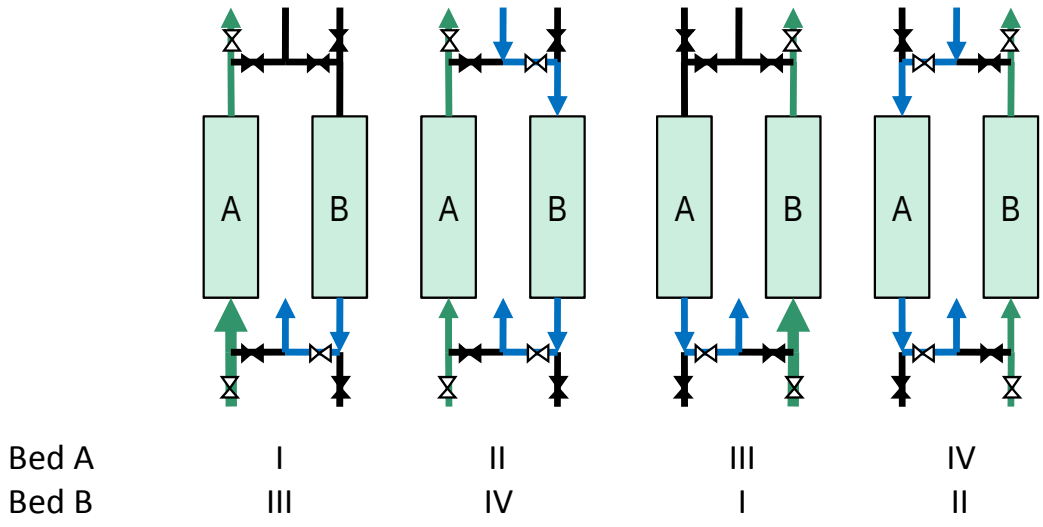

Figure 2-7 Two-Bed System (Skarstrom Cycle)

Generally, the following items are assessed for the PSA processes as separation performances;

- pressure drop (energy consumption)
- operating capacity (amount of product gas per cycle)
- adsorbent productivity (capacity per amount of adsorbent per cycle time)
- recovery (net amount of product gas per amount of feed gas)
- purity (composition of Component 1 in the product gas)

For multiple bed systems, the separation performances except pressure drop can be defined per system.

Allowable pressure drop in industrial scales is 1 ~ 4 kPa for atmospheric gas and 5 ~ 100 kPa for compressed gas [28]. Since the cost of compressing gas is significant, the operating cost is sensitive to available pressure of the feed gas and required pressure for the product gas and reduction of pressure drop is desired to save the compression energy.

Available capacity (operating capacity) used in the PSA process is determined by the difference of adsorption capacity at partial pressure of impurity gases in adsorption and desorption steps as shown in Figure 2-8. TSA employs temperature dependency of the adsorption capacity, while PSA employs pressure dependency of that. Typically adsorption capacity decreases as temperature rises. When the isotherm has a “favorable” shape, which means high capacity at low pressure, this is an advantage for adsorption step, but becomes a disadvantage for the desorption step. Depending on the adsorbents, combination of the PSA and the TSA would be helpful for the desired operating capacity.

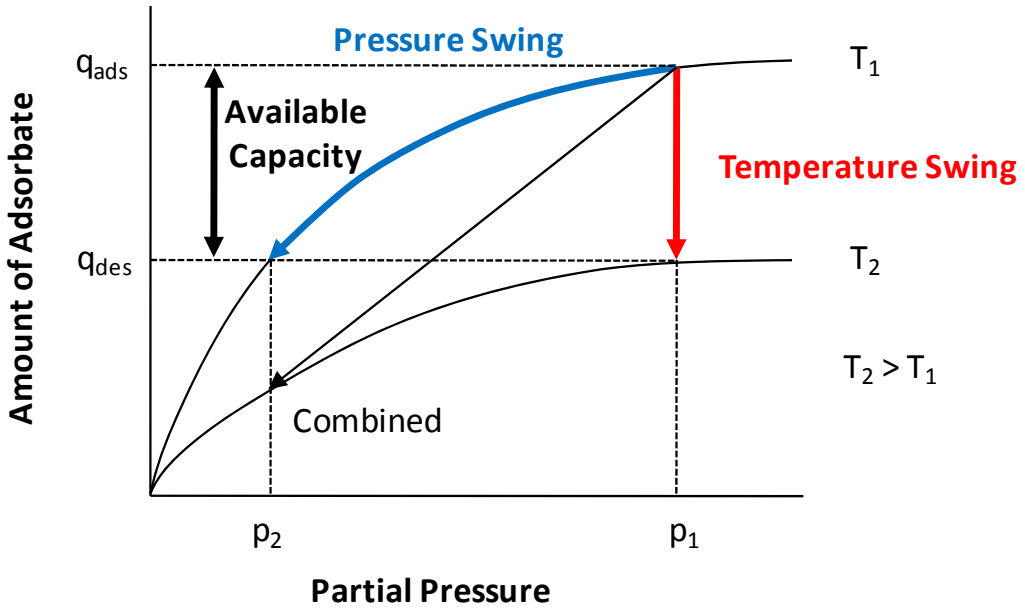

Figure 2-8 Representation of PSA and TSA Operational Trajectories on Isotherm

In Step IV, regeneration (desorption) conditions of the purge gas (composition, pressure, temperature and flow rate) can be designed independently from the operating (adsorption) conditions. The purge gas is usually a part of the product gas produced during the operation. This reduces recovery and adsorbent productivity since a part of the produced gas is consumed. If the desorption step consumes the same amount of product gas that is produced in the adsorption steps, nothing is produced as a useful net product. The total amount of product gas consumed in a cycle must be minimized by adjusting pressure, flow rate and/or time.

Purity of the product gas depends on residual adsorbate on the zeolite after the regeneration steps. Purity and amount of the purge gas determine the purity of the zeolite in the bed. As long as purity of the purge gas is high (which means partial pressures of the impurities in the purge gas are minimal), consumption of large amount of the purge gas gives higher purity, but results in

lower recovery in principle. However, an excess amount of the purge gas doesn't contribute to increase the purity further [29]. It implies there is an optimal or compromising point to satisfy both recovery and purity requirements. When the feed gas by-passes through the bed (mass transfer zone length is greater than bed depth), the feed gas contaminates the product gas and reduces the purity.

Aspect ratio and downsizing effects of packed beds were examined in Appendix B. Downsized bed volume increased recovery and adsorbent productivity and reduced the other separation performances. Reduction of pressure drop is preferred, but same or similar operating capacity is desired. Aspect ratio is also important for downsizing from the large industrial scale and is helpful to maintain the operating capacity with downsizing.

Adsorption and desorption (regeneration) time in the PSA processes are shorter (minutes) than those of the TSA. Heating entire beds of adsorbents in the desorption step of the TSA requires typically long time (hours) and the beds must be cooled down to restart the next adsorption step. In the ideal PSA processes, the large temperature increase in the bed because of exothermic adsorption could be cancelled out by the following endothermic desorption step. The temperature increase is detrimental to adsorption. For bulk separation and operation up to the breakthrough, however, the temperature increase may still present challenges.

The following operational conditions are recommended for the conventional PSA [27].

1) Shorter cycle (than the breakthrough time) and lower throughput (smaller amount of the product gas) for pseudo-isothermal operation
2) Purge gas volume / feed gas volume (= V_{IV} / V_{II}) = 1.0 (Usually 1.1 to 2.0 in practice)

3) Feed gas pressure / purge gas pressure (= p_{II} / p_{IV}) > $1/y_{fd2}$ (for V_{pg} / V_{fd} = 1.0)

4) Volume of feed gas (= V_{II}) = 15 ~ 30 times of bed volume per cycle (for V_{pg} / V_{fd} = 1.1)

In order to reduce the temperature increase, a "rapid" cycle of the PSA operation is preferred to realize nearly isothermal operation by switching adsorption and desorption steps rapidly (seconds) [15]. Especially with downsizing of the bed volume, some ideas of a rapid and a rapidly cycled operation were proposed [30-31]. To avoid confusion, the terms "rapid PSA (RPSA)" and "rapidly cycled PSA (RCPSA)" are distinguished clearly here. The RPSA is often referred as a rapid PSA operation with "single" module (packed bed) which gives a continuous product gas flow [30] (Figure 2-9). The single-column RPSA is a unique process applying with small particles to develop the pressure drop intentionally, which is used in the regeneration step. On the other hand, the RCPSA is a rapidly cycled conventional PSA operation with "multiple" modules to obtain a continuous product gas flow like Skarstorm cycle [31-32].

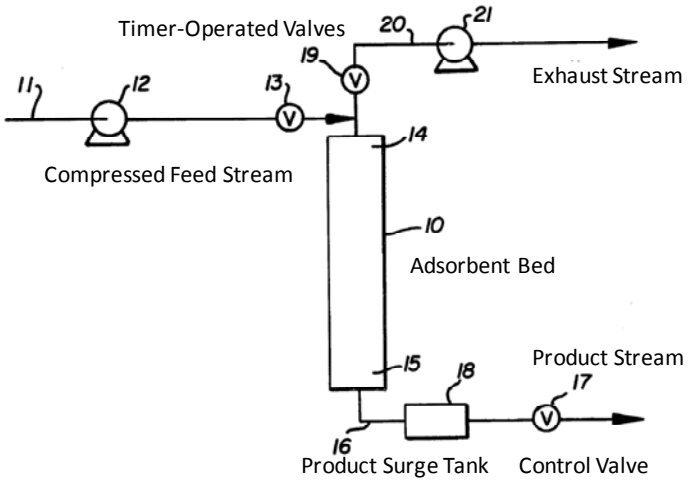

Figure 2-9 Rapid Pressure Swing Adsorption [30]

For higher recovery and purity, some improvement for PSA process sequence and system are proposed as summarized in Figure 2-10 [26-27]. Co-current depressurization is effective to recover the raffinate in the interstitial space of the packed bed ((a) in Figure 2-10). This step also increases the extract composition in gas phase at the lowered pressure and utilizes the region ahead of mass transfer zone developed in the preceding adsorption step for further adsorption capacity when the adsorption step is terminated earlier. Pressure equalization conserves mechanical energy by introducing high pressure used in the adsorption step in a bed to another bed for pressurization ((b) in Figure 2-10). This increases recovery of the raffinate. Rinse with the extract co-currently is expected to give higher purity of the extract product than co-current depressurization since the feed gas interstitial space of the bed is completely purged out ((c) in Figure 2-10). This step can desorb co-adsorbed lighter species prior to the depressurization and desorption steps. Multiple bed operation with more than three beds allows higher efficiency with the sequential improvements above ((d) in Figure 2-10). Very strongly adsorbed species such as water may be effectively removed by installation of a pretreatment bed in the upstream ((e) in Figure 2-10). The pre-bed can be regenerated independently from the main packed bed system. Evacuation instead of purge may be applicable to remove very strongly adsorbed species, but requires additional energy for vacuum.

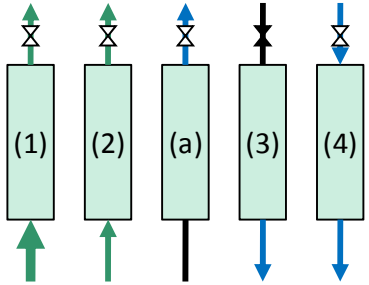

(a) Co-Current Depressurization

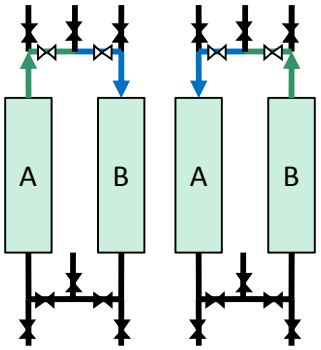

(b) Pressure Equalization

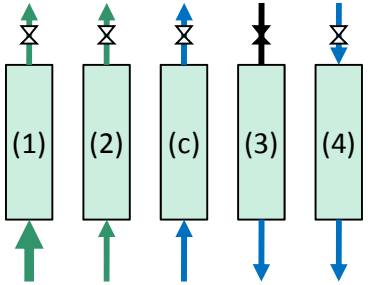

(c) Rinse

(with Extract Product Co-currently)

Time →

Bed A	**A**			**E1**	**CoD**	**E2**	**CntrD**	**D**	**E2**	**E1**	**P**	
Bed B	**E1**	**CoD**	**E2**	**CntrD**	**D**	**E2**	**E1**	**P**		**A**		
Bed C	**CntrD**	**D**	**E2**	**E1**	**P**		**A**			**E1**	**CoD**	**E2**
Bed D	**E1**	**P**		**A**			**E1**	**CoD**	**E2**	**CntrD**	**D**	**E2**

P	Pressurization (or Re-Pressurization)	CoD	Co-current Depressurization
A	Adsorption	CntrD	Counter-Current Depressurization
E1, E2	Pressure Equalization	D	Desorption (Purge)

(d) 4-Bed System

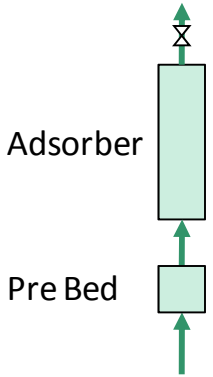

(e) Pretreatment Bed

Figure 2-10 Improvement on PSA Operations

For the proof of concept of the fiber sorbent and its module, the conventional PSA operational sequence is applied in this research as shown in Figure 2-11. Detailed operational sequence is described in Chapter 3, Section 3.6. To obtain continuous product gas flow, dual module operation is needed. The feed gas is introduced into the bore side of the fiber sorbents. The inlet pressure and temperature are 100 psig and 60 ºC, which are the same conditions required for the packed bed PSA designed for on-site hydrogen fueling station. To compete with the packed bed PSA, the target recovery and purity of the product gas are aimed at 75% and 99%, respectively. For the dual operation, the total cycle time should be twice the adsorption time (Step II). At the beginning of the cycle (Step I), the fiber module is pressurized with the product gas at high pressure to prevent contaminating the module and downstream due to the fast traveling of the feed gas. This technique is applied when high purity is required for the product gas, while it reduces the recovery [27].

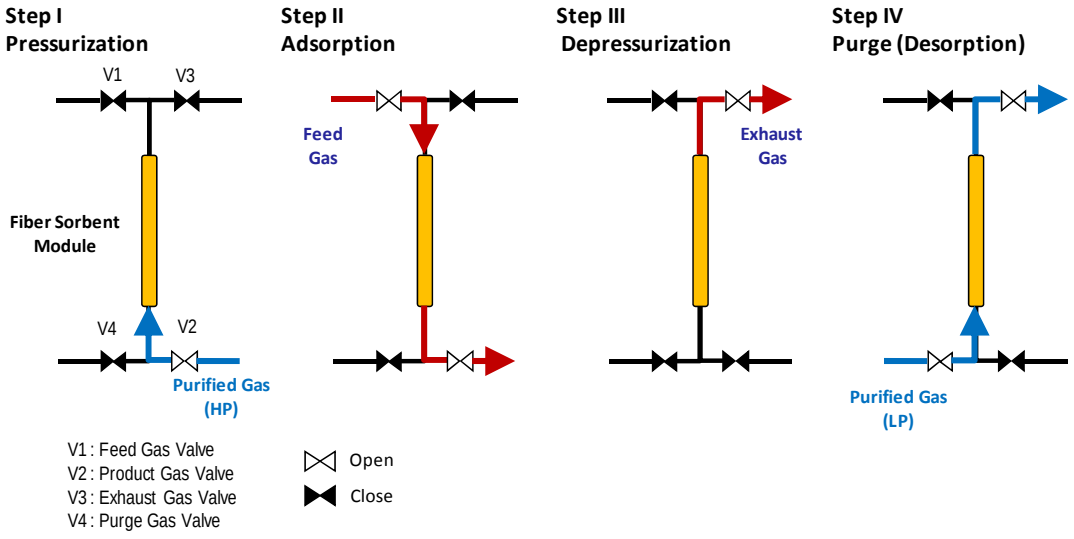

Figure 2-11 Rapidly Cycled Pressure Swing Adsorption for a Fiber Sorbent Module

2.5. Comparison between a Fiber Sorbent Module and an Equivalent Size Packed Bed

A fiber sorbent module for industrial use for hydrogen recovery was compared with an equivalent size packed bed. Pressure drop, mass transfer resistance, breakthrough time and adsorbent productivity under different conditions and constraints were evaluated for both cases. Detailed information is described in Appendix C. Only key aspects to allow comparison of the fiber sorbent module vs. packed bed are summarized here for efficiency of discussion.

2.5.1. Mass Transfer through a Fiber Sorbent Module

Both fiber sorbents and zeolite pellets are highly porous with macropore ($d_{pore} > 500$Å) and/or mesopores ($20 < d_{pore} < 500$Å) [5]. Zeolite is an aluminosilicate and classified into several types [33]. Each type of zeolite has a specific microporous structure with specific diameters ($d_{pore} <$ 20Å). Zeolite crystals are dispersed uniformly in both materials. Similarly to a zeolite pellet, three major mass transfer processes are anticipated as shown in Figure 2-12: 1) external film mass transfer, 2) intrafiber mass transfer and 3) intracrystalline mass transfer. The external film mass transfer is characterized by molecular diffusion from the bulk gas. The intrafiber/intraparticle mass transfer is characterized by diffusion through the pores. Mass transfer resistances for the fiber sorbent module and the packed bed are given in Table 2-4, which were derived in the cases discussed below (at the maximum breakthrough time in Figure 2-15).

Table 2-4 Mass Transfer Resistances for a Fiber Sorbent Module and an Equivalent Size Packed Bed

Mass Transfer Resistance	Fiber Sorbent Module		Packed Bed	
External Film, R_f [ms]	21.1	59%	3.1	6%
Intrafiber/Intraparticle, R_s [ms]	14.6	41%	79.9	94%
Intracrystalline, R_c [ms]	0.0016		0.0059	
Overall, R_{MT} [ms]	35.7	100%	83.0	100%

For the fiber sorbent module, the intrafiber mass transfer resistance was minimized because of thin wall of the fiber sorbent, and the external film mass transfer resistance was dominant. On the other hand, the intraparticle mass transfer resistance was dominant for the packed bed. Due to small size zeolite crystals, the intracrystalline mass transfer was negligibly small for both the fiber sorbent module and the packed bed. Larger bore diameter, d_{fb}, with thinner wall thickness is desired to reduce both external and intrafiber mass transfer resistances for the fiber sorbent module; however, breakthrough time depends on sorption capacity as well. Since the thin wall reduces total sorption capacity of the fiber sorbent, an appropriate packing fraction is required to provide adequate breakthrough time. Therefore, a maximum breakthrough time depending on both mass transfer resistance and sorption capacity at "optimized" dimensions and internal porous structure should exist, and these are adjustable by spinning.

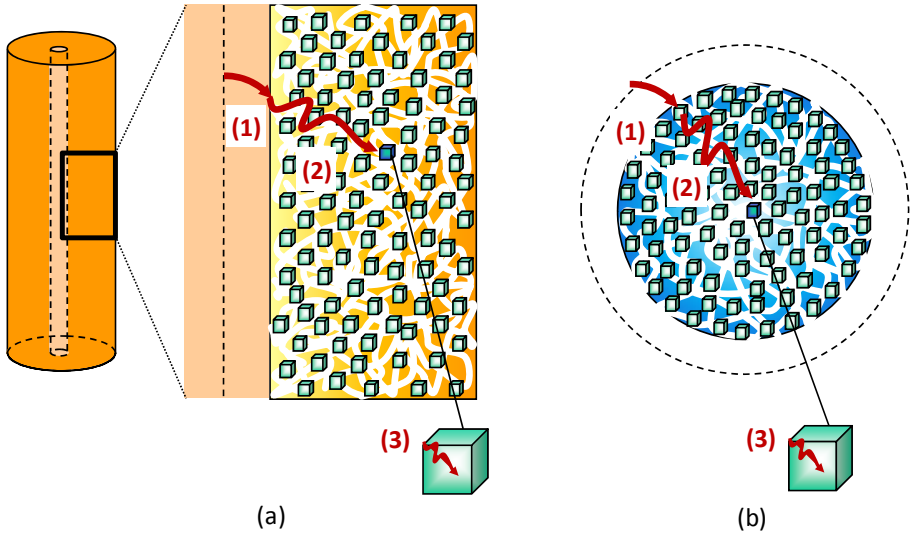

Figure 2-12 Mass Transfer Processes for (a) a Fiber Sorbent and (b) a Zeolite Pellet

2.5.2. Pressure Drop

As noted in Chapter 1, Section 1.4, the trade-off between pressure drop, $(\Delta p)_p$, and the intraparticle mass transfer resistance, $R_{s,p}$, was observed when the pellet size was varied (Figure 2-13). As the pellet size was decreased to reduce the $R_{s,p}$ as the controlling step discussed above, the $(\Delta p)_p$ was significantly increased. Pressure drop across the fiber sorbent module, $(\Delta p)_f$, with varied bore diameter, d_{fb}, was compared with the $(\Delta p)_p$ (Figure 2-14). At the same d_{fb} and dp, the Δp for the fiber sorbent module was one order of magnitude smaller than that for the packed bed. This Δp advantage implies that significant energy saving of feed gas compressor is possible with the same size equipment.

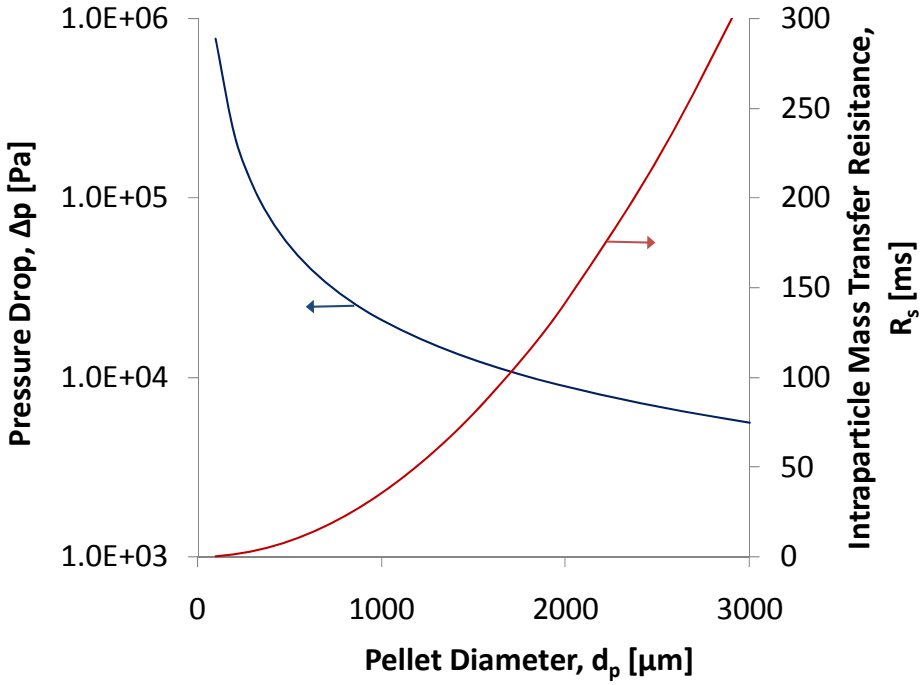

Figure 2-13 Pressure Drop and Intraparticle Mass Transfer Resistance for a Packed Bed with Varied Pellet Size

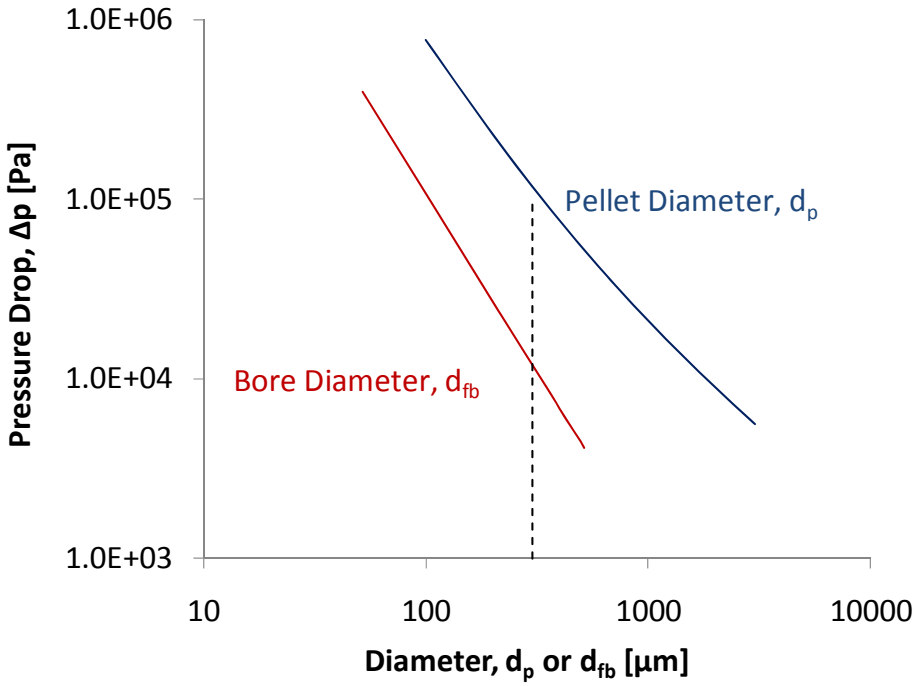

Figure 2-14 Pressure Drop Comparison between a Fiber Sorbent Module and an Equivalent Size Packed Bed

2.5.3. Breakthrough Behaviors

Breakthrough time, $t_{B,f}$, and packing fraction of the fiber sorbent module, ϕ_m, are plotted in Figure 2-15 when the outer diameter of the fiber sorbent, d_f, was varied under the same Δp as $(\Delta p)_p$ with d_p = 1.5 mm (1/16" pellet) and 3.0 mm (1/8" pellet) [34]. Maximum packing fraction of the fiber sorbent module, $\phi_{m,max}$ corresponds to the maximum number of fiber sorbents, $n_{f,max}$, and is constrained by the d_f when the module diameter, d_m, is fixed. Since different packing fraction gives different interstitial velocity, the d_{fb}, was also varied accordingly in order to maintain the same Δp. Breakthrough time and packing fraction for the equivalent size packed bed, $t_{B,p}$ and ϕ_b (= 0.60), are given as horizontal lines on the same figure. As discussed above, there was a maximum $t_{B,f}$ at a certain d_f and this point is indicated in Table 2-4. The hatched region shows the domain in which $t_{B,f}$ is longer than the $t_{B,p}$ and the $\phi_{m,max}$ is less than the ϕ_b. The ϕ_m which gave the same $t_{B,p}$ is also shown in addition to the $\phi_{m,max}$. These examples show the potential for system downsizing for the fiber sorbent module when zeolite loading between the fiber sorbent and zeolite pellet is the same. As summarized in Table 2-5, the maximum $t_{B,f}$ was longer by 22% than the $t_{B,p}$ while showing increased productivity of 5%. Since the difference of the t_B at a certain d_f and at the maximum may be huge, the optimized spinning of fiber sorbent and design of the fiber sorbent module are critical to obtain the desired breakthrough time.

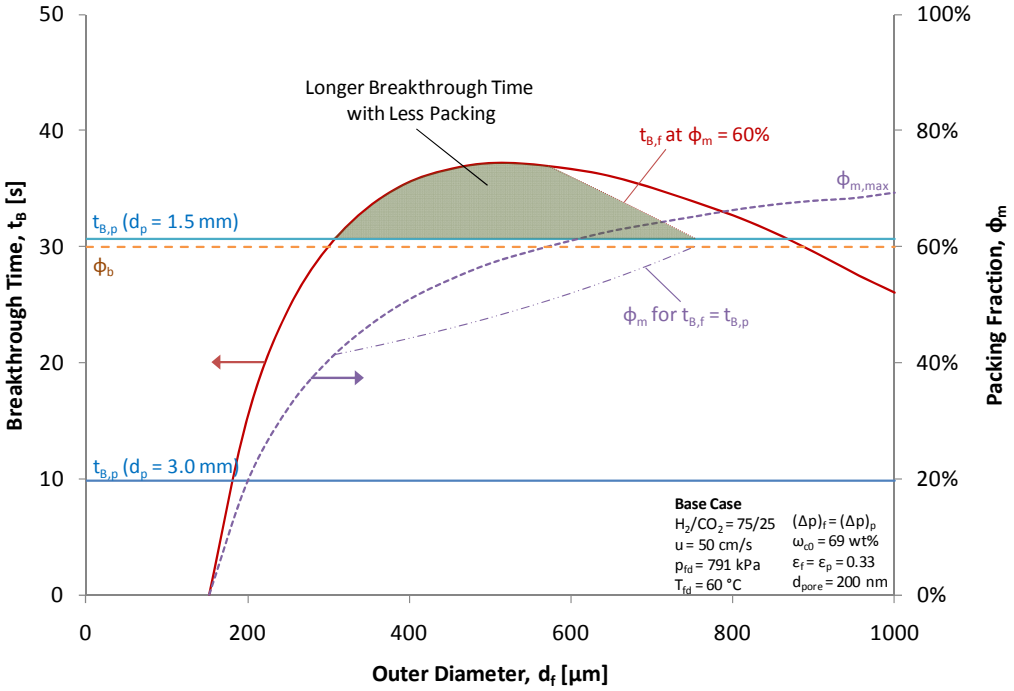

Figure 2-15 Breakthrough Time and Maximum Packing Fraction of a Fiber Sorbent Module and an Equivalent Size Packed Bed (Same Δp Case)

Another comparison result is shown in Figure 2-16: the $(\Delta p)_f$ was reduced down to half of $(\Delta p)_p$. There was still the region to have longer $t_{B,f}$ than the $t_{B,p}$. The maximum $t_{B,f}$ was longer by 8% with significant energy saving by applying 50% reduction in Δp and with further increased productivity of 10%. Hence, depending on operational requirements, there is an optimized design of fiber sorbent module to achieve superior separation performances to the packed bed.

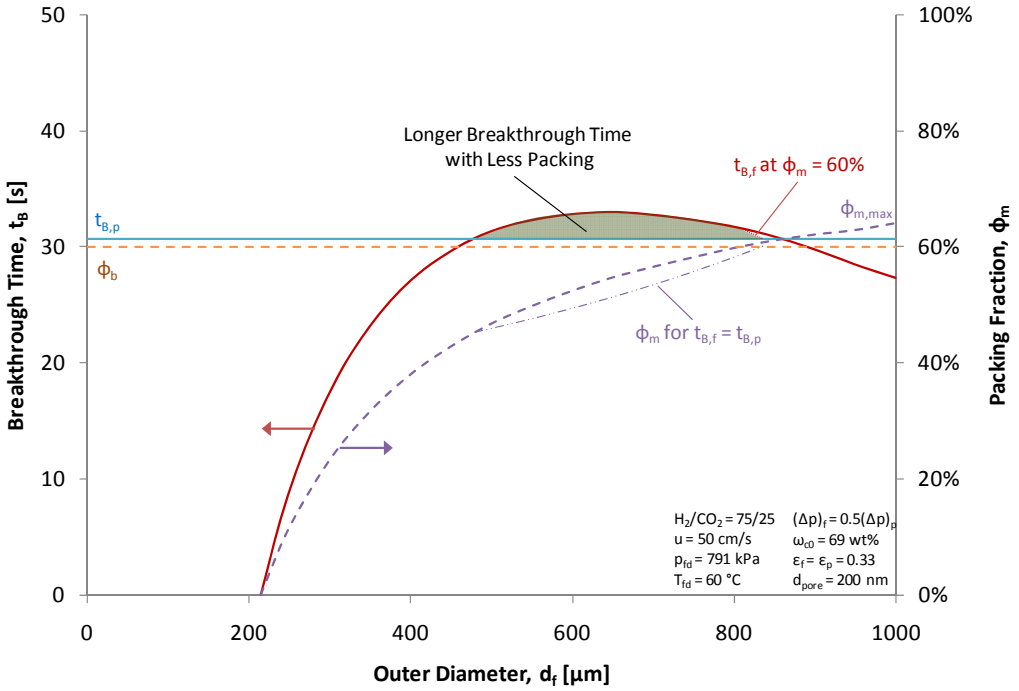

Figure 2-16 Breakthrough Time and Maximum Packing Fraction of a Fiber Sorbent Module and an Equivalent Size Packed Bed (Half Δp Case)

Table 2-5 Comparison Results between a Fiber Sorbent Module and an Equivalent Size Packed Bed

	Fiber Sorbent Module		Packed Bed
	Same Δp	Half Δp	
Outer Diameter, d_f [µm]	505	650	-
Bore Diameter, d_{fb} [µm]	277	374	-
Number of Fiber Sorbents, n_f [-]	128,760	77,479	-
Pressure Drop, Δp [kPa]	12.6	6.3	12.6
Breakthrough Time, t_B [s]	37.3	33.0	30.7
	(+22%)	(+8%)	
Adsorbent Productivity, η_p x 10^3 [kg-feed gas/kg-zeolite/s]	4.88 (+5%)	5.12 (+10%)	4.67

(at the maximum $t_{B,f}$ on Figure 2-15 and Figure 2-16 for the fiber sorbent module)

2.6. Thermal Moderation

Non-isothermal operation is anticipated in case of the temperature increase due to a significant heat of adsorption. The temperature excursion is detrimental to adsorption as noted above. An example of a packed bed is shown in Figure 2-17 and experimental breakthrough occurred earlier than the isothermal condition [35]. Increased temperature will reduce the operating capacity.

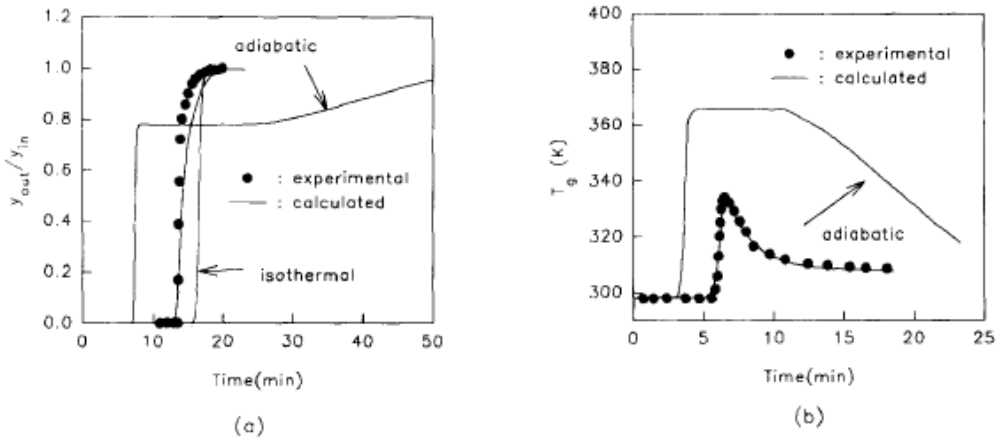

Figure 2-17 Breakthrough and Temperature Curves of CO_2 Adsorption to Activated Carbon [35]

A possible simple thermal moderation approach against the temperature excursion is explored to provide "thermal ballast" by applying the latent heat of a carefully selected wax in the shell side of the fiber sorbent modules. Paraffin wax fuses at slightly above the operating temperature, 62 ~ 64 °C. An impermeable layer is needed simply to prevent wax molecules from diffusing into the fiber sorbents when the wax fuses. It is expected to reduce the temperature increase significantly, thereby providing high productivity. Clearly, the interstitial space between the pellets in the packed bed *cannot be filled*, as it can be for the fiber sorbent module. Therefore, the large

temperature excursion noted above for the packed bed cannot be mitigated as it can be for the novel fiber sorbent module.

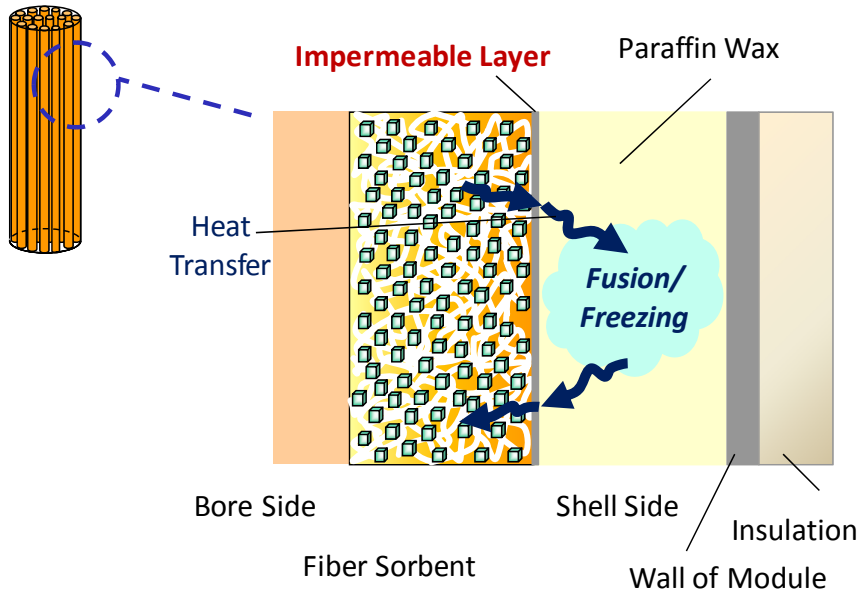

Figure 2-18 Thermal Management by the Latent Heat of Fusion of Paraffin Wax

At the maximum $t_{B,f}$ on Figure 2-15, the temperature increase were calculated at breakthrough time and summarized in Table 2-6. As longer $t_{B,f}$ was expected, the ΔT_f became 38 K, while ΔT_p was 27 K. With paraffin wax in the shell side of the fiber sorbent, the ΔT_f was reduced down to 3 K. Optimized arrangements of the fiber sorbents reduce the ΔT_f to realize the isothermal operation even with longer operation up to the breakthrough. Further results and discussion are described in Appendix C.

Table 2-6 Temperature Increase between a Fiber Sorbent Module and an Equivalent Size Packed Bed

	Fiber Sorbent Module		Packed Bed
	No Filler	Wax	
Temperature Increase, ΔT [K]	38	3	27

2.7. Dynamic Modeling

The simplified modeling used for the concept proof in Section 2.5 was not sufficient to predict the performance of thermally moderated fiber sorbent module. To investigate non-isothermal behavior of the fiber sorbent module, mass and energy balance equations described below were solved by gPROMS®. The parameters were estimated by the same manner described in Appendix C. The results are reported in Chapter 6 to compare with experimental results.

The following conditions were assumed;

1) Follow the ideal gas law and ideal mixture.
2) Follow the Hagen-Poiseuille equation for the pressure drop.
3) Apply linear driving force (LDF) approximation for mass and heat transfer between gas and solid phases.
4) Neglect viscous flow through pores in the fiber sorbent.
5) Assume temperature of impermeable layer and paraffin wax is the same as that of fiber sorbent.
6) Neglect diffusion and heat conduction in the axial direction.

7) Neglect contribution of the polymer used for the impermeable layer to the total sorption capacity.

The mass and heat balance equations for packed bed are applied for the fiber sorbent module replacing packing and void fractions, ϕ_b and ε_b, into $\phi_{bf,m}$ and ε_{mb} and modifying the parameters [26];

Mass Balance for Component 2 (CO_2);

$$\varepsilon_{mb}\left\{\frac{\partial C_2}{\partial t}+\frac{\partial}{\partial z}\left(vC_2\right)\right\}+\phi_{bf,m}\frac{\partial q_2}{\partial t}=0 \quad \text{.....(2.16)}$$

Overall Mass Balance;

$$\varepsilon_{mb}\left\{\frac{\partial C}{\partial t}+\frac{\partial}{\partial z}\left(vC\right)\right\}+\phi_{bf,m}\frac{\partial q_2}{\partial t}=0 \quad \text{.....(2.17)}$$

Adsorption Rate;

$$\frac{\partial q_2}{\partial t}=k\left(q_2^{*}-q_2\right)=\frac{1}{R_{MT}}\left(C_2-\frac{q_2}{K}\right) \quad \text{.....(2.18)}$$

Heat Balance in Gas Phase;

$$\varepsilon_{mb}\left\{\frac{\partial}{\partial t}\left(\rho_g c_{pg} T_g\right)+\frac{\partial}{\partial z}\left(v\rho_g c_{pg} T_g\right)\right\}+h_f a_f\left(T_g-T_{fx}\right)=0 \quad \text{.....(2.19)}$$

where,

t; time [s]

z; axial direction [m]

C; total concentration in gas phase [mol/m^3]

C_2; concentration of Component 2 (CO_2) in gas phase [mol/m^3]

q_2; concentration of Component 2 (CO_2) in fiber sorbent phase [mol/m^3]

T_g; temperature of gas phase [K]

T_{fx}; temperature of solid phase (the fiber sorbent including the impermeable layer and the shell-side material) [K]

v; interstitial velocity [m/s]

ε_{mb}; bore-side void fraction [-]

$\phi_{bf,m}$; packing fraction of a (bare) fiber sorbent [-]

ρ_g; density of mixed gas [kg/m^3]

c_{pg}; specific heat capacity [J/kg/K]

k; overall mass transfer coefficient [m/s]

R_{MT}; overall mass transfer resistance [s]

K; dimensionless sorption equilibrium constant [m^3-gas/m^3-fiber sorbent]

h_f; external heat transfer coefficient [W/m^2/K]

a_f; heat transfer area of a fiber sorbent (= mass transfer area of a fiber sorbent) [m^2/m^3]

In order to take the latent heat of fusion of the paraffin wax, enthalpy of solid phase, H [J/m^3], was defined, of which the reference state was at 0 K;

$$H = \left(\rho c_p\right)_{fx} T_{fx} + \phi_{bf,m}\left(-\Delta H_{ads}\right) q_2 \quad \text{.....(2.20)}$$

where,

$(\rho c_p)_{fx}$; volumetric heat capacity [J/m^3/K] (Equation (2.21))

$(-\Delta H_{ads})$; the heat of adsorption [J/mol]

$$\left(\rho c_p\right)_{fx} = \rho_{c,m} c_{p,c} + \rho_{pm,m} c_{p,pm} + \rho_{ct,m} c_{p,ct} + \rho_x \phi_x c_{px} + \rho_w c_{px} \frac{V_w}{V_m} \quad \text{.....(2.21)}$$

where,

ρ; density [kg/m^3]

c_p; specific heat capacity [J/kg/K]

ϕ; volume fraction [-]

V; volume [m^3]

subscript

x; paraffin wax

c; zeolite crystal

pm; polymer

ct; an impermeable layer

m; a fiber module

w; wall of stainless steel vessel

Heat balance in the fiber sorbent phase (solid phase) was described as;

Heat Balance in Fiber Sorbent Phase;

When $H < H_{m1}$ or $H > H_{m2}$,

$$\left(\rho c_p\right)_{fx} \frac{\partial T_{fx}}{\partial t} = \phi_{bf,m}\left(-\Delta H_{ads}\right)\frac{\partial q_2}{\partial t} - h_f a_f \left(T_g - T_{fx}\right) \quad \text{.....(2.22)}$$

When $H_{m1} \le H \le H_{m2}$,

$$\left(\rho c_p\right)_{fx} \frac{\partial T_{fx}}{\partial t} = -h_f a_f \left(T_g - T_{fx}\right) \quad \text{.....(2.23)}$$

where,

H_{m1}; enthalpy of solid phase at T_m [J/m^3]

$$H_{m1} = \left(\rho c_p\right)_{fx} T_m \quad \text{.....(2.24)}$$

H_{m2}; enthalpy of solid phase at T_m including ΔH_{fus} [J/m^3]

$$H_{m2} = \left(\rho c_p\right)_{fx} T_m + \rho_x \Delta H_{fus} \quad \text{.....(2.25)}$$

T_m; melting point of paraffin wax [K]

ΔH_{fus}; latent heat of fusion of paraffin wax [J/kg]

The density and the specific heat capacity of each material were assumed as constant. Solving the equations above simultaneously, a full solution of all of the equations with regard to time-derivatives of total concentration (or total pressure), concentration of each component (or partial pressure), temperatures of gas and solid, and velocity (or flow rate) is very difficult [26]. In this calculation, velocity was assumed as a constant. Although this assumption might over-approximate the phenomena of bulk gas separation since the volume changes due to sorption, it was enough to confirm the trend in behaviors of the fiber sorbent module compared with an equivalent packed bed. Temperature- and composition-dependent physical and transport properties were also assumed as constant at feed gas conditions. Sorption capacity of fiber sorbent was calculated based on the temperature of solid.

2.8. References

1. McKelvey, S.A., D.T. Clausi, and W.J. Koros, *A Guide to Establishing Hollow Fiber Macroscopic Properties for Membrane Applications.* Journal of Membrane Science, 1997. **124**(2): p. 223-232.

2. Pesek, S.C. and W.J. Koros, *Aqueous Quenched Asymmetric Polysulfone Hollow Fibers Prepared by Dry Wet Phase-Separation.* Journal of Membrane Science, 1994. **88**(1): p. 1-19.

3. Baker, R.W., *Membrane Technology and Applications*. 2nd ed. 2004, New York: John Wiley & Sons.

4. Liu, J.Q., et al., *Butane Isomer Transport Properties of 6FDA-DAM and MFI-6FDA-DAM Mixed Matrix Membranes.* Journal of Membrane Science, 2009. **343**(1-2): p. 157-163.

5. Ruthven, D.M., *Chapter 1 Microporous Adsorbents*, in *Principles of Adsorption and Adsorption Processes*. 1984, Wiley-Interscience Publication: New York. p. 1-28.

6. Mahajan, R. and W.J. Koros, *Mixed Matrix Membrane Materials with Glassy Polymers. Part 1.* Polymer Engineering and Science, 2002. **42**(7): p. 1420-1431.

7. Ward, J.K., *Crosslinkable Mixed Matrix Membranes for the Purification of Natural Gas*, in *Ph.D. Dissertation*. 2010, Georgia Institute of Technology.

8. Kiyono, R., et al., *Mixed Matrix Microporous Hollow Fibers with Ion-Exchange Functionality.* Journal of Membrane Science, 2004. **231**(1-2): p. 109-115.

9. Avramescu, M.-E., Z. Borneman, and M. Wessling, *Particle-Loaded Hollow-Fiber Membrane Adsorbers for Lysozyme Separation.* Journal of Membrane Science, 2008. **322**(2): p. 306-313.

10. Perera, S.P., *Hollow Fibres*, in *WO Patent 2007/007051A1*. 2007.

11. Perera, S.P. and C.C. Tai, *Regenerable Adsorption Unit*, in *WO Patent 2008/110820A1*. 2008.

12. Lively, R.P., et al., *Hollow Fiber Adsorbents for CO2 Removal from Flue Gas.* Industrial & Engineering Chemistry Research, 2009. **48**(15): p. 7314-7324.

13. Lively, R., et al., *Sorbent Fiber Compositions and Methods of Temperature Swing Adsorption*, in *U.S. Patent No.2009/0025555 A1*. 2009.

14. Bhandari, D.A., N. Bessho, and W.J. Koros, *Hollow Fiber Sorbents for Desulfurization of Natural Gas.* Industrial & Engineering Chemistry Research, 2010: p. null-null.

15. Keller, G.E., II, and R.L. Jones, *A New Process for Adsorption Separation of Gas Stream*, in *Adsorption and Ion Exchange with Synthetic Zeolites: Principles and Practice*, W.H. Flank, Editor. 1980, American Chemical Society: Washington, D.C. p. 275-286.

16. Yang, R.T., *Chapter 6 Cyclic Gas Separation Processes*, in *Gas Separation by Adsorption Processes*. 1997, World Scientific: Singapore ; River Edge, N.J. p. 201-235.

17. Koros, W.J. and G.K. Fleming, *Membrane-Based Gas Separation.* Journal of Membrane Science, 1993. **83**(1): p. 1-80.

18. Husain, S., *Mixed Matrix Dual Layer Hollow Fiber Membranes for Natural Gas Separation*, in *Ph.D. Dissertation*. 2006, Georgia Institute of Technology.

19. Ruthven, D.M., *Chapter 2 Physical Adsorption and the Characterization of Porous Adsorbents*, in *Principles of Adsorption and Adsorption Processes*. 1984, Wiley-Interscience Publication: New York. p. 29-61.

20. Koros, W.J., D.R. Paul, and G.S. Huvard, *Energetics of Gas Sorption in Glassy Polymers.* Polymer, 1979. **20**(8): p. 956-960.

21. Puleo, A.C., D.R. Paul, and S.S. Kelley, *The Effect of Degree of Acetylation on Gas Sorption and Transport Behavior in Cellulose-Acetate.* Journal of Membrane Science, 1989. **47**(3): p. 301-332.

22. Do, D.D., *Chapter 3 Practical Approaches of Pure Component Adsorption Equilibria*, in *Adsorption Analysis: Equilibria and Kinetics*. 1998, Imperial College Press: London. p. 49-148.

23. Walton, K.S. and M.D. LeVan, *A Novel Adsorption Cycle for CO2 Recovery: Experimental and Theoretical Investigations of a Temperature Swing Compression Process.* Separation Science and Technology, 2006. **41**(3): p. 485-500.

24. Choudhary, V.R., S. Mayadevi, and A.P. Singh, *Sorption Isotherms of Methane, Ethane, Ethene and Carbon-Dioxide on NaX, NaY and Na-Mordenite Zeolites.* Journal of the Chemical Society-Faraday Transactions, 1995. **91**(17): p. 2935-2944.

25. Stern, S.A. and A.H. De Meringo, *Solubility of Carbon-Dioxide in Cellulose-Acetate at Elevated Pressures.* Journal of Polymer Science Part B-Polymer Physics, 1978. **16**(4): p. 735-751.

26. Ruthven, D.M., S. Farooq, and K.S. Knaebel, *Pressure Swing Adsorption*. 1994, New York, N.Y.: VCH Publishers. xxiii, 352 p.

27. Yang, R.T., *Chapter 7 Pressure-Swing Adsorption: Principles and Processes*, in *Gas Separation by Adsorption Processes*. 1997, World Scientific: Singapore ; River Edge, N.J. p. 237-274.

28. LeVan, M.D., G. Carta, and C.M. Yon, *Adsorption and Ion Exchange*, in *Perry's Chemical Engineers' Handbook*, R.H. Perry, D.W. Green, and J.O. Maloney, Editors. 1997, McGraw-Hill: New York. p. 16-1-16-66.

29. Yang, R.T., *Chapter 8 Pressure-Swing Adsorption: Models and Experiments*, in *Gas Separation by Adsorption Processes*. 1997, World Scientific: Singapore ; River Edge, N.J. p. 275-338.

30. Jones, R.L., G.E.I. Keller, and R.C. Wells, *Rapid Pressure Swing Adsorption Process with High Enrichment Factor* in *U.S. Patent No.4,194,892*. 1980.

31. Feng, X., et al., *Hollow-Fiber-Based Adsorbers for Gas Separation by Pressure-Swing Adsorption.* AIChE Journal, 1998. **44**(7): p. 1555-1562.

32. Bhaumik, S., S. Majumdar, and K.K. Sirkar, *Hollow-Fiber Membrane-Based Rapid Pressure Swing Absorption.* Aiche Journal, 1996. **42**(2): p. 409-421.

33. International Zeolite Association. 2010 [cited 2010 August 20]; Available from: http://www.iza-online.org/.

34. Breck, D.W., *Zeolite Molecular Sieves: Structure, Chemistry, and Use*. 1974, New York: John Wiley & Sons.

35. Hwang, K.S., J.H. Jun, and W.K. Lee, *Fixed-Bed Adsorption for Bulk Component System - Nonequilibrium Nonisothermal and Nonadiabatic Model.* Chemical Engineering Science, 1995. **50**(5): p. 813-825.

CHAPTER 3 MATERIALS AND EXPERIMENTAL METHODS

3.1. Material Selection

For material selection, we applied some preferred criteria: 1) commercially available, 2) produces a porous structure to maximize contact area of zeolite in fiber sorbents, 3) mechanically durable to the pressure swing adsorption operation, and 4) easy handling with the existing spinning apparatus. Cellulose acetate (CA) and zeolite NaY were selected for the fiber sorbents used in this study to explore carbon dioxide separation from the hydrogen-rich feed gas. Both materials are commonly used in industry and low cost production of the fiber sorbents is expected for further scale-up. Another polymer and zeolite were explored, but were less preferred. The results are reported in Appendixes D and E.

3.2. Materials

3.2.1. Fiber Sorbent Dopes

3.2.1.1. Polymer

Cellulose acetate (CA, CA-394-60S, Eastman Chemical) was selected for the polymer matrix of the fiber sorbent to bind zeolite particles. Major properties of the CA are listed in Table 3-1. The CA was dried at 120 °C in vacuum ovens overnight prior to dope mixing.

Degree of substitution, DS, was converted from acetyl content ω_{CH3CO};

$$DS = \frac{\omega_{CH_3CO}\left(3M_H + 5M_{CH} + M_{CH_2} + 5M_O\right)}{\left(1-\omega_{CH_3CO}\right)M_{CH_3CO} + \omega_{CH_3CO}M_H} \quad \text{.....(3.1)}$$

where,

ωi; weight fraction of Component i [wt%]

Mi; molar weight of Component I [g/mol]

Table 3-1 Properties of Cellulose Acetate [1]

Structure	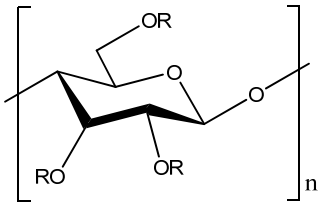 R = CH_3CO or H
Acetyl Content	39.5 wt%
Degree of Substitution, DS	2.42
Molecular Weight, M_n	60,000
Density, ρ_{pm}	1.32 g/cm^3
Glass Transition Temperature, T_G	185 °C

3.2.1.2. Zeolite

Zeolite NaY (CBV-100, Zeolyst International) was selected for the fiber sorbent used in hydrogen recovery application. Major properties of the NaY are listed in Table 3-2. NaY was dried at 285 °C in vacuum ovens overnight prior to dope mixing.

Table 3-2 Properties of Zeolite NaY [2]

Type	Faujasite 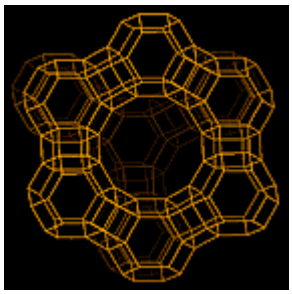
Composition [3]	$Na_{53.3}Al_{53.3}Si_{138.7}O_{384}$
Si/Al Ratio	2.6
Unit Cell Size	Cubic 24.65 Å x 24.65 Å x 24.65 Å
Density, ρ_c	1.408 g/cm^3 *)
Zeolitic Pore Size [4]	0.74 nm
Crystal Size, d_c	500 nm **)

* See below
** Based on SEM Image (Figure 3-1)

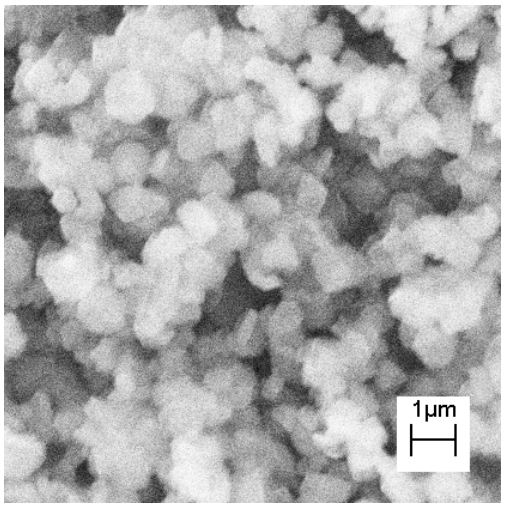

Figure 3-1 A SEM image of Zeolite NaY

True dry density of zeolite, ρ_c, was calculated based on the composition and unit cell length;

$$\rho_c = \frac{M_{NaY}}{V_{NaY} N_A} \quad \text{.....(3.2)}$$

where,

ρ_c; true density of zeolite crystal [kg/m^3]

M_{NaY}; formula weight of zeolite NaY [kg/mol]

V_{NaY}; unit cell volume of zeolite NaY [m^3]

N_A; Avogadro's number (= $6.02214179 \times 10^{23}$ particles/mol)

3.2.1.3. Solvents

1-Methyl-2-pyrrolidinone (*N*-Methyl-2-pyrrolidone, NMP, anhydrous grade, 99.5%, Sigma-Aldrich) was selected as a non-volatile solvent for the pure CA fiber and CA-NaY fiber sorbent dopes. Another solvent, acetone (ACS grade, BDH), was also examined for the pure CA fiber dope and also used to cast a dense CA film. Tetrahydrofuran (THF, anhydrous and inhibitor-free grade, ≥ 99.9%, Sigma-Aldrich) was used as a volatile solvent for a sheath dope to facilitate the skin formation. Important properties of the solvents are listed in Table 3-3.

Table 3-3 Properties of Solvent [5]

	NMP	Acetone	THF
Composition	C_5H_9NO 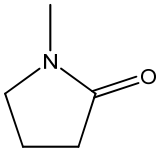	$(CH_3)_2CO$	C_4H_8O 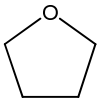
Molecular Weight [g/mol]	99.13	58.08	72.11
Density [g/cm^3 at 25 °C]	1.028	0.791	0.889
Boiling Point, T_{bp} [°C]	202	56	65~67

3.2.1.4. Non-Solvent

Water (deionized (DI) with ≥ 18MΩ, Barnstead B-Pure D4521, Thermo Scientific) was selected for the non-solvent used only for the dopes.

3.2.2. Materials for Impermeable Layer

3.2.2.1. Polyvinylidene Chloride

Polyvinylidene chloride (PVDC, IXAN PNE288, Solvay Advanced Polymers) was used for the dual layer spinning as described in Chapter 5. This polymer is a terpolymer of methacrylonitrile, vinylidene chloride, and methyl methacrylate [6]. Detailed information such molecular weight is not disclosed by the manufacturer.

3.2.2.2. PVDC Latex Solution

PVDC latex solution (emulsion solution) (DIOFAN XB203, 51% solid content, pH 1.5, Solvay Advanced Polymers) was used for post-treatment for impermeable layer development as described in Chapter 5. Particles of PDVC terpolymer (methacrylonitrile, vinylidene chloride, and methyl methacrylate) are suspended in aqueous solution. Detailed information such as molecular weight, particle size is not disclosed by the manufacturer. The solution was diluted four times in use of spray and dip coatings.

3.2.2.3. Poly(Vinyl Alcohol)

Poly(vinyl alcohol) (PVA, U228-08, 99.0-99.8% fully hydrolyzed, J.T.Baker) was also used for dip coating. The PVA did not dissolve in water at room temperature, but did with heating up to 95 °C in an oven for 1 hour. Once it dissolved, it was maintained as a solution. For the dip coating used in Chapter 5, Section 5.4, 5% PVA aqueous solution was prepared.

Table 3-4 Properties of PVA [7]

Composition	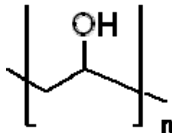
Molecular Weight	77,000-79,000

3.2.3. Quenching Bath and Solvent Exchange Media

In the spinning of fiber sorbents described below, cold (15 ~ 25 °C) and hot tap (~ 50 °C) water were used for the quenching bath. Ice made of tap water was added to lower the temperature of the quenching bath. DI water which was used for dopes was used as the first solvent exchange media. Methanol (ACS grade, EMD) and hexane (ACS grade, EMD) were used as the second and third solvent exchange media.

3.2.4. Paraffin Wax

Paraffin wax (residual ash ≤ 0.05%, Solidification Point 58-60 °C, Sigma-Aldrich) was selected. The TGA and DSC results, of which methods are described below, are shown in Figure 3-2. The wax melted at 64.3 °C slightly above the planned operating temperature and without evaporation loss below 100 °C.

3.2.5. Liquid Nitrogen

Liquid nitrogen (Airgas) was used for preparation of samples for the scanning electron microscopy (SEM). The liquid nitrogen was also used for the vacuum oven to trap and prvent reversed vapor flow of oil and solvents from the vacuum pump.

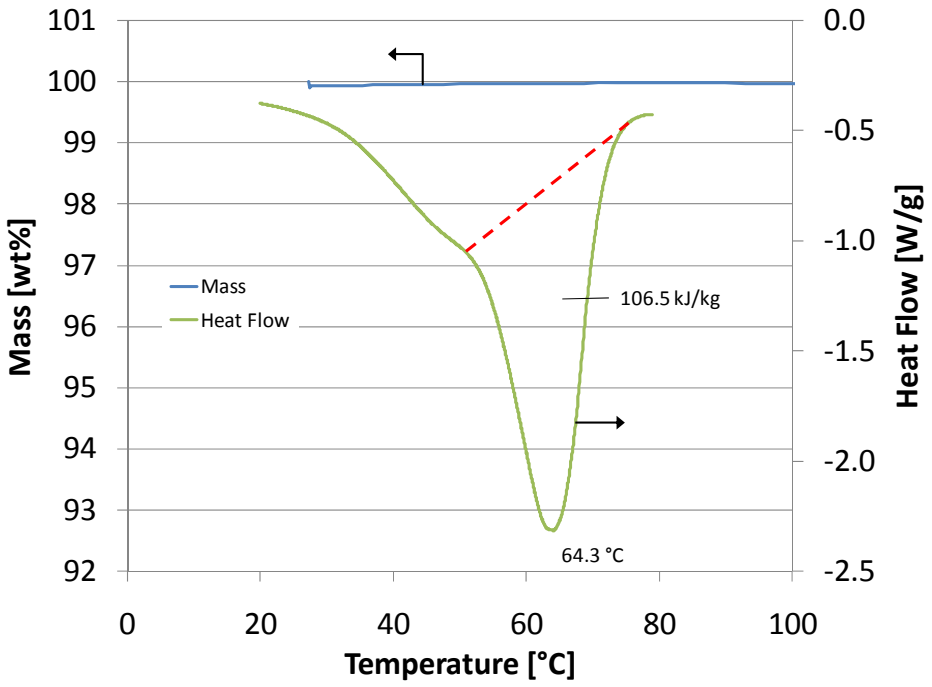

Figure 3-2 TGA and DSC Curves of Paraffin Wax

3.2.6. Gases for Permeation and Sorption Tests

Both pure (helium (He), nitrogen (N_2) and carbon dioxide (CO_2)) and mixed gases (He/CO_2, hydrogen(H_2)/CO_2) which were performed in permeation and sorption tests below were supplied by Airgas. All the pure and mixed gases are research grade (Ultra high purity).

3.3. Determination of Dope Composition

3.3.1. Phase Diagram of Polymer Solutions

Phase separation behavior during the spinning process depends on the initial composition of the dope. Each polymer solution system for a solvent and a non-solvent has a specific phase diagram.

NMP is a low-volatility (normal boiling point 202 °C), miscible with water and relatively low-toxicity. The binodal curve, which represents the boundary between one- and two-phase regions, on the ternary phase diagram for the CA/NMP/water system was determined experimentally by visual observation to identify cloud points with several vials [8]. It was difficult to distinguish cloud points for a zeolite-dispersed polymer solution, and effects on phase separation behavior are unknown when many zeolite crystals are dispersed in a polymer solution. Therefore, the dope composition for CA/NaY/NMP/water system was determined first based on that of the pure polymer solution, and then composition of the zeolite was determined based on the maximum limit of zeolite loading determined below. This approach worked well.

3.3.2. Maximum Limit of Zeolite Loading

There is a maximum limit of zeolite loading with regard to viscosity where the dope is still spinnable as a solution or a paste. Ultrasonication, using power input directly from an ultrasonic probe (1000 AUTO-TRAC, 20 kHz, 1 kW at 20 on dial, Dukane) inserted in solutions, is effective to disperse zeolite crystals homogeneously [9]. This involves heat generation and increases temperature of the solution due to the ultrasonic energy input and heat of adsorption. Volatile liquids may evaporate significantly during the ultrasonication. In addition, high viscosity polymer solutions inhibit dispersing zeolite crystals homogeneously with this method, so zeolite crystals were dispersed in a non-volatile liquid prior to mixing all of the components. The maximum limit was determined based on visual observation of fluidity on the mixture of NMP and zeolite in vials (Figure 3-3). Hand shaking and ultrasonication were repeated with gradual addition of the zeolite crystals and continued until the color of the solution turned from white into gray, which appeared to indicate that the small particles were dispersed well [10]. The maximum limit may vary depending on density and crystalline size of zeolite and type of liquid.

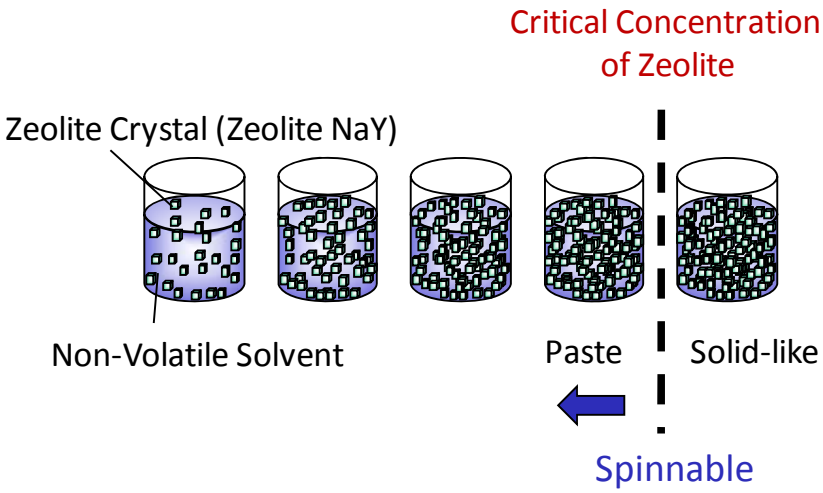

Figure 3-3 Dispersion of Zeolite Crystalline Particles in a Liquid

3.3.3. Amount of Saturated Water to Zeolite

The NaY is hydrophilic and water is strongly adsorbed by the zeolite, so the dope composition will change after all of the components are mixed together without considering the additional amount of water to be adsorbed. Additional water, which is presumably equivalent to the amount of water adsorbed by the zeolite, was determined experimentally. The "first" generation dope did not contain this amount of additional water, while the "second" generation dope took sorbed water into account. Dried NaY was stored in a glass bottle and exposed to water vapor in an enclosure for a week to insure saturation. The difference in weight before and after the drying at 285 °C in a vacuum oven gave the amount of the water saturation.

3.4. Hollow Fiber Spinning

The spinning apparatus used in this study is shown Figure 2-5 in Chapter 2, Section 2.2. The spinning conditions which were applied are summarized in Chapter 4 with the results. Dopes for

spinning were prepared in a glass jar (Quorpak) to give approximately 500 mL. Dried NaY was dispersed in the NMP with the ultrasonic power irradiation mentioned above. Water, including the additional amount for the saturation of the NaY, was then added. Finally dried CA was added and the dope was agitated by a motor-driven impeller shaft overnight at 90 °C. It was confirmed by thermal gravitational analysis (TGA), which is mentioned below, that compositions of CA and zeolite in the final fiber sorbent were equivalent to those as mixed for the dope. The dope was loaded into a high pressure syringe pump (D500, Teledyne Isco) immediately after the mixing was completed.

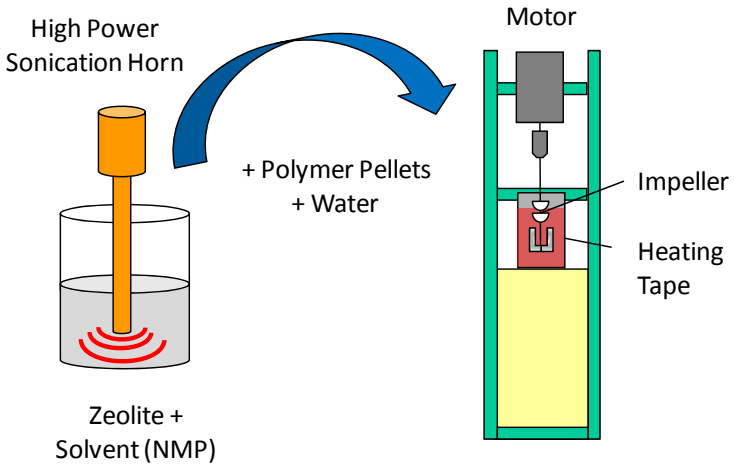

Figure 3-4 Schematic Diagram of Zeolite Dispersion and Moter-Driven Dope Mixing

Based on the preliminary spinning for the CA/NMP/water solution, the spinning conditions for fiber sorbent were determined. Due to slow phase separation behavior of the CA/NMP/water solution, a deep quenching bath, short air gap and slow take-up rate were applied as described in Chapter 4, Section 4.2. The spinneret design allows dual layer spinning to have an external thin layer (sheath layer), but the sheath dope was not applied in this study. After the completion of phase separation on the drum, the cut-off fiber sorbents were immersed in DI water to remove the residual solvent for 3 days with changing the water everyday followed by solvent exchanges;

methanol (20 minutes, 3 times) and hexane (20 minutes, 3 times). The solvent exchange method was developed for hollow fiber membranes [11] and the same manner was used with slight modifications. The conventional water bath and column result in severe bending of fiber sorbents during the solvent exchange. For a rubbery polymer used in Appendix D, the conventional solvent exchange resulted in the serious entanglement of fibers and adhesion to glass wall as well. After the solvent exchange, fiber sorbents were dried in the air for 30 minutes and in the vacuum oven for 1 hour at 120 °C.

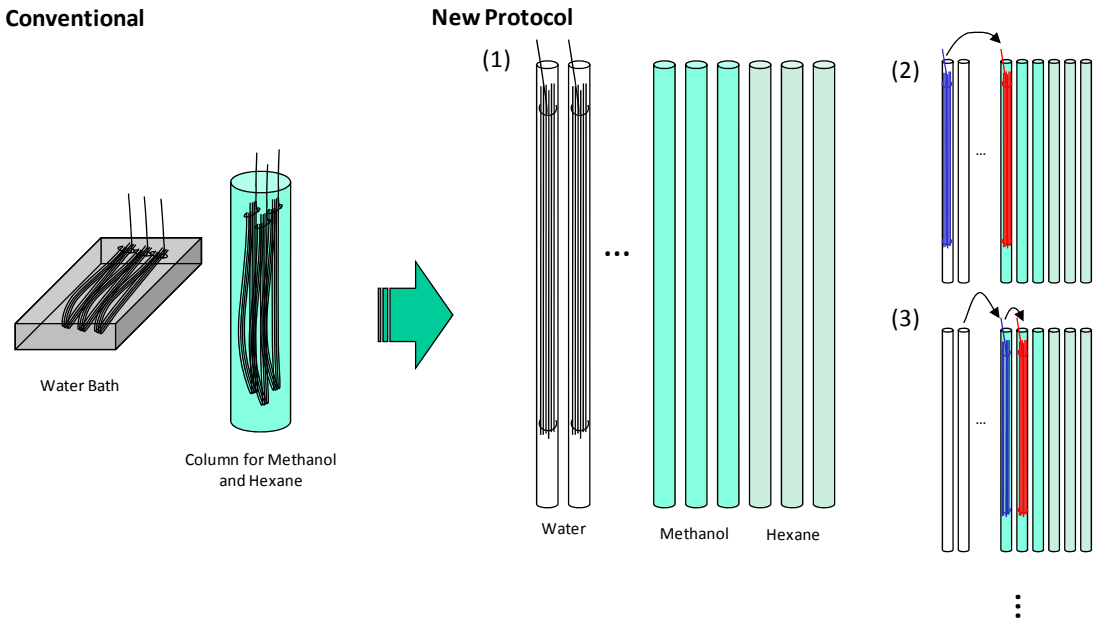

Figure 3-5 Schematic Diagram of Solvent Exchange for Fiber Sorbents

3.5. Characterization

3.5.1. Morphology Observation

Morphology of the fiber sorbents with gold coating (EMS500, Electron Microscopy Sciences) was observed with scanning electron microscopy (SEM) (LEO 1530, Leo Electron Microscopy)

[12]. Prior to mount the fiber sorbent samples, they were soaked in hexane for a short time followed by soaking them in liquid nitrogen to allow breaking them properly to show their cross sectional view.

3.5.2. Fiber Permeation Test

3.5.2.1. Standard Permeation Test for Fibers

A hollow fiber permeation test was developed for hollow fiber membranes [13] and also applied to assess the porous structure in terms of permeance. The modules made from 1/4" Swagelok® parts were assembled with a single fiber sorbent as shown in Figure 3-6. Detailed procedure of module preparation is described elsewhere [9]. Because of high permeance of the fiber sorbents, usually one fiber was loaded into a module. The module was held under the constant temperature (35 °C) with a PID temperature controller (EW-02155-54, Cole-Parmer) in an insulated steel box. The single gas was applied from a bore-side end of the module with another closed end. The permeate gas passed into the shell side of the module and was released from a shell-side end with the other end closed. The feed pressure was monitored by a pressure transducer (1000 psia Model, Honeywell Sensotec). Flow rate was measured with a glass bubble flow meter and was recorded with temperature at the measurement. Apparent permeance of fiber sorbents of Gas i, $(P/l_f)_i$;

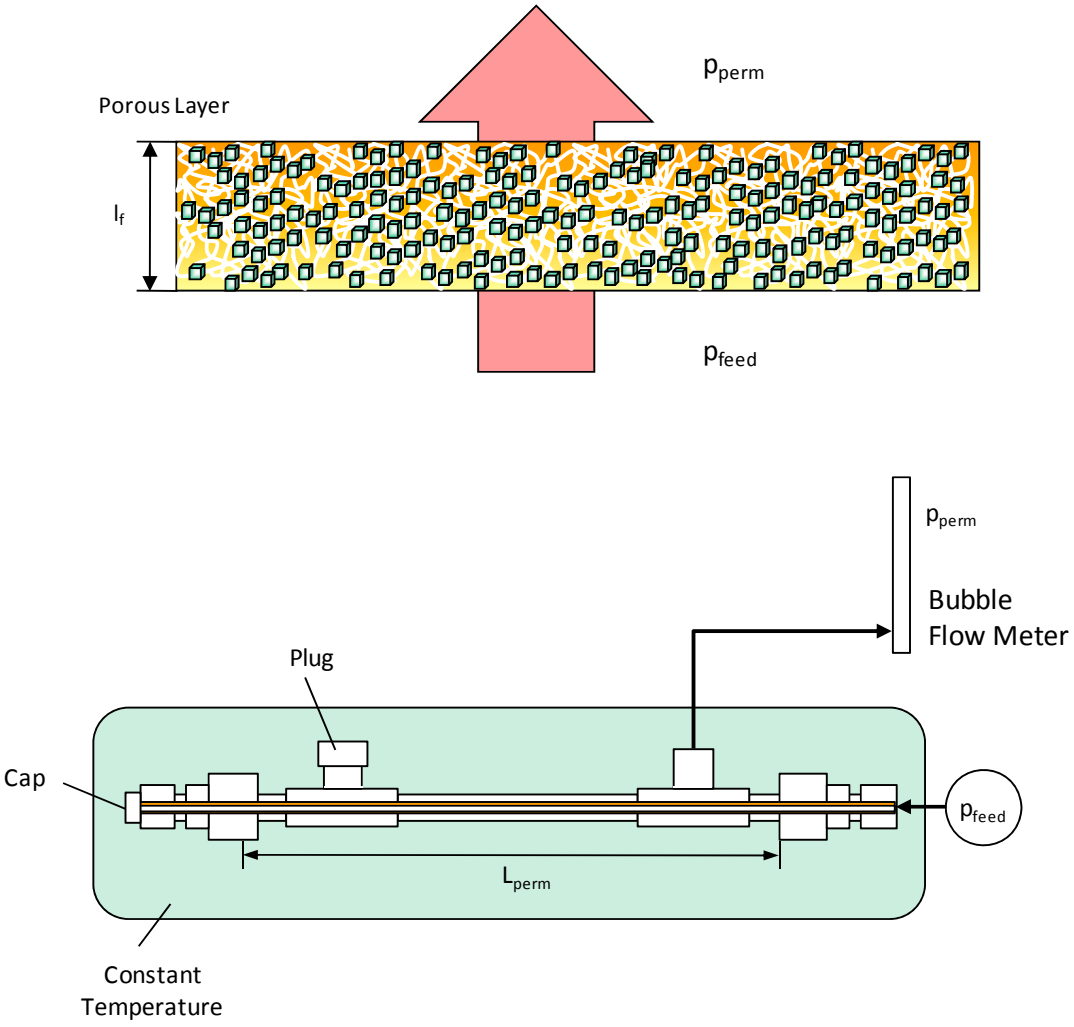

Figure 3-6 Schematic Diagram of Standard Permeation Test for Fibers

$$\left(\frac{P}{l_f}\right)_i = \frac{Q_{perm}}{\pi d_f L_{perm}\left(p_{feed} - p_{perm}\right)} \quad \text{.....(3.3)}$$

where,

$\left(\frac{P}{l_f}\right)_i$; pressure-normalized flux of Gas i, or permeance $\left[\frac{\text{mol}}{\text{m}^2\cdot\text{s}\cdot\text{Pa}}\right]$

Q_{perm}; permeate flow rate [mol/s] (converted from [m^3/s])

d_f; outer diameter of fiber sorbent [m]

L_{perm}; effective fiber sorbent length [m]

p_{feed}; feed pressure [Pa]

p_{perm}; permeate pressure [Pa] (≈ 1 atm)

In addition to the SI unit, permeance is often expressed in the unit of GPU;

$$1\text{GPU} = 1\times10^{-6}\,\frac{\text{cm}^3(\text{STP})}{\text{cm}^2\cdot\text{s}\cdot\text{cmHg}} = 3.347\times10^{-10}\,\frac{\text{mol}}{\text{m}^2\cdot\text{s}\cdot\text{Pa}} \quad \text{.....(3.4)}$$

where,

cm^3(STP); volume under the standard pressure (p_{STD} = 1 atm = 1.013 x 10^5 Pa) and temperature (T_{STD} = 0 °C = 273.15 K)

Due to magnitude of the permeance, the prefix k for one thousand is often used in this research;

$$1\text{kGPU} = 1\times10^{3}\,\text{GPU} \quad \text{.....(3.5)}$$

3.5.2.2. Permeation Test for Fiber Sorbents

For the fiber sorbents with highly porous structure, some modifications were required for the fiber permeation test: smaller size modules (made from 1/8" Swagelok® parts) with a single fiber sorbent were assembled as shown in Figure 3-7. The feed gas was introduced from both ends of the module to accommodate the high permeation of the fiber sorbents. Other features of the permeation test system were the same as those for the standard permeation test for fibers above. Changing feed pressure of pure nitrogen at 35 °C allows assessing apparent pore size, d_{pore}, by

considering the combination of the Knudsen diffusion (the first term) and viscous flows through the porous fiber wall (the second term) as shown Figure 3-8 [14].

$$\left(\frac{P}{l_f}\right)_i = \varepsilon_{f,K}\left(\frac{P}{l_f}\right)_{K,i} + \varepsilon_{f,P}\left(\frac{P}{l_f}\right)_{P,i} = \frac{\varepsilon_{f,K} d_{pore,K}}{2l_f}\frac{K_K}{\sqrt{M_i T}} + \frac{\varepsilon_{f,P} d_{pore,P}^2}{4l_f}\frac{K_P}{\mu_i T}\, p_{ave} \quad \text{.....(3.6)}$$

$$K_K = \frac{4}{3}\sqrt{\frac{2R_g}{\pi}}\frac{T_{STD}}{p_{STD}} = 3.4867\times10^4 \frac{\text{cm}^3(\text{STP})}{\text{cm}^2\cdot\text{s}\cdot\text{cmHg}}\left(\frac{\text{g}}{\text{mol}}\text{K}\right)^{0.5} \quad \text{.....(3.7)}$$

$$K_P = \frac{1}{8}\frac{T_{STD}}{p_{STD}} = 0.44926\frac{\text{cm}^3(\text{STP})\cdot\text{K}}{\text{cm}^3\cdot\text{cmHg}} \quad \text{.....(3.8)}$$

where,

subscript K: for Knudsen diffusion region

subscript P: for viscous flow region

$\left(\frac{P}{l_f}\right)_i$; permeance of Gas i $\left[\frac{\text{mol}}{\text{m}^2\cdot\text{s}\cdot\text{Pa}}\right]$

ε_f; porosity of fiber sorbent [-]

d_{pore}; pore size (diameter) of fiber sorbent [m]

l_f; wall thickness of fiber sorbent [m]

T; gas temperature [K]

p_{ave}; average pressure of feed and permeate pressures [Pa]

M_i; molecular weight of Gas i [kg/mol]

μ_i; viscosity of Gas i at T [Pa·s]

p_{STD}; standard pressure (= 1 atm = 1.013 x 10^5 Pa)

T_{STD}; standard temperature (= 0 °C = 273.15 K)

R_g; gas constant (= 8.314472 J/mol/K)

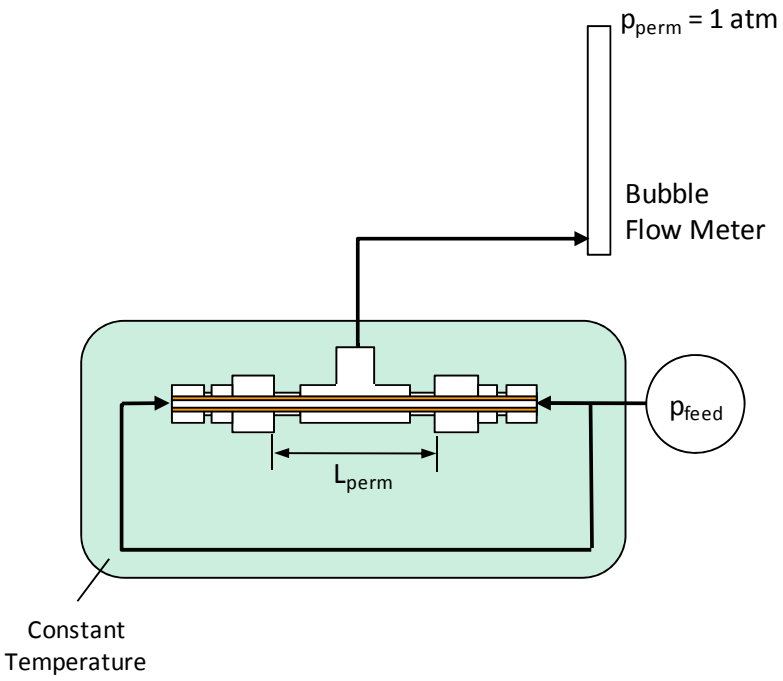

Figure 3-7 Schematic Diagram of Permeation Test for Fiber Sorbents

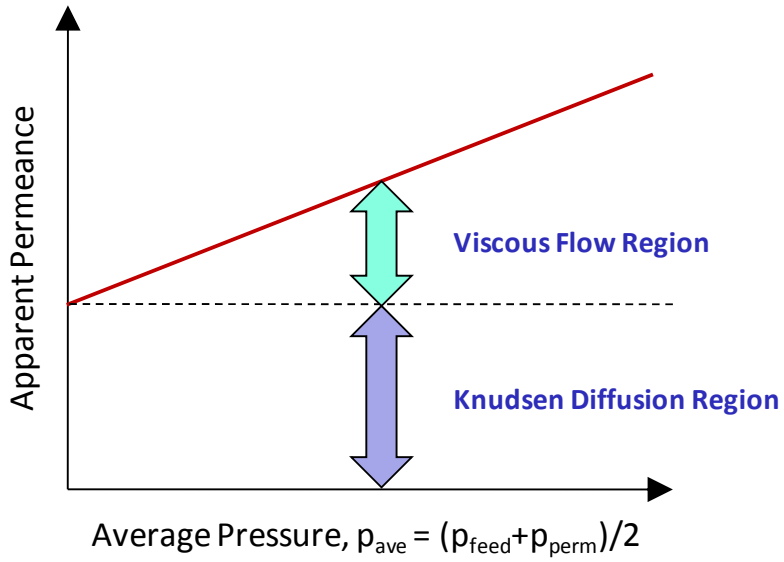

Figure 3-8 Apparent Permeance of Fiber Sorbents with Average Pressure

Thus, the apparent permeance is linear against average pressure of feed and permeate gases, p_{ave}. The apparent d_{pore} was approximated based on the slope and intercept of the line by assuming pore size and porosity in Knudsen diffusion and viscous flow regions are the same ($\varepsilon_f = \varepsilon_{f,K} = \varepsilon_{f,P}$, $d_{pore,i} = d_{pore,K} = d_{pore,P}$).

$$d_{pore,i} = \frac{S}{I}\frac{2K_K\mu_i}{K_P}\sqrt{\frac{T}{M_i}} \quad \text{.....(3.9)}$$

where,

dpore,i; pore size (diameter) of fiber sorbent evaluated by Gas i [m]

S; slope obtained from the fiber permeation test

I; intercept obtained from the fiber permeation test

3.5.2.3. Permeation Test for Post-Treated Fiber Sorbents

Permeance of post-treated fiber sorbents was expected to be as low as that of polymeric hollow fiber membranes. Due to low permeance, the permeate flow rate was not able to be measured directly with the bubble flow meter. In this permeation test system, the downstream with a constant volume (V_{dowm} = 32.5 cm^3) was evacuated and increase in the downstream pressure was monitored with time by recording signals from a low-pressure pressure transducer (122A 0-10 Torr Baratron® Capacitance Manometer, MKS Instruments), which was developed for the hollow fiber membranes [15] as shown in Figure 3-9. The equipment was assembled with Swagelok® parts and valves with a PID temperature controller (EW-02155-54, Cole-Parmer) to maintain 35 °C in an insulated steel box. The downstream pressure data was acquired by data acquisition board (KPCI-3116, Keithley Instruments, Inc.,) and the personalized software (LabVIEW®, National Instruments Corp). The upstream (feed) pressure was monitored by

another pressure transducer (1000 psia Model, Honeywell Sensotec). The module size was identical to that used in the standard permeation test for fibers. The system to which a test module was connected was evacuated by a vacuum pump (Model RV3, Edwards Vacuum Inc.) for 48 hours. The leak-in rate into the downstream volume (without pressure from the upstream) was monitored prior to each experiment. The rate of leak-in was subtracted from that of increase in the downstream pressure in the actual experiment. Pure nitrogen (research grade, Airgas) was applied.

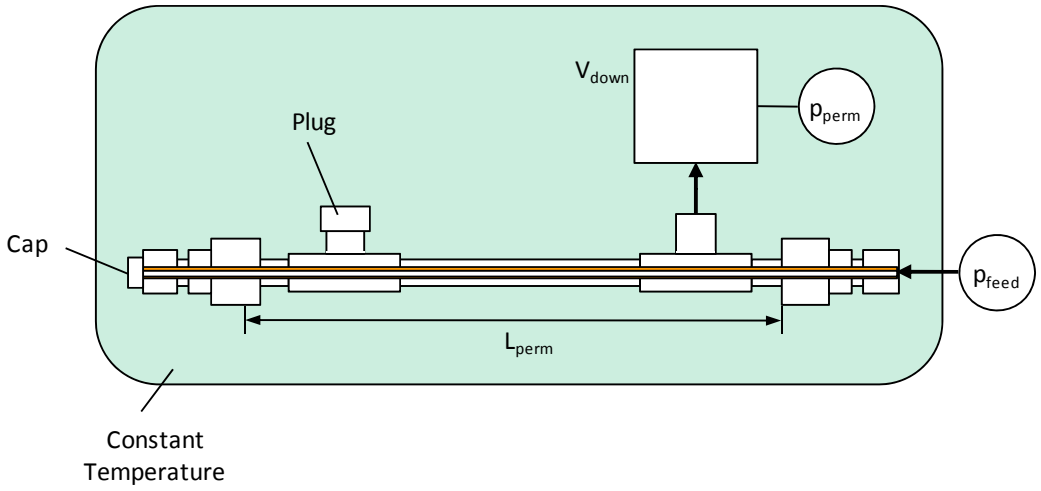

Figure 3-9 Schematic Diagram of Permeation Test for Fiber Sorbents with Impermeable Layers

$$\left(\frac{P}{l_f}\right)_i = \frac{V_{down}\left(\frac{dp_{perm}}{dt}\right)}{R_g T \pi d_f L_{perm}\left(p_{feed} - p_{perm}\right)} \quad \text{.....(3.10)}$$

where,

$\left(\frac{P}{l_f}\right)_i$; permeance of Gas i $\left[\frac{\text{mol}}{\text{m}^2\cdot\text{s}\cdot\text{Pa}}\right]$

V_{down}; downstream volume [m^3]

$\frac{dp_{perm}}{dt}$; rate of increase in downstream pressure [Pa/s] (converted from [Torr/s])

R_g; gas constant (= 8.314472 J/(mol·K))

T; gas temperature [K]

d_f; outer diameter of fiber sorbent [m]

L_{perm}; effective fiber sorbent length [m]

p_{feed}; feed pressure [Pa]

p_{perm}; permeate pressure [Pa] (< 10 Torr)

3.5.3. Thermal Gravimetric Analysis (TGA)

Thermal gravimetric analysis (TGA) (STA 409 TGA, Netzsch) was executed for some samples. A sample was held in a ceramic crucible, heated up to 1,300 °C at maximum with 10 K/min and purged with nitrogen gas with 30 ml/min.

3.5.4. Differential Scanning Calorimetry (DSC)

Differential scanning calorimetry (DSC) (DSC Q200, TA Instruments) was executed for some samples. A sample was held in an aluminum pan and heated up to 300 °C at maximum with 10 K/min and purged with nitrogen gas with 50 ml/min.

3.5.5. BET Surface Area

BET surface area was examined with nitrogen physisorption (ASAP 2020, Micrometrics) to determine the apparent surface area of zeolite in the fiber sorbents. Fiber sorbent samples were preheated and degassed for 48 hours at 120 °C.

3.5.6. Apparent Porosity

Apparent porosity, $\varepsilon_{f,app}$, was determined by measuring weight and volume of fiber sorbent samples. The samples were dried at 120 °C under the vacuum and weight and length of the samples were measured. Outer and bore diameters of the samples were measured by the SEM images. By using compositions of dopes (Chapter 4) and true densities of CA (Table 3-1) and NaY (Table 3-2), the apparent porosity was calculated.

3.5.7. Mercury Porosimetry

Macro-/mesopore distribution of fiber sorbents was analyzed by mercury porosimetry (AutoPore IV 9500, Micromeritics), which was conducted by Micromeritics Analytical Services (Norcross, GA). The analytical method is available on their website [16]. Mercury intrusion pressure was interpreted into macro- and mesopore size. The pressure was increased stepwise corresponding to the pore size. Pore size which gave maximum incremental volume was considered as apparent pore size, $d_{pore,Hg}$, for fiber sorbents. Total pore volume to calculate porosity, $\varepsilon_{f,Hg}$, was defined that for pore size with less than 100 μm.

3.5.8. Sorption Capacity

Sorption capacities (isotherms) of pure CA, pure NaY and CA-NaY fiber sorbents were evaluated by the pressure decay method [17] (Figure 3-10) with pure CO_2 (Ultra high purity, Airgas) and binary mixed gases (research grades, calibrated at 10%, 25% and 50% of CO_2 with the balance comprised of He and 25% of CO_2 with the balance comprised of H_2, Airgas). Helium was used as a surrogate for H_2. Based on mass balances of gas molecules before and after the valve opening, the sorbed gas moles were calculated as sorption capacity;

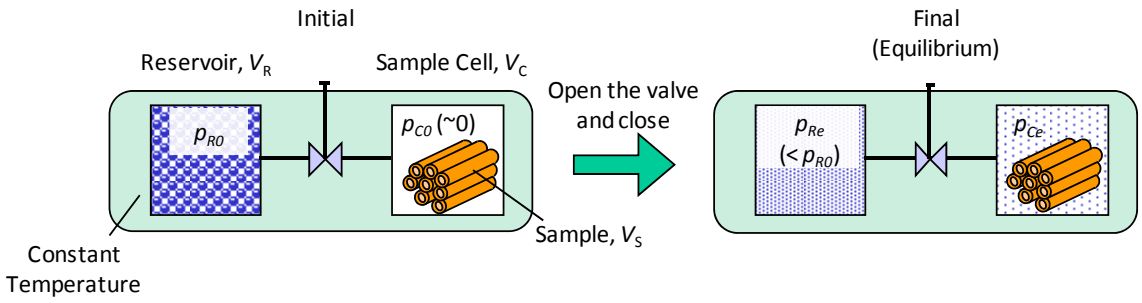

Figure 3-10 Schematic Diagram of Pressure Decay Method for Sorption Capacity

$$n_{T0} = n_{R0} + n_{C0} + n_{S0} \quad \text{.....(3.11)}$$

$$n_{Te} = n_{\mathrm{Re}} + n_{Ce} + n_{Se} = \rho'_{\mathrm{Re}} V_R + \rho'_{Ce} \left(V_C - V_S \right) + \Delta n_S \quad \text{.....(3.12)}$$

where,

subscript 0; at initial condition

subscript e; at final (equilibrium) condition

subscript T; for total in the closed system

subscript R; for reservoir

subscript C; for sample cell

subscript S; for sample

n; moles of the gas [mol]

V; volume [m^3]

ρ'; molar density [mol/m^3] at specific pressure, p [Pa]

Δn_S; moles sorbed into sample [mol]

The sorption system comprised of Swagelok® valves and specially designed reservoir and sample cell with pressure transducers (PA8224-1M-24050, AMTEK). Prior to the measurement, samples were evacuated by a vacuum pump (Model RV3, Edwards Vacuum Inc.) for more than 12 hours. Samples of pure CA were in dense film, which was casted as 10 wt% acetone solution with a stainless ring on a smooth surface glass under nitrogen atmosphere, and dried at 120 °C under the vacuum oven. Samples of pure NaY were filled in sintered porous metal filter (SS-4F-K4-05, pore size 0.5 μm, Swagelok®) and covered with aluminum foil and stainless steel strings. Fiber sorbent samples were bundle with stainless steel strings. The NaY and fiber sorbent samples were dried at 285 and 120 °C under the vacuum oven, respectively. However, those samples adsorb gases and water vapor quickly once they were removed from the vacuum oven. Therefore, those samples were weighed immediately after the drying, loaded into the sorption system and dried at 120 °C again in the sorption system bath using with silicone oil (Ultra 300, Lauda-Brinkmann) with vacuum for one day prior to the measurement. Temperatures of oil bath and air above the oil were controlled by a circulation heater (ISOTEMP 2150, Fisher Scientific Inc.) and by a PID temperature controller (EW-02155-54, Cole-Parmer), respectively.

For the mixed gases, another valve compared with the originally developed system was installed for the sample cell as shown in Figure 3-11, which was connected to a gas chromatograph (GC)

(GC-8A, TCD, Shimadzu) with N_2 carrier gas. The GC was calibrated with the standard gases of 10%, 25% and 50% of CO_2 with the balance comprised of He and H_2 prior to a series of measurement. Pressure of the sampled gas was reduced down to 10 Torrs monitored by a low-pressure pressure transducer (122A 0-10 Torr Baratron® Capacitance Manometer, MKS Instruments) and the sampled gas was introduced into a GC column (12390-U, 60/80 Carboxen-1000, 15'x 1/8" stainless steel column, Supelco).

Sorption capacity of CO_2 for the mixed gases was calculated based on the real gas data predicted by Aspen Properties® V7.1 (Aspen Technologies, Inc.). The software can employ the REFPROP mode, which was developed by the National Institute of Standards and Technology (NIST) and is based on the modified Benedict-Webb-Rubin equation of state to predict thermodynamic properties of fluids.

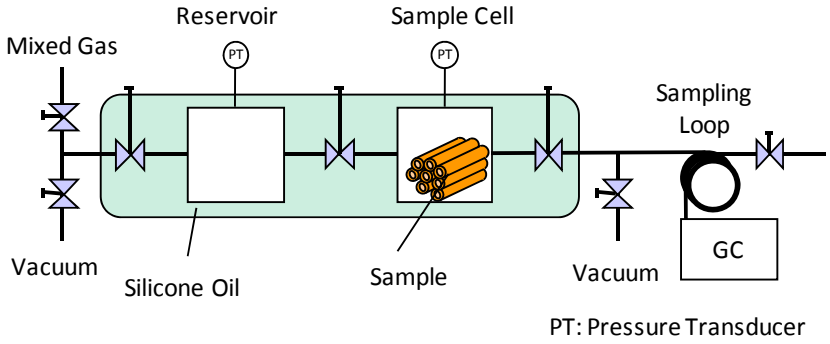

Figure 3-11 Schematic Diagram of Sorption System for Mixed Gas

3.6. Dynamic Test

3.6.1. Rapidly Cycled Pressure Swing Adsorption (RCPSA) Process

Experimental apparatus for RCPSA processes was assembled with Swagelok® pneumatic valves and tubing. The system was operated by the personalized software (LabVIEW®, National Instruments Corp) with a data acquisition board (KPCI-3116, Keithley Instruments, Inc.,) for pressure monitoring (PA8224-1M-24050, AMTEK) with a PID temperature controller (EW-02155-54, Cole-Parmer). A RCPSA sequence has been considered to operate a single module. There are five valves to operate the sequence. At the beginning of the cycle (Step I), the fiber module is pressurized with the product gas at high pressure (HP, ~100 psig) from a gas cylinder by opening the pressurization gas valve (V5) only as shown in Figure 3-12. At the end of the cycle (Step IV), the pressure in the module is lowered to the atmospheric pressure and the feed gas at high pressure travels very fast in the module. Step I prevents contaminating the module and downstream due to the fast traveling of the feed gas. In Step II, by opening both the feed (V1) and product gas valves (V2), the pre-heated feed gas at 60 °C is flowed into the module controlled by a mass flow controller (HFC-302, Teledyne Hastings). Step I and II are the common steps to measure the breakthrough times in the breakthrough test described below.

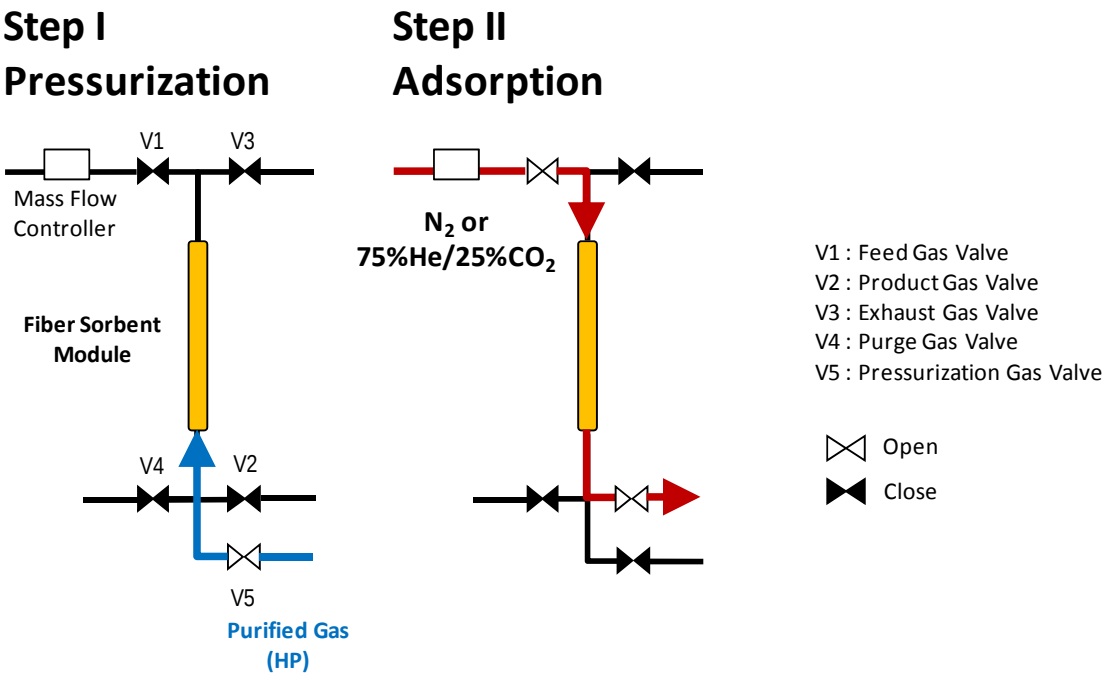

Figure 3-12 Schematic Diagram of Steps I and II (Common to the Breakthrough Test)

After the Step II, the module is depressurized by opening the exhaust gas valve (V3) only (Step III), followed by purging (Step IV) with the product gas at low pressure (LP, atmospheric pressure) by opening both the purge (V4) and exhaust valves as shown in Figure 3-13. Typically the feed gas was 25% of CO_2 with the balance comprised of He. For convenience, the HP and LP product gas were supplied directly from a gas cylinder into the laboratory scale RCPSA experiments. For the industrial cases, those product gases would be available from product gas holder in the downstream by a flow control valve instead of an on/off valve used in the experimental apparatus.

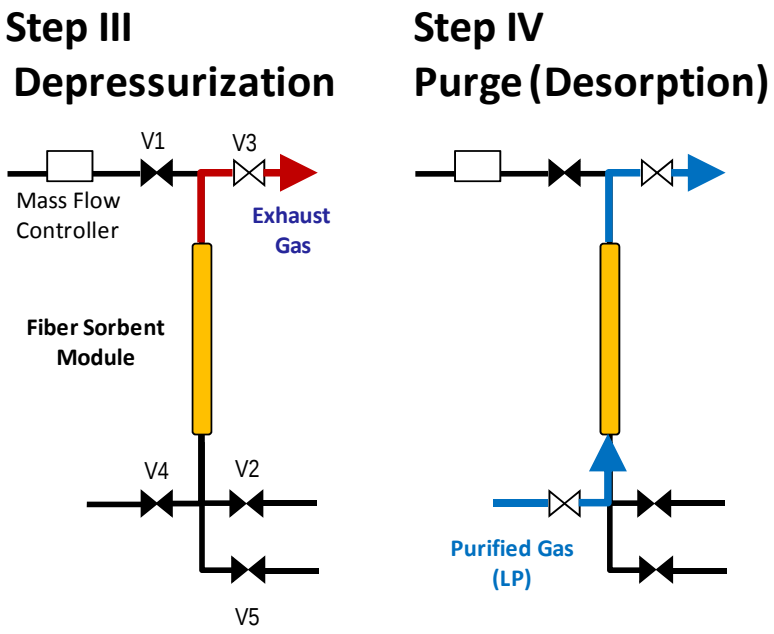

Figure 3-13 Schematic Diagram of Steps III and IV (Common to the Regeneration Test)

Multiple fiber sorbents were bundled into a module, which was the same module designed for conventional hollow fiber permeation tests. Mass transfer at the external surface of the fiber sorbent was prevented by an impermeable PVA layer as described in Chapter 5, Section 5.4, or by filling epoxy resins (DP-100, 3M) into the shell side.

3.6.2. Breakthrough Test

Breakthrough times were measured for modules with the RCPSA system described above. Initially the module was vacuumed at 60 °C for a specific time and filled with pure He (Ultra high purity, Airgas) at 60 °C and 100 psig (Step I). Pre-heated pure N_2 or mixed gas at 60 °C was fed at 100 psig with 40 – 180 cm^3(STP)/min (Step II). The module exit was connected to the GC (GC-8A, TCD, Shimadzu) and sampled at appropriate timing by the sampling valve to trace

breakthrough behavior of CO_2 with He carrier gas. The apparent breakthrough time for pure N_2 gives dead time for the experimental device. The dead time by applying pure He with N_2 carrier gas for the GC was also tested separately and gave similar dead time to the N_2, and it could assume negligible N_2 sorption relative to CO_2. For this proof of concept study, the difference between the apparent breakthrough time for pure N_2 and the mixed gas was taken as the actual breakthrough time for the fiber sorbent as shown in Figure 3-14.

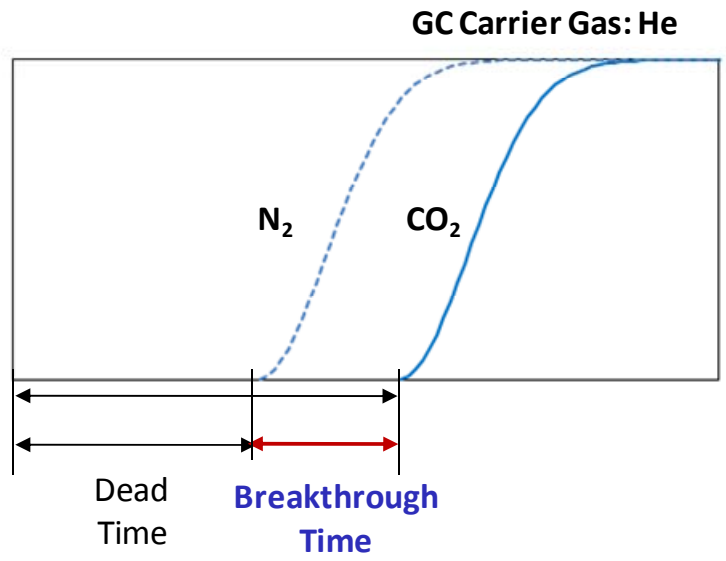

Figure 3-14 Determination of Breakthrough Time

3.6.3. Regeneration Test

Regeneration (desorption) conditions were assessed by measuring breakthrough time in the second cycle following to a whole cycle. Modules were operated in the same manner described in the breakthrough test as Step I and II in the first cycle. After the Step II, the module was

depressurized (Step III) and then purged (Step IV). After the completion of purging (the 1st cycle), the breakthrough time in the 2nd cycle was measured in the same manner used in the breakthrough test with the GC.

3.6.4. RCPSA Test

Fiber sorbent modules were operated with 100 cycles of the RCPSA sequence described above under specific conditions. The breakthrough time in the breakthrough test was obtained as maximum with completely regenerated capacity. For the RCPSA test, the modules were supposed to be in the cyclic steady state with actual operating capacity. After the 100 cycles, the breakthrough time was measured in the same manner used in the breakthrough test with the GC.

3.7. References

1. Eastman Chemical Company, *Eastman Cellulose Esters*. 2005, E-325C.

2. Zeolyst International. *Zeolite Y*. 2010 [cited 2010 August 31]; Available from: http://www.zeolyst.com.

3. Hunger, B., et al., *Adsorption of Water on Zeolites of Different Types.* Journal of Thermal Analysis, 1997. **49**(1): p. 553-565.

4. International Zeolite Association. 2010 [cited 2010 August 20]; Available from: http://www.iza-online.org/.

5. Sigma-Aldrich Co. 2010 [cited 2010 August 31]; Available from: http://www.sigmaaldrich.com.

6. Elhard, J., D.,, A. Heintz, M.,, and S. Risser, M., *Coating for Improved Carbon Nanotube Conductivity*, in *WO Patent 2009/052110*. 2009.

7. Mallinckrodt Baker, I. 2010 [cited 2010 August 31]; Available from: http://www.mallbaker.com/.

8. Kosuri, M.R. and W.J. Koros, *Defect-Free Asymmetric Hollow Fiber Membranes from Torlon (R), a Polyamide-Imide Polymer, for High-Pressure CO2 Separations.* Journal of Membrane Science, 2008. **320**(1-2): p. 65-72.

9. Husain, S. and W.J. Koros, *Mixed Matrix Hollow Fiber Membranes Made with Modified HSSZ-13 Zeolite in Polyetherimide Polymer Matrix for Gas Separation.* Journal of Membrane Science, 2007. **288**(1-2): p. 195-207.

10. Franses, E.I., et al., *Interpreting the Appearance of Dispersed Systems .1. Model Dispersions of Polymer Latex Microspheres.* Journal of the American Oil Chemists Society, 1983. **60**(5): p. 1029-1042.

11. Carruthers, S.B., G.L. Ramos, and W.J. Koros, *Morphology of Integral-Skin Layers in Hollow-Fiber Gas-Separation Membranes.* Journal of Applied Polymer Science, 2003. **90**(2): p. 399-411.

12. Lively, R.P., et al., *Hollow Fiber Adsorbents for CO2 Removal from Flue Gas.* Industrial & Engineering Chemistry Research, 2009. **48**(15): p. 7314-7324.

13. Al-Juaied, M. and W.J. Koros, *Performance of Natural Gas Membranes in the Presence of Heavy Hydrocarbons.* Journal of Membrane Science, 2006. **274**(1-2): p. 227-243.

14. Wang, R. and T.S. Chung, *Determination of Pore Sizes and Surface Porosity and the Effect of Shear Stress within a Spinneret on Asymmetric Hollow Fiber Membranes.* Journal of Membrane Science, 2001. **188**(1): p. 29-37.

15. Kosuri, M.R., *Polymeric Membranes for Super Critical Carbon Dioxide (scCO2) Separations*, in *Ph.D. Dissertation*. 2009, Georgia Institute of Technology.

16. Webb, P.A., *An Introduction To The Physical Characterization of Materials by Mercury Intrusion Porosimetry with Emphasis On Reduction And Presentation of Experimental Data*, M.I. Corp., Editor. 2001.

17. Koros, W.J. and C.M. Zimmerman, *Transport and Barrier Properties*, in *Comprehensive Desk Reference of Polymer Characterization and Analysis*, R.F. Brady, Editor. 2003, American Chemical Society; Oxford University Press: Washington, D.C.; Oxford. p. 680-699.

CHAPTER 4 FIBER SORBENT SPINNING

4.1. Introduction

This chapter provides experimental results of fiber spinning with pure (adsorbent-free) cellulose acetate (CA) fibers and CA-zeolite NaY fiber sorbents. Firstly the spinning conditions for the pure CA fibers were investigated to explore those for the CA-NaY fiber sorbents. Fiber permeation test was used to evaluate porous structure of the fiber sorbents. Sorption capacity was also accessed.

4.2. Pure Cellulose Acetate Fibers

4.2.1. Determination of Dope Composition

For the solvent, 1-methyl-2-pyrrolidinone (*N*-methyl-2-pyrrolidone, NMP) was selected because of its strong solvent power, low volatility, and good water miscibility. For the non-solvent, water was used and commonly used for the quenching bath as well. Despite the popularity of the CA in the industrial use for membrane formation, there was a limited amount of publicly available data for the CA/NMP/water system. The ternary phase diagram of the CA/NMP/water system at 25 °C was constructed experimentally as shown in Figure 4-1. Theoretically calculated binodal and spinodal curves, of which detailed information was described in Appendix A, were compared with the experimental results. The calculated binodal curve matched the reported binodal curve data, but didn't match exactly with the experimental results in this study. This may be caused by the difference in molecular weight and viscosity data of the cellulose acetate, which was used to

determine the interaction parameter. The grade of the CA (CA-398-30, Eastman Chemical Co.) used for the reported data has lower molecular weight and gives half of the viscosity compared with the CA used in this research [1]. For more analysis, viscosity and water sorption data of this grade of CA are necessary to obtain accurate interaction parameters of solvent/polymer and non-solvent/polymer.

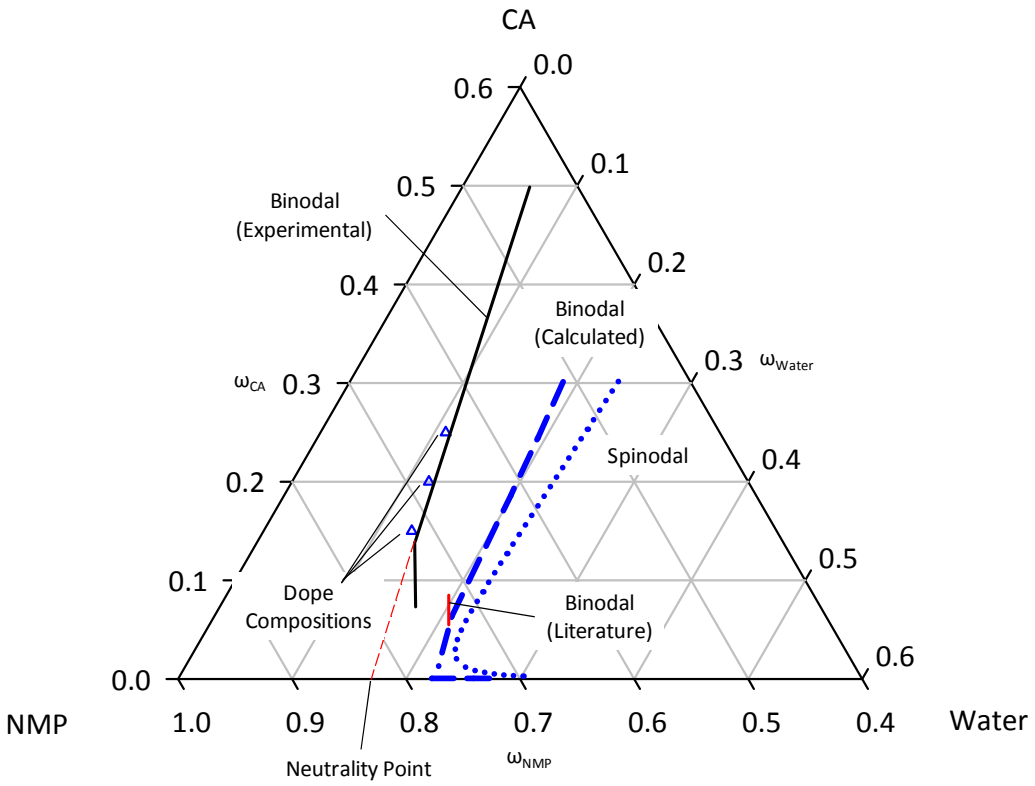

Figure 4-1 Ternary Phase Diagram of the CA/NMP/Water System at 25 °C

A dope of CA/NMP/water = 25:68:7, which was slightly far from the experimental binodal curve, was not successfully spun due to frequent fiber breaks. The reason for the problems was the slow phase separation kinetic behavior of the CA. Gas bubbles, which were generated in the dope mixing or in the transfer from the glass jar into the pump, may also contribute to the breaks [2],

but the slow phase separation attributed to the nature of the grade of CA in this research was the main problem. Another grade of CA (Sigma-Aldrich) showed similar phase separation behavior. From a stand point of dope composition, the initial dope composition should be close to the binodal curve on the ternary phase diagram to reduce diffusion time of water as non-solvent to reach the binodal curve for rapid phase separation in the spinning. The dope was not close enough to enable rapid phase separation. Other dope compositions were considered and three dope compositions were used for this research as shown in Figure 4-1 and summarized in Table 4-1. Under the spinning conditions summarized in Table 4-2, the CA fibers showed clearly porous structure because of the phase separation in the spinning as compared to the CA dense film cast on a glass plate using acetone as a solvent, as shown in Figure 4-2. As expected, the lower CA composition fiber gave more porous structure, but the fiber was mechanically weak due to high porosity.

Table 4-1 Dope Compositions for Pure CA Fibers

Pure CA Dope	ω_{CA} [wt%]	ω_{NMP} [wt%]	ω_{Water} [wt%]
15% CA	15	72	13
20% CA	20	68	12
25% CA	25	64	11

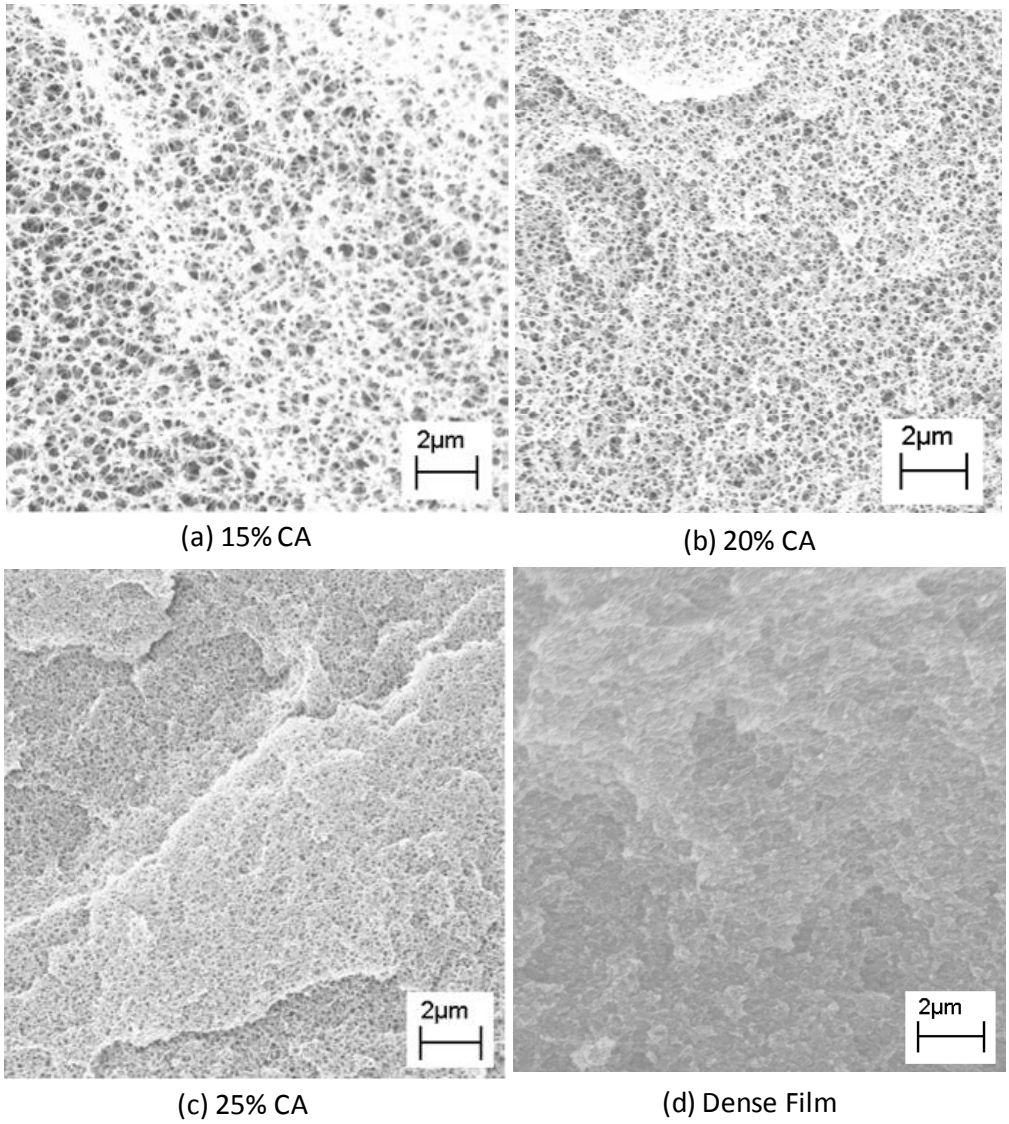

Figure 4-2 Porous Structures of Pure CA Fibers with Different Dopes Compared with CA Dense Film

Another polymer solution system, CA/acetone/water, was also explored. The acetone has traditionally been used to form flat sheet and hollow fiber membranes [3-6]. A dope of CA:acetone:water = 25:70:5 was spun with wet (submerged) spinning conditions which was specified in a U.S. patent to produce commercial reverse osmosis (RO) and ultrafiltration (UF)

membranes [4] in addition to dry-jet/wet-spinning. The wet spinning means spinning with a spinneret submerged in the quenching bath, while dry-jet/wet-spinning is usually applied to spin hollow fiber membranes for gas separations by applying an air gap to form skin layer at the outer surface of the fibers. Since the CA is a common material to be spun for RO/UF membranes, the wet spinning conditions were expected to be successful. However, the dope composition was far from its binodal curve which was defined experimentally as shown in Figure 4-3. Similarly to the CA/NMP/water dope, slow phase separation was observed and could not be spun well due to continued fiber breaks. In addition, significant amount of acetone was vaporized around the experimental system and was hazardous to experiment operators. The CA/acetone/water system was not advantageous over the CA/NMP/water.

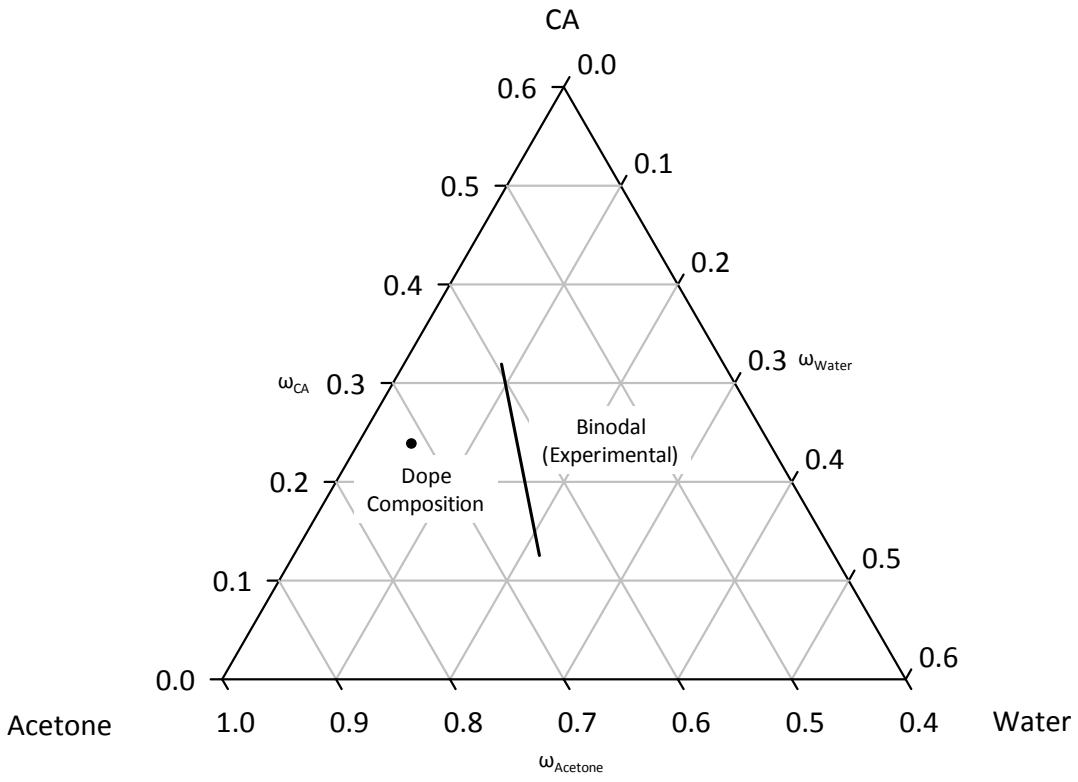

Figure 4-3 Ternary Phase Diagram of the CA/Acetone/Water System at 25 °C

4.2.2. Other Spinning Conditions

There are many spinning conditions as mentioned in Chapter 2, Section 2.2. Even only for a selection of bore fluid, there are numerous choices of chemicals and composition. A bore fluid is desired to interact minimally with the dope, which results in very slow phase separation from the bore side relative to the quenching (coagulant) bath side [7]. A mixture of a solvent and a non-solvent which is used for the dope is a typical bore fluid. On the ternary phase diagram, a composition of the solvent/non-solvent mixture which is approximated by extrapolating to the solvent/non-solvent axis a line tangent to the binodal at the polymer concentration of the dope is supposed to be a thermodynamically neutral point. For the CA/NMP/water system, the neutral point was determined as NMP:water = 83:17 by weight. The SEM images in Figure 4-5 show the bore side of pure CA fibers with bore fluids of NMP:water = (a) 80:20 and (b) 70:30 by weight. For case (a), very rough surface was observed. This potentially might generate fine particles of polymer and zeolite from the bore side of the fiber sorbents. By increasing the composition of non-solvent up to 30 % (case (b)), the surface became smoother. The bore fluid composition was set at NMP:Water = 70:30 by weight.

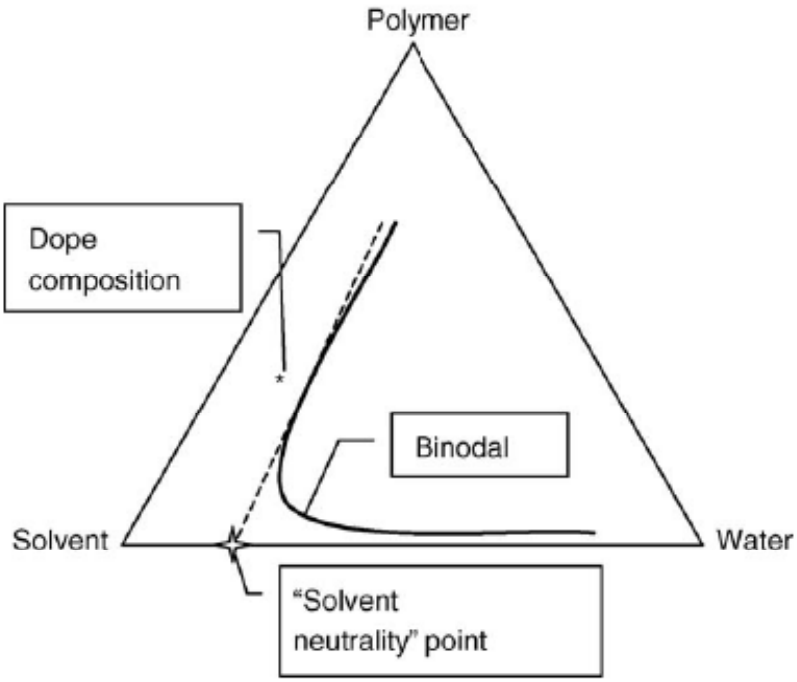

Figure 4-4 Thermodynamically Neutral Point for Bore Fluid [7]

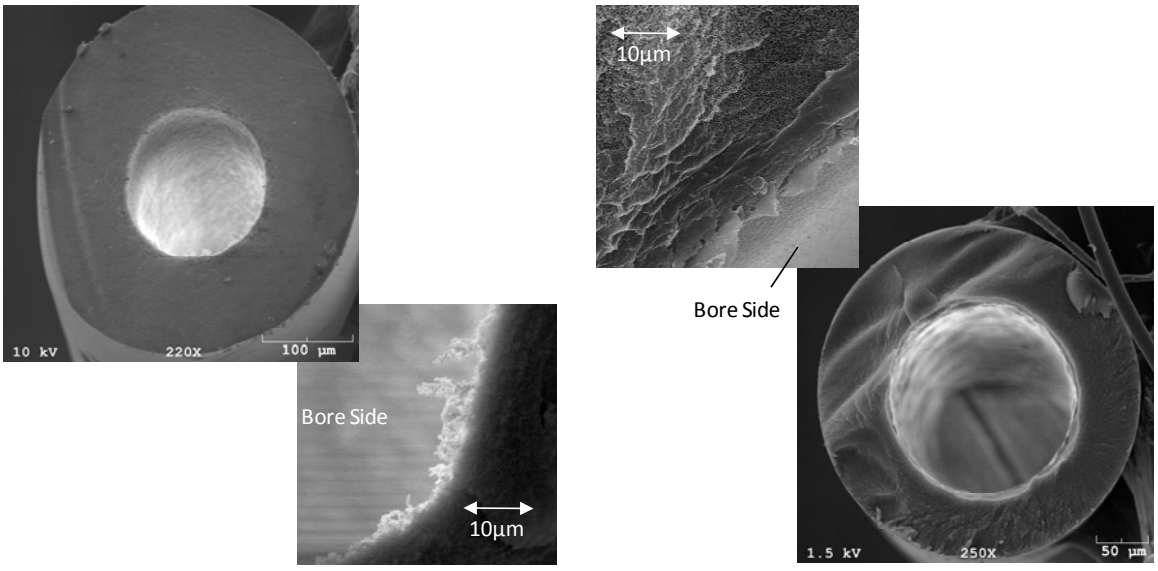

(a) NMP:Water = 80:20 (b) NMP:Water = 70:30

Figure 4-5 Surface of Bore Side of Pure CA Fiber with a Dope of CA:NMP:Water = 25:64:11 and Bore Fluids of NMP:Water = (a) 80:20 and (b) 70:30 by Weight

To achieve necessary economies of scale for hollow fiber membrane, the production rate should be 50 m/min or higher [7] and requires some tensile strength of the dope. Visco-elasticity of the dope is a critical factor to realize the high speed spinning. Increased composition and/or molecular weight of polymer give higher viscosity, but there is a limitation in pressure drop of the spinning system, especially dope feed pump, in terms of engineering practices. Increasing temperatures of dope in pump and in lines are effective to reduce viscosity and pressure drop, and can be cooled down in the quenching bath. The 25% CA dope was highly viscous and difficult to spin at the room temperature, while the 15% CA dope could spin at room temperature.

Typically higher quenching bath temperature, T_{bath}, was desired for faster diffusion of water into the dope [8]. The spinning at T_{bath} = 50 °C was not successful since the hydrophilic CA did not precipitate well and resulted in frequent fiber breaks, so coherent fibers could not be spun well.

To obtain proper hollow structures of pure CA fibers, the nascent fiber needs to be phase-separated enough to hold the shape before it contacts with a guide roll in the quenching bath [2]. Residence time, at which nascent fiber touches the guide roll in the quenching bath, was increased by applying a deeper quenching bath (L = 1 m) instead of the standard quenching bath (L = 30 cm) used for hollow fiber membrane spinning.

Based on a number of spinning experiments, appropriate spinning conditions for the pure CA fibers were investigated and are summarized in Table 4-2.

Table 4-2 Spinning Conditions for Pure CA Fibers

Dope (Core and Sheath)	Composition	See Table 4-1
	Pump Temperature	25 – 90 °C
	In-Line Temperature	25 – 90 °C
	Flow Rate	120 – 240 mL/h
Bore Fluid	Composition	NMP:Water = 70:30
	Temperature	Room Temperature
	Flow Rate	60 – 90 mL/h
Spinneret	Type	Pesek 1st Generation Spinneret
		Dual Layer Spinneret
	Temperature	25 – 90 °C
Air Gap	Distance	1 cm
	Temperature	Room Temperature
	Humidity	23.5 – 76.0 %RH
		(Not Controllable)
	Air Flow	No
Quenching Bath	Media	Cold Tap Water
		Utility Hot Water
	Depth	1 m
	Temperature	25 – 50 °C
Collection	Take-Up Rate	10 m/min
	Media	Tap Water
	Temperature	Room Temperature
Solvent Exchange	Non-Solvent	Water
		Methanol
		n-Hexane
Drying	Temperature	120 °C
	Pressure	Vacuum
	Time	1 hour

4.3. Cellulose Acetate – Zeolite NaY Fiber Sorbents

4.3.1. Determination of Dope Composition

It was difficult to distinguish cloud points for a zeolite-dispersed polymer solution due to its turbidity, and effects on phase separation behavior are unknown when many zeolite crystals are dispersed in a polymer solution. Therefore, the dope composition for fiber sorbents of the CA/NaY/NMP/water system first was determined based on that of the pure polymer solution of the CA/NMP/water system as described in Section 4.2, and then composition of the zeolite was determined based on the maximum limit of zeolite loading, which was 40 wt% of NaY in the mixture of NMP and NaY determined by the method described in Chapter 3, Section 3.3. The dopes were defined as the "first" generation dopes and are summarized in Table 4-3 corresponding to the pure CA dopes in Table 4-2. Lower polymer composition dope allows higher zeolite loading since more zeolite can be dispersed in the solvent.

Table 4-3 1st Generation Fiber Sorbent Dopes

1st Generation Fiber Sorbent Dopes	ω_{CA} [wt%]	ω_{NMP} [wt%]	ω_{Water} [wt%]	ω_{NaY} [wt%]
G-I 15% CA/76% Loading				
Polymer Solution Basis	15	72	13	-
Fiber Sorbent Dope Basis	10	49	9	32
Dry Fiber Sorbent Basis	24	-	-	76
G-I 20% CA/69% Loading				
Polymer Solution Basis	20	68	12	-
Fiber Sorbent Dope Basis	14	47	8	31
Dry Fiber Sorbent Basis	31	-	-	69
G-I 25% CA/64% Loading				
Polymer Solution Basis	25	64	11	-
Fiber Sorbent Dope Basis	17	45	8	30
Dry Fiber Sorbent Basis	36	-	-	64

Fiber sorbents were expected to have a homogenous dispersion of zeolite particles in the porous structure of polymer matrix. The 1st generation dope was successfully spun as hollow fibers and gave appropriate surface area and sorption capacity as mentioned below, but showed relatively dense polymer matrix as shown in Figure 4-6, not as porous as the pure CA fibers observed in Figure 4-2. Regardless of CA composition and zeolite loading, the similar dense polymer matrix was observed. Other factors which might affect the morphology were: 1) dope composition change due to adsorption by dried zeolite since zeolite was dried completely prior to dope preparation; 2) temperatures of spinneret and quenching bath; 3) zeolite surface and size.

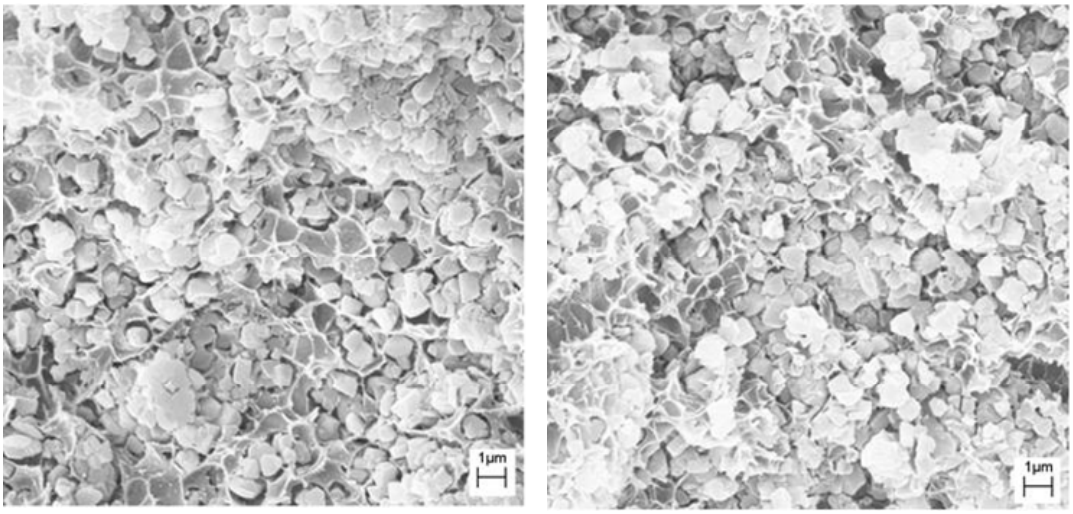

(a) G-I 15% CA/76% Loading (b) G-I 25% CA/64% Loading

Figure 4-6 Morphology of Fiber Sorbents of the 1st Generation Dopes

The dope composition shift was anticipated as shown in Figure 4-7. During the dispersion of zeolite crystals in the NMP in the dope preparation, dried zeolite adsorbed NMP completely. However, hydrophilic zeolite NaY might exchange NMP into water after the water was mixed, and then the dope composition shifted from the original one to that far from the binodal curve.

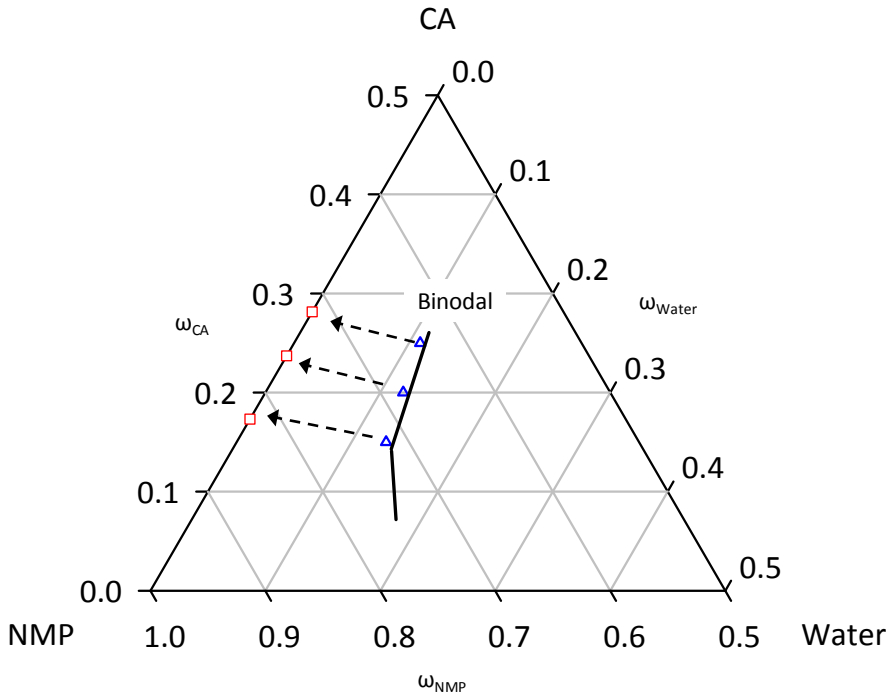

Figure 4-7 Anticipated Dope Composition Shift Due to Adsorption of Water to Dried Zeolite

Porous structures of a pure 15% CA fiber and a fiber sorbent of G-I 15% CA/64% loading were compared in Figure 4-8. The G-I 15% CA/64% loading has lower zeolite loading than the maximum limit of 76% and was spun to examine effect of loading. For the pure CA fiber, the polymer matrix was relatively denser close to the external surface (quenching bath side) and gradually became more porous toward the bore side. Porous structure of the polymer matrix in the fiber sorbent was similar to that of pure CA fiber close to the external surface. This indicates the phase separation of the polymer solution in the fiber sorbent dope took longer time due to the longer and different diffusion path of non-solvent (water) to reach the binodal curve as a result of the dope composition shift as mentioned above. The longer and different diffusion path might cause the denser polymer matrix.

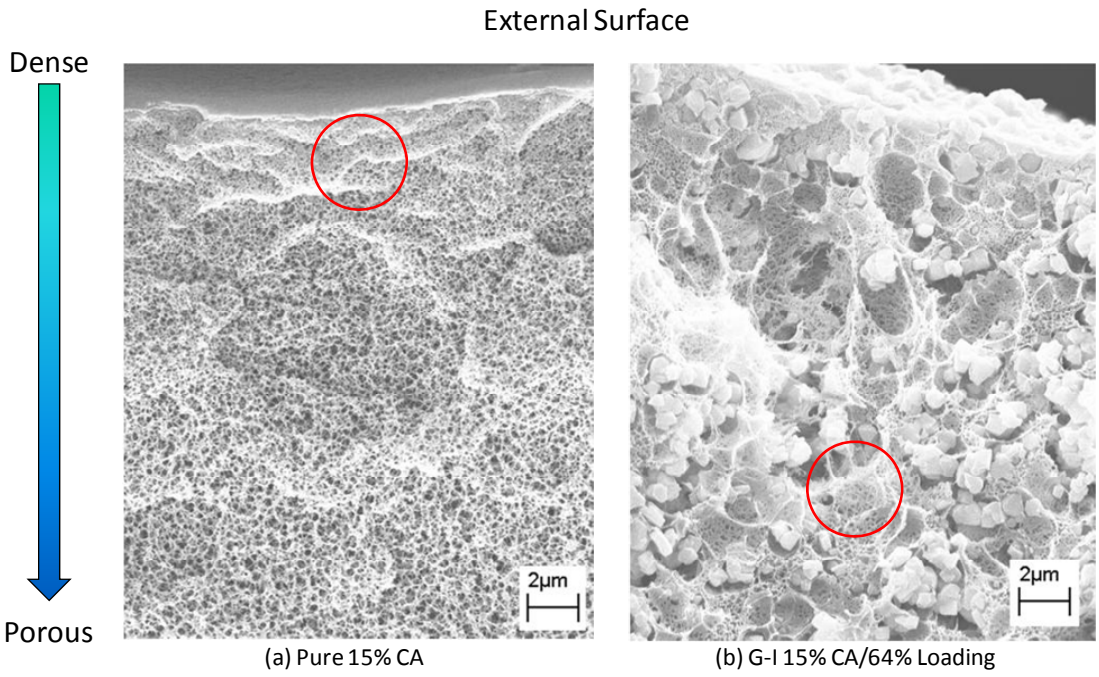

Figure 4-8 Comparison of Porous Structure in Pure 15% CA Fiber and Polymer Matrix of Fiber Sorbent (G-I 15% CA / 64% Loading)

"Extra" water was desired to be added to the fiber sorbent dopes. The amount of the extra water was assumed as that equivalent to the saturation of water vapor to the NaY. The saturated NaY with water vapor showed weight increase of 32 % by weight against the dried NaY by the method described in Chapter 3, Section 3.3. The 2nd generation dopes took the extra water into account and are summarized in Table 4-4 corresponding to the pure CA dopes in Table 4-2. Fiber sorbents of the 2nd generation dopes were also successfully spun under the conditions specified in Table 4-2. The morphology of fiber sorbents of the 1st and the "second" generation dopes, which contains "extra" water mentioned below, was compared in Figure 4-9. The fiber sorbents of the 1st generation dopes showed rigid morphology and were mechanically stronger than those of the 2nd generation dopes. As described below, fiber permeance test data for the fiber sorbents with the 1st generation dopes showed lower than that for the fiber sorbents with the 2nd generation dopes.

The fiber sorbents were somewhat brittle compared to the CA hollow fibers, but strong enough to assemble modules and to be operated under high pressure. Qualitatively fiber sorbents with lower CA composition/higher zeolite loading fiber sorbent was mechanically weaker; however, increasing CA composition for higher mechanical strength reduces the zeolite loading and sorption capacity of the fiber sorbent. Smaller size zeolite crystal may increase mechanical strength of the polymer/zeolite dense composite material [9]. For the fiber sorbent, some optimum dope composition with high mechanical strength, high sorption capacity and highly porous structure can be developed using this formation platform. Impermeable layers will also contribute to mechanical strength of the bare fiber sorbent, while such an additional structural support is prohibited for traditional zeolite pellets.

Table 4-4 2nd Generation Fiber Sorbent Dopes

2nd Generation Fiber Sorbent Dopes	ω_{CA} [wt%]	ω_{NMP} [wt%]	ω_{Water} [wt%]	ω_{NaY} [wt%]
G-II 15% CA/76% Loading				
Polymer Solution Basis	15	72	13	-
Fiber Sorbent Dope Basis	9	44.5	17.5	29
Dry Fiber Sorbent Basis	24	-	-	76
G-II 20% CA/69% Loading				
Polymer Solution Basis	20	68	12	-
Fiber Sorbent Dope Basis	12.5	42.5	16.5	28.5
Dry Fiber Sorbent Basis	31	-	-	69
G-II 25% CA/64% Loading				
Polymer Solution Basis	25	64	11	-
Fiber Sorbent Dope Basis	15.5	41	16	27.5
Dry Fiber Sorbent Basis	36	-	-	64

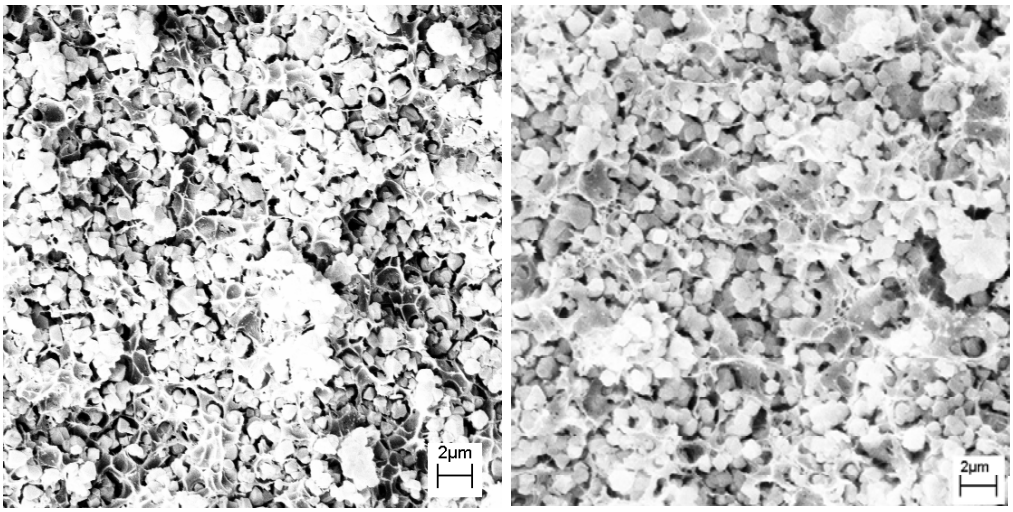

(a) 1st Generation Dope (No Extra Water)

(b) 2nd Generation Dope (Extra Water)

Figure 4-9 Morphology of Fiber Sorbents with (a) 1st and (b) 2nd Generation Fiber Sorbent Dopes

To prepare the 2nd generation dopes, two different methods to add "extra" water were tested; 1) dried zeolite was exposed to water vapor with 100% relative humidity for several days until the zeolite was saturated; 2) equivalent amount of water was added to the dope when it was prepared. The second method was easier and more convenient to control the extra water addition. The difference between the two methods didn't give significant impact on the morphology as shown in Figure 4-10.

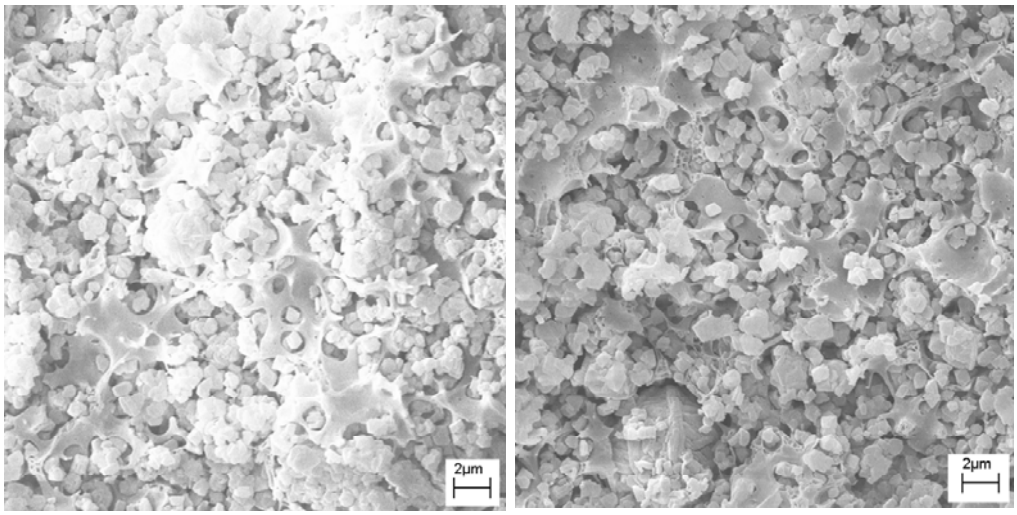

(a) Saturated Zeolite (b) Addition of Extra Water

Figure 4-10 Morphology of Fiber Sorbents with Different Dopes

(a) Saturated Zeolite and (b) Addition of Extra Water

The detailed phase separation mechanism is still unknown, but it is hypothesized that rheology (high viscosity), local dope composition (adsorption of polymer molecules at zeolite surface) and/or diffusive path of non-solvent (zeolitic pores and sieve-in-a-cage voids) are changed as a result of presence of zeolite particles in addition to the temperature effects. The dope composition shift observed for the 1st generation dope should involve slower phase separation as observed for the pure CA and might have given frequent fiber breaks, but the CA-NaY fiber sorbents with the 1st generation dopes were spun successfully. High temperature of quenching bath could be applied for the CA-NaY fiber sorbent relatively easier than the pure CA fibers. Systematic rheological studies of zeolite-dispersed polymer solutions are required to pursue more optimized spinning conditions. Spinning of fiber sorbents with surface modified zeolite for hydrophobization might be helpful to test this hypothesis related to surface conditions of zeolite.

In conclusion, the hydrophobization described in Appendix F was not meaningful to change the morphology.

4.3.2. Porous Structure

For some fiber sorbents with different dopes, apparent pore size (diameter) and apparent porosity were examined by the different methods; fiber permeation test with small size module, volume/weight measurement of dry fiber sorbent, and mercury (Hg) porosimetry, which are described in Chapter 3, Section 3.5. The morphology of those fiber sorbents are shown in Figure 4-11.

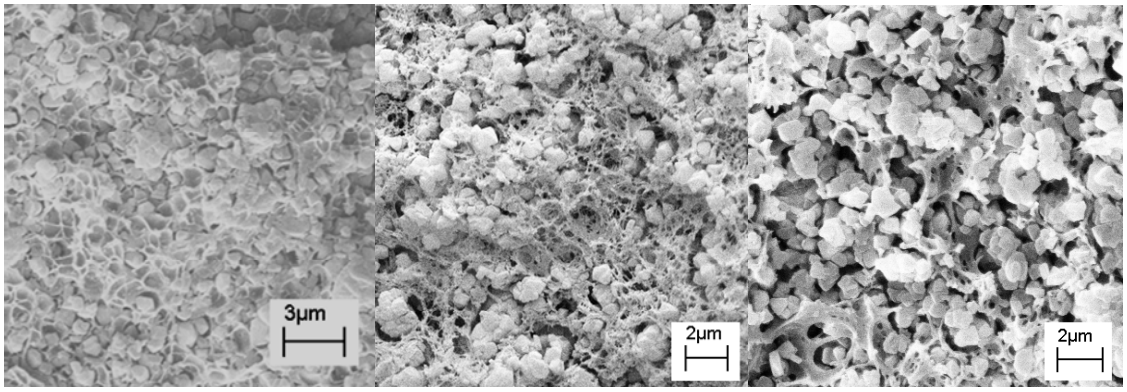

Figure 4-11 Morphology of Fiber Sorbents Used in Porous Structure Analyses

Permeance for porous materials such as fiber sorbents varies linearly over a wide range of feed pressure. A set of the fiber permeation test results of fiber sorbents (G-I 25% CA/64% loading, G-II 20% CA/69% loading and G-II 15% CA/76% loading) with N_2 at 35 °C is shown in Figure 4-12. The permeance of the fiber sorbents was enormous (10^3~10^5 GPU) compared with the typical permeance of polymeric hollow fiber membranes (1~100 GPU), which is also evidence of

the highly porous structure in addition to the morphology observation. Depending on the dope, the magnitude of permeance dramatically changed. The 2nd generation dope with addition of extra water showed much higher permeance than the 1st generation dope and proved that the dope composition change due to adsorption of water by the zeolite was reasonable for less phase separation during the spinning in the 1st generation dopes. As described in Chapter 3, Section 3.5, apparent pore size was obtained from the slope and intercept of the fiber permeation curve.

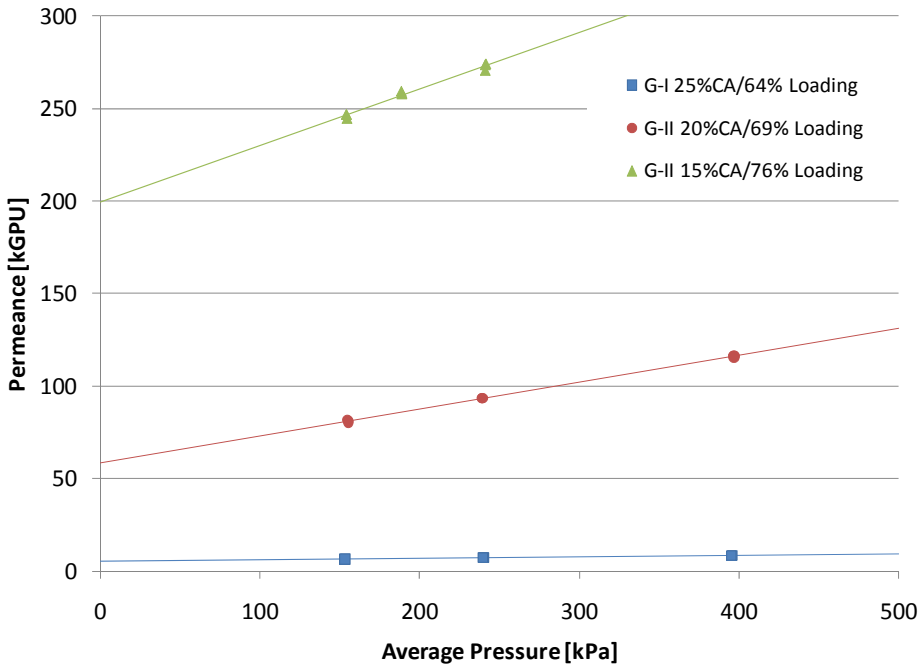

Figure 4-12 Examples of Fiber Permeation Test Results (N_2, 35 °C)

Another set of the fiber permeation test results for a fiber sorbent (G-II 15% CA/76% loading) with three different gases (N_2, He and CO_2) at 35 °C is shown in Figure 4-13.

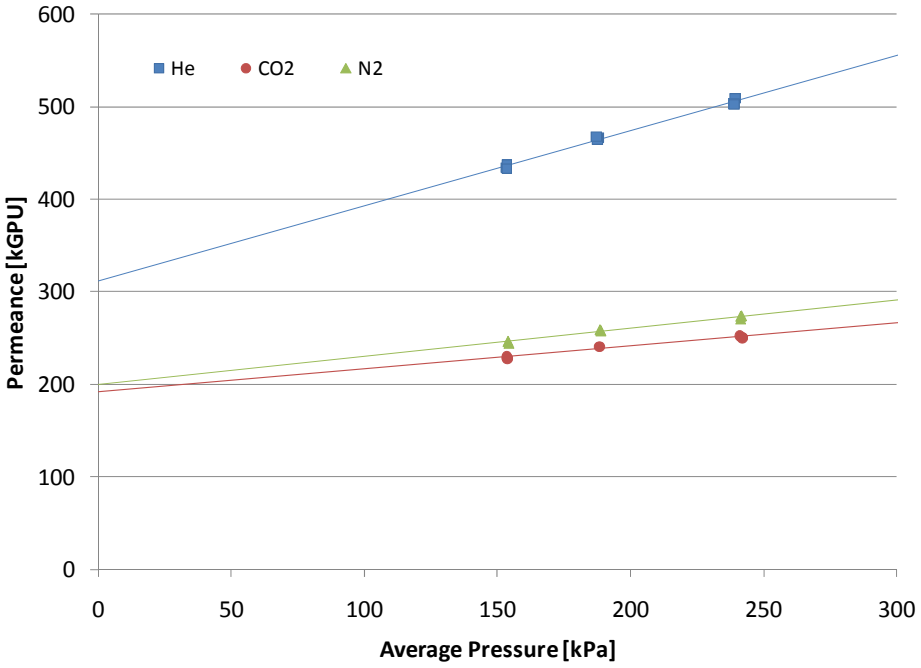

Figure 4-13 Examples of Fiber Permeation Test Results (G-II 15% CA/76% Loading, 35 °C)

The permeance curves of N_2 and CO_2 were similar each other. Selectivity is calculated as a ratio of permeance of Gas i to Gas j;

$$\alpha_{i/j} = \left(\frac{P}{l_f}\right)_i \Big/ \left(\frac{P}{l_f}\right)_j \quad \text{..... (4.1)}$$

where,

$\alpha_{i/j}$; selectivity of Gas i to Gas j [-]

$\left(\frac{P}{l_f}\right)$; permeance [GPU]

Knudsen selectivity, $\alpha_{K,i/j}$, is obtained from Equation (C.101);

$$\alpha_{K,i/j} = \frac{D_{K,i}}{D_{K,j}} = \sqrt{\frac{M_j}{M_i}} \quad \text{..... (4.2)}$$

where,

$\alpha_{K,i/j}$; Knudsen selectivity of Gas i to Gas j [-]

D_K; Knudsen diffusivity [m^2/s]

Selectivities of the three gases for the fiber sorbents were calculated based on the intercepts and was summarized in Table 4-5 with Knudsen selectivity.

Table 4-5 Selectivity of CO_2, He and N_2 for Fiber Sorbents

	$\alpha_{CO2/N2}$	$\alpha_{He/N2}$	$\alpha_{He/CO2}$
Knudsen Selectivity	0.80	2.65	3.32
G-I 25% CA/64% Loading	0.75	2.81	3.76
G-II 20% CA/69% Loading	0.87	2.27	2.62
G-II 15% CA/76% Loading	0.96	1.56	1.62

The selectivities for G-I 25% CA/64% loading were closed to the Knudsen selectivities. This indicated that pore size was small enough in the Knudsen region. Since the CO_2 is strongly adsorbed to the zeolite surface, the selectivity of CO_2 to N_2, $\alpha_{CO2/N2}$, might be lower than Knudsen selectivity for G-I 25% CA/64% loading due to surface diffusion contributions. The selectivities for G-II 15% CA/76% loading were close to unity and indicated non-selective gas flow through the porous structure with large pore size. The selectivities for G-II 20% CA/69% loading were located between G-I 25% CA/64% loading and G-II 15% CA/76% loading and indicated the pore size ranged between Knudsen and viscous flow regions.

Pore size distributions measured by Hg porosimetry for the fiber sorbents used above are shown in Figure 4-14. The fiber sorbent of the 1st generation dope (G-I 25% CA/64% loading), which gave rigid morphology, gave small pores with a wide range. On the other hand, the fiber sorbents of the 2nd generation dopes (G-II 20% CA/69% loading and G-II 15% CA/76% loading), which gave more porous morphology, gave a narrower distribution with a larger median pore size. Comparing with the morphology in Figure 4-11, the peak at small pores for the fiber sorbent of G-I 25% CA/64% loading was because the phase-separated polymer matrix mainly and sieve-in-a-cage morphology contributing at a range of 150 – 250 nm. For the fiber sorbent of G-II 20% CA/69% loading, the largest peak was contributed by both phase-separated polymer matrix and sieve-in-a-cage morphology. For the fiber sorbent of G-II 15% CA/76% loading, the void space at the largest peak was mostly because of combined sieve-in-a-cage morphology around crowded zeolite crystals as a result of high loading. Based on the SEM image (Figure 4-11), it is reasonable that pores because of sieve-in-a-cage morphology around 500 nm zeolite crystals range between 150 – 250 nm.

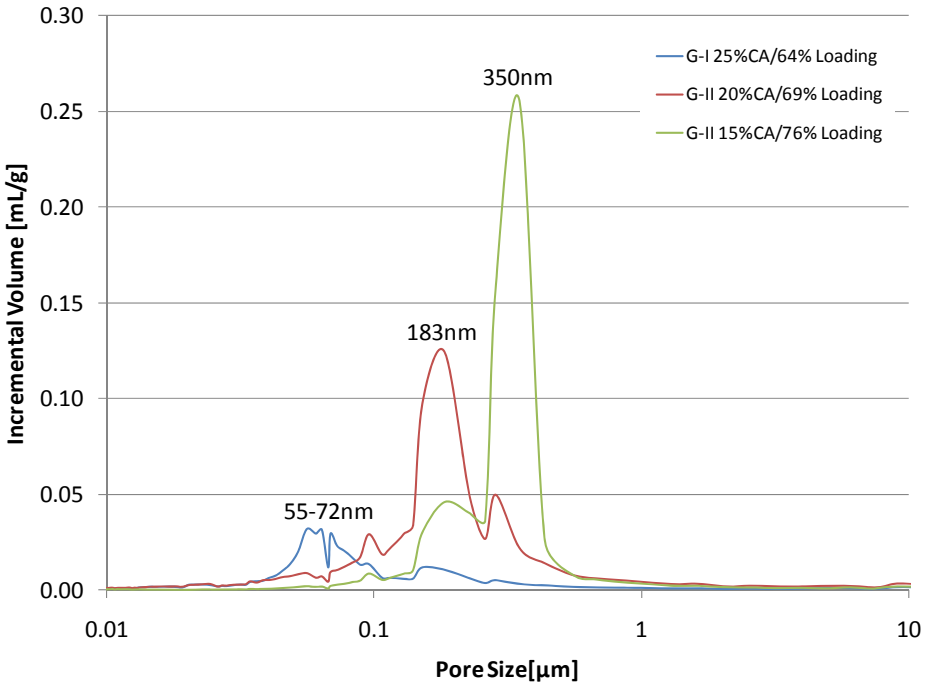

Figure 4-14 Pore Size Distribution of Fiber Sorbents by Mercury Porosimetry

The results from the fiber permeation test and the Hg porosimetry were compared in Figure 4-15. Pore sizes based on the fiber permeation test were determined by averaged data of the multiple modules. For the fiber sorbent of G-I 25% CA/64% loading, the pore sizes determined by permeation analyses for the different gases were similar to one another and larger than that by the Hg porosimetry. On the other hand, for the fiber sorbents of G-II 20% CA/69% loading and G-II 15% CA/76% loading, the pore sizes were varied with the gases, and did not have a consistent relationship with that by the Hg porosimetry except He.

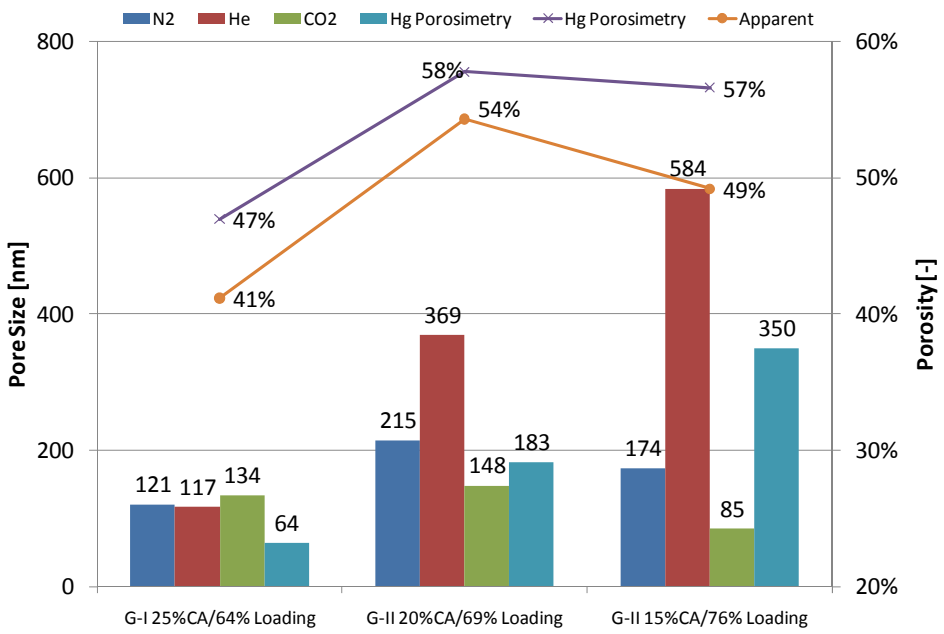

Figure 4-15 Comparison in Pore Size and Porosity with Mercury Porosimetry

The pore size determined by the He fiber permeation test and the Hg porosimetry test have a linear relationship;

$$d_{pore,Hg} = 0.609 d_{pore,He} - 18.2 \quad \text{..... (4.3)}$$

where,

$d_{pore,Hg}$; pore size determined by the mercury porosimetry [nm]

$d_{pore,He}$; pore size determined by the He permeation test at 35 °C [nm]

Note the squared residual $R^2 = 0.98$ for the linear regression.

Apparent porosity based on the volume/weight measurement gave lower values, but a reasonable linear relationship with those by the Hg porosimetry;

$$\varepsilon_{f,Hg} = 0.86\varepsilon_{f,app} + 0.13 \quad \text{..... (4.4)}$$

where,

$\varepsilon_{f,Hg}$; porosity determined by the mercury porosimetry [-]

$\varepsilon_{f,app}$; apparent porosity [-]

Note the squared residual $R^2 = 0.91$ for the linear regression.

It was concluded that the He fiber permeation test and volume/weight measurement of fiber sorbents are convenient methods to evaluate pore size and porosity instead of the Hg porosimetry.

Based on permeance for He and apparent porosity, pore size and porosity equivalent to the Hg porosimetry were evaluated for other fiber sorbent samples. As described above, the dopes including extra water exhibited more porous structure. Less porous (rigid) fiber sorbent resulted in significantly lower pore size and porosity for both 15 and 25 wt% of CA in polymer solution basis as shown in Figure 4-16.

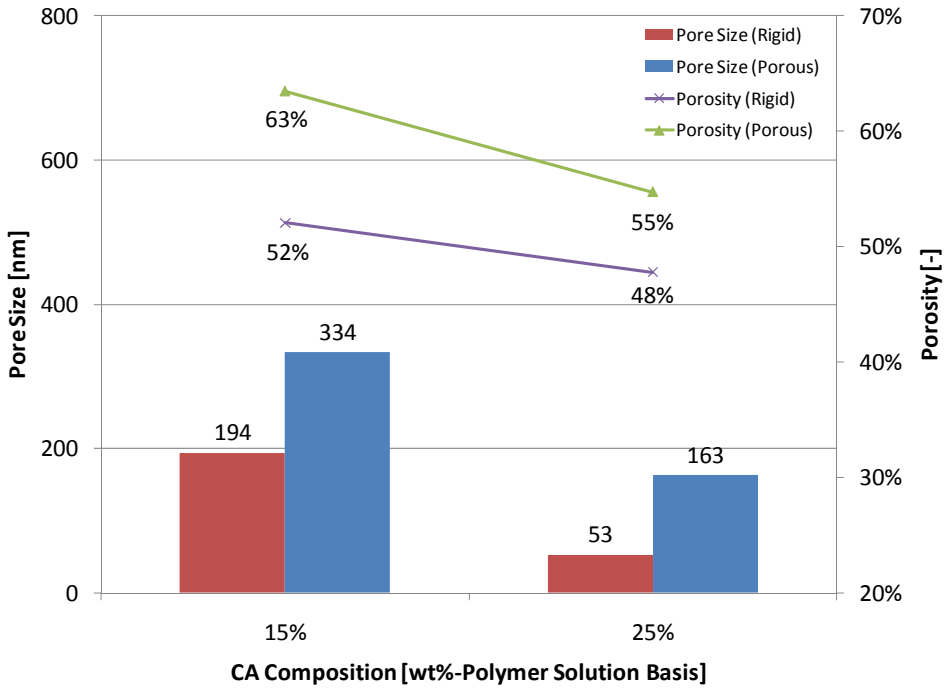

Figure 4-16 Pore Size and Porosity for Fiber Sorbents (Rigid and Porous Fiber Sorbents)

4.3.3. Temperature Effects on Morphology

Morphologies of fiber sorbents (G-II 15% CA/76% loading) are shown in Figure 4-17 when spinneret and quenching bath temperatures, $T_{spinneret}$ (25, 50 and 90 °C) and T_{quench} (25 and 50 °C) were changed. The fiber sorbents were all spun under the same conditions except those temperatures. Permeance at 30 psia of feed pressure of three different gases (N_2, He and CO_2), apparent pore size (diameter) based on the fiber permeation test and apparent porosity are summarized in Table 4-6. As intended, the fiber sorbents were porous with homogeneously dispersed zeolite crystals. The different $T_{spinneret}$ and T_{quench} gave different morphologies: Fiber sorbents of (a), (d) and (e) in Figure 4-17 were porous, but those of (b), (c) and (f) showed denser portion in the polymer matrix and seemed less porous. For the fiber sorbents of (b), (c) and (f), the $T_{spinneret}$ was higher than the T_{quench} and the nascent fiber sorbent was rapidly quenched in the

water bath in the spinning process. The denser portion in the polymer matrix might be expected to hinder gas permeation; however, the highest $T_{spinneret}$ and T_{quench} resulted in the highest permeance, regardless of the appearance of the morphologies. The higher T_{quench} presumably causes faster diffusion of water through the dope to drive a rapid change of the dope composition. As shown in Figure 4-18, the permeation curves of Cases (d) and (e) were similar each other, and the morphology for those cases were closed to Sample (b) in Figure 4-11. Cases (d) and (e) have similar pore size for the viscous flow region and a sieve-in-a-morphology contributed the viscous flow region and resulted in a range of 250 – 330 μm in the pore size. On the other hand, slope and intercept for Case (f) was steeper and higher than those for Cases (d) and (e). Case (f) has more number of pores in the Knudsen diffusion region and larger pore size in the viscous flow region than Cases (d) and (e). As noted above, combined sieve-in-a-morphology created larger pore size with denser polymer matrix. As $T_{spinneret}$ increased, the pore size became larger except Case (e). Based on the behavior of permeance compared with (d), it is considered still within the error. The porosity became clearly smaller for higher $T_{spinneret}$.

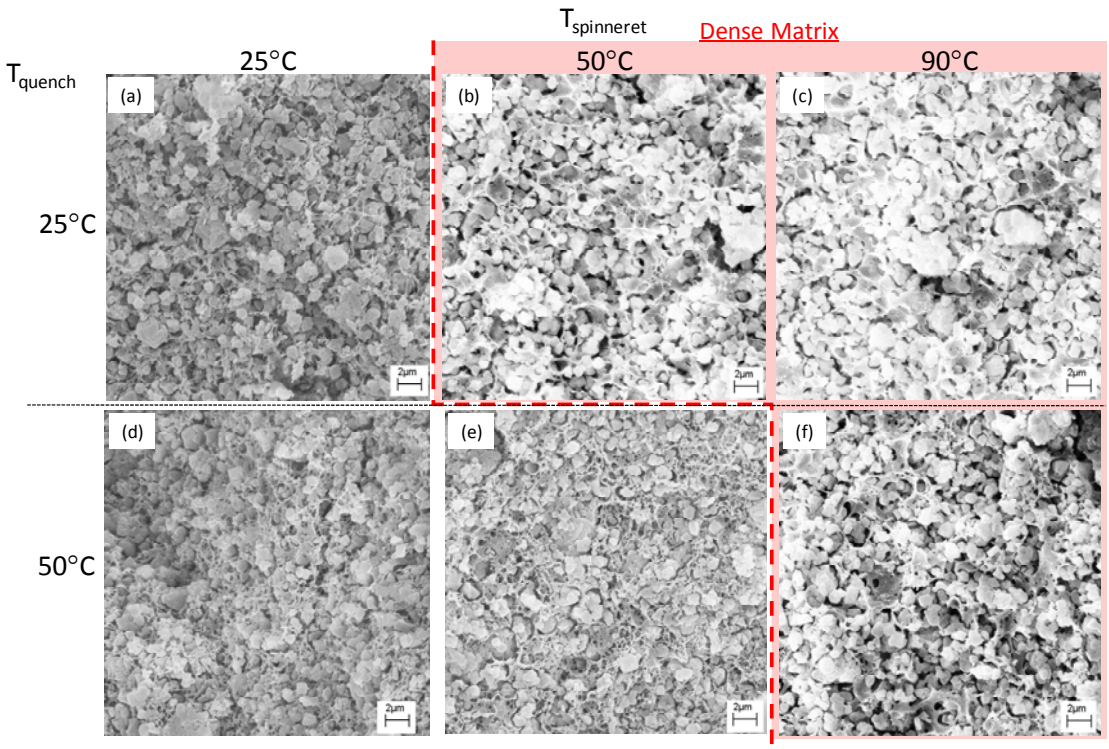

Figure 4-17 Morphology of Fiber Sorbents (G-II 15% CA/76% Loading) at Different Temperatures of Spinneret (25, 50 and 90 °C) and Quenching Bath (25 and 50 °C)

Table 4-6 Permeance, Apparent Pore Size and Apparent Porosity of Fiber Sorbents Corresponding to Figure 4-17

	Gas		$T_{spinnerert}$		
		T_{quench}	25 °C	50 °C	90 °C
Morphology (Figure 4-17)		25 °C	(a)	(b)	(c)
		50 °C	(d)	(e)	(f)
Permeance [kGPU]	N_2	25 °C	- [1)]	128	157
		50 °C	168	153	234
	He	25 °C	- [1)]	243	284
		50 °C	311	292	412
	CO_2	25 °C	- [1)]	120	146
		50 °C	153	142	221
Apparent Pore Size [nm]	N_2	25 °C	- [1)]	311	184
		50 °C	160	227	174
	He	25 °C	- [1)]	578	665
		50 °C	573	436	584
	CO_2	25 °C	- [1)]	211	116
		50 °C	103	169	85
	Hg eq.[2)]	25 °C	- [1)]	334	387
		50 °C	331	248	337
Apparent Porosity [vol%]		25 °C	- [1)]	59	53
		50 °C	52	50	49
	Hg eq.[3)]	25 °C	- [1)]	63	58
		50 °C	57	56	55

1) Easily broken in the spinning and not collected by the take-up drum

2) Equivalent pore size to mercury porosimetry based on Equation (4.3)

3) Equivalent porosity to mercury porosimetry based on Equation (4.4)

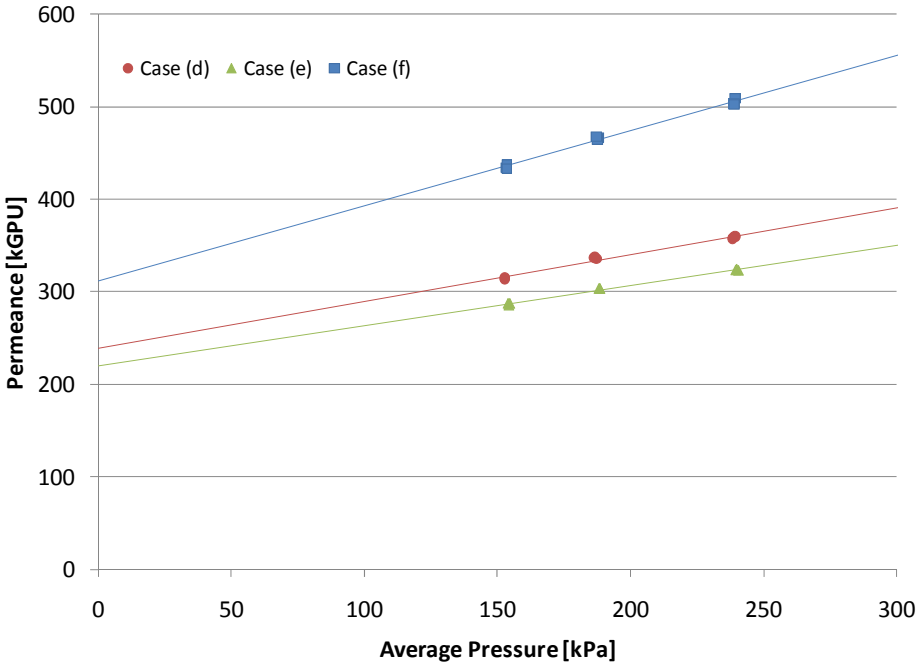

Figure 4-18 Fiber Permeation Test Results with He (Cases (d), (e) and (f) in Figure 4-17)

4.3.4. Sorption Capacity of CO_2

BET surface area of even the fiber sorbent (G-I 25% CA / 64% loading) was similar to the pure NaY as shown in Table 4-7. This result suggests that the zeolite crystals were dispersed without blockage of the zeolitic pores by the polymer.

Table 4-7 BET Surface Area of Pure NaY and CA-NaY Fiber Sorbent

Sample	BET Surface Area m^2/g
Pure NaY	778.1
CA-NaY Fiber Sorbent (G-I 64% Loading)	
As Measured	487.4
Corrected by Loading Level	761.0

Sorption capacities (sorption isotherms) of pure CO_2 to pure NaY and CA are shown in Figure 4-19 and Figure 4-20, respectively. For the NaY, a simple Langmuir type isotherm was postulated and the parameters were obtained by curve fitting for experimental data at 35 and 60 °C as shown in Table 4-8.

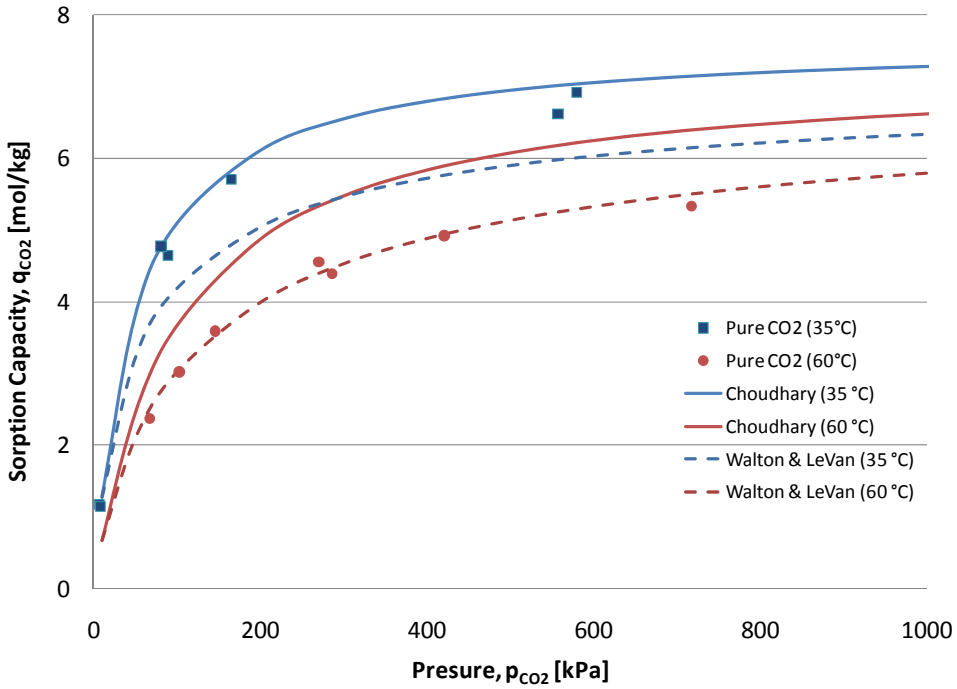

Figure 4-19 Sorption Isotherms of CO_2 to Zeolite NaY at 35 and 60 °C

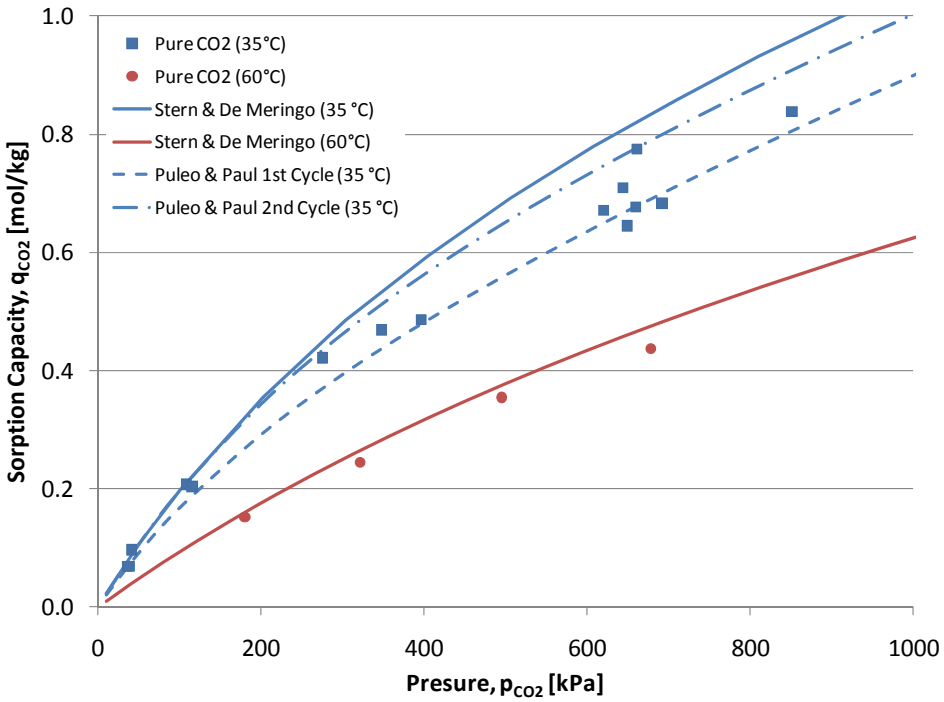

Figure 4-20 Sorption Isotherms of CO_2 to Cellulose Acetate at 35 and 60 °C

Table 4-8 Experimental Sorption Parameters for CO_2 to Zeolite NaY

	$q_{c,s0}$ [mol/kg]	$-\Delta H_{qc}$ [kJ/mol]	b_{c0} [Pa^{-1}]	$-\Delta H_{ads,c}$ [kJ/mol]
	0.7693	5.750	2.172×10^{-10}	29.59
	$q_{c,s}$ [mol/kg]		b_c [Pa^{-1}]	
35 °C	7.258		2.254×10^{-5}	
60 °C	6.133		9.472×10^{-6}	

The sorption capacity of pure CO_2 in the CA is significantly lower than that in the NaY, emphasizing the need for maximizing the zeolite loading to give high sorption capacity of fiber sorbents. Experimental sorption capacity of a fiber sorbent (G-I 25% CA / 64 wt% loading) was

plotted and was close to a predicted isotherm by applying the isotherms of pure NaY (experimental curve) and pure CA (Stern's curve) as shown in Figure 4-21. This result also indicates that the zeolite crystals were dispersed without blockage of the zeolitic pores by the polymer.

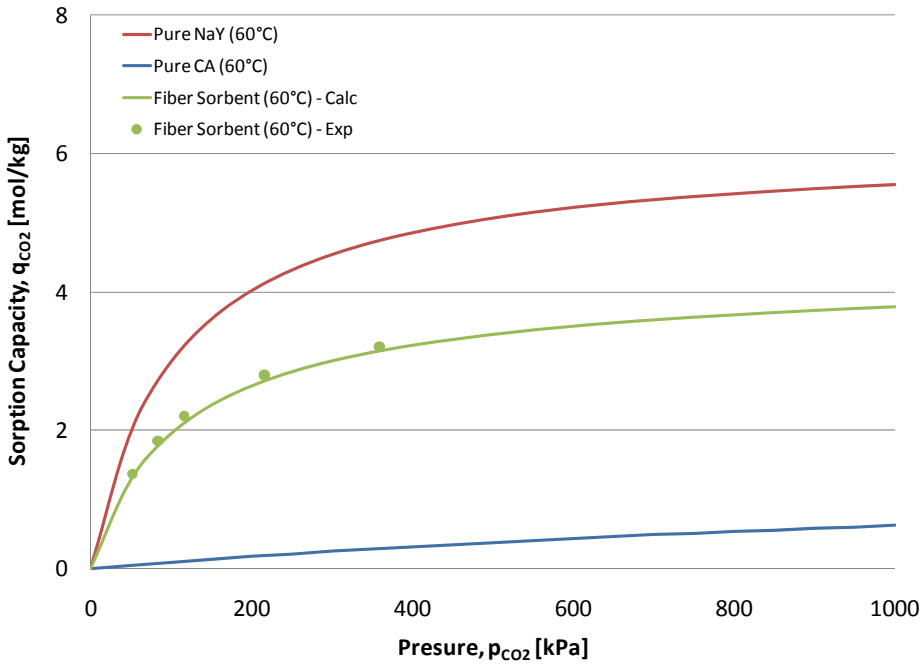

Figure 4-21 Sorption Isotherms of CO_2 to Fiber Sorbent (G-I 25% CA/64% Loading) at 60 °C

Sorption capacities of CO_2 in the mixtures with He and H_2 to pure NaY and CA were also assessed and are shown in Figure 4-22 and Figure 4-23. The experimental data was close to the isotherms for pure CO_2 implying the NaY and the CA adsorbed CO_2 more preferably than He and H_2, so the NaY is expected to separate CO_2 effectively from the reformate gas. The isotherm for the H_2/CO_2 mixed gas to the NaY showed slightly lower than that of pure CO_2 due to the error in measurement of weight of the NaY sample as described in Chapter 7. As expected, experimental sorption capacity of a fiber sorbent (G-I 25% CA / 64 wt% loading) was also close to a predicted

isotherm used in Figure 4-21. Fiber sorbents were successfully produced with appropriate sorption capacity of CO_2.

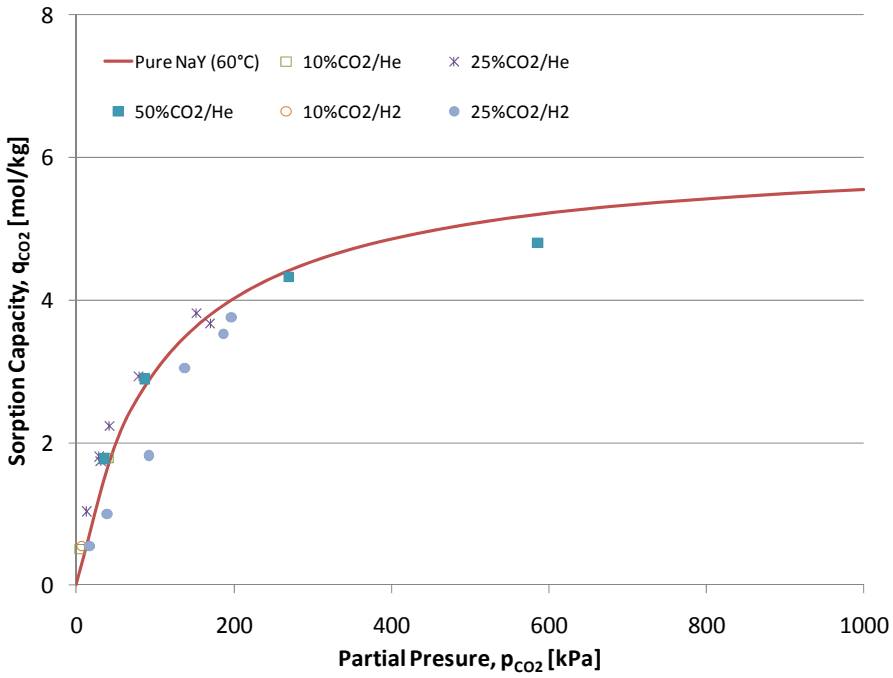

Figure 4-22 Sorption Isotherms of CO_2 in Mixed Gases to Zeolite NaY at 60 °C

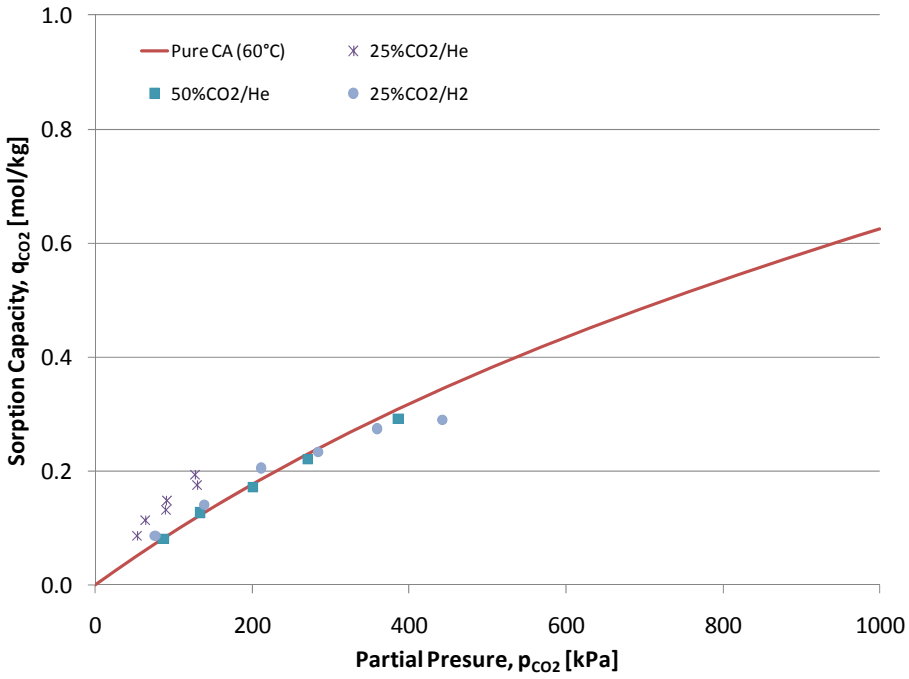

Figure 4-23 Sorption Isotherms of CO_2 in Mixed Gases to Cellulose Acetate at 60 °C

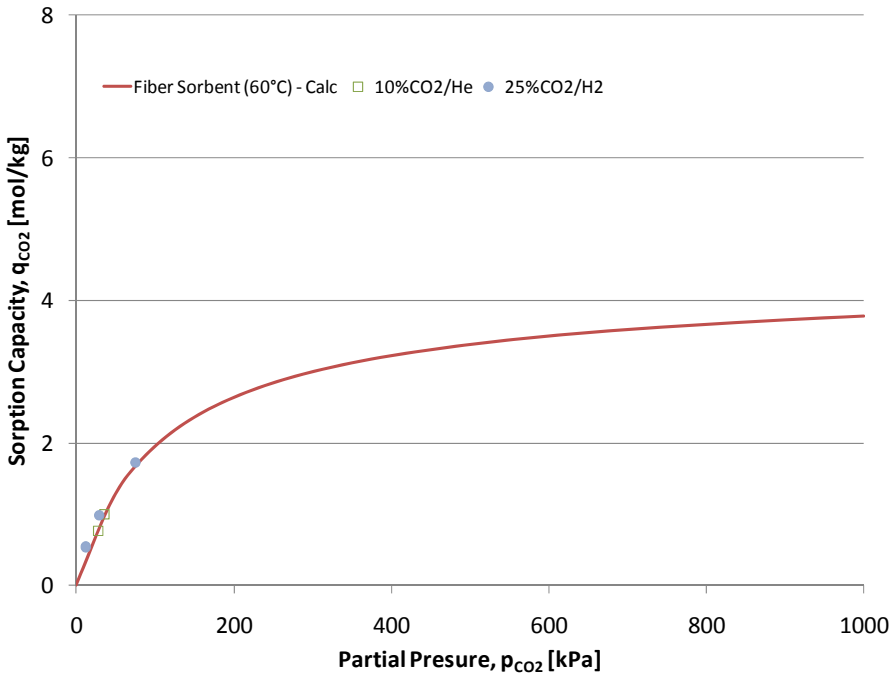

Figure 4-24 Sorption Isotherms of CO_2 in Mixed Gases to Fiber Sorbent (G-I 25% CA/64% Loading) at 60 °C

4.4. References

1. Eastman Chemical Company, *Eastman Cellulose Esters*. 2005, E-325C.

2. McKelvey, S.A., D.T. Clausi, and W.J. Koros, *A Guide to Establishing Hollow Fiber Macroscopic Properties for Membrane Applications.* Journal of Membrane Science, 1997. **124**(2): p. 223-232.

3. Kunst, B. and Souriraj.S, *Evaporation Rate and Equilibrium Phase Separation Data in Relation to Casting Conditions and Performance of Porous Cellulose Acetate Reverse Osmosis Membranes.* Journal of Applied Polymer Science, 1970. **14**(8): p. 1983-&.

4. Browne, C.L., *Process for Forming a Skinless Hollow Fiber of a Cellulose Ester*, in *U.S. Patent No.4,744,932*. 1988.

5. Barton, B.F. and A.J. McHugh, *Kinetics of Thermally Induced Phase Separation in Ternary Polymer Solutions. I. Modeling of Phase Separation Dynamics.* Journal of Polymer Science Part B-Polymer Physics, 1999. **37**(13): p. 1449-1460.

6. Tsay, C.S. and A.J. Mchugh, *Mass-Transfer Modeling of Asymmetric Membrane Formation by Phase Inversion.* Journal of Polymer Science Part B-Polymer Physics, 1990. **28**(8): p. 1327-1365.

7. Wallace, D.W., C. Staudt-Bickel, and W.J. Koros, *Efficient Development of Effective Hollow Fiber Membranes for Gas Separations from Novel Polymers.* Journal of Membrane Science, 2006. **278**(1-2): p. 92-104.

8. Omole, I.C., *Crosslinked Polyimide Hollow Fiber Membranes for Aggressive Natural Gas Feed Streams*, in *Ph.D. Dissertation*. 2008, Georgia Institute of Technology.

9. Vollenberg, P.H.T. and D. Heikens, *Particle-Size Dependence of the Young Modulus of Filled Polymers .1. Preliminary Experiments.* Polymer, 1989. **30**(9): p. 1656-1662.

CHAPTER 5 IMPERMEABLE LAYER DEVELOPMENT

5.1. Introduction

As discussed in Chapter 2, Section 2.6, a temperature increase due to the significant heat of adsorption is anticipated during the adsorption step. This is detrimental to the adsorption. Preliminary study indicated that a thermal moderation approach by using the latent heat of a carefully selected wax in the shell side reduces the temperature excursion in the case of bore-side feed to fiber sorbent modules. Paraffin wax fuses at a temperature slightly above the desired operating temperature. In order to utilize the shell-side space, an impermeable layer is needed on the external (outer) surface of fiber sorbents to prevent wax molecules from diffusing into the fiber sorbents when the wax fuses. In this research, two approaches to form the impermeable layer were investigated: 1) spinning with a dual layer spinneret and 2) post treatment to bare fiber sorbents. This chapter describes the approaches used to form an impermeable layer and results.

5.2. Dual Layer Spinning

Dual layer spinning, which introduces another dope into the "sheath" side of the dual layer spinneret as shown in Figure 5-1, was an attractive method for forming an impermeable layer on the external surface of a bare fiber sorbent in one step. Two types of polymer were examined: 1) poly(vinylidene chloride) (PVDC) and cellulose acetate (CA). To form the dense layer, the polymer concentration should be as high as possible while maintaining viscosity in an appropriate range for spinning. Depending on the air gap and type of solvent, a "skin" layer could be formed in the same manner as in hollow fiber membranes and can enhance impermeability in addition to

forming a dense sheath layer. Due to a narrow channel in the sheath side of the spinneret, the pressure drop and flow rate limitation for the sheath dope are tighter than those for the core dope. The sheath dope flow rate was as slow as 10 – 50 mL/min.

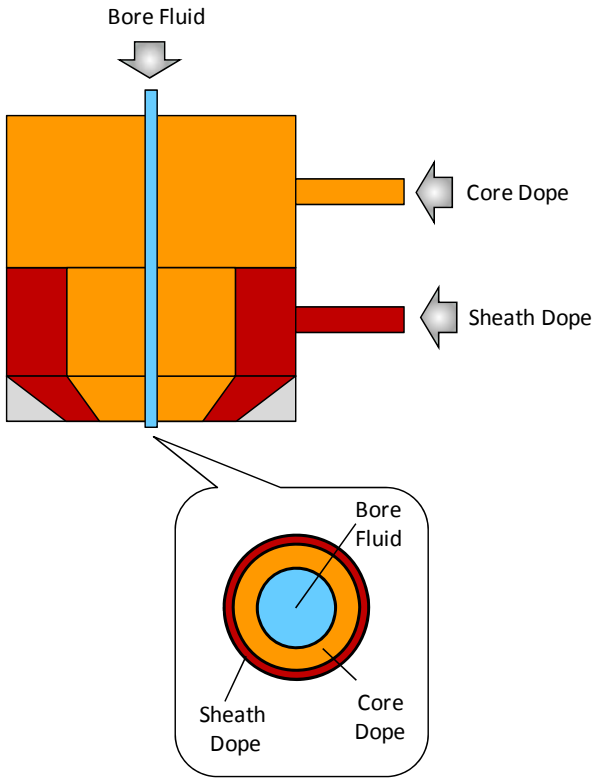

Figure 5-1 Schematic Diagram of Dual Layer Spinneret

PVDC is popularly used as a barrier material [1]. In order to spin the 1st generation dope of fiber sorbents into the "core" side of spinneret, it was necessary to spin the PVDC sheath dope at the same temperature as high as 90 °C. For solvent and non-solvent, NMP and water were selected for the high temperature spinning. Sheath dopes of PVDC:NMP:Water = 25:72:3 and 35:62:3 were spun, but were not successful. The main issue was that PVDC solidified within the spinneret during spinning due to crosslikage at high temperature (dehydrochlorination) and produced

hydrochloric acid [2]. This was a serious problem for spinning operation and maintenance. Another issue was the deformation of the hollow structure as shown in Figure 5-2. The PVDC layer might block non-solvent inflow to the nascent fiber. It was concluded that the dual layer spinning with PVDC at high temperature was difficult.

Figure 5-2 Deformed Hollow Fiber Structure of Dual Layer Spinning

Lower temperature spinning of the PVDC sheath dopes was possible with lower CA composition core dopes as described Chapter 4, but another dope based on CA appeared to be attractive for further efforts. Generally there is an adhesion issue (delamination) between two different polymers. The same CA was the ideal polymer for the sheath layer to the CA-NaY fiber sorbents. For the sheath dopes, CA/NMP/THF/$LiNO_3$ system was examined. THF is more volatile than the NMP and it allows one to form a skin layer effectively even in a short air gap as discussed in Chapter 4. Some CA/THF sheath dopes without NMP were also examined, but could not be spun successfully due to rapid vitrification of the CA in the sheath dopes at the exit of the spinneret. This caused frequent fiber breaks. To reduce the skin layer problem caused by evaporation of the

volatile solvent, a non-volatile solvent was used to control the rate of vitrification. Due to boiling point of the THF, core and sheath dopes needed to be spun below 50 °C with lower CA composition. The $LiNO_3$ associates with NMP increases the viscosity. The increase was expected to allow a larger air gap and improve skin layer formation. Sheath dopes of CA:NMP:THF:$LiNO_3$ = a) 25:54:13:8 and b) 30:31.5:31.5:7 were successfully spun as shown in Figure 5-3. With N_2 at 30 psia and 35 °C permeance changed from 65 kGPU to 12 kGPU for the sheath dope a) with thin CA layer, from 79 kGPU to 0.4 (kGPU) for the sheath dope b) with thick CA layer.

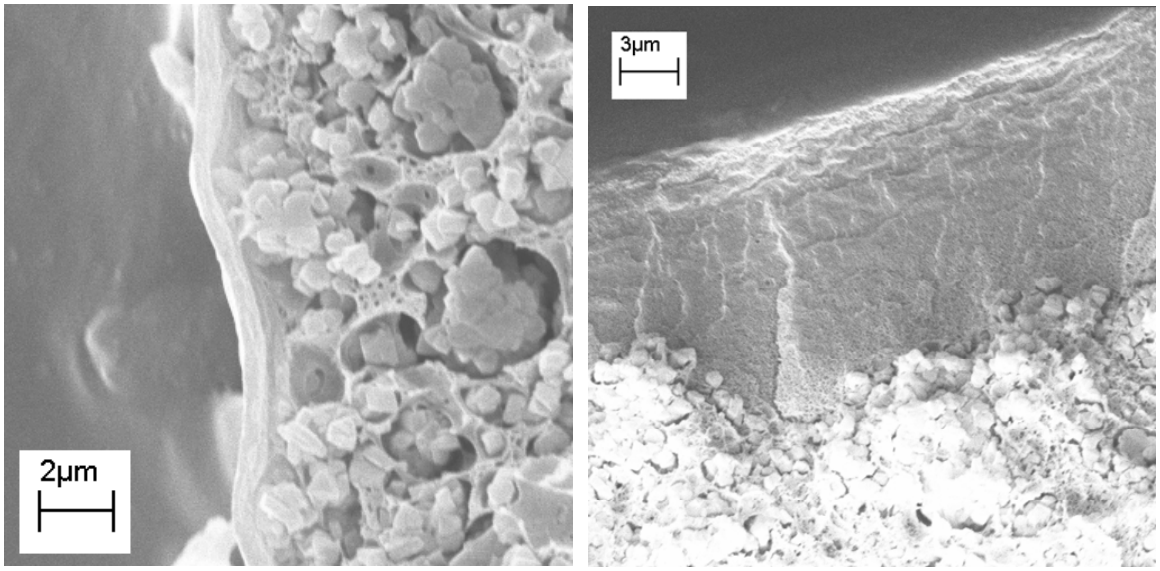

(a) Sheath Dope of CA:NMP:THF:$LiNO_3$ = 25:54:13:8

(b) Sheath Dope of CA:NMP:THF:$LiNO_3$ = 30:31.5:31.5:7

Figure 5-3 CA/CA-NaY Dual Layered Fiber Sorbents with Sheath Dopes of CA/NMP/THF/$LiNO_3$

However, the $LiNO_3$ did not enable the longer air gap and frequent fiber breaks made this approach unattractive. This indicates phase separation and rheological behavior are characterized mostly by those of the core dope. Subsequently, CA/NMP/THF dope was used. In addition,

similarly to the PVDC sheath dope as discussed above, the CA sheath dope might also hinder the non-solvent inflow from the quenching bath side, and resulted in slower phase separation than the single layer spinning of the bare fiber sorbents. For stable spinning, it was necessary to reduce the take-up rate of fiber collection to less than 1 m/min. A sheath dope of CA:NMP:THF = 20:56:24 was spun successfully as shown in Figure 5-4. Permeance was reduced from 79 kGPU to 19 kGPU with 10-μm thickness of the CA layer.

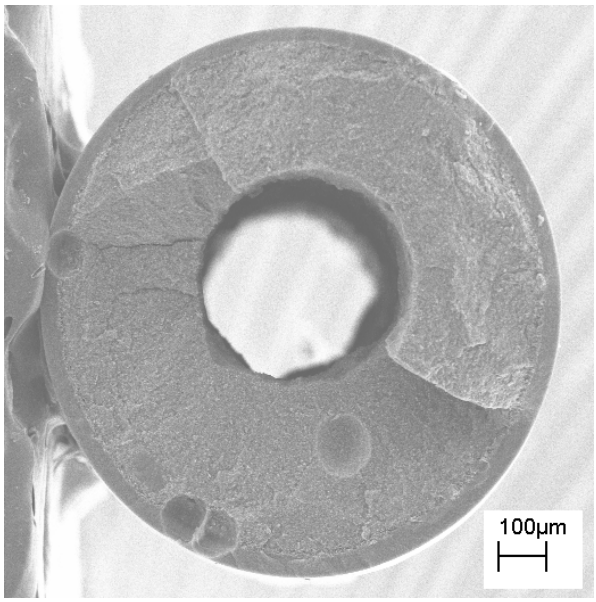

Figure 5-4 CA/CA-NaY Dual Layer Fiber Sorbent with Sheath Dope of CA/NMP/THF

As discussed in Section 5.3, reductions in the permeance were achievable by post treatment. The reduction of the permeance was correlated to thickness of the CA layer. Because of simplicity, it was desirable to use only dual layer spinning to form the impermeable layer with appropriate thickness, but post treatment was still necessary to proper function of impermeability as mentioned in Section 5.4.

5.3. Post-Treatment with Latex Solutions

Two types of post treatment were examined: i) spray coating and ii) dip coating with the PVDC latex solution. For spray coating, the raw latex solution was diluted two times to prevent air brush plugging. Fiber sorbents were hung inside a hood with a weight to place them in tension. The diluted latex solution was sprayed with the air brush by using utility compressed air at 50 psig. The fiber sorbents were manually rotate as shown in Figure 5-5. To make the coated areas stand out from uncoated areas, a few drops of food additive (red color) were added into the dilute latex solution. For the dip coating, the same diluted solution was installed in a 1.2-m long column as shown in Figure 5-6. To prevent the solution penetrating into the bore side of the fiber sorbent from the bottom during the dipping, the bottom end of the fiber sorbent was capped with a plastic tape and cured with epoxy resin (DP-100, 3M). Fiber sorbents were dipped in the column and pulled up immediately with a slow speed. The dipping process was repeated three times and then dried in the hood. Post-treated fiber sorbents with both methods were dried at 120 °C under the vacuum and evaluated with the standard fiber permeation test for multiple modules as shown in Figure 5-7. Both methods could reduce the permeance from 6 kGPU for the bare fiber sorbents (G-I 25% CA/64% loading), but down to only 2 kGPU for the spray-coated fiber sorbents and 1 kGPU for the dip-coated fiber sorbents. Note that the permeance of coated fiber sorbents was calculated based on the external surface area of the bare fiber sorbents. Fluctuation in permeance was serious, especially for spray-coated fiber sorbent.

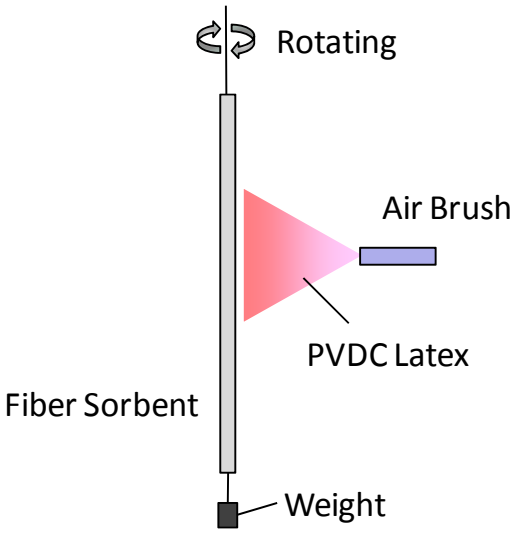

Figure 5-5 Schematic Diagram of Spray Coating

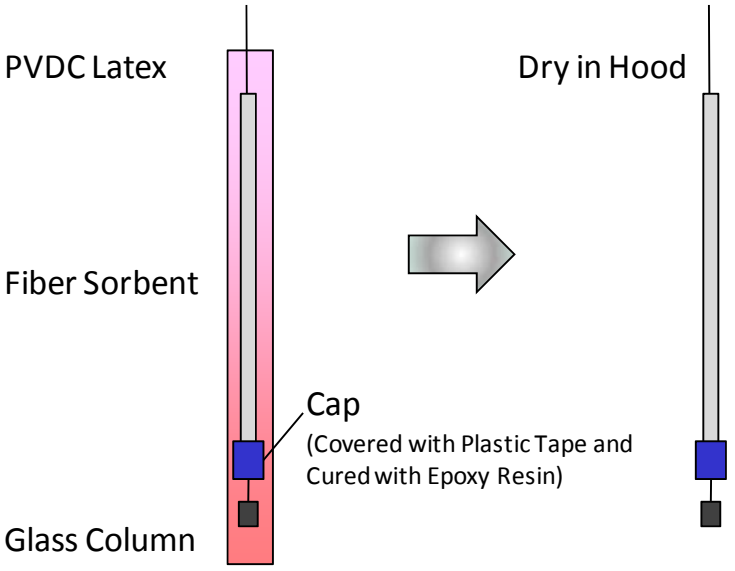

Figure 5-6 Schematic Diagram of Dip Coating

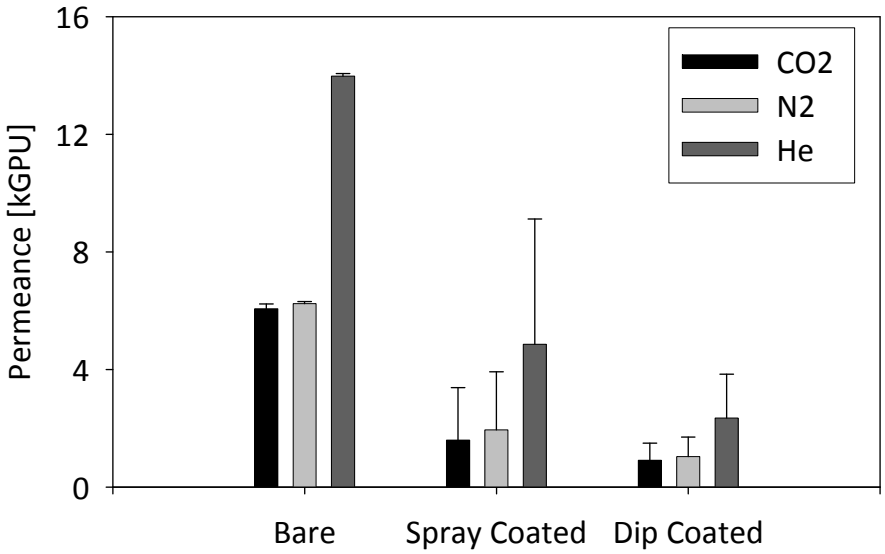

Figure 5-7 Standard Fiber Permeation Test Results for Bare, Spray-Coated and Dip-Coated Fiber Sorbents of G-I 25% CA/64% Loading

The external surface of the fiber sorbent is very rough and defective with some pores as shown in Figure 5-8. The defective surface resulted in high permeance for the fiber sorbents. The spray coating gave relatively thin layer (28 μm) and many cracks on the still rough surface as shown in Figure 5-9. In addition, thickness of the coated layer was fluctuated depending on the position of the fiber sorbents. The dip coating gave relatively thick layer (51 μm) and some cracks on the smooth surface as shown in Figure 5-10. It was also found that the latex solution penetrated into the bore side of the fiber sorbents when the epoxy capping failed or there was a large crack on the body of the fiber sorbents. Permeance of more than 1 kGPU was still high compared with hollow fiber membranes. The cracks on the external surface even after both post treatments resulted in the high permeance. However, the dip coating was more reliable than the spray coating to form the coated layer for lower permeance.

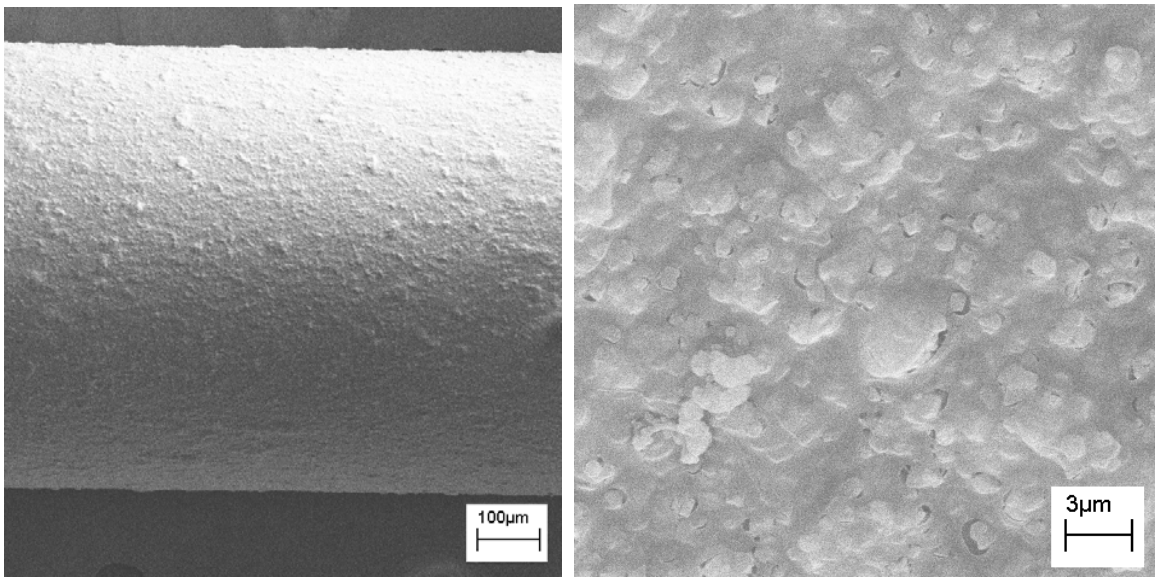

(a) External Surface (b) External Surface (High Magnification)

Figure 5-8 External Surface of Fiber Sorbent (G-I 25% CA/64% Loading)

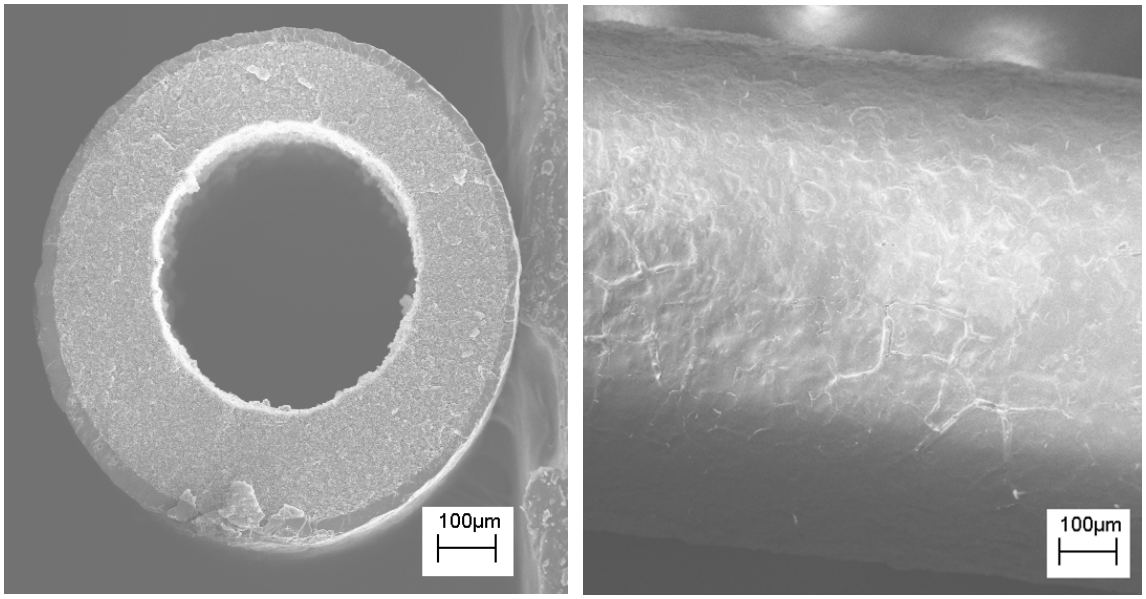

(a) Cross Section (b) External Surface

Figure 5-9 Spray-Coated Fiber Sorbent (G-I 25% CA/64% Loading)

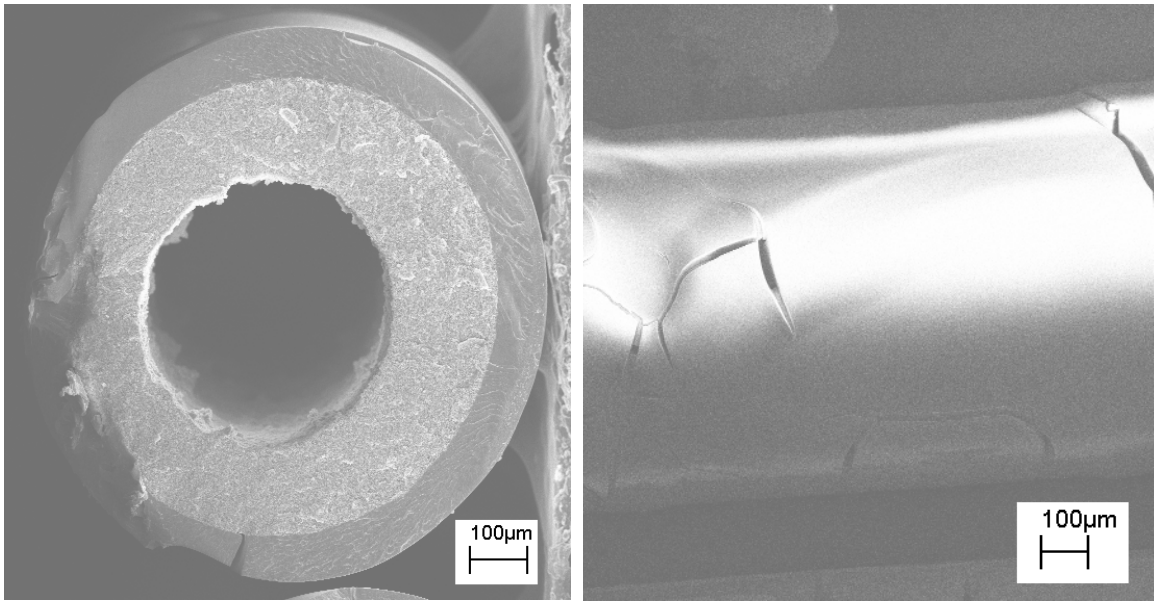

(a) Cross Section (b) External Surface

Figure 5-10 Dip-Coated Fiber Sorbent (G-I 25% CA/64% Loading)

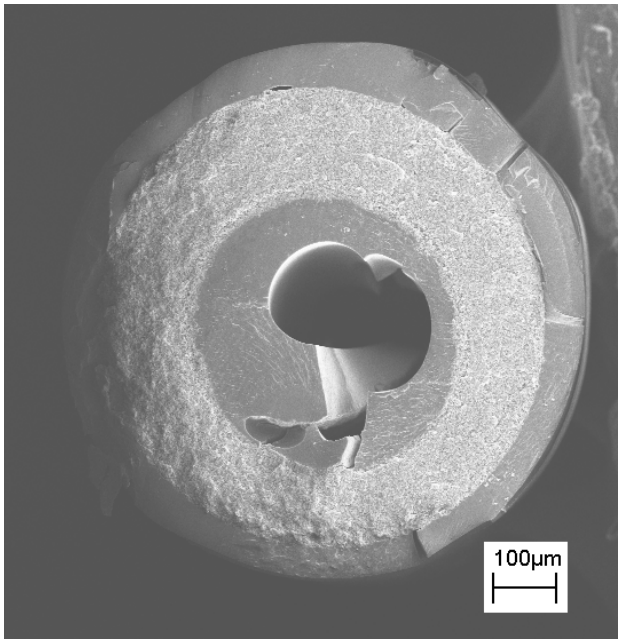

Figure 5-11 PVDC Latex Penetrated in Bore Side of Fiber Sorbent

5.4. Post-Treatment with PVA for Dual Layered Fiber Sorbent

A CA sheath layer was successfully formed by dual layer spinning and reduced permeance as discussed above. However, it was not dense enough to preventing paraffin wax molecules from diffusing into fiber sorbents. The fused paraffin wax penetrated into the bore side of the CA-NaY fiber sorbent by passing through the sheath CA layer when wax filled modules were kept at 70 °C. Even if the skin layer developed after evaporation of the THF in the air gap, it was not sufficient. Those fiber sorbents might still be defective on the external surface and no defect-free CA hollow fiber membranes were fabricated without any post treatments. It was concluded that the dual layer spinning with the CA sheath layer needs to be combined with post treatment (dip coating) for further impermeable performance. However, the sheath CA layer was important to prevent coating solutions penetrating the interior of the fiber sorbent especially for the 2nd generation dope, which resulted in a very porous structure. PVDC latex was applied to the CA/CA-NaY dual layered fiber sorbents, but it was also not successful in preventing fused wax leakage. Poly(vinyl alcohol) is a hydrophilic polymer and often used as a coating material to resist oil and grease [3]. Good adhesion between CA and PVA was expected because of strong hydrogen bonding of hydroxyl groups. The PVA coated CA/CA-NaY dual layer fiber sorbents was successfully prepared as shown in Figure 5-12. The thickness was around 20 μm, which was thinner than the PVDC case mentioned above. The permeance was evaluated by the vacuum fiber permeation test with N_2 and was 6.8 x 10^{-6} GPU with an upstream (feed) pressure of 200 psia and 35 °C, while the bare fiber sorbent and the CA/CA-NaY fiber sorbent resulted in 79 kGPU and 19 kGPU at 30 psia, respectively. The PVA coated CA/CA-NaY fiber did not show any wax leakage at 70 °C.

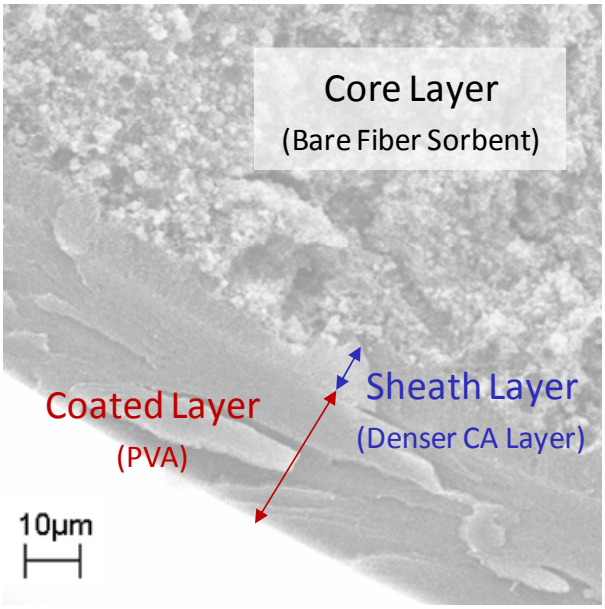

Figure 5-12 PVA Coated CA/CA-NaY Fiber Sorbent

5.5. References

1. SolVin S.A., *IXAN DIOFAN The Reference in the Barrier Polymer Market*. 2001, Br 1756 c - B -1 - 1001.

2. Burnett, G.M., R.A. Haldon, and J.N. Hay, *Dehydrochlorination of Polymers -I Polyvinylidene Chloride.* European Polymer Journal, 1967. **3**: p. 449-457.

3. Sekisui Specialty Chemicals America, L. *PVOH - Fields of Application - Paper*. 2010 [cited 2010 Oct. 1, 2010]; Available from: http://www.sekisui-sc.com/sekisui/sek_paper.htm.

CHAPTER 6 DYNAMIC BEHAVIOR OF FIBER SORBENT MODULES

6.1. Introduction

As mentioned in Chapter 4, the CA-NaY fiber sorbents were produced successfully and proved to have the appropriate porous structure and sorption capacity for CO_2. In addition, an impermeable layer was also developed that enabled the use of the shell-side void space by filling paraffin wax to manage the heat of adsorption. The fiber sorbents are bundled into modules for industrial use and are expected to work equivalently to packed beds. This chapter provides the dynamic behavior of the fiber sorbent modules with regard to breakthrough, regeneration (desorption) and process operation with a rapidly cycled pressure swing adsorption (RCPSA). Dynamic modeling is also constructed and described in Appendix G.

6.2. Dynamic Modeling

The mass and heat balance equations for fiber sorbent module and packed were solved with gPROMS®. Corresponding to the case described at Table 2-4 in Chapter 2, Section 2.5, the breakthrough behaviors in the adsorption step (Step II) of the fiber sorbent and the equivalent size packed bed are shown in Figure 6-1 and Figure 6-2 and summarized in Table 6-1 with temperature increase at the breakthrough. For non-isothermal conditions, the breakthrough times were reduced by 16% for the fiber sorbent module and 13% for the packed bed due to heat of adsorption. Compared with the simplified model used in the feasibility study, the dynamic modeling gave shorter breakthrough time. The approximation of the mass transfer length and

operating capacity used in the simplified model caused the overestimation. However, the trend shown in Figure 2-15 is the same and actual fiber sorbent module performance showed a longer breakthrough time with less packing. The temperature increase for both models gave similar results for the fiber sorbent module, but higher for the packed bed. Even if the breakthrough time for the packed bed was shorter with the dynamic modeling, the temperature increase was high. It demonstrates the lower heat transfer coefficient for the packed bed. Solid filling in shell-side such as PDMS extended the breakthrough time because of the additional heat capacity. The paraffin wax case showed almost the same results of isothermal operation. In addition to the pressure drop reduction as discussed in Chapter 2, the heat management is a very attractive aspect of the fiber sorbent module.

Table 6-1 Comparison of Breakthrough Time and Temperature Increase between Dynamic and Simplified Modeling

		Shell Side	t_B [s] (Dynamic)	t_B [s] (Simplified, Table 2-4)	ΔT [K] (Dynamic)	ΔT [K] (Simplified, Table 2-6)
Fiber Sorbent Module	Isothermal		25.4	37.3		
	Non-Isothermal	Gas	21.3		40	38
		PDMS	22.4		29	-
		Wax	25.4		0	3
Packed Bed	Isothermal		17.6	30.7		
	Non-Isothermal		15.3		40	27

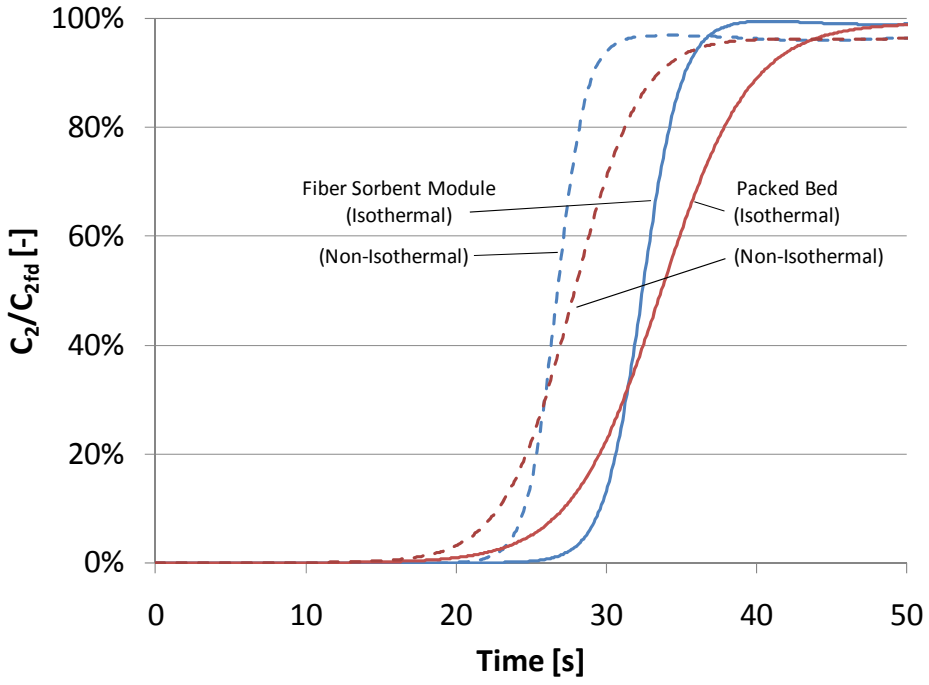

Figure 6-1 Breakthrough Curves at Exit of a Fiber Sorbent Module and an Equivalent Size Packed Bed (Isothermal and Non-Isothermal Conditions)

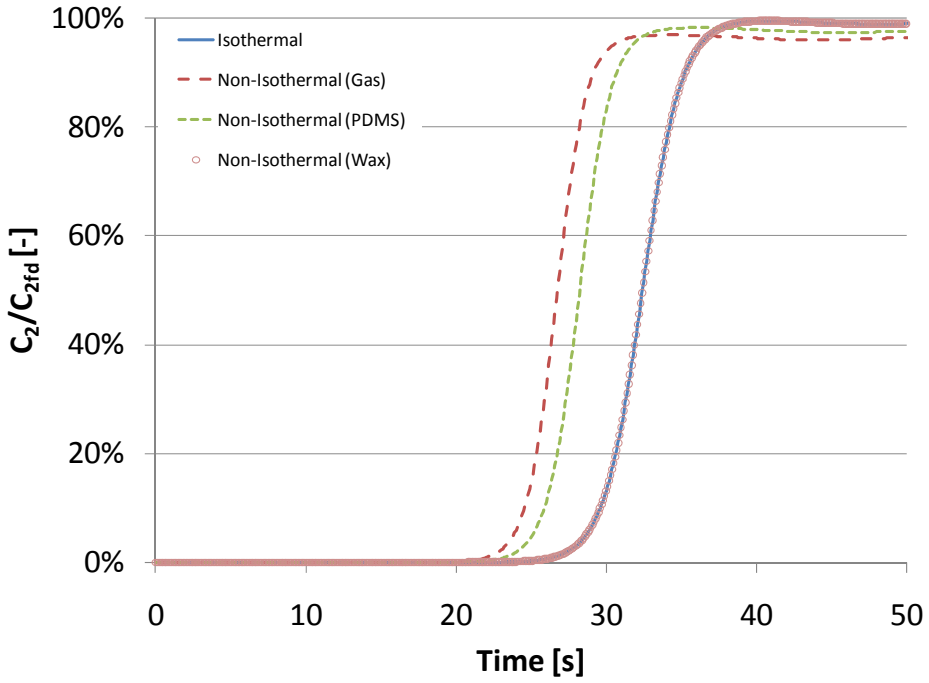

Figure 6-2 Breakthrough Curves at Exit of a Fiber Sorbent Module (Isothermal and Non-Isothermal Conditions with Gas, PDMS and Paraffin Wax in the Shell-Side Void)

6.3. Breakthrough Test

The CA-NaY fiber sorbents with the impermeable PVA layer were assembled in a module and its breakthrough behavior was examined by the method described in Chapter 3, Section 3.6. The actual breakthrough time was defined as the difference between the apparent breakthrough time for the He/CO_2 mixed gas and dead time by N_2 as shown in Figure 6-3.

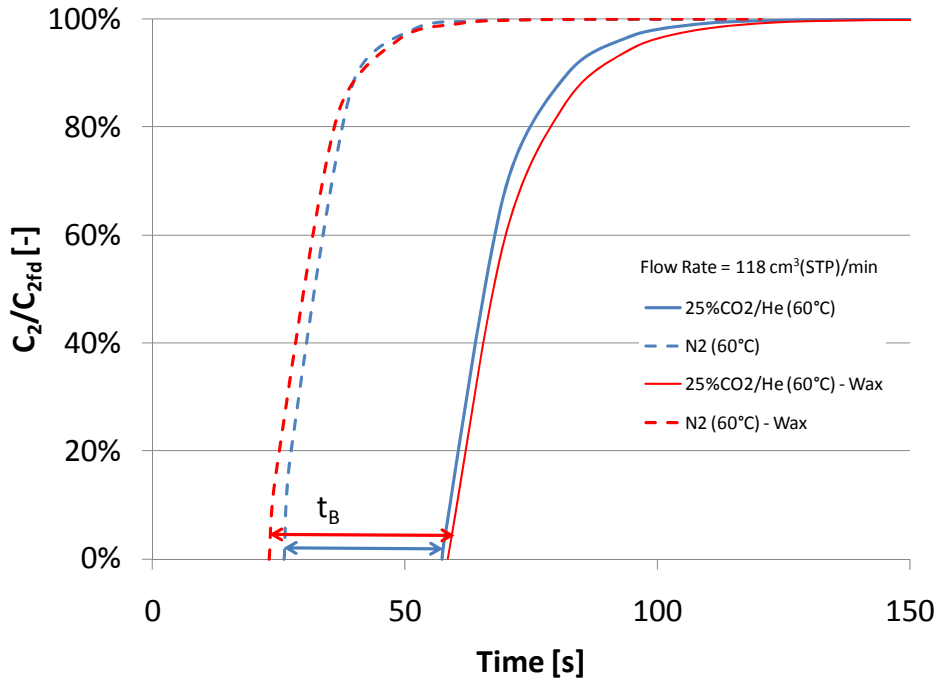

Figure 6-3 Breakthrough Curves for the Fiber Sorbent Module of G-II 20% CA/69% Loading with the PVA Coating

As discussed in Chapter 2, Section 2.5, the overall mass transfer comprises three mass transfer steps; external, intrafiber and intracrystalline mass transfer. It results in higher order dynamics due to the multiple steps. The higher order dynamics are approximated into the first-order plus time-delay (FOPTD) model [1];

$$\frac{C_2}{C_{2\,fd}} = \frac{I}{I_{\max}} = 1 - \exp\left(-\frac{t-\theta}{\tau}\right) \quad \text{.....(6.1)}$$

where,

C_2; concentration of CO_2 [mol/m^3]

C_{2fd}; feed concentration of CO_2 [mol/m^3]

I; intensity measured by gas chromatograph (GC) [-]

I_{max}; maximum intensity which corresponding to the feed concentration of CO_2 [-]

t; time [s]

θ; time delay (= dead time for N_2 and apparent breakthrough time for mixed gas) [s]

τ; time constant [s]

By applying curve fitting of the FOPTD to the breakthrough curves of several runs, the dead time and the apparent breakthrough time under the several feed gas and flow rate conditions were obtained as shown in Table 6-2 and Table 6-3. Definitely the fiber sorbent modules worked similarly to the packed bed resulting in breakthrough time actually. The experimental result of a case (G-II 20% CA/69% Loading, T_g = 60 °C, y_{2fd} = 25 mol%, p_{fd} = 113 psia and $Q_{V,fd}$ = 118 cm^3(STP)/min) was compared with the dynamic modeling (Figure 6-4).

Table 6-2 Breakthrough Times under the Several Conditions (G-II 20% CA/69% Loading)

T_{gfd} [°C]	y_{2fd} [mol%]	p_{fd} [psia]	$Q_{V,fd}$ [sccm*]	τ_g [s]	θ_g [s]	τ_{N2} [s]	θ_{N2} [s]	t_B [s]
Without Paraffin Wax								
60	**25**	**112**	**118**	**10.9**	**57.3**	**6.4**	**26.1**	**31.2**
60	25	112	***59***	16.2	105.4	11.9	33.4	72.0
			177	7.8	42.4	5.5	17.9	24.5
60	***10***	113	118	15.0	82.5	6.4	26.1	56.4
35	25	113	118	9.0	76.8	10.0	27.6	49.2
60	25	***63***	59	13.4	84.1	7.6	30.4	53.8
			118	7.2	48.1	4.5	15.7	32.4
With Paraffin Wax								
60	25	109	118	12.5	58.4	7.9	23.2	35.2
			177	5.8	45.1	5.5	17.9	27.2

L = 25 cm, d_f = 1,030 μm, d_{fb} = 463 μm, l_{ct} = 48 μm, n_f = 8

* cm^3(STP)/min

Table 6-3 Breakthrough Times under the Several Conditions (Other fiber sorbents with epoxy resins in the shell-side)

d_f [μm]	d_{fb} [μm]	n_f [-]	ω_{c0} [wt%]	t_B [s]
913	531	5	69	29.1
666	365	8	69	11.2
553	158	20	64	86.8
707	397	9	64	30.1

T_{gfd} = 60 °C, y_{2fd} = 25 mol%, p_{fd} = 105 psia, $Q_{V,fd}$ =59 [cm^3(STP)/min]

T_g; gas temperature, y_2; composition of CO_2, p total pressure, Q_V; volumetric flow rate, t_B; breakthrough time, L, d_f and d_{fb}; length, outer diameter and bore diameter of a (bare) fiber sorbent, l_{ct}; thickness of impermeable layer, nf; number of fiber sorbent, subscript fd, g and N_2; feed gas, mixed gas and pure nitrogen

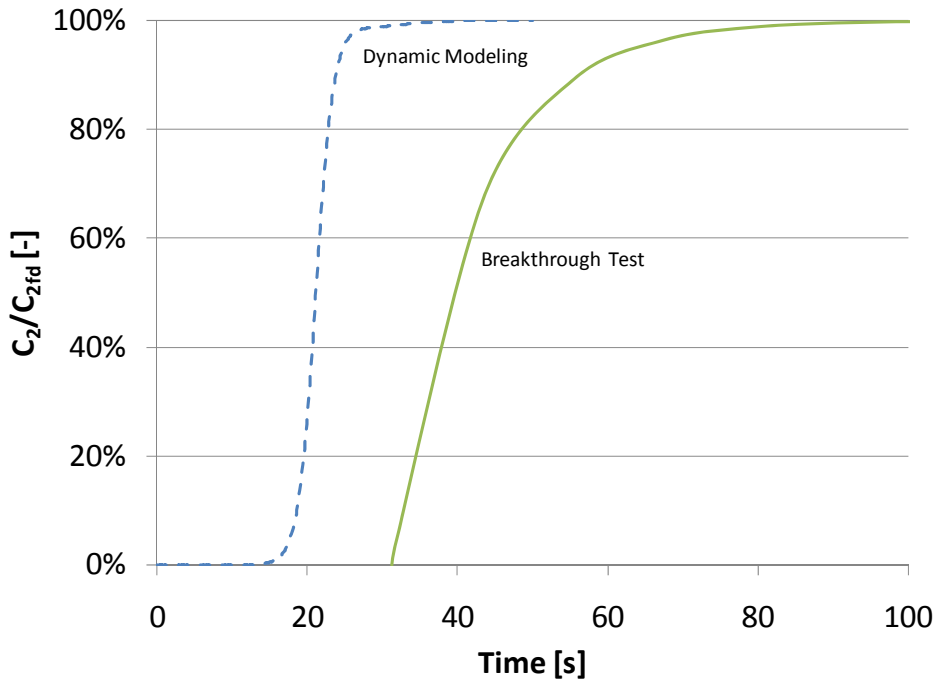

Figure 6-4 Breakthrough Test Result (G-II 20% CA/69% Loading) Compared with Dynamic Modeling Calculation (Experimental Isotherm) at 60 °C, 25 mol% 113 psia, and 118 sccm

6.4. Regeneration Test

The some regeneration conditions were tested; 1) time for Step II (adsorption), 2) purge gas flow rate, and 3) time for Step IV (purge time). The results are shown in Figure 6-5 ~Figure 6-7 and summarized in Table 6-4. The feed gas conditions were T_g = 60 °C, y_{2fd} = 25 mol%, p_{fd} = 113 psia and $Q_{V,fd}$ = 118 cm^3(STP)/min. As the amount of purge gas increased, purity became high. Based on the maximum amount of product gas at the breakthrough time for the feed gas condition (t_B = 31.2 s), recovery, R_1, was calculated;

$$R_1 = 1 - \frac{V_{IV}(STP)}{V_{II}(STP)} \quad \text{..... (6.2)}$$

where,

V_{IV}(STP); amount of purge gas [cm^3(STP)]

V_{II}(STP); amount of product gas [cm^3(STP)]

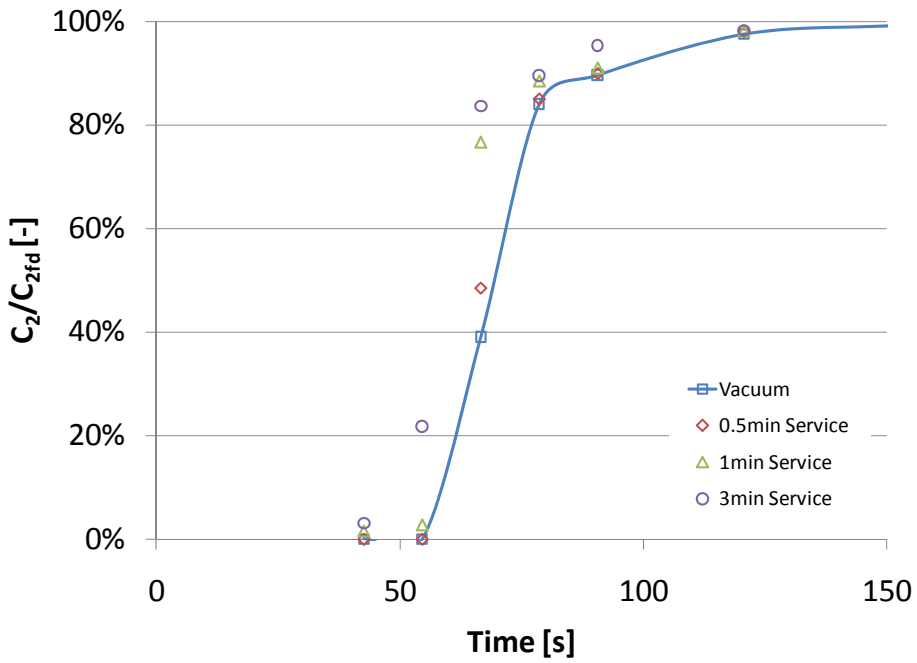

Figure 6-5 Effect of Adsorption Time (Step II) on the Regeneration

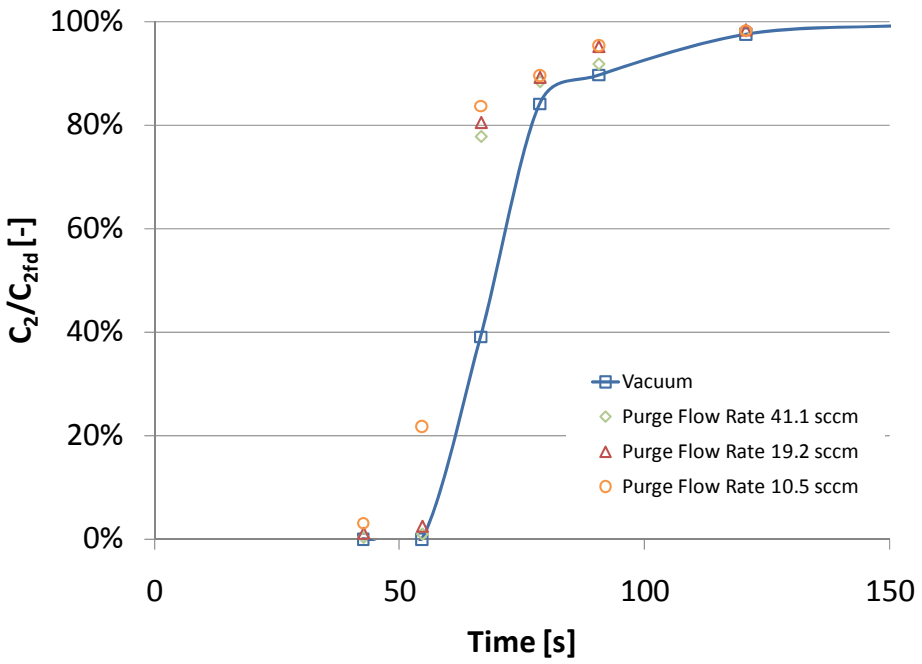

Figure 6-6 Effect of Purge Flow Rate on the Regeneration

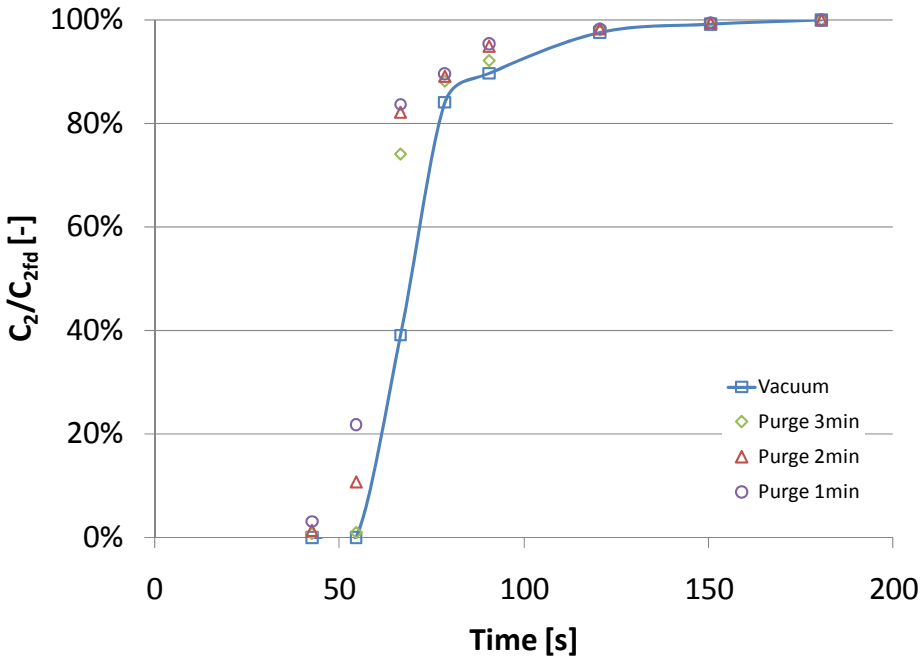

Figure 6-7 Effect of Purge Time (Step IV) on the Regeneration

Table 6-4 Effect of CO_2 Loading and Purge Gas Conditions

t_{II} [s] (CO_2 Loading)	$Q_{V,pg}$ [sccm*]	t_{IV} [s]	Purity [%]	Recovery [%]
30	10.5	60	100.0	76.2
60	10.5	60	99.6	77.1
180	10.5	60	99.2	77.1
180	19.2	60	99.7	58.2
180	41.1	60	99.9	10.4
180	10.5	120	99.7	54.2
180	10.5	180	99.8	31.4

t_{II} and t_{IV}; time for adsorption (II) and purge step (IV), $Q_{V,pg}$; volumetric flow rate of purge gas

* cm^3(STP)/min

The purity and the recovery are plotted in Figure 6-8. For the cases of 180 s in the time for the Step II, the fiber sorbent module was completely saturated with CO_2, and the purity and the recovery implies the worst case. The "worst case" is only given for reference and would not apply in any realistic process. The 99% in purity as a realistic target was relatively easier to achieve, but the 99.99 % as specified for hydrogen fuel cell vehicles was quite difficult. For a case of t_{II} = 30 s, which was similar to the t_B, the purity and the recovery were kept high. Although typically packed beds cannot be operated up to the breakthrough for the pseudo-isothermal operation due to heat of adsorption [2], the fiber sorbent module potentially could be operated under the pseudo-isothermal condition because of the thermal moderation with paraffin wax, and resulted in the high purity and recovery.

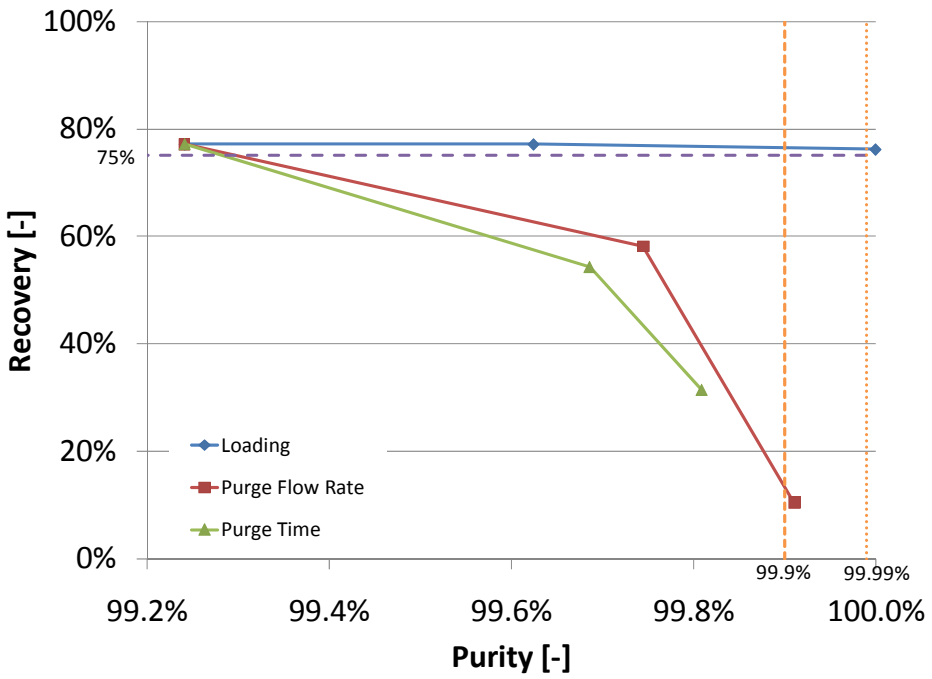

Figure 6-8 Recovery vs. Purity

6.5. Rapid Cycled Pressure Swing Adsorption (RCPSA) Test

The fiber sorbent module was operated with a RCPSA operational sequence.

Step I	Pressurization	t_I = 0.1 s
Step II	Adsorption	t_{II} = 20.0 s
Step III	Depressurization	t_{III} = 0.1 s
Step IV	Purge (Desorption)	t_{IV} = 20.0 s
	Total cycle time	t_{cyc} = 40.2 s

The time for Step II was set based on the breakthrough time determined in the breakthrough test above specifically for this fiber sorbent. The breakthrough curve in the Step I of the 101st cycle is shown in Figure 6-9 compared with that obtained in the breakthrough test. The shape of curve changed. Purity was 99.8% and recovery was 88.1% based on the t_{II}. These results satisfied the

research targets (99% purity and 75% recovery). This recovery did not take into account the amount of purified gas in pressurization step (Step I), which is very small since total bore-side volume is very small, and impact of dead space in the experimental system.

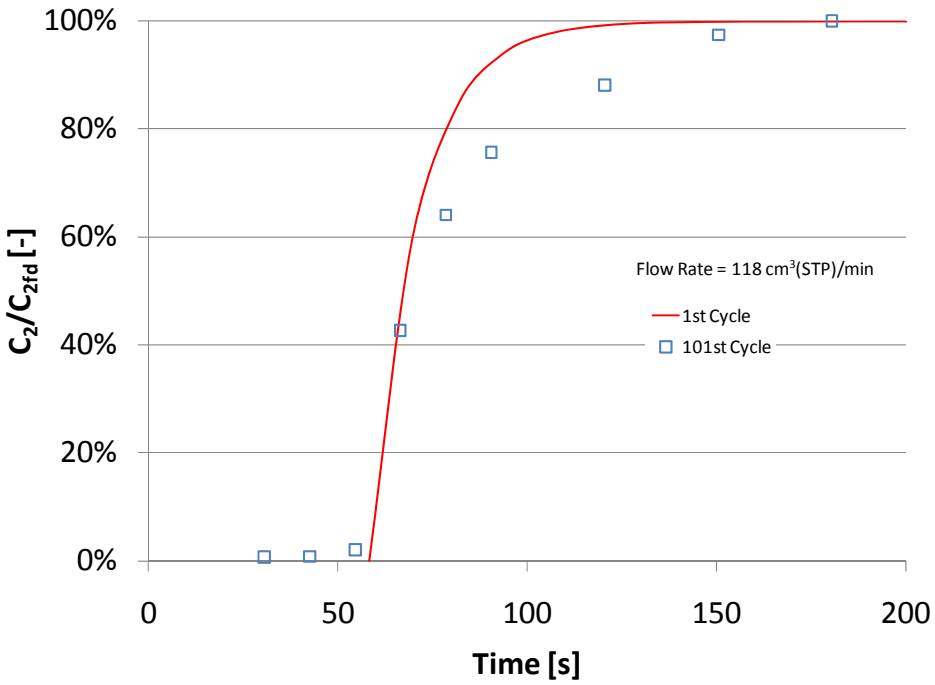

Figure 6-9 Breakthrough Curve after the RCPSA cycles

With the same conditions were applied to the dynamic modeling, but it did not match with the experimental results. In the calculation, the fiber sorbent module was not regenerated as shown Figure 6-10 when the regeneration conditions were kept. After some cycles, the fiber sorbent module became saturated at the end of the adsorption step with high leakage and was hard to be regenerated to give the breakthrough time after 100 cycles as same as the experimental result. The equations used in the purge step were exactly same as the adsorption step and adsorption step shows reasonable behaviors. Further improvement of the code is necessary.

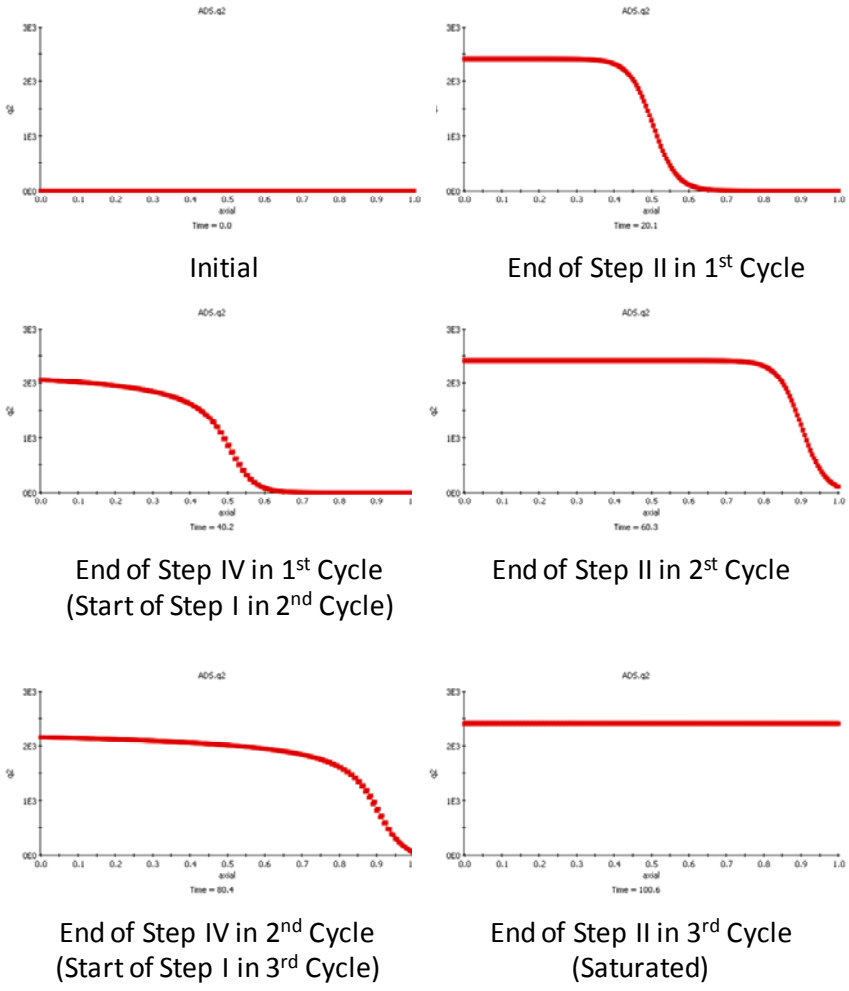

Figure 6-10 Concentration of CO_2 in Fiber Sorbent Phase in a RCPSA

6.6. References

1. Seborg, D.E., T.F. Edgar, and D.A. Mellichamp, *Chapter 7 Development of Emprical Models from Process Data*, in *Process Dynamics and Control*. 2004, Wiley: Hoboken, NJ. p. 157-184.

2. Yang, R.T., *Chapter 7 Pressure-Swing Adsorption: Principles and Processes*, in *Gas Separation by Adsorption Processes*. 1997, World Scientific: Singapore ; River Edge, N.J. p. 237-274.

CHAPTER 7 CONCLUSIONS AND RECOMMENDATIONS

7.1. Summary and Conclusions

In Chapter 1, the needs for downsized separation equipment for hydrogen fueling station for emerging fuel cell vehicles was identified. The final goal was to show the viability of a new concept related to “fiber sorbents” by producing and comparing the pros and cons of the fiber sorbent versus traditional packed bed sorbents.

In Chapter 2, the concept of a “fiber sorbent” and its application to a specific challenging separation was outlined. As background to produce fiber sorbents and to operate a realistic fiber sorbent module, fiber spinning technology and pressure swing adsorption were reviewed. Sorption capacity was explained as a critical property of the fiber sorbents that had to be considered. A feasibility study with a simplified model was first conducted to compare the fiber sorbent module with an equivalent size packed bed. The quantitative results indicated advantages of pressure drop reduction and breakthrough time extension with less packing fraction. Thermal effect due to heat of adsorption was anticipated, but the use of the shell-side void space by filling paraffin wax potentially provided thermal moderation.

In Chapter 3, materials and experimental methods used in this research were summarized and basis for their selection considered. Cellulose acetate and zeolite NaY were selected for the fiber sorbent. Detailed procedure of the spinning process was mentioned. To characterize fiber sorbents in addition to pure materials, several analytical and test methods were applied. SEM imaging,

Fiber permeation test and sorption test were core technologies in this research. Rapidly cycled pressure swing adsorption was shown to be feasible with a newly constructed system.

In Chapter 4, experimental results and discussion of pure CA fibers and CA-NaY fiber sorbents were reported. The pure CA fibers were spun successfully and the potential spinning conditions for CA-NaY fiber sorbents were determined. The CA-NaY fiber sorbents were spun successfully with porous structure and homogenous zeolite crystal dispersion. The dope composition was shown to require adjustment due to adsorption of water in the dope by the dried zeolite fillers. Extra water was added to the dope and the fiber sorbent was shown to become more porous based on the morphology observation by SEM imaging and porous structure analysis by fiber permeation test and mercury porosimetry. Sorption tests of fiber sorbent showed high sorption capacity for pure CO_2 and selective adsorption of CO_2 from the mixed gases of He/CO_2 and H_2/CO_2.

In Chapter 5, impermeable layer formation was examined by dual layer spinning and post treatment. Dual layer spinning was expected to form an impermeable layer by applying a sheath dope of another polymer solution to the external surface (shell side) of a core dope of a fiber sorbent dope. The CA sheath/CA-NaY core fiber sorbent was successfully spun with permeance reduction. Unfortunately, this integrated approach was still not effective to avoid penetrating fused paraffin wax into the fiber sorbent wall from the shell side at the temperature above melting point of the wax. Post treatment of PVDC latex solution with spray or dip coating were applied, but the permeance for the coated fiber was not sufficient. Combining with dual layer spinning and PVA dip coating, the wax-leak free CA-NaY fiber sorbent was successfully produced.

In Chapter 6, the fiber sorbent was assembled into a module and operated with a pressure swing adsorption process. The breakthrough time was definitely observed and it was confirmed that the fiber sorbent modules could work equivalently or better to the packed beds and with more compact volume. Purity and recovery after the 100 cycles of the RCPSA cycles met with the research goals.

Here are important conclusions of this research;

1. Mass transfer of fiber sorbent modules in PSA processes was modeled and showed advantages of optimally designed fiber sorbent modules versus identically sized packed beds.

2. Fiber sorbents comprised of cellulose acetate and zeolite NaY were successfully produced with appropriately porous structure, homogenous zeolite crystal dispersion and high sorption capacity of CO_2.

3. Fiber sorbents with an impermeable layer of poly(vinyl alcohol) was successfully developed and modules with the coated fiber sorbent with filling paraffin wax in the shell-side was demonstrated to moderate thermal effect of heat of adsorption with a PSA process.

7.2. Recommendations for Further Research

As this research proceeded, potential research needs have become obvious in order to improve the current status of fiber sorbent production and operation with pressure swing adsorption processes. These issues are noted below.

7.2.1. Intrinsic Phase Diagram of Fiber Sorbent Dopes

As mentioned in Chapter 3, due to turbidity, it is difficult to observe “cloud” points to determine binodal curve, which indicates phase separation. In addition, dispersed zeolite crystals adsorbed water and resulted in dope composition change. Temperatures of spinneret and quenching bath impacted on the morphology. Different method needs to be developed to predict binodal curves at different temperatures to select an appropriate dope composition. Visco-elastic behaviors of polymer blend melts or solutions at different composition and temperature can indicate phase separation or gelation [1-2]. Monitoring the storage (G’) and loss moduli (G”) at different oscillating frequency for shear stress may show the difference between one-phase and two-phase solution of fiber sorbent dopes with the dispersed zeolite crystals. For a polymer blend melt, plotting of G’ vs G’ shows different curves as shown in Figure 7-1. For a polymer solution, G’ = G” implies a gelation point.

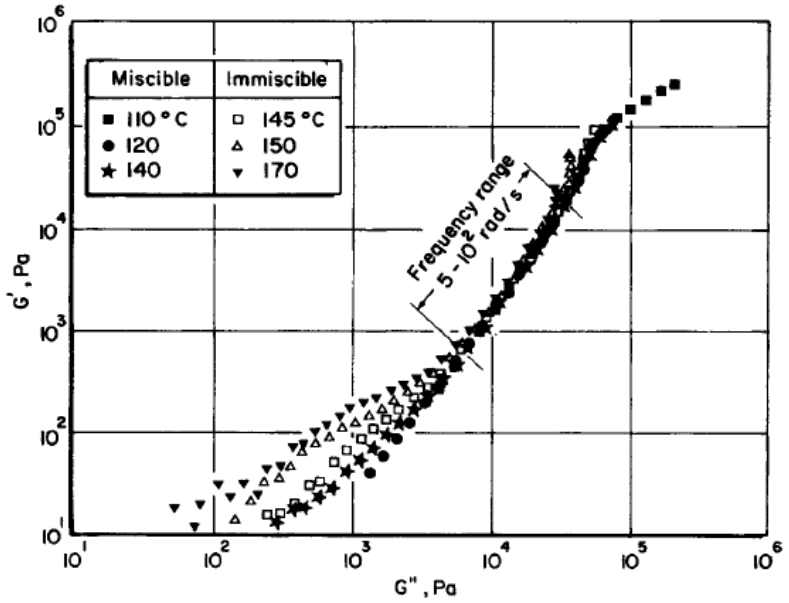

Figure 7-1 G' vs G" of the 80:20 Blend of Polystyrene/Poly(Vinyl Methyl Ether) at Different Temperatures [1]

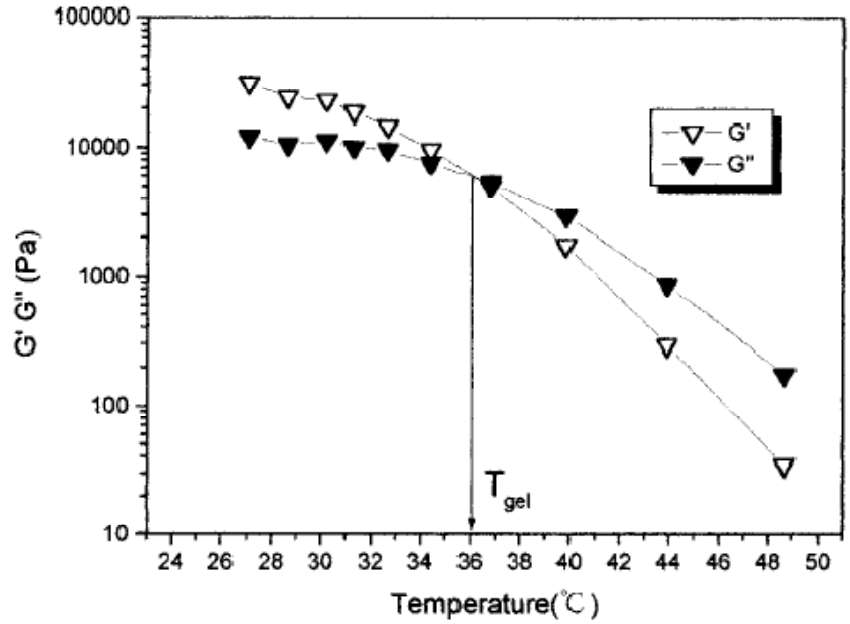

Figure 7-2 Crossover of the G' and G" and the determination of gelation temperature [2]

7.2.2. Sorption Behavior of Solvent and Non-Solvent to Zeolite in Dopes

Related to the Section 7.2.1, the impact of dried or saturated zeolite on dope composition changes are mostly unknown at present. Clarifying this behavior, especially competitive sorption of NMP and CA for CA-NaY fiber sorbent dope is critical for the determination of the spinning dope and helpful to translate the data obtained in Section 7.2.1. A preliminary experiment was conducted and reported in Appendix H, and NMP is probably adsorbed to the NaY as well as water after all of the components are mixed.

7.2.3. Intrinsic Sorption Isotherms for Zeolites

Due to rapid sorption of gases and water vapor, it was quite difficult to measure the weight of zeolite sample for sorption capacity experiments. It was concluded that it was necessary to measure sorption capacity of different type of gases to the NaY or fiber sorbents in a series. Different sample of the same NaY gave different sorption capacity. The error in the weight measurement was 10%. A new method to evaluate the zeolite was necessary. Similarly to a procedure of the volume calibration for the reservoir and the sample cell, zeolite intrinsic volume can be measured by helium. It was confirmed that the zeolite NaY gave zero capacity for pure helium. Pressure change before and after the valve opening is only related to the volume of NaY samples. In the same manner described in Chapter 3, a mole balance gave the volume occupied by the NaY. Separately, volumes of sintered metal filter, aluminum foil and stainless steel string need to be measured. Applying true density, the mass sorption capacity is available.

7.2.4. Further Improvement on Dynamic Modeling Calculation

The code successfully gave the behaviors of breakthrough and cyclic operation. In addition to the error in experimental data such as sorption capacity, the calculated results do not match exactly with experimental data. And also the calculated variables were oscillated depending on the conditions. Further modification of the coding is necessary. In addition, the function of parameter optimization embedded in gPROMS® was not employed in this research. This is advantageous function to be explored for optimized fiber sorbent conditions.

7.3. References

1. Ajji, A., L. Choplin, and R.E. Prud'homme, *Rheology and phase separation in polystyrene/poly(vinyl methyl ether) blends.* Journal of Polymer Science Part B: Polymer Physics, 1988. **26**(11): p. 2279-2289.

2. Lin, K.-Y., D.-M. Wang, and J.-Y. Lai, *Nonsolvent-Induced Gelation and Its Effect on Membrane Morphology.* Macromolecules, 2002. **35**(17): p. 6697-6706.

APPENDIX A PREDICTION OF BINODAL AND SPINODAL CURVES FOR POLYMER SOLUTIONS

A.1. Introduction

This appendix describes theoretical calculations to predict binodal and spinodal curves on a ternary phase diagram for a ternary polymer solution (polymer/solvent/non-solvent) [1-5]. The ternary phase diagram for the cellulose Acetate (CA) – NMP – water system was examined at 25 °C.

A.2. Thermodynamics of Phase Separation

Gibbs free energy of mixing, ΔG_M [J], for ternary polymer solution based on the Flory-Huggins theory is given as [1];

$$\frac{\Delta G_M}{R_g T} = n_1 \ln \phi_1 + n_2 \ln \phi_2 + n_3 \ln \phi_3 + g_{12} n_1 \phi_2 + g_{13} n_1 \phi_3 + g_{23} n_2 \phi_3 \quad \text{.....(A.1)}$$

$$\phi_i = \frac{n_i v_i}{\sum_j n_j v_j} \quad \text{.....(A.2)}$$

where,

subscript 1; for non-solvent (NS)

subscript 2; for solvent (S)

subscript 3; for polymer (P)

ΔG_M; Gibbs free energy of mixing [J]

R_g; gas constant (= 8.314472 J/mol/K)

T; temperature [K]

ϕ; volume fraction

n; number of moles [mol]

v; molar volume [m^3/mol]

Interaction parameters, g12, g13 and g23, are as functions of volume fraction in pseudo-binary mixtures of non-solvent and solvent, non-solvent and polymer, and solvent and polymer, respectively [1];

$$g_{12} = g_{12}(u_2)\text{: NS/S Interaction Parameter} \quad \text{(A.3)}$$

$$g_{13} = g_{13}(y_3)\text{: NS/P Interaction Parameter} \quad \text{(A.4)}$$

$$g_{23} = g_{23}(w_3)\text{: S/P Interaction Parameter} \quad \text{(A.5)}$$

where,

$$u_1 = \frac{\phi_1}{\phi_1 + \phi_2} \quad \text{(A.6)}$$

$$u_2 = \frac{\phi_2}{\phi_1 + \phi_2} \quad \text{(A.7)}$$

$$y_1 = \frac{\phi_1}{\phi_1 + \phi_3} \quad \text{(A.8)}$$

$$y_3 = \frac{\phi_3}{\phi_1 + \phi_3} \quad \text{(A.9)}$$

$$w_2 = \frac{\phi_2}{\phi_2 + \phi_3} \quad \text{(A.10)}$$

$$w_3 = \frac{\phi_3}{\phi_2 + \phi_3} \quad \text{.....(A.11)}$$

Chemical potential, Δμ [J/mol], is defined as [1];

$$\frac{\Delta\mu_i}{R_g T} = \frac{\partial}{\partial n_i}\left(\frac{\Delta G_M}{R_g T}\right)_{T,p,n_j,j\neq i} \quad \text{.....(A.12)}$$

Differentiating Equation (A.1) according to Equation (A.2), the chemical potential for each component was obtained as follows.

$$\frac{\Delta\mu_1}{R_g T} = \ln\phi_1 - \frac{v_1\phi_2}{v_2} - \frac{v_1\phi_3}{v_3} + \left(1 + g_{12}\phi_2 + g_{13}\phi_3\right)\left(1-\phi_1\right) - \frac{v_1 g_{23}\phi_2\phi_3}{v_2} - \phi_1\left(u_2^2\frac{dg_{12}}{du_2} + y_3^2\frac{dg_{13}}{dy_3}\right) \quad \text{.....(A.13)}$$

$$\frac{\Delta\mu_2}{R_g T} = \ln\phi_2 - \frac{v_2\phi_1}{v_1} - \frac{v_2\phi_3}{v_3} + \left(1 + \frac{v_2 g_{12}\phi_1}{v_1} + g_{23}\phi_3\right)\left(1-\phi_2\right) - \frac{v_2 g_{13}\phi_1\phi_3}{v_1} + \phi_2\left(\frac{v_2 u_1^2}{v_1}\frac{dg_{12}}{du_2} - w_3^2\frac{dg_{23}}{dw_3}\right) \quad \text{.....(A.14)}$$

$$\frac{\Delta\mu_3}{R_g T} = \ln\phi_3 - \frac{v_3\phi_1}{v_1} - \frac{v_3\phi_2}{v_2} + \left(1 + \frac{v_3 g_{13}\phi_1}{v_1} + \frac{v_3 g_{23}\phi_2}{v_2}\right)\left(1-\phi_3\right) - \frac{v_3 g_{12}\phi_1\phi_2}{v_1} + v_3\phi_3\left(\frac{y_1^2}{v_1}\frac{dg_{13}}{dy_3} + \frac{w_2^2}{v_2}\frac{dg_{23}}{dw_3}\right) \quad \text{.....(A.15)}$$

At thermodynamic equilibrium, chemical potential of each component in both polymer-rich and polymer-lean phases should be equal [1].

$$\Delta\mu_{i,A} = \Delta\mu_{i,B} \quad \text{(A.16)}$$

where,

Subscript A: in Polymer-Rich Phase

Subscript B: in Polymer-Lean Phase

Solving Equation (A.16) for each component with material balances in each phase, it results in the binodal curve [1].

$$\sum_i \phi_{i,A} = \sum_i \phi_{i,B} = 1 \quad \text{(A.17)}$$

The spinodal curve is and thermodynamically defined as;

$$\frac{\partial^2 G}{\partial \phi^2} = 0 \quad \text{(A.18)}$$

The following relationship is derived from Equation (A.18) [1];

$$G_{22} \cdot G_{33} = G_{23}^2 \quad \text{(A.19)}$$

where,

$$G_{ij} = \frac{\partial^2 \Delta G_M}{\partial \phi_i \partial \phi_j} v_{ref} \quad \text{(A.20)}$$

The 1st derivative of the Gibbs free energy of mixing was expressed in terms of chemical potentials [1];

$$\left(\frac{\partial \Delta G_M}{\partial \phi_2}\right)_{T,p,\phi_3} = \frac{\Delta\mu_2}{v_2} - \frac{\Delta\mu_1}{v_1} \quad \text{.....(A.21)}$$

$$\left(\frac{\partial \Delta G_M}{\partial \phi_3}\right)_{T,p,\phi_2} = \frac{\Delta\mu_3}{v_3} - \frac{\Delta\mu_1}{v_1} \quad \text{.....(A.22)}$$

Differentiating Equations (A.21) and (A.22), the G_{22}, G_{23} and G_{23} were obtained as Equations (A.23) – (A.26).

$$\frac{\left(\frac{\partial \Delta G_M}{\partial \phi_2}\right)_{T,p,\phi_3}}{R_g T} v_1 = \frac{\left(\frac{\Delta \mu_2}{v_2} - \frac{\Delta \mu_1}{v_1}\right)}{R_g T} v_1$$

$$= \frac{v_1}{v_2}\ln\phi_2 - \phi_1 - \frac{v_1}{v_3}\phi_3 + \left(\frac{v_1}{v_2} + g_{12}\phi_1 + \frac{v_1}{v_2} g_{23}\phi_3\right)(1-\phi_2) - g_{13}\phi_1\phi_3 + \phi_2\left(u_1^2 \frac{dg_{12}}{du_2} - \frac{v_1}{v_2} w_3^2 \frac{dg_{23}}{dw_3}\right)$$

$$-\left\{\ln\phi_1 - \frac{v_1}{v_2}\phi_2 - \frac{v_1}{v_3}\phi_3 + (1 + g_{12}\phi_2 + g_{13}\phi_3)(1-\phi_1) - g_{23}\frac{v_1}{v_2}\phi_2\phi_3 - \phi_1\left(u_2^2 \frac{dg_{12}}{du_2} + y_3^2 \frac{dg_{13}}{dy_3}\right)\right\} \quad \text{.....(A.23)}$$

$$\frac{G_{22}}{R_g T} = \frac{\partial}{\partial \phi_2}\left\{\frac{\left(\frac{\partial \Delta G_M}{\partial \phi_2}\right)_{T,p,\phi_3}}{R_g T} v_1\right\}_{T,p,\varphi_3}$$

$$= \frac{1}{\phi_1} + \frac{v_1}{v_2\phi_2} - 2g_{12} + 2(u_1 - u_2)\frac{dg_{12}}{du_2} + u_1 u_2 \frac{d^2 g_{12}}{du_2^2} - 2y_3^3 \frac{dg_{13}}{dy_3} + y_1 y_3^3 \frac{d^2 g_{13}}{dy_3^2} - \frac{2v_1 w_3^3}{v_2}\frac{dg_{23}}{dw_3} + \frac{v_1 w_2 w_3^3}{v_2}\frac{d^2 g_{23}}{dw_3^2} \quad \text{.....(A.24)}$$

$$\frac{G_{33}}{R_gT}=\frac{\partial}{\partial\phi_3}\left\{\frac{\left(\frac{\partial\Delta G_M}{\partial\phi_3}\right)_{T,p,\phi_2}}{R_gT}v_1\right\}_{T,p,\phi_2}$$

$$=\frac{1}{\phi_1}+\frac{v_1}{v_3\phi_3}-2g_{13}-2u_2^3\frac{dg_{12}}{du_2}+u_1u_2^3\frac{d^2g_{12}}{du_2^2}+2\left(y_1-y_3\right)\frac{dg_{13}}{dy_3}+y_1y_3\frac{d^2g_{13}}{dy_3^2}+\frac{2v_1w_2^3}{v_2}\frac{dg_{23}}{dw_3}+\frac{v_1w_3w_2^3}{v_2}\frac{d^2g_{23}}{dw_3^2} \quad \text{.....(A.25)}$$

$$\frac{G_{23}}{R_gT}=\frac{\partial}{\partial\phi_2}\left\{\frac{\left(\frac{\partial\Delta G_M}{\partial\phi_3}\right)_{T,p,\phi_2}}{R_gT}v_1\right\}_{T,p,\phi_3}\left(=\frac{G_{32}}{R_gT}=\frac{\partial}{\partial\phi_3}\left\{\frac{\left(\frac{\partial\Delta G_M}{\partial\phi_2}\right)_{T,p,\phi_3}}{R_gT}v_1\right\}_{T,p,\phi_2}\right)$$

$$=\frac{1}{\phi_1}-g_{12}-g_{13}+\frac{v_1g_{23}}{v_2}+u_2\left(u_1-2u_2\right)\frac{dg_{12}}{du_2}+u_1u_2^2\frac{d^2g_{12}}{du_2^2}+y_3\left(y_1-2y_3\right)\frac{dg_{13}}{dy_3}+y_1y_3^2\frac{d^2g_{13}}{dy_3^2}$$

$$+\frac{v_1w_2w_3}{v_2}\left(w_3-w_2\right)\frac{dg_{23}}{dw_3}-\frac{v_1w_2^2w_3^2}{v_2}\frac{d^2g_{23}}{dw_3^2} \quad \text{.....(A.26)}$$

Critical point where the binodal and spinodal curves touch each other is thermodynamically defined as [1];

$$\frac{\partial^2 G}{\partial \phi^2} = \frac{\partial^3 G}{\partial \phi^3} = 0 \quad \text{.....(A.27)}$$

The following relationship is derived from Equation (A.27) [1];

$$G_{222} \cdot G_{33}^2 - 3G_{223} \cdot G_{23} \cdot G_{33} + 3G_{233} \cdot G_{23}^2 - G_{22} \cdot G_{23} \cdot G_{333} = 0 \quad \text{.....(A.28)}$$

where,

$$G_{ijk} = \frac{\partial^3 \Delta G_M}{\partial \phi_i \partial \phi_j \partial \phi_k} v_{ref} \quad \text{.....(A.29)}$$

Calculation of critical points was not executed in this research.

A.3. Interaction Parameters

Concentration-dependent non-solvent/solvent interaction parameter, g_{12}, for NMP/water system is determined as [1];

$$g_{12} = 0.4860 + 0.8029 u_2 \quad \text{.....(A.30)}$$

$$\frac{dg_{12}}{du_2} = 0.8029 \quad \text{.....(A.31)}$$

$$\frac{d^2 g_{12}}{du_2^2} = 0 \quad \text{.....(A.32)}$$

Non-solvent/polymer interaction parameter, g_{13}, can be determined by swelling or sorption measurements [6]. The swelling behavior is described by Flory-Rehner theory and determined as:

$$g_{13} = -\frac{\ln\left(1-\phi_{3,swell}\right)+\phi_{3,swell}}{\phi_{3,swell}^2} \quad \text{.....(A.33)}$$

where,

$\phi_{3,swel}$; volume fraction of polymer in the swelling experiment [-]

The concentration-independent g_{13} for water/CA system evaluated based on swelling and sorption measurements were g_{13} = 1.35 and 1.4±0.1, respectively [6].

The solvent/polymer interaction parameter, g_{23}, can be determined by dilute viscosity data [1]. Osmotic pressure of a polymer solution, Π [Pa], is expressed as;

$$\frac{\Pi}{c} = \frac{R_g T}{\overline{M_n}}\left(1+\frac{A_2^* \overline{M_n} c}{2}\right)^2 \quad \text{.....(A.34)}$$

where,

c; mass concentration of polymer [kg/m^3]

$\overline{M_n}$; number-average molecur weight [kg/mol]

R_g; gas constant (= 8.314472 J/mol/K)

T; temperature [K]

A_2^*; concentration-dependent second virial coefficient [m^3·mol/kg^2]

The concentration-dependent second virial coefficient, A_2^*, is given as;

$$A_2^* = \frac{16\pi N_A [\eta]}{9.3\times10^{24}\overline{M_n}\left\{1+\frac{[\eta]-[\eta]_\theta}{[\eta]_\theta}\left[1-\exp\left(-\frac{c}{c^*}\right)\right]\right\}}\left(1-\frac{[\eta]_\theta}{[\eta]}\right) \quad \text{.....(A.35)}$$

$$[\eta] = \frac{\sqrt{2\left(\eta_{sp}-\ln\eta_r\right)}}{c} \quad \text{.....(A.36)}$$

$$\eta_{sp} = \frac{\eta-\eta_2}{\eta_2} \quad \text{.....(A.37)}$$

$$\eta_r = \frac{\eta}{\eta_2} \quad \text{.....(A.38)}$$

$$c^* = \frac{3F}{4\pi N_A [\eta]} \quad \text{.....(A.39)}$$

where,

[η]; intrinsic viscosity of diluted polymer solution [m^3/kg]

η_{sp}; specific viscosity of the polymer solution [-]

η_r; relative viscosity of the polymer solution [-]

c^*; overlap concentration of the polymer solution [kg/m^3]

N_A; Avogadro's number (= 6.023 x 10^{23} particles/mol)

$[\eta]_\theta$ is intrinsic viscosity under theta conditions and is determined from the measurement of [η] in a non-theta solvent;

$$[\eta]_\theta = \frac{[\eta]\left[1-\exp\left(-\frac{c}{c^*}\right)\right]}{\frac{0.77^3\rho_{coil}}{c^*}-\exp\left(-\frac{c}{c^*}\right)} \quad \text{.....(A.40)}$$

$$\rho_{coil} = \frac{c}{\eta_{sp}}\left(1.25 + 0.5\sqrt{56.4\eta_{sp} + 6.25}\right) \quad \text{(A.41)}$$

where,

ρ_{coil}; coil density of a polymer molecule [kg/m^3]

The solvent/polymer interaction parameter, g23, is determined as;

$$g_{23} = 0.5 - A_2\rho_3^2 v_2 \quad \text{(A.42)}$$

where,

A_2 : concentration-independent virial coefficient [m^3·mol/kg^2]

ρ_3; density of polymer [kg/m^3]

v_2; molar volume of solvent [m^3/mol]

The intrinsic viscosity of the NMP/CA diluted solution is 166 mL/g [7]. Assuming $A_2 = A_2^*$ (concentration-independent), g_{23} for NMP/CA solution becomes 0.50.

A.4. Calculation of Binodal and Spinodal Curves

By applying the solver function of Microsoft® Office Excel®, binodal and spinodal curves were calculated for the CA-NMP-Water system. The numerical calculation is sensitive to initial values, especially for binodal curve. To assure a valid binodal curve, spinodal curve was calculated firstly. For a specific ϕ_3, the ϕ_1 was determined by changing ϕ_2 in Equation (A.19) for the spinodal curve. For a specific $\phi_{3,A}$, the $\phi_{1,A}$ and $\phi_{1,A}$ were determined by changing $\phi_{2,A}$, $\phi_{2,B}$ $\phi_{3,B}$ in Equations (A.13) – (A.16) for the binodal curve. Generally ternary phase diagram is described

experimentally based on weight fraction. Volume fraction for each component obtained in this calculation was converted into weight fraction to compare with experimental data.

$$\omega_i = \frac{\phi_i \rho_i}{\sum_j \phi_j \rho_j} \quad \text{.....(A.43)}$$

where,

ω; weight fraction [-]

ϕ; volume fraction [-]

ρ; density [kg/m^3]

The results are shown in Chapter 4, Section 4.2 with the experimental results.

A.5. References

1. Barzin, J. and B. Sadatnia, *Theoretical Phase Diagram Calculation and Membrane Morphology Evaluation for Water/Solvent/Polyethersulfone Systems.* Polymer, 2007. **48**(6): p. 1620-1631.

2. Hao, J.H. and S.C. Wang, *Calculation of Alcohol-Acetone-Cellulose Acetate Ternary Phase Diagram and Their Relevance to Membrane Formation.* Journal of Applied Polymer Science, 2001. **80**(10): p. 1650-1657.

3. Wei, Y.M., et al., *Mathematical Calculation of Binodal Curves of a Polymer/Solvent/Nonsolvent System in the Phase Inversion Process.* Desalination, 2006. **192**(1-3): p. 91-104.

4. Shieh, J.J. and T.S. Chung, *Effect of Liquid-Liquid Demixing on the Membrane Morphology, Gas Permeation, Thermal and Mechanical Properties of Cellulose Acetate Hollow Fibers.* Journal of Membrane Science, 1998. **140**(1): p. 67-79.

5. Yilmaz, L. and A.J. Mchugh, *Analysis of Nonsolvent Solvent Polymer Phase-Diagrams and Their Relevance to Membrane Formation Modeling.* Journal of Applied Polymer Science, 1986. **31**(4): p. 997-1018.

6. Karimi, M., et al., *A Lattice-Fluid Model for the Determination of the Water/Polymer Interaction Parameter from Water Uptake Measurements.* Journal of Membrane Science, 2007. **292**(1-2): p. 80-91.

7. Li, Z.S., et al., *Influence of Solvent on the Structure and Performance of Cellulose Acetate Membranes.* Journal of Membrane Science, 2006. **279**(1-2): p. 601-607.

APPENDIX B BED SHAPE AND SIZE EFFECTS ON SEPARATION PERFORMANCES OF PACKED BEDS

B.1. Introduction

Packed beds for industrial scale typically with large bed size are economical for mass production, but require large capital cost. The large amount of produced gas is consumed or stored. Medium and small bed sizes are desired to produce the gas for appropriate demands, or to be installed in the limited space depending on applications such as distributed hydrogen fueling stations for fuel cell, potable medical oxygen production, etc. Separation performance parameters below are generally desired for the packed beds in practical PSA processes;

- Low pressure drop
- High operating capacity
- High adsorbent productivity
- High recovery
- High purity

In this appendix, bed shape (aspect ratio) and size effects on the separation performances of packed beds except purity were assessed with a simplified modeling. This discussion is substantially applicable to fiber sorbent module based on discussion of mass transfer zone theory.

B.2. Separation Performances in Comparisons

Important quantities of dimensions, operating conditions and separation performance parameters are compared between a reference state and a state with changes on aspect ratio and/or bed volume as shown in Figure B-1. Detailed theoretical information of the simplified modeling for a packed bed is described in Appendix C.

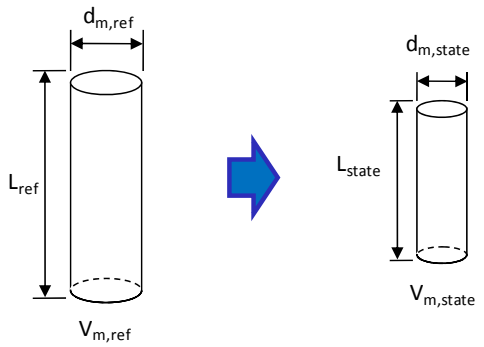

Figure B-1 Packed Beds at a Reference State (ref) and at a State with Changes (state)

To represent the comparison, ratio, r(Q), of each quantity at a state, Q_{state}, to a reference state, Q_{ref}, is defined in this appendix;

$$r(Q) = \frac{Q_{state}}{Q_{ref}} \quad \text{.....(B.1)}$$

Ratio of volume, V_m [m^3], and aspect ratio, k [-], are;

$$r(V_m) = \frac{V_{m,state}}{V_{m,ref}} \quad \text{.....(B.2)}$$

$$r(k) = \frac{k_{state}}{k_{ref}} \quad \text{.....(B.3)}$$

Ratio of cross-sectional area, S_m [m^2], is obtained from Equation (C.1);

$$S_{m,ref} = \pi d_{m,ref}^2 \big/ 4 \quad \text{.....(B.4)}$$

$$S_{m,state} = \pi d_{m,state}^2 \big/ 4 \quad \text{.....(B.5)}$$

$$r(S_m) = \frac{S_{m,state}}{S_{m,ref}} = \left\{ r(d_m) \right\}^2 \quad \text{.....(B.6)}$$

In the same manner, ratio of bed depth, L [m], is obtained from Equation (C.2);

$$r(L) = \frac{L_{state}}{L_{ref}} = r(k) \cdot r(d_m) \quad \text{.....(B.7)}$$

Ratio of diameter, d_m [m], is obtained based on the ratio of volume from Equation (C.3);

$$r(V_m) = \frac{V_{m,state}}{V_{m,ref}} = r(k) \left\{ r(d_m) \right\}^3 \quad \text{.....(B.8)}$$

$$r(d_m) = \left\{ \frac{r(V_m)}{r(k)} \right\}^{\frac{1}{3}} \quad \text{.....(B.9)}$$

Equations (B.6) and (B.7) are rearranged with Equation (B.9);

$$r(S_m) = \left\{ \frac{r(V_m)}{r(k)} \right\}^{\frac{2}{3}} \quad \text{(B.10)}$$

$$r(L) = \left[r(V_m) \cdot \left\{ r(k) \right\}^2 \right]^{\frac{1}{3}} \quad \text{(B.11)}$$

From Equation (C.72) and (C.73), relations among volumetric flow rate, Q_V [m^3/s], space time, τ_u [s], and linear velocity (superficial velocity), u [m/s], are given in the same manner above;

$$r(Q_V) = r(u) \cdot r(S_m) \quad \text{(B.12)}$$

$$r(u) = \frac{r(Q_V)}{r(S_m)} \quad \text{(B.13)}$$

$$r(\tau_u) = \frac{r(V_m)}{r(Q_V)} \left(= \frac{r(L)}{r(u)} \right) \quad \text{(B.14)}$$

Pressure drop, Δp [Pa], across the bed depth is simply assumed to be proportional to the linear velocity and bed depth rather than Equation (C.115);

$$\Delta p \simeq K_{\Delta p} u L \quad \text{(B.15)}$$

$$r(\Delta p) = r(u) \cdot r(L) \quad \text{(B.16)}$$

where,

$K_{\Delta p}$; constant [$Pa \cdot s/m^2$]

For packed beds, intraparticle diffusion is dominant rather than film diffusion around zeolite pellet when meso- and macropore diffusion is the controlling step as discussed in Chapter 2,

Section 2.5. When the same pellet size, compositions and type of zeolite are used in the comparisons, the overall mass transfer resistance, R_{MT} [s], can be assumed as a constant for the packed beds regardless of flow rate or linear velocity. To obtain ratio of utilization, U [-], another quantity U_N [-] (unutilization) is conveniently defined and given from Equation (C.174);

$$U_N \equiv 1-U \simeq 2\sqrt{\frac{R_{MT}}{\tau_u}} \quad \text{.....(B.17)}$$

$$r\left(U_N\right)=\frac{U_{N,state}}{U_{N,ref}}=\frac{1-U_{state}}{1-U_{ref}}=\frac{1}{\sqrt{r\left(\tau_u\right)}} \quad \text{.....(B.18)}$$

Equation (B.18) is rearranged and ratio of U is obtained;

$$U_{state}=1+r\left(U_N\right)\cdot\left(U_{ref}-1\right) \quad \text{.....(B.19)}$$

$$r\left(U\right)=\frac{1}{U_{ref}}+r\left(U_N\right)\cdot\left(1-\frac{1}{U_{ref}}\right) \quad \text{.....(B.20)}$$

Utilization at the reference state, U_{ref}, is given and depends on the zeolite (type, size) and operating (adsorption) conditions (composition, pressure, temperature and flow rate) at the reference state.

Ratio of breakthrough time, t_B [s], is obtained from Equation (C.176);

$$r\left(t_B\right)=r\left(U\right)\cdot r\left(\tau_u\right) \quad \text{.....(B.21)}$$

Volumes of feed, product, purge, and exhaust gases in each step in a PSA process, and operating and regenerated capacities of the packed bed are summarized in Table B-1. To calculate operating capacity, recovery and adsorbent productivity, the following conditions are assumed;

- Hydrogen is used in Step I and the amount of hydrogen to pressurize interstitial space of the packed bed is negligibly small compared with amount of purge gas.
- The time for Step I and III, t_I and t_{III}, are completed for a very short time.
- The packed bed is operated up to its breakthrough time in Step II, $t_{II} = t_B$.
- Consumption level of purge gas (flow rate of purge gas per bed volume), c_{reg1} [m^3-purge gas/s/m^3-bed], used in Step IV is constant and results in high purity.
- Regeneration time in Step IV, t_{IV}, is the same as the breakthrough time, and then cycle time becomes 2 times of the t_B.

Table B-1 Gas Volumes in Each PSA Step and Operating/Regenerated Capacities of the Packed Bed

Step		Component 1	Component 2
Step I Pressurization	Feed Gas Volume	$V_{1fd,I} = \left(y_{1,I}\,p_I - y_{1,IV}\,p_{IV}\right)\varepsilon_b V_m \simeq 0$ ..... (B.22)	$V_{2fd,I} = \left(y_{2,I}\,p_I - y_{2,IV}\,p_{IV}\right)\varepsilon_b V_m \simeq 0$ ..... (B.23)
Step II	Feed Gas Volume	$V_{1fd,II} = y_{1fd} Q_{V,fd} t_{II}$ ..... (B.24)	$V_{2fd,II} = y_{2fd} Q_{V,fd} t_{II}$ ..... (B.25)
Adsorption	Product Gas Volume	$y_{1pr} \simeq 1$ ..... (B.26)	$y_{2pr} \simeq 0$ ..... (B.27)
		$V_{1pr,II} = y_{pr1} Q_{V,pr} t_{II} \simeq Q_{V,pr} t_{II}$ ..... (B.28)	$V_{2pr,II} = y_{pr2} Q_{V,pr} t_{II} \simeq 0$ ..... (B.29)
		$Q_{V,pr} \simeq y_{fd1} Q_{V,fd}$ ..... (B.30)	
	Adsorbed Volume	$V_{1,ads} = V_{1fd,II} - V_{1pr,II} \simeq 0$ ..... (B.31)	$V_{2,ads} = V_{2fd,II} - V_{2pr,II} \simeq y_{fd2} Q_{V,fd} t_{II}$ ..... (B.32)
Step III Depressurization	Exhaust Gas Volume	$V_{1ex,III} = \left(y_{1,II}\,p_{II} - y_{1,III}\,p_{III}\right)\varepsilon_b V_m$ ..... (B.33)	$V_{2ex,III} = \left(y_{2,II}\,p_{II} - y_{2,III}\,p_{III}\right)\varepsilon_b V_m$ ..... (B.34)
Step IV	Purge Gas Volume	$y_{1pg} = y_{1pr} \simeq 1$ ..... (B.35)	$y_{2pg} = y_{2pr} \simeq 0$ ..... (B.36)
Purge		$V_{1pg,IV} = y_{1pg} Q_{V,pg} t_{IV} \simeq Q_{V,pg} t_{IV}$ ..... (B.37)	$V_{2pg,IV} = y_{2pg} Q_{V,pg} t_{IV} \simeq 0$ ..... (B.38)
(Desorption)	Exhaust Gas Volume	$V_{1ex,IV} = y_{1ex} Q_{V,ex} t_{IV}$ ..... (B.39)	$V_{2ex,IV} = y_{2ex} Q_{V,ex} t_{IV}$ ..... (B.40)
		$Q_{V,ex} \simeq \frac{1}{y_{1ex}} Q_{V,pg}$ ..... (B.41)	$y_{2ex} = \frac{V_{2,ads}}{Q_{V,pg} t_{IV} + V_{2,ads}}$ ..... (B.42)
	Desorbed Volume	$V_{1,des} = V_{1ex,IV} - V_{1pg,IV} = q_{V1,II} \simeq 0$ ..... (B.43)	$V_{2,des} = V_{2ex,IV} - V_{2pg,IV} = \frac{y_{ex2}}{y_{ex1}} Q_{V,pg} t_{IV}$ ..... (B.44)

V; volume [m^3], Q_V; volumetric flow rate [m^3/s], y; composition [-], p: total pressure [Pa], t; time [s], ε_b; void fraction of packed bed
subscript 1 and 2; Component 1 (H_2) and 2 (CO_2), subscript I, II, III and IV; for Step I, II, III and IV, subscript fd, pr, ex and pg; for feed, product, exhaust and purge gases, subscript ads and des; for adsorption and desorption

Cycle time, t_{cyc} [s], is described;

$$t_{cyc} = t_I + t_{II} + t_{III} + t_{IV} \simeq 0 + t_B + 0 + t_B = 2t_B \quad \text{(B.45)}$$

Adsorbed volume in Equation (B.28) means total operating capacity of the packed bed, $V_{2,op}$ [m^3];

$$V_{2,op} = V_{2,ads} = \frac{q_{V2,op} V_m}{C_{2fd}} \quad \text{(B.46)}$$

where,

$q_{v2,op}$; volumetric sorption capacity for a packed bed (Equation (C.175)) [mol/m^3]

V_m; volume of a packed bed [m^3]

C_{2fd}; feed concentration of Component 2 (CO_2) (Table C-1) [mol/m^3]

Ratio of the $V_{2,op}$ is described from Equation (B.28) by applying Equation (C.176);

$$V_{2,op} = y_{2fd} Q_{V,fd} t_B = y_{2fd} UKV_m \quad \text{(B.47)}$$

$$r\left(V_{2,op}\right) = r\left(U\right) \cdot r\left(V_m\right) \quad \text{(B.48)}$$

where,

K; dimensionless sorption equilibrium constant [m^3-gas/m^3-bed]

Recovery, R_1 [-], is a ratio of net amount of Component 1 in the product gas to that in the feed gas, and defined as;

$$R_{\mathrm{l}} = \frac{V_{1\,pr,II} - V_{1\,pg,IV}\dfrac{p_{IV}}{p_{II}}}{\sum_{n=I}^{II} V_{1\,fd,n}} \simeq 1 - \frac{Q_{V,pg}\,t_{IV}\dfrac{p_{IV}}{p_{II}}}{y_{1\,fd}\,Q_{V,fd}\,t_{II}} \quad \text{(B.49)}$$

To obtain ratio of the R_1, another quantity R_N (unrecovery) is conveniently defined and ratio of recovery is calculated;

$$R_{\mathrm{l}} \simeq 1 - \frac{Q_{V,pg}\,t_B\dfrac{p_{IV}}{p_{II}}}{y_{1\,fd}\,Q_{V,fd}\,t_B} = 1 - \frac{c_{reg1}V_m}{y_{1\,fd}\,Q_V} = 1 - \frac{c_{reg1}\tau_u}{y_{1\,fd}} \quad \text{(B.50)}$$

$$R_N \equiv 1 - R_{\mathrm{l}} = \frac{c_{reg1}\tau_u}{y_{1\,fd}} \quad \text{(B.51)}$$

$$r\left(R_N\right) = \frac{R_{N,state}}{R_{N,ref}} = \frac{1-R_{\mathrm{l},state}}{1-R_{\mathrm{l},ref}} = r\left(\tau_u\right) \quad \text{(B.52)}$$

where,

c_{reg1}; Consumption level of purge gas [m^3-purge gas/s/m^3-bed]

Equation (B.52) is rearranged and ratio of the R_1 is obtained;

$$R_{state} = 1 + r\left(R_N\right)\cdot\left(R_{\mathrm{l},ref} - 1\right) \quad \text{(B.53)}$$

$$r\left(R_{\mathrm{l}}\right) = \frac{1}{R_{\mathrm{l},ref}} + r\left(R_N\right)\cdot\left(1 - \frac{1}{R_{\mathrm{l},ref}}\right) \quad \text{(B.54)}$$

Recovery at the reference state, $R_{1,ref}$, is given and depends on the zeolite (type, size) and purge (regeneration, desorption) conditions (composition, pressure, temperature and flow rate) at the reference state.

Several adsorbent productivities can be defined in Table B-2;

Table B-2 Adsorbent Productivity

Basis	Adsorbent Productivity, η_p
Feed Gas Basis [kg-feed gas/kg-zeolite crystals]	$\eta_{p,fd} = \frac{\rho_{g,fd}\sum_{n=I}^{II}\left(V_{1fd,n}+V_{2fd,n}\right)}{\rho_{c,b}V_m t_{cyc}} \simeq \frac{\rho_{g,fd}Q_{V,fd}t_{II}}{\rho_{c,b}V_m t_{cyc}}$ .....(B.55)
Gross Product Gas Basis [kg-product gas/kg-zeolite crystals]	$\eta_{p1,pr} = \frac{\rho_1 V_{1pr,II}}{\rho_{c,b}V_m t_{cyc}} \simeq \frac{\rho_1 y_{1fd}Q_{V,fd}t_{II}}{\rho_{c,b}V_m t_{cyc}}$ .....(B.56)
Net Product Gas Basis [kg-product gas/kg-zeolite crystals]	$\eta_{p1,net} = \frac{\rho_1\left(V_{1pr,II} - V_{1pg,III}\frac{p_{IV}}{p_{II}}\right)}{\rho_{c,b}V_m t_{cyc}} = \frac{\rho_1 R_1\sum_{n=I}^{II}V_{1fd,n}}{\rho_{c,b}V_m t_{cyc}} = \frac{\rho_1 R_1 y_{1fd}Q_{V,fd}t_{II}}{\rho_{c,b}V_m t_{cyc}}$ .....(B.57)

ρ; density [kg/m^3], V_m; volume of a packed bed [m^3]; R_1; recovery of Component 1 (H_2) [-], t_{cyc}; cycle time [s], subscript c, g and 1; for zeolite crystals, a mixed gas and H_2, subscript b; for a packed bed, See Table B-1 for other symbols

Ratios of adsorbent productivities based on feed and net product gases are described when $t_{cyc} = 2t_B$;

$$\eta_{p,fd} = \frac{\rho_{g,fd}Q_{V,fd}t_B}{\rho_{c,b}V_m t_{cyc}} = \frac{\rho_{g,fd}}{2\rho_{c,b}\tau_u} \quad \text{.....(B.58)}$$

$$r\left(\eta_{p,fd}\right)=\frac{1}{r\left(\tau_u\right)} \quad \text{.....(B.59)}$$

$$\eta_{p1,net}=\frac{\rho_1 R_1 y_{1\,fd} Q_{V,fd} t_B}{\rho_{c,b} V_m t_{cyc}}=\frac{\rho_1 R_1 y_{1\,fd}}{2\rho_{c,b}\tau_u} \quad \text{.....(B.60)}$$

$$r\left(\eta_{p1,net}\right)=\frac{r\left(R_1\right)}{r\left(\tau_u\right)} \quad \text{.....(B.61)}$$

B.3. Case Studies

Three size conditions were compared to the reference state;

Case a) A state with a different aspect ratio keeping the same bed volume [$r(V_m) = 1$] (Figure B-2)

Case b) A state with a different downsized bed volume keeping the same aspect ratio [$r(k) = 1$] (Figure B-3)

Case c) A state with a different downsized bed volume and a different aspect ratio [combination of Cases a) and b)]

Three operating conditions were also assessed for each configuration;

Condition 1) same flow rate [$r(Q_V) = 1$]

Condition 2) same space time [$r(\tau_u) = 1$]

Condition 3) same pressure drop [$r(\Delta p) = 1$] (same energy consumption)

Utilization and recovery at the reference state impact on those for the states in which the changes are noted for the aspect ratio and/or downsizing. Three conditions were evaluated; 1) U_{ref} = 0.90 and $R_{1,ref}$ = 0.75, 2) U_{ref} = 0.60 and $R_{1,ref}$ = 0.75 and 3) U_{ref} = 0.90 and $R_{1,ref}$ = 0.90.

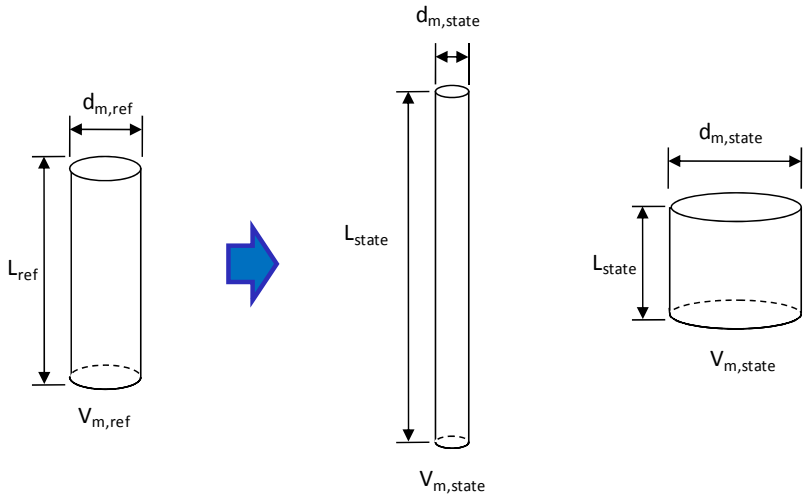

Figure B-2 Different Aspect Ratio with Same Bed Volume

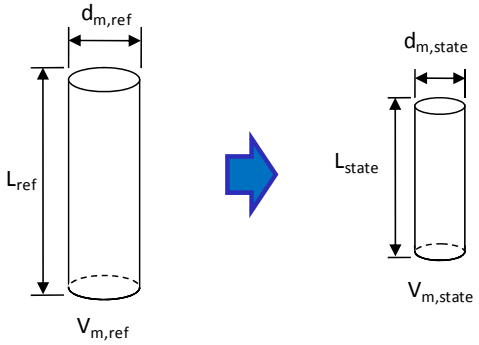

Figure B-3 Downsizing with Same Aspect Ratio

B.4. Results and Discussions

The calculation results for several column sizes under each aspect ratio and condition are shown in Table B-3 to Table B-10. To assist the readers, the some relevant cases are discussed here from many reported cases in these tables. First, however, some general trends can be extracted from consideration of many cases;

- Slow linear velocity, u, and/or shorter bed depth, L, give less pressure drop, Δp. (Equation (B.16))
- Slower flow rate, Q_V, and/or larger bed volume, V_m, give longer space time, τ_u, which gives larger utilization, U, and longer breakthrough time, t_B. (Equations (B.14), (B.20) and (B.21))
- Larger U and/or larger V_m give higher operating capacity, $V_{2,op}$. (Equation (B.47))
- Shorter τ_u gives higher recovery, R_1, and higher adsorbent productivity, $\eta_{p,fd}$ and $\eta_{p1,net}$. (Equations (B.54), (B.59) and (B.61))

Although the last bullet point may not be intuitively obvious to readers, as long as the purge time is the same as the breakthrough time, the amount of purge gas is reduced in case of shorter space time and then recovery is improved. Separation performances U and t_B behave oppositely to R_1, $\eta_{p,fd}$ and $\eta_{p1,net}$ with regard to τ_u.

As long as τ_u maintained (Case a Conditions 1 and 2, Case b Condition 2, and Case c Condition 2) in the comparisons, the U, t_B, R_1, and $\eta_{p,fd}$ and $\eta_{p1,net}$ were maintained. The $V_{2,op}$ depended on V_m and downsized bed volume gave smaller $V_{2,op}$. The Δp changed according to the bed depth due to the changes on aspect ratio and/or downsizing and deeper beds resulted in higher Δp.

Depending on the utilization and recovery at the reference state, U_{ref} and R_{ref}, negative r(U), $r(R_1)$ and ratios of other related quantities were shown in some cases. The negative r(U) (Cases D-2-3 and E-2-1) means that the mass transfer zone was greater than bed depth and leakage starts immediately after the adsorption step starts. The negative $r(R_1)$ (Cases A-1-3, A-2-3 and A-3-3) means that amount of purge gas was shorter for the bed size. To give $r(U) \geq 0$ and $r(R_1) \geq 0$ in the comparison, the following conditions should be satisfied from Equations (B.19) and (B.53);

$$U_{state} = 1 + r\left(U_N\right) \cdot \left(U_{ref} - 1\right) \geq 0 \quad \text{(B.62)}$$

$$R_{1,state} = 1 + r\left(R_N\right) \cdot \left(R_{1,ref} - 1\right) \geq 0 \quad \text{(B.63)}$$

Combined with Equations (E.18) and (B.52),

$$r\left(U_N\right) = \frac{1}{\sqrt{r\left(\tau_u\right)}} \leq \frac{1}{1 - U_{ref}} \quad \text{(B.64)}$$

$$r\left(R_N\right) = r\left(\tau_u\right) \leq \frac{1}{1 - R_{1,ref}} \quad \text{(B.65)}$$

Then, the following condition was obtained for the positive r(U) and $r(R_1)$;

$$\left(1 - U_{ref}\right)^2 \leq r\left(\tau_u\right) \leq \frac{1}{1 - R_{1,ref}} \quad \text{(B.66)}$$

For the same Q_V, downsized bed with the same aspect ratio (Case b Condition 1) reduced the U, t_B and $V_{2,op}$ and increased the Δp, R_1, $\eta_{p,fd}$ and $\eta_{p1,net}$ as the τ_u was reduced. This tendency was

regardless of aspect ratio changes on downsized bed (Case c Condition 1). Downsizing is effective to increase recovery and adsorbent productivity.

For the same Δp, downsized bed with the same aspect ratio (Case b Condition 3) also showed the reduced U, t_B and $V_{2,op}$ and the increased R_1, $\eta_{p,fd}$ and $\eta_{p1,net}$ since the τ_u was reduced as well. Aspect ratio change with the same V_m (Case a Condition 3), however, resulted in higher U, t_B and q_{op2} with the reduced Q_V for deeper beds, and higher R_1, $\eta_{p,fd}$ and $\eta_{p1,net}$ with increased Q_V for shallower beds. It indicated aspect ratio change may improve some performances in downsizing when pressure drop is only restricted. Downsizing with aspect ratio changes (Case c Condition 3) resulted in increased some performances for deeper beds compared with just downsized bed (Case b Condition 3). The U was improved from 0.87 (Case E-1-3) to 0.96 (Case I-3), the $\eta_{p1,net}$ became from 5.86 to 2.12. For shallower beds, the Q_V was increased significantly from 0.91 (Case H-1-3) to 2.29 (Case P-3), $\eta_{p1,net}$ became from 1.28 to 3.74. Both deeper and shallower bed cases still have advantages in adsorbent productivity because of downsizing.

Deeper beds take longer time to collect a specific amount of product gas since the Q_V was reduced (Case a Condition 3). On the other hand, shallower beds have advantage in case the adsorption step is operated for a specific time prior to its breakthrough since the flow rate was increased. For example, Cases A-1-3 and D-1-3 give 0.02 and 0.83, respectively in amount of the product gas when they are operated up to 0.13 in time, which is the t_B for Case D-1-3. Since Case A-1-3 was capable producing 1.07 in the $V_{2,op}$ at its breakthrough, most of adsorbent is not used when the operation was terminated at 0.13. Operational time sequence of rapid pressure swing adsorption (RPSA) processes is determined independently from the breakthrough time of packed bed and very short in seconds. Shallower bed seems attractive for the RPSA processes, but practically problematic. First of all, flow rate fluctuation is not tolerated. When flow rate or linear

velocity becomes significantly greater than the designed value, mass transfer zone becomes larger than the bed depth and results in the feed gas slippage. Secondary, flow distribution may be non-uniform due to the large cross-section of the bed. Additionally, footprint of the column is larger compared to deeper beds (taller columns). Effective arrangement of the shallow beds is desired. Stacking of shallow bend in a tall column (layered structure), or annular bed structure with radial flow may be helpful to utilize the space, but those requires some capital cost increase for more complicated internal structures than a simple column.

When the packed bed is regenerated by heating in thermal swing adsorption (TSA), or by displacement with another component, the regeneration step costs additionally and interrupts the process for a long time. It means number of regeneration per amount of product gas should be minimized, and utilization may be mostly prioritized. For this purpose, deeper beds are preferred when the packed bed are compared under the same Δp operation (Case a Condition 3). With lower utilization at a reference state (Case A-2-3), longer bed depth is effective to increase utilization.

B.5. Conclusions

Depending on the priority in the process, designing the column for deeper or shallow beds is possible with increased adsorbent productivity for downsizing. These results are substantially applicable to fiber sorbent modules. Pressure drop restriction is critical to design packed beds or fiber sorbents module. As discussed in Chapter 2, Section 2.5, fiber sorbent module has advantage of less pressure drop. So, it indicates longer fiber sorbent module allows increased flow rate as similar to shallow packed bed, but with advantages with deeper packed beds.

Table B-3 Case a) Different Aspect Ratio – 1 (U_{ref} = 0.90 and $R_{1,ref}$ = 0.75)

Size	$r(V_m)$	k_{ref}	k_{state}	r(k)	$r(d_m)$	$r(S_m)$	r(L)				
A	1.00	1.00	5.00	5.00	0.58	0.34	2.92				
B	1.00	1.00	2.00	2.00	0.79	0.63	1.59				
C	1.00	1.00	0.50	0.50	1.26	1.59	0.63				
D	1.00	1.00	0.25	0.25	1.59	2.52	0.40				
Cond. 1 (Q_V)	$r(V_m)$	$r(Q_V)$	r(u)	$r(\tau_u)$	$r(\Delta p)$	r(U)	$r(t_B)$	$r(V_{2,op})$	$r(R_1)$	$r(\eta_{p,fd})$	$r(\eta_{p1,net})$
A-1-1	1.00	1.00	2.92	1.00	8.55	1.00	1.00	1.00	1.00	1.00	1.00
B-1-1	1.00	1.00	1.59	1.00	2.52	1.00	1.00	1.00	1.00	1.00	1.00
C-1-1	1.00	1.00	0.63	1.00	0.40	1.00	1.00	1.00	1.00	1.00	1.00
D-1-1	1.00	1.00	0.40	1.00	0.16	1.00	1.00	1.00	1.00	1.00	1.00
Cond. 2 (τ_u)	$r(V_m)$	$r(Q_V)$	r(u)	$r(\tau_u)$	$r(\Delta p)$	r(U)	$r(t_B)$	$r(V_{2,op})$	$r(R_1)$	$r(\eta_{p,fd})$	$r(\eta_{p1,net})$
A-1-2	1.00	1.00	2.92	1.00	8.55	1.00	1.00	1.00	1.00	1.00	1.00
B-1-2	1.00	1.00	1.59	1.00	2.52	1.00	1.00	1.00	1.00	1.00	1.00
C-1-2	1.00	1.00	0.63	1.00	0.40	1.00	1.00	1.00	1.00	1.00	1.00
D-1-2	1.00	1.00	0.40	1.00	0.16	1.00	1.00	1.00	1.00	1.00	1.00
Cond. 3 (Δp)	$r(V_m)$	$r(Q_V)$	r(u)	$r(\tau_u)$	$r(\Delta p)$	r(U)	$r(t_B)$	$r(V_{2,op})$	$r(R_1)$	$r(\eta_{p,fd})$	$r(\eta_{p1,net})$
A-1-3	1.00	0.12	0.34	8.55	1.00	1.07	9.17	1.07	-1.52	0.12	-0.18
B-1-3	1.00	0.40	0.63	2.52	1.00	1.04	2.62	1.04	0.49	0.40	0.20
C-1-3	1.00	2.52	1.59	0.40	1.00	0.93	0.37	0.93	1.20	2.52	3.03
D-1-3	1.00	6.35	2.52	0.16	1.00	0.83	0.13	0.83	1.28	6.35	8.13

Table B-4 Case a) Different Aspect Ratio – 2 (U_{ref} = 0.60 and $R_{1,ref}$ = 0.75)

Size	$r(V_m)$	k_{ref}	k_{state}	r(k)	$r(d_m)$	$r(S_m)$	r(L)
A	1.00	1.00	5.00	5.00	0.58	0.34	2.92
B	1.00	1.00	2.00	2.00	0.79	0.63	1.59
C	1.00	1.00	0.50	0.50	1.26	1.59	0.63
D	1.00	1.00	0.25	0.25	1.59	2.52	0.40

Cond. 1 (Q_V)	$r(V_m)$	$r(Q_V)$	r(u)	$r(\tau_u)$	$r(\Delta p)$	r(U)	$r(t_B)$	$r(V_{2,op})$	$r(R_1)$	$r(\eta_{p,fd})$	$r(\eta_{p1,net})$
A-2-1	1.00	1.00	2.92	1.00	8.55	1.00	1.00	1.00	1.00	1.00	1.00
B-2-1	1.00	1.00	1.59	1.00	2.52	1.00	1.00	1.00	1.00	1.00	1.00
C-2-1	1.00	1.00	0.63	1.00	0.40	1.00	1.00	1.00	1.00	1.00	1.00
D-2-1	1.00	1.00	0.40	1.00	0.16	1.00	1.00	1.00	1.00	1.00	1.00
Cond. 2 (τ_u)	$r(V_m)$	$r(Q_V)$	r(u)	$r(\tau_u)$	$r(\Delta p)$	r(U)	$r(t_B)$	$r(V_{2,op})$	$r(R_1)$	$r(\eta_{p,fd})$	$r(\eta_{p1,net})$
A-2-2	1.00	1.00	2.92	1.00	8.55	1.00	1.00	1.00	1.00	1.00	1.00
B-2-2	1.00	1.00	1.59	1.00	2.52	1.00	1.00	1.00	1.00	1.00	1.00
C-2-2	1.00	1.00	0.63	1.00	0.40	1.00	1.00	1.00	1.00	1.00	1.00
D-2-2	1.00	1.00	0.40	1.00	0.16	1.00	1.00	1.00	1.00	1.00	1.00
Cond. 3 (Δp)	$r(V_m)$	$r(Q_V)$	r(u)	$r(\tau_u)$	$r(\Delta p)$	r(U)	$r(t_B)$	$r(V_{2,op})$	$r(R_1)$	$r(\eta_{p,fd})$	$r(\eta_{p1,net})$
A-2-3	1.00	0.12	0.34	8.55	1.00	1.44	12.30	1.44	-1.52	0.12	-0.18
B-2-3	1.00	0.40	0.63	2.52	1.00	1.25	3.14	1.25	0.49	0.40	0.20
C-2-3	1.00	2.52	1.59	0.40	1.00	0.61	0.24	0.61	1.20	2.52	3.03
D-2-3	1.00	6.35	2.52	0.16	1.00	-0.01	0.00	-0.01	1.28	6.35	8.13

Table B-5 Case a) Different Aspect Ratio – 3 (U_{ref} = 0.90 and $R_{1,ref}$ = 0.90)

Size	$r(V_m)$	k_{ref}	k_{state}	r(k)	$r(d_m)$	$r(S_m)$	r(L)
A	1.00	1.00	5.00	5.00	0.58	0.34	2.92
B	1.00	1.00	2.00	2.00	0.79	0.63	1.59
C	1.00	1.00	0.50	0.50	1.26	1.59	0.63
D	1.00	1.00	0.25	0.25	1.59	2.52	0.40

Cond. 1 (Q_V)	$r(V_m)$	$r(Q_V)$	r(u)	$r(\tau_u)$	$r(\Delta p)$	r(U)	$r(t_B)$	$r(V_{2,op})$	$r(R_1)$	$r(\eta_{p,fd})$	$r(\eta_{p1,net})$
A-3-1	1.00	1.00	2.92	1.00	8.55	1.00	1.00	1.00	1.00	1.00	1.00
B-3-1	1.00	1.00	1.59	1.00	2.52	1.00	1.00	1.00	1.00	1.00	1.00
C-3-1	1.00	1.00	0.63	1.00	0.40	1.00	1.00	1.00	1.00	1.00	1.00
D-3-1	1.00	1.00	0.40	1.00	0.16	1.00	1.00	1.00	1.00	1.00	1.00
Cond. 2 (τ_u)	$r(V_m)$	$r(Q_V)$	r(u)	$r(\tau_u)$	$r(\Delta p)$	r(U)	$r(t_B)$	$r(V_{2,op})$	$r(R_1)$	$r(\eta_{p,fd})$	$r(\eta_{p1,net})$
A-3-2	1.00	1.00	2.92	1.00	8.55	1.00	1.00	1.00	1.00	1.00	1.00
B-3-2	1.00	1.00	1.59	1.00	2.52	1.00	1.00	1.00	1.00	1.00	1.00
C-3-2	1.00	1.00	0.63	1.00	0.40	1.00	1.00	1.00	1.00	1.00	1.00
D-3-2	1.00	1.00	0.40	1.00	0.16	1.00	1.00	1.00	1.00	1.00	1.00
Cond. 3 (Δp)	$r(V_m)$	$r(Q_V)$	r(u)	$r(\tau_u)$	$r(\Delta p)$	r(U)	$r(t_B)$	$r(V_{2,op})$	$r(R_1)$	$r(\eta_{p,fd})$	$r(\eta_{p1,net})$
A-3-3	1.00	0.12	0.34	8.55	1.00	1.07	9.17	1.07	0.16	0.12	0.02
B-3-3	1.00	0.40	0.63	2.52	1.00	1.04	2.62	1.04	0.83	0.40	0.33
C-3-3	1.00	2.52	1.59	0.40	1.00	0.93	0.37	0.93	1.07	2.52	2.69
D-3-3	1.00	6.35	2.52	0.16	1.00	0.83	0.13	0.83	1.09	6.35	6.94

Table B-6 Case b) Downsizing – 1 (U_{ref} = 0.90 and $R_{1,ref}$ = 0.75)

Size	$r(V_m)$	k_{ref}	k_{state}	r(k)	$r(d_m)$	$r(S_m)$	r(L)				
E	0.10	1.00	1.00	1.00	0.46	0.22	0.46				
F	0.25	1.00	1.00	1.00	0.63	0.40	0.63				
G	0.50	1.00	1.00	1.00	0.79	0.63	0.79				
H	0.75	1.00	1.00	1.00	0.91	0.83	0.91				
Cond. 1 (Q_V)	$r(V_m)$	$r(Q_V)$	r(u)	$r(\tau_u)$	$r(\Delta p)$	r(U)	$r(t_B)$	$r(V_{2,op})$	$r(R_1)$	$r(\eta_{p,fd})$	$r(\eta_{p1,net})$
E-1-1	0.10	1.00	4.64	0.10	2.15	0.76	0.08	0.08	1.30	10.00	13.00
F-1-1	0.25	1.00	2.52	0.25	1.59	0.89	0.22	0.22	1.25	4.00	5.00
G-1-1	0.50	1.00	1.59	0.50	1.26	0.95	0.48	0.48	1.17	2.00	2.33
H-1-1	0.75	1.00	1.21	0.75	1.10	0.98	0.74	0.74	1.08	1.33	1.44
Cond. 2 (τ_u)	$r(V_m)$	$r(Q_V)$	r(u)	$r(\tau_u)$	$r(\Delta p)$	r(U)	$r(t_B)$	$r(V_{2,op})$	$r(R_1)$	$r(\eta_{p,fd})$	$r(\eta_{p1,net})$
E-1-2	0.10	0.10	0.46	1.00	0.22	1.00	1.00	0.10	1.00	1.00	1.00
F-1-2	0.25	0.25	0.63	1.00	0.40	1.00	1.00	0.25	1.00	1.00	1.00
G-1-2	0.50	0.50	0.79	1.00	0.63	1.00	1.00	0.50	1.00	1.00	1.00
H-1-2	0.75	0.75	0.91	1.00	0.83	1.00	1.00	0.75	1.00	1.00	1.00
Cond. 3 (Δp)	$r(V_m)$	$r(Q_V)$	r(u)	$r(\tau_u)$	$r(\Delta p)$	r(U)	$r(t_B)$	$r(V_{2,op})$	$r(R_1)$	$r(\eta_{p,fd})$	$r(\eta_{p1,net})$
E-1-3	0.10	0.46	2.15	0.22	1.00	0.87	0.19	0.09	1.26	4.64	5.86
F-1-3	0.25	0.63	1.59	0.40	1.00	0.93	0.37	0.23	1.20	2.52	3.03
G-1-3	0.50	0.79	1.26	0.63	1.00	0.97	0.61	0.49	1.12	1.59	1.78
H-1-3	0.75	0.91	1.10	0.83	1.00	0.99	0.82	0.74	1.06	1.21	1.28

Table B-7 Case b) Downsizing – 2 (U_{ref} = 0.60 and $R_{1,ref}$ = 0.75)

Size	$r(V_m)$	k_{ref}	k_{state}	r(k)	$r(d_m)$	$r(S_m)$	r(L)				
E	0.10	1.00	1.00	1.00	0.46	0.22	0.46				
F	0.25	1.00	1.00	1.00	0.63	0.40	0.63				
G	0.50	1.00	1.00	1.00	0.79	0.63	0.79				
H	0.75	1.00	1.00	1.00	0.91	0.83	0.91				
Cond. 1 (Q_V)	$r(V_m)$	$r(Q_V)$	r(u)	$r(\tau_u)$	$r(\Delta p)$	r(U)	$r(t_B)$	$r(V_{2,op})$	$r(R_1)$	$r(\eta_{p,fd})$	$r(\eta_{p1,net})$
E-2-1	0.10	1.00	4.64	0.10	2.15	-0.44	-0.04	-0.04	1.30	10.00	13.00
F-2-1	0.25	1.00	2.52	0.25	1.59	0.33	0.08	0.08	1.25	4.00	5.00
G-2-1	0.50	1.00	1.59	0.50	1.26	0.72	0.36	0.36	1.17	2.00	2.33
H-2-1	0.75	1.00	1.21	0.75	1.10	0.90	0.67	0.67	1.08	1.33	1.44
Cond. 2 (τ_u)	$r(V_m)$	$r(Q_V)$	r(u)	$r(\tau_u)$	$r(\Delta p)$	r(U)	$r(t_B)$	$r(V_{2,op})$	$r(R_1)$	$r(\eta_{p,fd})$	$r(\eta_{p1,net})$
E-2-2	0.10	0.10	0.46	1.00	0.22	1.00	1.00	0.10	1.00	1.00	1.00
F-2-2	0.25	0.25	0.63	1.00	0.40	1.00	1.00	0.25	1.00	1.00	1.00
G-2-2	0.50	0.50	0.79	1.00	0.63	1.00	1.00	0.50	1.00	1.00	1.00
H-2-2	0.75	0.75	0.91	1.00	0.83	1.00	1.00	0.75	1.00	1.00	1.00
Cond. 3 (Δp)	$r(V_m)$	$r(Q_V)$	r(u)	$r(\tau_u)$	$r(\Delta p)$	r(U)	$r(t_B)$	$r(V_{2,op})$	$r(R_1)$	$r(\eta_{p,fd})$	$r(\eta_{p1,net})$
E-2-3	0.10	0.46	2.15	0.22	1.00	0.23	0.05	0.02	1.26	4.64	5.86
F-2-3	0.25	0.63	1.59	0.40	1.00	0.61	0.24	0.15	1.20	2.52	3.03
G-2-3	0.50	0.79	1.26	0.63	1.00	0.83	0.52	0.41	1.12	1.59	1.78
H-2-3	0.75	0.91	1.10	0.83	1.00	0.93	0.77	0.70	1.06	1.21	1.28

Table B-8 Case b) Downsizing – 3 (U_{ref} = 0.90 and $R_{1,ref}$ = 0.90)

Size	$r(V_m)$	k_{ref}	k_{state}	r(k)	$r(d_m)$	$r(S_m)$	r(L)
E	0.10	1.00	1.00	1.00	0.46	0.22	0.46
F	0.25	1.00	1.00	1.00	0.63	0.40	0.63
G	0.50	1.00	1.00	1.00	0.79	0.63	0.79
H	0.75	1.00	1.00	1.00	0.91	0.83	0.91

Cond. 1 (Q_V)	$r(V_m)$	$r(Q_V)$	r(u)	$r(\tau_u)$	$r(\Delta p)$	r(U)	$r(t_B)$	$r(V_{2,op})$	$r(R_1)$	$r(\eta_{p,fd})$	$r(\eta_{p1,net})$
E-3-1	0.10	1.00	4.64	0.10	2.15	0.76	0.08	0.08	1.10	10.00	11.00
F-3-1	0.25	1.00	2.52	0.25	1.59	0.89	0.22	0.22	1.08	4.00	4.33
G-3-1	0.50	1.00	1.59	0.50	1.26	0.95	0.48	0.48	1.06	2.00	2.11
H-3-1	0.75	1.00	1.21	0.75	1.10	0.98	0.74	0.74	1.03	1.33	1.37
Cond. 2 (τ_u)	$r(V_m)$	$r(Q_V)$	r(u)	$r(\tau_u)$	$r(\Delta p)$	r(U)	$r(t_B)$	$r(V_{2,op})$	$r(R_1)$	$r(\eta_{p,fd})$	$r(\eta_{p1,net})$
E-3-2	0.10	0.10	0.46	1.00	0.22	1.00	1.00	0.10	1.00	1.00	1.00
F-3-2	0.25	0.25	0.63	1.00	0.40	1.00	1.00	0.25	1.00	1.00	1.00
G-3-2	0.50	0.50	0.79	1.00	0.63	1.00	1.00	0.50	1.00	1.00	1.00
H-3-2	0.75	0.75	0.91	1.00	0.83	1.00	1.00	0.75	1.00	1.00	1.00
Cond. 3 (Δp)	$r(V_m)$	$r(Q_V)$	r(u)	$r(\tau_u)$	$r(\Delta p)$	r(U)	$r(t_B)$	$r(V_{2,op})$	$r(R_1)$	$r(\eta_{p,fd})$	$r(\eta_{p1,net})$
E-3-3	0.10	0.46	2.15	0.22	1.00	0.87	0.19	0.09	1.09	4.64	5.05
F-3-3	0.25	0.63	1.59	0.40	1.00	0.93	0.37	0.23	1.07	2.52	2.69
G-3-3	0.50	0.79	1.26	0.63	1.00	0.97	0.61	0.49	1.04	1.59	1.65
H-3-3	0.75	0.91	1.10	0.83	1.00	0.99	0.82	0.74	1.02	1.21	1.23

Table B-9 Case c) Combination – 1 (Longer Column, $U_{ref} = 0.90$ and $R_{1,ref} = 0.75$)

Size	$r(V_m)$	k_{ref}	k_{state}	r(k)	$r(d_m)$	$r(S_m)$	r(L)				
I	0.10	1.00	2.00	2.00	0.37	0.14	0.74				
J	0.25	1.00	2.00	2.00	0.50	0.25	1.00				
K	0.50	1.00	2.00	2.00	0.63	0.40	1.26				
L	0.75	1.00	2.00	2.00	0.72	0.52	1.44				
Cond. 1 (Q_V)	$r(V_m)$	$r(Q_V)$	r(u)	$r(\tau_u)$	$r(\Delta p)$	r(U)	$r(t_B)$	$r(V_{2,op})$	$r(R_1)$	$r(\eta_{p,fd})$	$r(\eta_{p1,net})$
I-1	0.10	1.00	7.37	0.10	5.43	0.76	0.08	0.08	1.30	10.00	13.00
J-1	0.25	1.00	4.00	0.25	4.00	0.89	0.22	0.22	1.25	4.00	5.00
K-1	0.50	1.00	2.52	0.50	3.17	0.95	0.48	0.48	1.17	2.00	2.33
L-1	0.75	1.00	1.92	0.75	2.77	0.98	0.74	0.74	1.08	1.33	1.44
Cond. 2 (τ_u)	$r(V_m)$	$r(Q_V)$	r(u)	$r(\tau_u)$	$r(\Delta p)$	r(U)	$r(t_B)$	$r(V_{2,op})$	$r(R_1)$	$r(\eta_{p,fd})$	$r(\eta_{p1,net})$
I-2	0.10	0.10	0.74	1.00	0.54	1.00	1.00	0.10	1.00	1.00	1.00
J-2	0.25	0.25	1.00	1.00	1.00	1.00	1.00	0.25	1.00	1.00	1.00
K-2	0.50	0.50	1.26	1.00	1.59	1.00	1.00	0.50	1.00	1.00	1.00
L-2	0.75	0.75	1.44	1.00	2.08	1.00	1.00	0.75	1.00	1.00	1.00
Cond. 3 (Δp)	$r(V_m)$	$r(Q_V)$	r(u)	$r(\tau_u)$	$r(\Delta p)$	r(U)	$r(t_B)$	$r(V_{2,op})$	$r(R_1)$	$r(\eta_{p,fd})$	$r(\eta_{p1,net})$
I-3	0.10	0.18	1.36	0.54	1.00	0.96	0.52	0.10	1.15	1.84	2.12
J-3	0.25	0.25	1.00	1.00	1.00	1.00	1.00	0.25	1.00	1.00	1.00
K-3	0.50	0.31	0.79	1.59	1.00	1.02	1.62	0.51	0.80	0.63	0.51
L-3	0.75	0.36	0.69	2.08	1.00	1.03	2.15	0.78	0.64	0.48	0.31

Table B-10 Case c) Combination – 2 (Shallower Column, $U_{ref} = 0.90$ and $R_{1,ref} = 0.75$)

Size	$r(V_m)$	k_{ref}	k_{state}	r(k)	$r(d_m)$	$r(S_m)$	r(L)
M	0.10	1.00	0.50	0.50	0.58	0.34	0.29
N	0.25	1.00	0.50	0.50	0.79	0.63	0.40
O	0.50	1.00	0.50	0.50	1.00	1.00	0.50
P	0.75	1.00	0.50	0.50	1.14	1.31	0.57

Cond. 1 (Q_V)	$r(V_m)$	$r(Q_V)$	r(u)	$r(\tau_u)$	$r(\Delta p)$	r(U)	$r(t_B)$	$r(V_{2,op})$	$r(R_1)$	$r(\eta_{p,fd})$	$r(\eta_{p1,net})$
M-1	0.10	1.00	2.92	0.10	0.85	0.76	0.08	0.08	1.30	10.00	13.00
N-1	0.25	1.00	1.59	0.25	0.63	0.89	0.22	0.22	1.25	4.00	5.00
O-1	0.50	1.00	1.00	0.50	0.50	0.95	0.48	0.48	1.17	2.00	2.33
P-1	0.75	1.00	0.76	0.75	0.44	0.98	0.74	0.74	1.08	1.33	1.44

Cond. 2 (τ_u)	$r(V_m)$	$r(Q_V)$	r(u)	$r(\tau_u)$	$r(\Delta p)$	r(U)	$r(t_B)$	$r(V_{2,op})$	$r(R_1)$	$r(\eta_{p,fd})$	$r(\eta_{p1,net})$
M-2	0.10	0.10	0.29	1.00	0.09	1.00	1.00	0.10	1.00	1.00	1.00
N-2	0.25	0.25	0.40	1.00	0.16	1.00	1.00	0.25	1.00	1.00	1.00
O-2	0.50	0.50	0.50	1.00	0.25	1.00	1.00	0.50	1.00	1.00	1.00
P-2	0.75	0.75	0.57	1.00	0.33	1.00	1.00	0.75	1.00	1.00	1.00

Cond. 3 (Δp)	$r(V_m)$	$r(Q_V)$	r(u)	$r(\tau_u)$	$r(\Delta p)$	r(U)	$r(t_B)$	$r(V_{2,op})$	$r(R_1)$	$r(\eta_{p,fd})$	$r(\eta_{p1,net})$
M-3	0.10	1.17	3.42	0.09	1.00	0.73	0.06	0.07	1.30	11.70	15.26
N-3	0.25	1.59	2.52	0.16	1.00	0.83	0.13	0.21	1.28	6.35	8.13
O-3	0.50	2.00	2.00	0.25	1.00	0.89	0.22	0.44	1.25	4.00	5.00
P-3	0.75	2.29	1.75	0.33	1.00	0.92	0.30	0.69	1.22	3.05	3.74

APPENDIX C A SIMPLIFIED MODELING OF A FIBER SORBENT MODULE AND AN EQUIVALENT SIZE PACKED BED

C.1. Introduction

A fiber sorbent module in industrial use for hydrogen recovery was compared with an equivalent size packed bed. In all of the following discussions, both module diameters and lengths are identical for the novel fiber sorbent module and packed bed. The flow channels in the bore side of the hollow fiber sorbents *and* the void space between fiber sorbents (which is filled with heat moderating wax) is accommodated within the same physical space as that in conventional packed bed. This makes the device even more revolutionary than a monolith which can contains the flow channels analogous to bores of fiber sorbents, but cannot accommodate heat moderating wax without a very complex monolith structure. The fiber sorbents were comprised of cellulose acetate (CA) and zeolite NaY as described in Chapter 3, Section 3.1. A set of base case conditions was considered as shown in Table C-1. The feed gas conditions in Table C-1 are typical of the main components of the standard reformate gas on a dry basis [1]. For the comparison with a typical packed bed, outer and inner (bore) diameters of the fiber sorbent, d_f and d_{fb}, were varied under the reference and other specific conditions, and then packing fraction, ϕ_m, was calculated accordingly combined with number of fiber sorbents, n_f. Separation performance factors such as pressure drop, Δp, mass transfer resistance, R_{MT}, breakthrough time, t_B, and adsorbent productivity, η_p, were first evaluated under the ***isothermal condition at 60 °C***. Gas properties were obeyed to the ideal gas law and the ideal mixture law. Although the gas properties derived below are as function of temperature, pressure and composition for the mixed gas, they were assumed as constants at the feed conditions during the adsorption step in the PSA process for

simplicity. Properties, dimensions and fractions of the porous materials were maintained at the initial (feed) temperature without changes. Next, temperature increase was accounted for under the ***adiabatic condition***. Detailed definition and calculation are described bellow followed by the results and discussions.

Table C-1 Base Case Conditions

Parameter		Condition
Feed Gas		
Total Pressure	p_{fd}	791 kPa (= 100 psig)
Temperature	T_{fd}	60 °C
Composition		
Hydrogen	y_{1fd}	75 mol%
Carbon Dioxide	y_{2fd}	25 mol%
Operation		
Linear Velocity	u	50 cm/s
Pressure Drop	$(\Delta p)_f$	Same as $(\Delta p)_p$
Zeolite		
Loading	ω_{c0}	69 wt%
Porosity	ε_f (= ε_p)	0.33
Pore Size	d_{pore}	200 nm

C.2. Dimensions and Fractions

Dimensions, packing and void fractions of a fiber sorbent module and an equivalent size packed bed were defined in Figure C-1. Fiber sorbents were packed as a bundle in a module for the PSA process. The dimensions were given in Table C-2. The term “porosity” in this thesis was defined

as the volume fraction of void space inside individual fiber sorbents due to porous wall structure (vol% per fiber sorbent). On the other hand, "void fraction" was defined to comprise void spaces for shell and bore sides in the module between fiber sorbents (vol% per module).

Table C-2 Dimensions Used in Comparison between a Fiber Sorbent Module and an Equivalent Size Packed Bed

	Fiber Sorbent Module	Packed Bed
Module/Column Size		
Diameter	d_m = 20 cm	d_m = 20 cm
Length/Depth	L = 1 m	L = 1 m
Material		
Geometry	Hollow Cylinder	Spherical Pellet
Diameter	Outer, d_f (varied)	d_p = 1.5 mm (1/16") [2]
	Inner (bore), d_{fb} (varied)	
Number	n_f (varied)	Not Applicable
Void Fraction	Bore-side, ε_{mb} (varied)	ε_b = 0.4
	Shell-side, ε_{ms} (varied)	

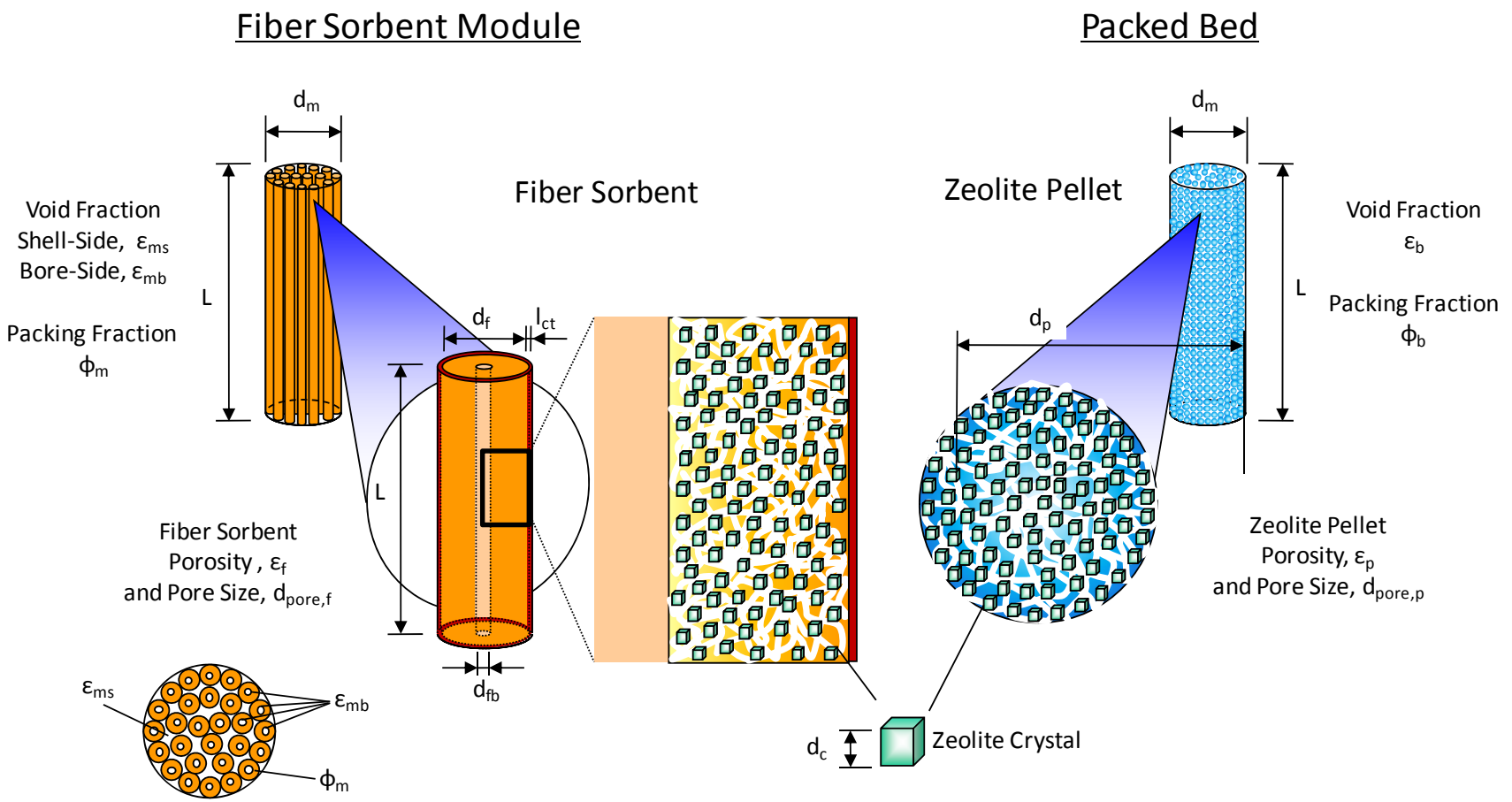

Note: The definition of the various parameters in this fibure are clearly dicussed and sepcified in the following section.

Figure C-1 Schematic Diagram of a Fiber Sorbent Module and an Equivalent Size Packed Bed

Cross-sectional area, module length/bed depth and volume of the fiber sorbent module and the packed bed were described as follows;

$$S_m = \pi d_m^2 / 4 \quad \text{(C.1)}$$

$$L = k d_m \quad \text{(C.2)}$$

$$V_m = S_m L = \pi k d_m^3 / 4 \quad \text{(C.3)}$$

where,

S_m; cross-sectional area of a fiber sorbent module or a packed bed [m^2]

d_m; diameter of a fiber sorbent module or a packed bed [m]

L; length of a fiber sorbent and its module or bed depth of a packed bed [m]

k; aspect ratio of a fiber sorbent module or a packed bed (= L/d_m) [-]

V_m; volume of a fiber sorbent module or a packed bed [m^3]

When fiber sorbents were arranged with maximum numbers in vertical and horizontal directions, $n_{f,V}$ and $n_{f,H}$, as shown in Figure C-2, the maximum number, $n_{f,max}$, was obtained as follows.

$$n_{f,V} \le \frac{d_m}{d_{f+ct}} \quad \text{(C.4)}$$

$$n_{f,H} \le \frac{d_m / d_{f+ct} - 1}{\sqrt{3}} \quad \text{(C.5)}$$

$$\begin{aligned} n_{f,\max} &= n_{f,V} + 2\sum_{k=1}^{n_{f,H}} \left(n_{f,V} - k \right) \\ &= n_{f,V} \left(1 + 2 n_{f,H} \right) - n_{f,H} \left(n_{f,H} + 1 \right) \end{aligned} \quad \text{(C.6)}$$

$$d_{f+ct} = d_f + 2 l_{ct} \quad \text{(C.7)}$$

where,

$n_{f,max}$; maximum number of fiber sorbents [-]

$n_{f,V}$; maximum number of fiber sorbents in vertical direction [-]

$n_{f,H}$; maximum number of fiber sorbents in horizontal direction [-]

d_m; diameter of a fiber sorbent module or a packed bed [m]

d_{f+ct}; diameter of a fiber sorbent including an impermeable layer [m]

d_f; outer diameter of a fiber sorbent [m]

l_{ct}; thickness of impermeable layer [m]

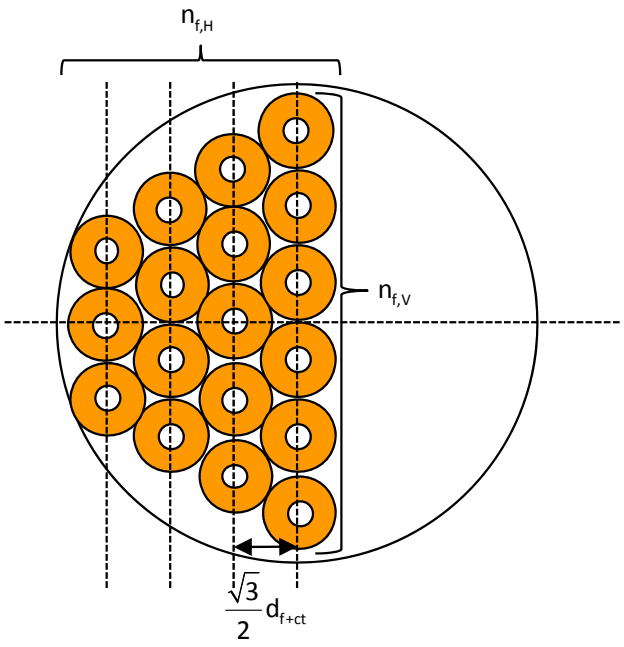

Figure C-2 Definition of Maximum Packing Fraction of a Fiber Sorbent Module

Actual number of fiber sorbent, n_f, must be less than maximum value, $n_{f,max}$.

Packing and void fractions by weight or by volume were defined in Table C-3 ~ Table C-5 corresponding to different basis. For different analyses, it is useful to use these different fractions; however, these different bases can be confusing, unless one has a "key" to relate them simply. The schematic diagram shown in Figure C-3 provides such a key to visualize the relationship between volume fractions of each basis.

The fiber sorbent solid phase basis in Figure C-3 defines fractions based on a fiber sorbent *excluding* the bores and macro- and meso-pores in the fiber sorbent. This basis is corresponding to pellet solid phase basis defined for a zeolite pellet, and is used to calculate weight fractions of zeolite (zeolite loading), ω_{c0}, and polymer, ω_{pm0}, which are given as a result of the spinning of fiber sorbents. By applying densities of zeolite crystal and polymer for the fiber sorbent or a binder material for the zeolite pellet, volume fractions of zeolite crystals in the fiber sorbent or in a zeolite pellet, ϕ_{c0}, can be converted from ω_{c0}. The range of ω_{c0} was between 64 to 76% as discussed in Chapter 4, Section 4-4.

The bare fiber sorbent basis defines fractions based on a fiber sorbent including macro- and meso-pores, but not including the bore volumes. This basis is corresponding to pellet basis defined for a zeolite pellet. Porosity, ε_f, and pore size (diameter) of fiber sorbent, $d_{pore,f}$, are determined by the phase separation process through the spinning and are obtained experimentally. By knowing porosity of the fiber sorbent with a separate analytical method such as mercury porosimetry, volume fractions can be converted from the solid phase basis. For the conversion between weight and volume fractions in this basis, weight of gas which is filled in pores *can be neglected* since that is very small compared with weight of the solid phase. In the calculations here, the ε_f and the $d_{pore,f}$ were assumed to be 0.33 and 200 nm, respectively, which were equivalent to zeolite pellet in the comparison.

Fiber Sorbent ***Solid*** Phase Basis

$$\phi_{c0} + \phi_{pm0} = 1$$

Bare Fiber Sorbent Basis

$$\varepsilon_f + \phi_f = 1$$

Coated Fiber Sorbent Basis

$$\phi_{bf} + \phi_{ct} = 1$$

Fiber Sorbent Module Basis

$$\phi_m + \varepsilon_{mb} + \varepsilon_{ms} = 1$$

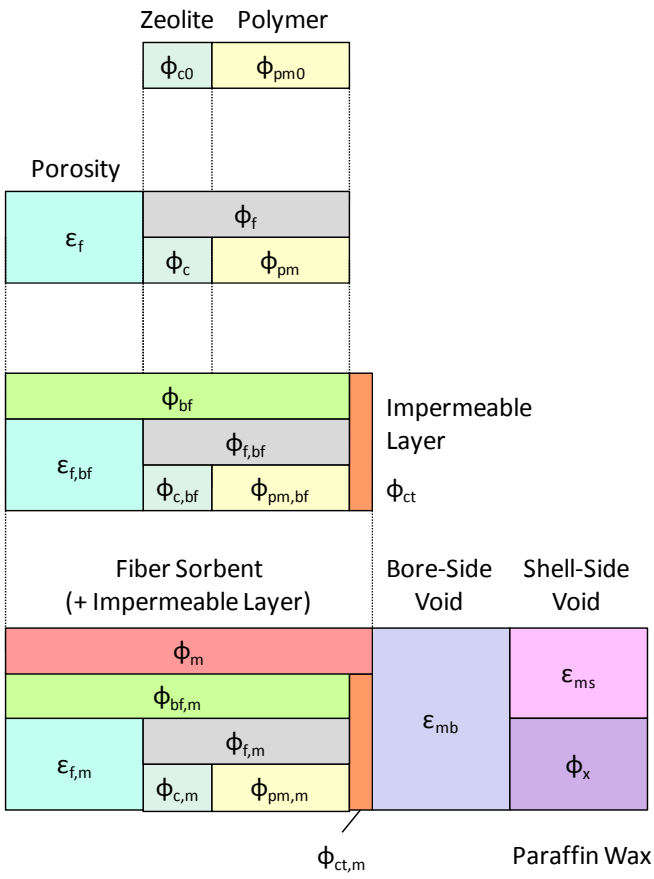

Figure C-3 Volume Fractions for Each Basis

The coated fiber sorbent basis defines fractions based on a fiber sorbent including an impermeable (coated) layer, but again excluding the bore volumes. Since the impermeable layer does not contribute sorption capacity of a fiber sorbent module, the volume of the impermeable layer reduces volumetric sorption capacity of a fiber sorbent module.

It is important to distinguish the volume of the impermeable layer ***in the module***. As mentioned in Chapter 5, there are two approaches; dual layer spinning and post treatment. Thickness of the impermeable layer (or sheath layer, coated layer), l_{ct}, is usually determined by SEM imaging. The impermeable layer around a fiber sorbent was assumed as dense layer without void spaces. For

simplicity, it was assumed that mass transfer was prevented at the external surface of fiber sorbents without any impermeable layers (l_{ct} = 0 μm) for this simplified modeling. For further dynamic analysis in Chapter 6, actual thickness was applied. In the module itself, it is important to recognize that no void volume exits since the interfiber sorbent space is filled with heat moderating phase change material (typically a custom selected wax).

The fiber sorbent module basis defines fractions based on multiple fiber sorbents in a module, which is corresponding to packed bed basis. Two parameters beyond the packing, bore-side and shell-side void fractions for a fiber sorbent module, ϕ_m, ε_{mb} and ε_{ms}, in Equation (C.35) can be varied independently by changing outer and inner (bore) diameters of the fiber sorbent, d_f and d_{fb}, and number of fiber sorbents, n_f. On the other hand, packing and void fractions for a packed bed, ϕ_b and ε_b, are correlated to each other and mainly depend on shape of materials. Spherical pellets in a packed bed give typically ε_b = 0.4 [3]. For the conversion between weight and volume fractions in this basis, weight of gas which is filled in void spaces can be neglected since that is very small compared with weight of the solid phase. Corresponding with the $n_{f,max}$, maximum packing fraction, $\phi_{m,max}$, and maximum bore-side void fraction, $\varepsilon_{mb,max}$, were widely varied with the d_{fb} as described in Figure C-4 as an example case when d_f = 800 μm, d_m = 20 cm and l_{ct} = 0. For desired separation performances, those parameters need to be optimized systematically. All variables and parameters used in this modeling are correlated with each other and one must confirm whether other conditions were satisfied or not whenever one of key parameters has been changed.

As noted above, the final item in Figure C-3 considers the overall module. In this case, the overall fiber sorbent module basis defines fractions based on multiple fiber sorbents in a module with paraffin wax filling in the shell side of the module. Volume fractions do not changes except

volume fraction of the wax, ϕ_x, is the same as the shell-side void fraction, ε_{ms}, as defined in Equation (C.53). Weight fractions change since density of the wax contributes largely compared to the fiber sorbent module basis without paraffin wax.

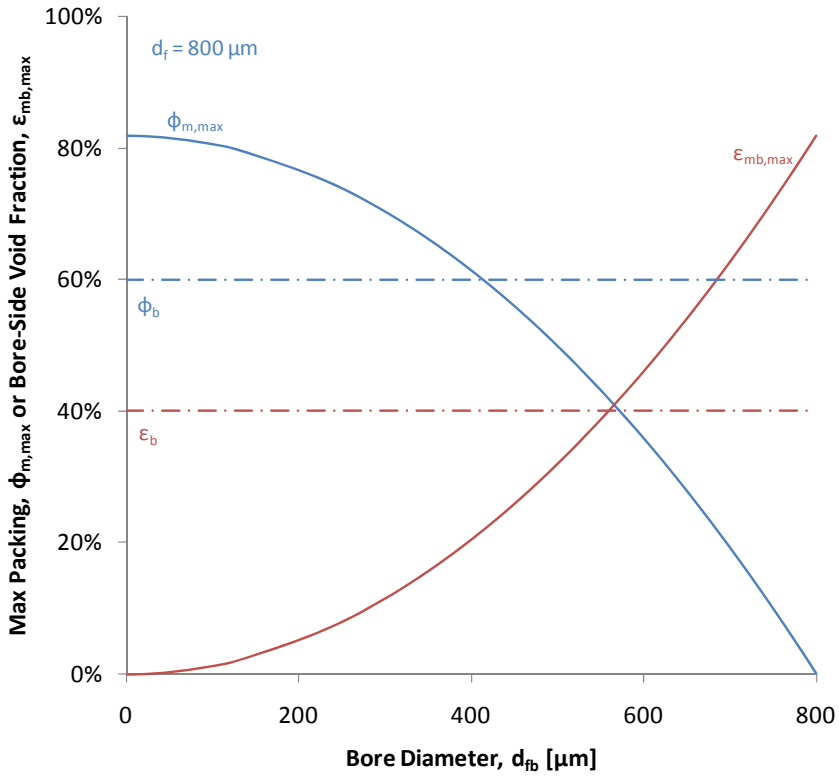

Figure C-4 Maximum Packing and Bore-Side Void Fractions with Varied Bore Diameter

Table C-3 Weight and Volume Fractions for a Fiber Sorbent

Basis	**Weight Fraction, ω**	**Volume Fraction, ϕ**	Key Relationship
Fiber Sorbent Solid Phase Basis (excluding pores)	$\omega_{c0} + \omega_{pm0} = 1$ .....(C.8)	$\phi_{c0} + \phi_{pm0} = 1$ .....(C.9)	$\phi_{c0} = \dfrac{\dfrac{\rho_c}{\omega_{c0}}}{\dfrac{\rho_c}{\omega_{c0}} + \dfrac{\rho_{pm}}{\omega_{pm0}}}$ .....(C.10)
Bare Fiber Sorbent Basis (including pores)	$\omega_c + \omega_{pm} \simeq 1$ .....(C.11) $\omega_c \simeq \omega_{c0}$ .....(C.12) $\omega_{pm} \simeq \omega_{pm0}$ .....(C.13)	$\varepsilon_f + \phi_f = 1$ .....(C.14) $\phi_f = \phi_c + \phi_{pm}$ .....(C.15) $\phi_c = \phi_{c0}\phi_f$ .....(C.16) $\phi_{pm} = \phi_{pm0}\phi_f$ .....(C.17)	
Coated Fiber Sorbent Basis (with an Impermeable Layer)	$\omega_{f,bf} + \omega_{ct} \simeq 1$ .....(C.18) $\omega_{f,bf} \simeq \omega_{c,bf} + \omega_{pm,bf}$ .....(C.19) $\omega_{c,bf} \simeq (1-\omega_{ct})\omega_c$ .....(C.20) $\omega_{pm,bf} \simeq (1-\omega_{ct})\omega_{pm}$ .....(C.21)	$\phi_{bf} + \phi_{ct} = 1$ .....(C.22) $\phi_{bf} = \varepsilon_{f,bf} + \phi_{f,bf}$ .....(C.23) $\phi_{f,bf} = \phi_{c,bf} + \phi_{pm,bf}$ .....(C.24) $\varepsilon_{f,bf} = (1-\phi_{ct})\varepsilon_f$ .....(C.25) $\phi_{c,bf} = (1-\phi_{ct})\phi_c$ .....(C.26) $\phi_{pm,bf} = (1-\phi_{ct})\phi_{pm}$ .....(C.27)	$\phi_{ct} = \dfrac{d_{f+ct}^2 - d_f^2}{d_{f+ct}^2 - d_{fb}^2}$ .....(C.28) $\omega_{ct} = \dfrac{\rho_{ct}\phi_{ct}}{1+\rho_{ct}\phi_{ct}}$ .....(C.29)

ρ; density [kg/m^3], ε_f; porosity of a fiber sorbent [-]
d_{f+ct}, d_f and d_{fb}; outer (including an impermeable layer), outer and inner (bore) diameter of fiber sorbent [m]
subscript 0; for a solid phase basis, subscript c, pm and f; for zeolite crystals, polymer, and a bare fiber sorbent
subscript bf and ct; for a bare fiber sorbent and an impermeable (coated) layer

Table C-4 Weight and Volume Fractions for a Fiber Sorbent Module

Basis	**Weight Fraction, ω**	**Volume Fraction, ϕ**	Key Relationship
Fiber Sorbent Module Basis (without Paraffin Wax)	$\omega_{f,m} + \omega_{ct,m} \simeq 1$ .....(C.30) $\omega_{ct,m} \simeq \omega_{ct}$ .....(C.31) $\omega_{f,m} = \omega_{c,m} + \omega_{pm,m}$ .....(C.32) $\omega_{c,m} \simeq \omega_{c}$ .....(C.33) $\omega_{pm,m} \simeq \omega_{pm}$ .....(C.34)	$\phi_m + \varepsilon_{mb} + \varepsilon_{ms} = 1$ .....(C.35) $\phi_m = \phi_{bf,m} + \phi_{ct,m}$ .....(C.36) $\phi_{bf,m} = \varepsilon_{f,m} + \phi_{f,m}$ .....(C.37) $\phi_{f,m} = \phi_{c,m} + \phi_{pm,m}$ .....(C.38) $\varepsilon_{f,m} = \varepsilon_f \phi_{bf,m}$ .....(C.39) $\phi_{c,m} = \phi_c \phi_{bf,m}$ .....(C.40) $\phi_{pm,m} = \phi_{pm} \phi_{bf,m}$ .....(C.41)	$\varepsilon_{ms} = 1 - n_f \left(\frac{d_{f+ct}}{d_m} \right)^2$ ..... (C.42) $\varepsilon_{mb} = n_f \left(\frac{d_{fb}}{d_m} \right)^2$ ..... (C.43) $\phi_{ct,m} = \frac{n_f \left(d_{f+ct}^2 - d_f^2 \right)}{d_m^2}$ ..... (C.44) $\phi_{f,m} = \frac{n_f \left(d_f^2 - d_{fb}^2 \right)}{d_m^2}$ ..... (C.45)
Fiber Sorbent Module Basis (with Paraffin Wax)	$\omega_x + \omega_{f,x} + \omega_{ct,x} \simeq 1$ .....(C.46) $\omega_{f,x} = \omega_{c,x} + \omega_{pm,x}$ .....(C.47) $\omega_{ct,x} \simeq (1 - \omega_x) \omega_{ct,m}$ .....(C.48) $\omega_{c,x} \simeq (1 - \omega_x) \omega_{c,m}$ .....(C.49) $\omega_{pm,x} \simeq (1 - \omega_x) \omega_{pm,m}$ .....(C.50)	$\phi_m + \varepsilon_{mb} + \phi_x = 1$ .....(C.51) $\phi_x = \varepsilon_{ms}$ .....(C.52)	$\omega_x = \frac{\rho_x \phi_x}{1 + \rho_x \phi_x}$ ..... (C.53)

ρ; density [kg/m^3], ε_{ms} and ε_{mb}; shell- and bore-side void fraction [-], ε_f; porosity of a fiber sorbent [-], n_f; number of fiber sorbents [-]
d_{f+ct}, d_f and d_{fb}; outer (including an impermeable layer), outer and inner (bore) diameter of fiber sorbent [m]
subscript c, pm, f and x; for zeolite crystals, polymer, a bare fiber sorbent and wax
subscript bf and ct; for a bare fiber sorbent and an impermeable (coated) layer, subscript m and x; for a fiber sorbent module with and without wax

Table C-5 Weight and Volume Fractions for a Zeolite Pellet and for a Packed Bed

Basis	**Weight Fraction, ω**	**Volume Fraction, ϕ**	Key Relationship
Pellet Solid Phase Basis (excluding pores)	$\omega_{c0} + \omega_{bd0} = 1$ .....(C.54)	$\phi_{c0} + \phi_{bd0} = 1$ ..... (C.55)	$\phi_{c0} = \dfrac{\dfrac{\rho_c}{\omega_{c0}}}{\dfrac{\rho_c}{\omega_{c0}} + \dfrac{\rho_{bd}}{\omega_{bd0}}}$ ..... (C.56)
Pellet Basis (including pores)	$\omega_p = \omega_c + \omega_{bd} \simeq 1$ .....(C.57) $\omega_c \simeq \omega_{c0}$ .....(C.58) $\omega_{bd} \simeq \omega_{bd0}$ .....(C.59)	$\varepsilon_p + \phi_p = 1$ ..... (C.60) $\phi_p = \phi_c + \phi_{bd}$ ..... (C.61) $\phi_c = \phi_{c0}\phi_p$ ..... (C.62) $\phi_{bd} = \phi_{bd0}\phi_p$ ..... (C.63)	
Packed Bed Basis	$\omega_b = \omega_{c,b} + \omega_{bd,b} \simeq 1$ .....(C.64) $\omega_{c,b} \simeq \omega_c$ .....(C.65) $\omega_{bd,b} \simeq \omega_{bd}$ .....(C.66)	$\varepsilon_b + \phi_b = 1$ ..... (C.67) $\phi_b = \phi_{c,b} + \phi_{bd,b}$ ..... (C.68) $\varepsilon_{p,b} = \varepsilon_p\phi_b$ ..... (C.69) $\phi_{c,b} = \phi_c\phi_b$ ..... (C.70) $\phi_{bd,b} = \phi_{bd}\phi_b$ ..... (C.71)	

ρ; density [kg/m^3], ε_p; porosity of a zeolite pellet [-], ε_b; void fraction of a packed bed [-]
d_{f+ct}, d_f and d_{fb}; outer (including an impermeable layer), outer and inner (bore) diameter of fiber sorbent [m]
subscript 0; for a solid phase basis, subscript c, bd and p; for zeolite crystals, a binder material and a zeolite pellet

C.3. Operational Parameters

Volumetric flow rate, Q_V [m^3/s], space time, τ_u [s], and linear velocity (superficial velocity), u [m/s], were defined with regard to dimensional properties of a fiber sorbent module and a packed bed;

$$Q_V = uS_m \quad \text{.....(C.72)}$$

$$\tau_u = \frac{V_m}{Q_V}\left(=\frac{L}{u}\right) \quad \text{.....(C.73)}$$

where,

S_m; cross-sectional area of a fiber sorbent module or a packed bed [m^2]

V_m; volume of a fiber sorbent module or a packed bed [m^3]

L; length of a fiber sorbent and its module or bed depth of a packed bed [m]

C.4. Density and Heat Capacity of Materials

Densities, ρ [kg/m^3], and specific heat capacities of materials, c_p [J/kg/K] in this modeling are summarized in Table C-6. For the packed bed in the comparison, the zeolite pellet was assumed to contain the same zeolite used in the fiber sorbent with a binder material such as clay (Kaolin). For simplicity, the binder material was supposed to have the same density, ρ_{bd}, and heat capacity, $c_{p,bd}$, as those of CA, ρ_{pm} and $c_{p,pm}$.

In addition to paraffin wax for thermal moderation approach, polydimethylsiloxane (PDMS) was also assessed for the temperature increase, ΔT [K].

Table C-6 Densities and Thermal Properties of Materials

Material	ρ [g/cm^3]	c_p [kJ/kg/K]	References
Zeolite NaY	1.408 *	0.779	[4]
Cellulose Acetate	1.32	1.465	[5-6]
Paraffin Wax	0.8	2.0	[7-8]
PDMS	0.97	1.46	[9]
Steel (for Vessel)	7.83	0.465	[10]

* See Chapter 3, Section 3.2

Heat of adsorption is shown in the temperature-dependent parameter for sorption capacity and that of NaY for CO_2 is listed in Table 2-2. The wax melts slightly above operating temperature ($T_m \approx 60$ °C) and the latent heat of fusion (ΔH_{fus} = 189 kJ/kg) [11] was applied for the heat handling.

Combined with the volume fractions defined in Table C-3~Table C-5, apparent densities for different basis were also derived and summarized in Table C-7 and Table C-8. Note that weight of gas which is filled in the void spaces can be neglected since that is very small compared with weight of the solid phase.

Table C-7 Apparent Densities Defined for a Fiber Sorbent Module

Basis	**Apparent Density**	Key Relationship
Fiber Sorbent Solid Phase Basis (excluding pores)	$\rho_{f0} = \rho_{c,f0} + \rho_{pm,f0}$ ..... (C.74)	$\rho_{c,f0} = \phi_{c0}\rho_c$ .....(C.75) $\rho_{pm,f0} = \phi_{pm0}\rho_{pm}$ .....(C.76)
Bare Fiber Sorbent Basis (including pores)	$\rho_f \simeq \rho_{c,f} + \rho_{pm,f}$ ..... (C.77)	$\rho_{c,f} = \phi_c\rho_c$ .....(C.78) $\rho_{pm,f} = \phi_{pm}\rho_{pm}$ .....(C.79)
Coated Fiber Sorbent Basis (with Impermeable Layer)	$\rho_{cf} \simeq \rho_{ct,cf} + \rho_{c,bf} + \rho_{pm,bf}$ ..... (C.80)	$\rho_{ct,cf} = \phi_{ct}\rho_{ct}$ .....(C.81) $\rho_{c,bf} = \phi_{c,bf}\rho_c$ .....(C.82) $\rho_{pm,bf} = \phi_{pm,bf}\rho_{pm}$ .....(C.83)
Fiber Sorbent Module Basis (without Paraffin Wax)	$\rho_m \simeq \phi_m\rho_{cf} = \rho_{ct,m} + \rho_{c,m} + \rho_{pm,m}$ ..... (C.84)	$\rho_{ct,m} = \phi_{ct,m}\rho_{ct}$ .....(C.85) $\rho_{c,m} = \phi_{c,m}\rho_c$ .....(C.86) $\rho_{pm,m} = \phi_{pm,m}\rho_{pm}$ .....(C.87)
Fiber Sorbent Module Basis (with Paraffin Wax)	$\rho_{m,x} \simeq \phi_m\rho_{cf} + \phi_x\rho_x$ ..... (C.88)	$\rho_{ct,m} = \phi_{ct,m}\rho_{ct}$ .....(C.89) $\rho_{c,m} = \phi_{c,m}\rho_c$ .....(C.90) $\rho_{pm,m} = \phi_{pm,m}\rho_{pm}$ .....(C.91)

ϕ; volume fraction [-], ρ; density [kg/m^3]
subscript 0, f, cf, m and x; for a solid phase, a bare fiber sorbent, a fiber sorbent including an impermeable (coated) layer, a fiber sorbent module with and without paraffin wax
subscript c, pm, and ct; for zeolite crystals, polymer, and an impermeable (coated) layer

Table C-8 Apparent Densities Defined for a Packed Bed

Basis	**Apparent Density**	Key Relationship
Pellet Solid Phase Basis (excluding pores)	$\rho_{p0} = \rho_{c,p0} + \rho_{bd,p0}$ ..... (C.92)	$\rho_{c,p0} = \phi_{c0}\rho_c$ .....(C.93) $\rho_{bd,p0} = \phi_{bd0}\rho_{bd}$ .....(C.94)
Pellet Basis (including pores)	$\rho_p \simeq \rho_{c,p} + \rho_{bd,p}$ ..... (C.95)	$\rho_{c,p} = \phi_c\rho_c$ .....(C.96) $\rho_{bd,p} = \phi_{bd}\rho_{bd}$ .....(C.97)
Packed Bed Basis	$\rho_b \simeq \phi_b\rho_p = \rho_{c,b} + \rho_{bd,b}$ ..... (C.98)	$\rho_{c,b} = \phi_{c,b}\rho_c$ .....(C.99) $\rho_{bd,b} = \phi_{bd,b}\rho_{bd}$ .....(C.100)

ϕ; volume fraction [-], ρ; density [kg/m^3]
subscript 0, p and b; for a solid phase, a zeolite pellet and a packed bed
subscript c and bd; for zeolite crystals and a binder material

C.5. Transport and Physical Properties of Gas

C.5.1. Molecular Weight and Lennard-Jones Parameters

Molecular weight, M [kg/mol], and Lennard-Jones parameters (collision diameter, σ [m], and energy parameter, ϵ/k_B [K]) of hydrogen and CO_2 are summarized in Table C-9 and were applied to predict physical and transport properties of the mixed gas in the following sections. Data for He is also listed since it was used in the experiment instead of H_2 as a surrogate gas.

Table C-9 Molecular Weight and Lennard-Jones Parameters of Gases

Gas		M [g/mol]	σ [Å]	ϵ/k_B [K]
Hydrogen	H_2	2.016	2.915	38.0
Carbon Dioxide	CO_2	44.01	3.996	190
Helium	He	4.003	2.576	10.22

Extracted from [12]

C.5.2. Concentration, Density and Composition

Mixed gas in this modeling is an ideal mixture of ideal gases [13-14] and concentration, C_i [mol/m^3], partial pressure, p_i [Pa], composition, y_i [-], of each component and density of mixed gas, ρ_g [kg/m^3], were described as;

$$C_i = \frac{p_i}{R_g T_g} \quad \text{.....(C.101)}$$

$$p_i = y_i p \quad \text{(C.102)}$$

$$y_1 + y_2 = 1 \quad \text{(C.103)}$$

$$\rho_g = \frac{\left(y_1 M_1 + y_2 M_2\right) p}{R_g T_g} \quad \text{(C.104)}$$

where,

subscript 1; for H_2

subscript 2; for CO_2

p; total pressure [Pa]

R_g; gas constant (= 8.314472 J/mol/K)

T_g; gas temperature [K]

C.5.3. Viscosity

Viscosity of single gas, μ_i [Pa·s], was estimated simply based on the kinetic molecular theory [15];

$$\mu_i = 8.4411 \times 10^{-25} \frac{\sqrt{M_i T_g}}{\sigma_i^2 \Omega_{\mu i}} \quad \text{(C.105)}$$

where,

M_i; molecular weight of Component i [kg/mol]

T_g; gas temperature [K]

σ_i; Lennard-Jones collision diameter of Component i (Table C-9) [m]

$\Omega_{\mu i}$; collision integral for viscosity [-]

Note that the coefficient was converted into SI units.

Collision integral for viscosity of single gas, $\Omega_{\mu i}$ [-], was estimated by [15];

$$\Omega_{\mu i} = \frac{1.16145}{\left(k_B T_g / \epsilon_i\right)^{0.14874}} + \frac{0.52487}{\exp\left(0.7732 k_B T_g / \epsilon_i\right)} + \frac{2.16178}{\exp\left(2.43787 k_B T_g / \epsilon_i\right)} \quad \text{.....(C.106)}$$

where,

ϵ_i/k_B; Lennard-Jones energy parameter of Component i (Table C-9) [K]

Then, viscosity of mixed gas, μ_g [Pa·s], was estimated [15];

$$\mu_g = \sum_i \frac{y_i \mu_i}{\sum_j y_j \Phi_{ij}} \quad \text{.....(C.107)}$$

$$\Phi_{ij} = \frac{1}{\sqrt{8\left(1 + M_i / M_j\right)}} \left\{ 1 + \left(\frac{\mu_i}{\mu_j} \right)^{1/2} \left(\frac{M_j}{M_i} \right)^{1/4} \right\}^2 \quad \text{.....(C.108)}$$

$$\Phi_{11} = \Phi_{22} = 1 \quad \text{.....(C.109)}$$

where,

μ_i; viscosity of Component i [Pa·s]

y_i; composition of Component i [mol%]

Φ_{ij}; dimensionless quantities defined in Equation (C.105)

The calculated values of Equations (C.105) ~ (C.109) at the feed gas conditions (Table C-1) were in Table C-10.

Table C-10 Viscosity of Single Gases at the Feed Gas Conditions

	Ω_μ [-]	μ_i [μPa·s]	Φ_{12} [-]	Φ_{21} [-]
H_2	0.8415	9.675	2.447	0.1900
CO_2	1.234	16.40	-	-
He	0.6917	21.24	3.195	0.2244

For the mixed gas of H_2/CO_2 at 333.15 K, Equation (C.107) became;

$$\mu_g\,[\mu\text{Pa}\cdot\text{s}] = \frac{y_1\mu_1}{y_1 + y_2\Phi_{12}} + \frac{y_2\mu_2}{y_1\Phi_{21} + y_2} = \frac{9.675(1-y_2)}{1+1.447y_2} + \frac{16.40y_2}{0.19+0.81y_2} \quad \text{.....(C.110)}$$

Then, μ_g = 15.77 μPa·s at y_2 = 0.25.

C.5.4. Diffusivity

In this modeling, both molecular and Knudsen diffusions contribute to the mass transfer through porous material. Discussion on diffusivity through porous media is described elsewhere [16-20]. Molecular diffusivity in bulk gas, D_M [m^2/s], was calculated based on binary diffusion;

$$D_M = 5.9543\times10^{-24}\sqrt{T_g^3\left(\frac{1}{M_1}+\frac{1}{M_2}\right)}\frac{1}{p\sigma_{12}^2\Omega_D} \quad \text{.....(C.111)}$$

$$\sigma_{12} = \left(\sigma_1 + \sigma_2\right)/2 \quad \text{.....(C.112)}$$

where,

subscript 1; for H_2

subscript 2; for CO_2

M_i; molecular weight of Component i [kg/mol]

p; total pressure [Pa]

T_g; gas temperature [K]

σ_{12}; average Lennard-Jones collision diameter [m]

$\Omega_{\mu i}$; collision integral for diffusivity [-]

Note that the coefficient was converted into SI units.

Collision integral for diffusivity, Ω_D [-], was estimated by [16];

$$\Omega_D = \frac{1.06036}{\left(k_B T_g / \epsilon_{12}\right)^{0.15610}} + \frac{0.19300}{\exp\left(0.47635 k_B T_g / \epsilon_{12}\right)} + \frac{1.03587}{\exp\left(1.52996 k_B T_g / \epsilon_{12}\right)} + \frac{1.76474}{\exp\left(3.89411 k_B T_g / \epsilon_{12}\right)} \quad \text{(C.113)}$$

$$\epsilon_{12} = \sqrt{\epsilon_1 \epsilon_2} \quad \text{(C.114)}$$

where,

ϵ_{12}/k_B; average Lennard-Jones energy parameter [K]

The calculated values of Equations (C.111) ~ (C.114) at the feed gas conditions (Table C-1) are in Table C-11.

Table C-11 Molecular Diffusivity of Mixed Gases at the Feed Gas Conditions

Mixed Gas	σ_{12} [Å]	ϵ_{12}/k_B [K]	Ω_D [-]	D_M [m^2/s]
$H_2 - CO_2$	3.456	84.97	0.8891	9.820×10^{-6}
$He - CO_2$	3.286	44.07	0.7785	8.992×10^{-6}

Knudsen diffusivity, D_K [m^2/s] was calculated as follows:

$$D_K = \frac{d_{pore}}{3}\sqrt{\frac{8R_gT_g}{M_2}} = 1.534 d_{pore}\sqrt{\frac{T_g}{M_2}} \quad \text{.....(C.115)}$$

where,

d_{pore}; pore size (diameter) [m]

M_2; molecular weight of Component 2 (CO_2) [kg/mol]

R_g; gas constant (= 8.314472 J/mol/K)

T_g; gas temperature [K]

Note that the coefficient was converted into SI units.

Combined diffusivity, D_{MK} [m^2/s], in the range under both molecular and Knudsen diffusion was applied for effective diffusivity used for the intrafiber and intraparticle mass transfer coefficients:

$$\frac{1}{D_{MK}} = \frac{1}{D_M} + \frac{1}{D_K} \quad \text{.....(C.116)}$$

There are three possible diffusion paths between external surface and zeolite crystals in the fiber sorbent; (1) diffusion in pores, (2) diffusion in polymer matrix and (3) diffusion in both pores and polymer matrix. For typical zeolite pellet, binder materials do not allow diffusion inside and gas molecules pass only through pores. However, CO_2 is generally sorbed and diffuses inside polymers. However, the diffusivity of CO_2 through CA, D_{pm}, is 8.287 x 10^{-13} m^2/s based on permeability and sorption capacity data [5] and significantly slower than diffusion through pores. Dimensionless sorption equilibrium constant of CO_2 for CA is also low (Chapter 2, Section 2.3). On the other hand, the D_K became 2.669 x 10^{-5} m^2/s at 333.15 K and was comparable to the D_M when the d_{pore} = 200 nm. Therefore, diffusion through the polymer matrix phase in the fiber sorbents was negligible.

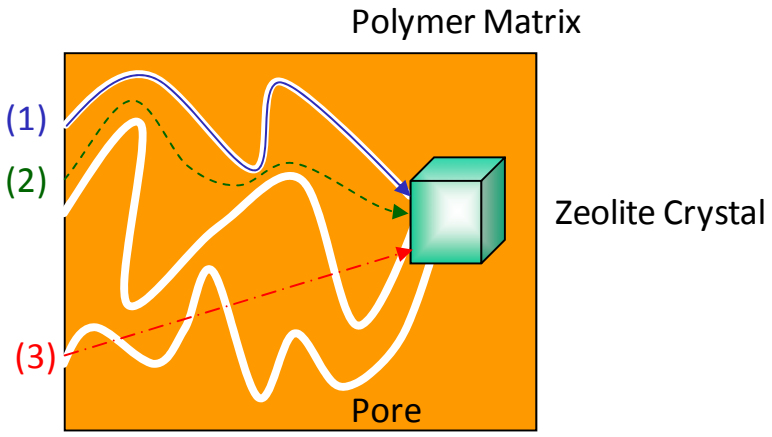

Figure C-5 Possible Diffusion Paths in Fiber Sorbents

Then, effective diffusivity, $D_{e,f}$ [m^2/s] was simply defined as;

$$D_{e,f} = \frac{\varepsilon_f}{\tau_f} D_{MK} \quad \text{.....(C.117)}$$

where,

D_{MK}; combined diffusivity of molecular and Knudsen diffusion [m^2/s]

ε_f; porosity of fiber sorbent

τ_f; yortuosity of fiber sorbent [-]

Tortuosity for diffusion through pores, τ_f, was assumed as the reciprocal of the porosity, ε_f [21].

$$\tau_f = \frac{1}{\varepsilon_f} \quad \text{.....(C.118)}$$

The calculated values of Equations (C.111), (C.115) ~ (C.117) at the feed gas conditions (Table C-1) are in Table C-12.

Table C-12 Effective Diffusivity through the Fiber Sorbent at the Feed Gas Conditions

Mixed Gas	D_M [m^2/s]	D_K [m^2/s]	D_{MK} [m^2/s]	D_{ef} [m^2/s]
H_2 - CO_2	9.820×10^{-6}	2.669×10^{-5}	7.179×10^{-6}	7.818×10^{-7}
He - CO_2	8.992×10^{-6}	2.669×10^{-5}	6.726×10^{-6}	7.325×10^{-7}

C.5.5. Heat Capacity

Molar heat capacity of single gas, c_{pmi} [J/mol/K], was estimated as a function of gas temperature and summarized in Table C-13 [22-23];

Table C-13 Temperature-Dependent Molar Heat Capacity

	c_{pmi} [J/mol/K]
H_2	$(3.249 + 0.422 \times 10^{-3} T_g + 0.083 \times 10^5 / T_g^2) R_g$ ..... (C.119)
CO_2	$(5.457 + 1.045 \times 10^{-3} T_g - 1.157 \times 10^5 / T_g^2) R_g$ ..... (C.120)
He	$2.5 R_g$ ..... (C.121)

T_g; gas temperature [K], R_g; gas constant (= 8.314472 J/mol/K)

Then, specific heat capacity of mixed gas, c_{pg} [J/kg/K], was obtained;

$$c_{pg} = \frac{\sum_i y_i c_{pmi}}{\sum_i y_i M_i} \quad \text{.....(C.122)}$$

where,

y_i; composition of Component i [mol%]

M_i; molecular weight of Component i [kg/mol]

c_{pmi}; molar heat capacity [J/mol/K]

C.5.6. Thermal Conductivity

Based on the kinetic molecular theory [24], thermal conductivity of single gas, κ_i [W/m/K], was derived by applying molar heat capacity and viscosity;

$$\kappa_i = \left(c_{pmi} + \frac{5}{4} R_g \right) \frac{\mu_i}{M_i} \quad \text{.....(C.123)}$$

where,

c_{pmi}; molar heat capacity [J/mol/K]

R_g; gas constant (= 8.314472 J/mol/K)

μ_i; viscosity of Component i [Pa·s]

M_i; molecular weight of Component i [kg/mol]

Thermal conductivity of mixed gas, κ_g [W/m/K], was calculated in the same manner for viscosity of mixed gas;

$$\kappa_g = \sum_i \frac{y_i \kappa_i}{\sum_j y_j \Phi_{ij}} \quad \text{.....(C.124)}$$

where,

κ_i; thermal conductivity of Component i [Pa·s]

y_i; composition of Component i [mol%]

Φ_{ij}; dimensionless quantities defined in Equation (C.105)

The calculated values of Equations (C.119) ~ (C.121) and (C.123) at the feed gas conditions (Table C-1) are in Table C-14.

Table C-14 Thermal Properties of Single Gases at at the Feed Gas Conditions

	c_{pm}/ R_g [-]	κ [mW/m/K]
H_2	3.464	194.4
CO_2	4.763	11.36
He	2.5	77.89

For the mixed gas of H_2/CO_2 at 333.15 K, Equations (C.122) and (C.124) became;

$$c_{pg}\left[\frac{\text{kJ}}{\text{kg}\cdot\text{K}}\right]=\frac{3.464+1.299y_2}{2.016+41.99y_2}R_g \quad \text{.....(C.125)}$$

$$\kappa_g\left[\frac{\text{mW}}{\text{m}\cdot\text{K}}\right]=\frac{y_1\kappa_1}{y_1+y_2\Phi_{12}}+\frac{y_2\kappa_2}{y_1\Phi_{21}+y_2}=\frac{194.4(1-y_2)}{1+1.447y_2}+\frac{11.36y_2}{0.19+0.81y_2} \quad \text{.....(C.126)}$$

Then, c_{pg} = 2.517 kJ/kg/K and κ_g = 114.3 mW/m/K at y_2 = 0.25.

C.6. Intracrystalline Diffusivity

There are several discussions around intracrystalline diffusivity, D_c. Some reported diffusivity of CO_2 for faujasite-type zeolites are summarized in Table C-15. Currently different types of experimental methods were applied to measure the intracrystalline diffusivity based on macroscopic or microscopic approaches at non-equilibrium or equilibrium [25]. There is huge discrepancy and not determined conclusively. In this modeling, 1 x 10^{-10} m^2/s was assumed for the CO_2-NaY system.

Time constant, τ_c [s], is a characteristic number to judge the magnitude of the intracrystalline diffusivity.

$$\tau_c=\frac{\left(\frac{d_c}{2}\right)^2}{D_c} \quad \text{.....(C.127)}$$

where,

d_c; diameter of a zeolite crystal [m]

D_c; intracrystalline diffusivity of CO_2 for zeolite NaY [m^2/s]

Table C-15 Intracrystalline Diffusivity of CO_2 for Faujasite-Type Zeolites

Method	T_g [K]	D_c [m^2/s]	References
CO_2-NaY			
Uptake	323	$0.91\sim10.83 \times 10^{-17}$	[26]
Chromatographic	333	1.1×10^{-16} **	[27]
QENS *	300	$2\sim0.2 \times 10^{-8}$	[28]
CO_2-NaX (CO_2-13X)			
Uptake	343	1.14×10^{-14}	[29]
Frequency Response	302	$3.4\sim43 \times 10^{-10}$	[30]
Frequency Response	373	$1.8\sim6.4 \times 10^{-15}$	[31]
QENS	300	$1.5\sim0.15 \times 10^{-8}$	[28]
CO_2-CaX			
Uptake	313	5.6×10^{-16} ***	[32]

* Quasi-Elastic Neutron Scattering

** Calculated for T = 333 K and d_c = 500 nm

*** Corrected diffusivity calculated for d_c = 500 nm

Pore size of NaY is 7.4 Å and the Knudsen diffusivity of CO_2 at the feed gas condition for the zeolitic pore was close to 10^{-7} m^2/s. Therefore, actual diffusivity should be slower than this value because attraction forces from the zeolite surface drag the CO_2 molecules. The time constants for d_c = 500 nm were 0.625μs and 0.625 ms for $D_c = 10^{-7}$ and 10^{-10} m^2/s, respectively. Compared with

the intrafiber/intraparticle mass transfer resistance, the time constants for intracrystalline diffusion were very small. The assumption of $D_c = 10^{-10}$ m^2/s is acceptable.

C.7. Pressure Drop

The flow inside of each fiber sorbent was assumed as an analogy to a flow through a pipe to predict pressure. Hagen-Poiseuille equation is generally applicable to laminar flow [33];

$$\left(\Delta p\right)_f = 32\frac{\mu_g u L}{\varepsilon_{mb} d_{fb}^2} \quad \text{.....(C.128)}$$

where,

$(\Delta p)_f$; pressure drop for a fiber sorbent module [Pa]

μ_g; viscosity of mixed gas [Pa·s]

u; linear velocity (superficial velocity) [m/s]

L; length of a fiber sorbent module [m]

ε_{mb}; bore-side void fraction of a fiber sorbent module [-]

d_{fb}; inner (bore) diameter of a fiber sorbent [m]

For packed bed, Ergun's equation is widely accepted [34];

$$\left(\Delta p\right)_p = \frac{1-\varepsilon_b}{\varepsilon_b^3}\left\{150\frac{\left(1-\varepsilon_b\right)\mu_g}{\rho_g u d_p} + 1.75\right\}\frac{L}{d_p}\rho_g u^2 \quad \text{.....(C.129)}$$

where,

$(\Delta p)_p$; pressure drop for a packed bed [Pa]

ε_b; void fraction of a packed bed [-]

ρ_g; density of mixed gas [kg/m^3]

μ_g; viscosity of mixed gas [Pa·s]

u; linear velocity (superficial velocity) [m/s]

d_p; diameter of a zeolite pellet [m]

L; bed depth of a packed bed [m]

C.8. Mass Transfer

C.8.1. Mass Transfer Area

Mass transfer area per module volume or bed volume is defined by geometry and volume packing fraction of materials. Mass transfer area for fiber sorbents in a module, a_f [m^2/m^3];

$$a_f = n_f \frac{A_f}{V_f} = \frac{4d_{fb}}{d_f^2 - d_{fb}^2} \phi_{bf,m} \quad \text{(C.130)}$$

where,

n_f; number of fiber sorbents [-]

A_f; mass transfer area for a (bare) fiber sorbent [m^2]

V_f; volume of a fiber sorbent [m^3]

d_f; outer diameter of a (bare) fiber sorbent [m]

d_{fb}; inner (bore) diameter of a (bare) fiber sorbent [m]

$\phi_{bf,m}$; packing fraction of (bare) fiber sorbents in a module [-]

This area is identical to the heat transfer area used in Eqs (4·6) and (4·8).

$$a_p = \frac{6}{d_p}\phi_b \quad \text{(C.131)}$$

where,

d_p; diameter of a zeolite pellet [m]

ϕ_b; packing fraction of a packed bed [-]

Mass transfer areas for zeolite crystals within fiber sorbents in a module and within zeolite pellets in a packed bed, a_c [m^2/m^3], are described;

$$a_{c,f} = \frac{6}{d_c}\phi_{c,m} \quad \text{(C.132)}$$

$$a_{c,p} = \frac{6}{d_c}\phi_{c,b} \quad \text{(C.133)}$$

where,

d_c; diameter of a zeolite crystal [m]

$\phi_{c,m}$; packing fraction of zeolite crystals in a fiber sorbent module [-]

$\phi_{c,b}$; packing fraction of zeolite crystals in a packed bed [-]

C.8.2. Mass Transfer Coefficient

With the same concept of a flow through a pipe, mass transfer coefficient through external film for each fiber sorbent was predicted by [35];

$$Sh_f = 1.62Gz_{M0}^{1/3} = 1.495Gz_M^{1/3} \quad \text{(C.134)}$$

$$Sh_f = \frac{k_{f,f} d_{fb}}{D_M} \quad \text{(C.135)}$$

$$Gz_{M0} = \frac{\pi d_{fb}^2 v}{4 D_M L} \quad \text{(C.136)}$$

$$Gz_M = \frac{d_{fb}^2 v}{D_M L} \quad \text{(C.137)}$$

where,

Sh_f; Sherwood number for a fiber sorbent [-]

Gz_{M0}; Graetz number for mass transfer (with $\pi/4$) [-]

Gz_M; Graetz number for mass transfer (without $\pi/4$) [-]

$k_{f,f}$; external mass transfer coefficient for a fiber sorbent [m/s]

d_{fb}; inner (bore) diameter of a fiber sorbent [m]

v; interstitial velocity [m/s]

D_M; molecular diffusivity in bulk gas [m^2/s]

L; length of a fiber sorbent module [m]

Note that the Graetz number is defined with or without the $\pi/4$ factor depending on the reference [36].

For a packed bed, the flowing empirical equation is proposed [37];

$$Sh_p = 2.0 + 1.1 Re_p^{0.6} Sc^{1/3} \quad \text{(C.138)}$$

$$Sh_p = \frac{k_{f,p} d_p}{D_M} \quad \text{(C.139)}$$

$$Re_p = \frac{\rho_g u d_p}{\mu_g} \quad \text{(C.140)}$$

$$Sc = \frac{\rho_g}{\mu_g D_M} \quad \text{.....(C.141)}$$

where,

Sh_p; Sherwood number for a packed bed [-]

Re_p; Reynolds number for a packed bed [-]

Sc; Schmidt number [-]

$k_{f,p}$; external mass transfer coefficient for a zeolite pellet [m/s]

d_p; diameter of a zeolite pellet [m]

D_M; molecular diffusivity in bulk gas [m^2/s]

ρ_g; density of mixed gas [kg/m^3]

u; linear velocity (superficial velocity) [m/s]

μ_g; viscosity of mixed gas [Pa·s]

Intrafiber and intraparticle mass transfer coefficients were predicted by applying linear driving force (LDF) approximation for specific geometries by Patton et al [38]. When diffusion only occurs from the bore side for the fiber sorbent modules, intrafiber mass transfer coefficient of a (bare) fiber sorbent, $k_{s,f}$ [m/s], was calculated by;

$$k_{s,f} = \frac{4\left(d_f - d_{fb}\right) D_{e,f}}{\left(d_f - d_{fb}\right)^2 - \left(\frac{1}{2} \frac{d_f^4 - d_{fb}^4}{d_f^2 - d_{fb}^2} - \frac{4 d_f}{3} \frac{d_f^3 - d_{fb}^3}{d_f^2 - d_{fb}^2} + d_f^2 \right)} \quad \text{.....(C.142)}$$

where,

d_f; outer diameter of a (bare) fiber sorbent [m]

d_{fb}; inner (bore) diameter of a fiber sorbent [m]

$D_{e,f}$; effective diffusivity for a (bare) fiber sorbent [m^2/s]

For spherical shape, intraparticle mass transfer coefficient for a zeolite pellet, $k_{s,p}$ [m/s], was given by [38];

$$k_{s,p} = \frac{10 D_{e,p}}{d_p} \quad \text{.....(C.143)}$$

where,

$k_{s,p}$; intraparticle mass transfer coefficient for a zeolite pellet [m/s]

d_p; diameter of a zeolite pellet [m]

$D_{e,p}$; effective diffusivity for a zeolite pellet [m^2/s]

The crystal shape of the zeolite NaY is cubic, but spherical geometry was assumed and the diameter, d_c = 500 nm. The intracrystalline mass transfer coefficient, k_c [m/s], was described for a sphere based on the LDF approximation;

$$k_c = \frac{10 D_c}{d_c} = 0.002 \text{ m/s} \quad \text{.....(C.144)}$$

where,

d_c; diameter of a zeolite crystal [m]

D_c; intracrystalline diffusivity of CO_2 for zeolite NaY [m^2/s]

As long as the same zeolite crystal is used for fiber sorbents and pellets, the intracrystalline mass transfer coefficient is clearly the same in the two formats.

C.9. Sorption Capacity

Sorption capacities of CO_2 to the CA and the NaY and fiber sorbents, which were applied, are summarized in Chapter 2, Section 2.3. Volumetric sorption capacity and dimensionless sorption equilibrium constant of a fiber sorbent module, $q_{V2,m}$ [mol/m_3] and K_m [m^3-gas/m^3-module], became;

$$q_{V2,m} = \phi_{bf,m} q_{V2,f} \quad \text{.....(C.145)}$$

$$K_m = \frac{q_{V2,m}}{C_2} = \phi_{bf,m}\left(\phi_c K_c + \phi_{pm} K_{pm}\right) \quad \text{.....(C.146)}$$

where,

$\phi_{bf,m}$; packing fraction of (bare) fiber sorbents in a module [-]

$q_{V2,f}$; sorption capacity of a (bare) fiber sorbent [mol/m_3]

C_2; concentration of Component 2 (CO_2) [mol/m^3]

ϕ_c; volume faction of zeolite crystals in a fiber sorbent [-]

ϕ_{pm}; volume faction of polymer in a fiber sorbent [-]

Volumetric sorption capacity and dimensionless sorption equilibrium constant for a zeolite pellet, $q_{V2,p}$ [mol/m^3] and K_p [m^3-gas/m^3-zeolite pellet], are described as;

$$q_{V2,p} = K_p C_2 \quad \text{.....(C.147)}$$

$$K_p = \varepsilon_p + \phi_c K_c + \phi_{bd} K_{bd} \quad \text{.....(C.148)}$$

where,

ε_p; porosity of zeolite pellet [-]

ϕ_c; volume faction of zeolite crystal in a zeolite pellet [-]

K_c; dimensionless sorption equilibrium constant for a zeolite crystal [m^3-gas/m^3-zeolite crystal]

ϕ_{bd}; volume faction of polymer in a binder material [-]

K_{bd}; dimensionless sorption equilibrium constant for a binder material [m^3-gas/m^3-binder material]

Binder material such as clay (Kaolin) is not capable adsorbing CO_2 [39], which means $K_{bd} = 0$ The $q_{V2,p}$ and the K_p were approximated;

$$q_{V2,p} \simeq \phi_c \rho_c q_c \quad \text{(C.149)}$$

$$K_p \simeq \phi_c K_c \quad \text{(C.150)}$$

Volumetric sorption capacity and dimensionless sorption equilibrium constant of a packed bed, $q_{V2,b}$ [mol/m_3] and K_b [m^3-gas/m^3-bed], became;

$$q_{V2,b} = \phi_b q_{V2,p} \quad \text{(C.151)}$$

$$K_b = \frac{q_{V2,b}}{C_2} = \phi_{c,b} K_c \quad \text{(C.152)}$$

C.10. Moments Analysis for Overall Mass Transfer Resistance

Overall mass transfer resistance, R_{MT}, for packed beds is derived based on moments analysis [40-41]. Overall mass transfer coefficient (or reciprocal of overall mass transfer resistance) is used in

the LDF model. The same concept was applied for fiber sorbent modules to calculate R_{MT}. First and second moments are defined as follows.

First moment (mean residence time), m_1 [s];

$$m_1 \equiv t_m \equiv \frac{\int_0^\infty C_2 t dt}{\int_0^\infty C_2 dt} = -\lim_{s\to 0} \frac{\partial \widetilde{C_2}}{\partial s} \frac{1}{C_{2\,fd}} \quad \text{.....(C.153)}$$

where,

t_m; mean residence time [s]

C_2; concentration of Component 2 (CO_2) [mol/m^3]

t; time [s]

$\widetilde{C_2}$; Laplace transform of C_2

C_{2fd}; feed concentration of Component 2 (CO_2) [mol/m^3]

s; Laplace variable [1/s]

Second moment (variance), m_2^2 [s^2];

$$m_2^2 \equiv \sigma_m^2 = \frac{\int_0^\infty C_2 \left(t - m_1\right)^2 dt}{\int_0^\infty C_2 dt} = -\lim_{s\to 0} \frac{\partial^2 \widetilde{C_2}}{\partial s^2} \frac{1}{C_{2\,fd}} - m_1^2 \quad \text{.....(C.154)}$$

where,

σ_m; standard deviation in residence time [s]

Equations (C.153) and (C.154) can be transformed into the following equations for packed beds [40-41];

$$m_1 = \frac{L}{v}\left\{1+\left(\frac{1-\varepsilon_b}{\varepsilon_b}\right)K_p\right\} = \frac{L}{u}\left\{\varepsilon_b + (1-\varepsilon_b)K_p\right\} \quad \text{.....(C.155)}$$

$$\frac{m_2^2}{2} = \frac{L}{v}\left[\left(\frac{D_{ax}}{v^2}\right)\left\{1+\left(\frac{1-\varepsilon_b}{\varepsilon_b}\right)K_p\right\}^2 + \frac{d_p}{6k_{f,p}}\left(\frac{1-\varepsilon_b}{\varepsilon_b}\right)K_p^2 + \frac{d_p^2}{60D_{p,e}}\left(\frac{1-\varepsilon_b}{\varepsilon_b}\right)K_p^2 + \frac{d_c^2}{60D_c}\left(\frac{1-\varepsilon_b}{\varepsilon_b}\right)(1-\varepsilon_p)\phi_c K_c\right] \quad \text{(C.156)}$$

where,

L; bed depth of a packed bed [m]

v; interstitial velocity [m/s]

u; linear velocity (superficial velocity) [m/s]

D_{ax}; diffusivity in axial direction [m^2/s]

ε_b; void fraction of a packed bed [-]

K_p; dimensionless sorption equilibrium constant for a zeolite pellet [m^3-gas/m^3-zeolite pellet]

d_p; diameter of a zeolite pellet [m]

$k_{f,p}$; external mass transfer coefficient for a zeolite pellet [m/s]

$D_{e,p}$; effective diffusivity for a zeolite pellet [m^2/s]

d_c; diameter of a zeolite crystal [m]

D_c; intracrystalline diffusivity of CO2 for zeolite NaY [m^2/s]

ε_p; porosity of zeolite pellet [-]

ϕ_c; volume faction of zeolite crystal in a zeolite pellet [-]

K_c; dimensionless sorption equilibrium constant for a zeolite crystal [m^3-gas/m^3-zeolite crystal]

Reduced second moment is shown as;

$$\frac{m_2^2}{2m_1^2} = \frac{L}{v}\left[\left(\frac{D_{ax}}{v^2}\right) + \frac{\frac{d_p}{6k_f}\left(\frac{1-\varepsilon_b}{\varepsilon_b}\right)K_p^2 + \frac{d_p^2}{60D_{p,e}}\left(\frac{1-\varepsilon_b}{\varepsilon_b}\right)K_p^2 + \frac{d_c^2}{60D_c}\left(\frac{1-\varepsilon_b}{\varepsilon_b}\right)\left(1-\varepsilon_p\right)\phi_c K_c}{\left\{1+\left(\frac{1-\varepsilon_b}{\varepsilon_b}\right)K_p\right\}^2}\right] \quad \text{(C.157)}$$

K_p for typical zeolites is greater than 1 significantly. For a typical bed void fraction, ε_b, the following relationship is obtained;

$$1+\left(\frac{1-\varepsilon_b}{\varepsilon_b}\right)K_p \simeq \left(\frac{1-\varepsilon_b}{\varepsilon_b}\right)K_p \quad \text{(C.158)}$$

Therefore, by applying Equations (C.131), (C.143), (C.144), (C.140) and (C.158), Equation (C.157) is simplified;

$$\frac{m_2^2}{2m_1^2} = \left(\frac{v}{L}\right)\left\{\left(\frac{D_{ax}}{v^2}\right)+\left(\frac{\varepsilon_b}{1-\varepsilon_b}\right)\left(\frac{d_p}{6k_{f,p}}+\frac{d_p^2}{60D_{p,e}}+\frac{d_c^2}{60K_{e,p}D_c}\right)\right\}$$
$$= \frac{1}{Pe}+\left(\frac{u}{L}\right)\left(\frac{1}{k_{f,p}a_p}+\frac{1}{k_{s,p}a_p}+\frac{1}{K_c k_c a_{c,p}}\right) \quad \text{(C.159)}$$

$$Pe = \frac{vL}{D_{ax}} \quad \text{(C.160)}$$

$$K_{e,p} \equiv \frac{K_p^2}{\phi_c K_c} = \phi_c K_c \quad \text{(C.161)}$$

where,

a_p; mass transfer area for zeolite pellets in a packed bed [m^2/m^3]

$k_{s,p}$; intraparticle mass transfer coefficient for a zeolite pellet [m/s]

k_c; intracrystalline mass transfer coefficient [m/s]

$a_{c,p}$; mass transfer area for zeolite crystals in a packed bed [m^2/m^3]

Pe; Peclet number [-]

$K_{e,p}$; effective dimensionless sorption equilibrium constant for a zeolite pellet [m^3-gas/m^3-zeolite pellet]

For the simplicity in discussion, the axial diffusion term was neglected, and Equation (C.159) was simplified further;

$$\frac{m_2^2}{2m_1^2} = \frac{u}{L} R_{MT,p} \quad \text{.....(C.162)}$$

$$R_{MT,p} = \frac{1}{k_{f,p} a_p} + \frac{1}{k_{s,p} a_p} + \frac{1}{K_c k_c a_{c,p}} \quad \text{.....(C.163)}$$

where,

$R_{MT,p}$; overall mass transfer resistance for a packed bed [s]

The first, second and third terms in right-hand side of Equation (C.163) are corresponding to external, intraparticle and intracrystalline mass transfer resistances for a packed bed, $R_{f,p}$, $R_{s,p}$ and $R_{c,p}$ [s], respectively, as discussed in Chapter 2, Section 2.5.

$$R_{f,p} = \frac{1}{k_{f,p} a_p} \quad \text{.....(C.164)}$$

$$R_{s,p} = \frac{1}{k_{s,p} a_p} \quad \text{.....(C.165)}$$

$$R_{c,p} = \frac{1}{K_c k_c a_{c,p}} \quad \text{.....(C.166)}$$

Applying this concept to fiber sorbent modules, Equation (C.163) can be replaced by;

$$R_{MT,f} = \frac{1}{k_{f,f} a_f} + \frac{1}{k_{s,f} a_f} + \frac{1}{K_{e,f} k_c a_{c,f}} \quad \text{.....(C.167)}$$

$$K_{e,f} \equiv \frac{K_f^2}{\phi_c K_c} = \frac{\left(\phi_c K_c + \phi_{pm} K_{pm}\right)^2}{\phi_c K_c} \quad \text{.....(C.168)}$$

where,

$R_{MT,f}$; overall mass transfer resistance for a fiber sorbent module [s]

$k_{f,f}$; external mass transfer coefficient for a (bare) fiber sorbent [m/s]

a_f; mass transfer area for fiber sorbents in a module [m^2/m^3]

$k_{s,f}$; intrafiber mass transfer coefficient for a zeolite pellet [m/s]

k_c; intracrystalline mass transfer coefficient [m/s]

$a_{c,f}$; mass transfer area for zeolite crystals in a fiber sorbent module [m^2/m^3]

$K_{e,f}$; effective dimensionless sorption equilibrium constant for a fiber sorbent [m^3-gas/m^3-fiber sorbent]

K_f; dimensionless sorption equilibrium constant for a (bare) fiber sorbent [m^3-gas/m^3-fiber sorbent]

ϕ_c; volume faction of zeolite crystal in a (bare) fiber sorbent [-]

K_c; dimensionless sorption equilibrium constant for a zeolite crystal [m^3-gas/m^3-zeolite crystal]

ϕ_{pm}; volume faction of polymer in a (bare) fiber sorbent [-]

K_{pm}; dimensionless sorption equilibrium constant for polymer [m^3-gas/m^3-polymer]

The height equivalent to a theoretical plate (HETP), H [m], is often referred for chromatographic separations and defined as;

$$H = \frac{m_2^2}{m_1^2} L \quad \text{.....(C.169)}$$

where,

m_1; the first moment[s]

m_2^2; the second moment (variance) [s^2]

L; length of a fiber sorbent and its module or bed depth of a packed bed [m]

From Equations (C.162) and (C.169),

$$H = 2uR_{MT} \quad \text{.....(C.170)}$$

where,

u; linear velocity (superficial velocity) [m/s]

R_{MT}; overall mass transfer resistance [s]

C.11. Breakthrough and Productivity

Breakthrough time is typically determined experimentally in laboratory scale because there are many factors to impact on the actual breakthrough. The data is used for the scale up with the concept of length of unused bed (LUB) [42-43]. The LUB is equivalent to a half of the mass transfer zone (MTZ) length, L_{MTZ} [m]. In this modeling for the proof of the concept of the fiber sorbents, the L_{MTZ} was estimated based on a simplified Rosen model for a breakthrough curve [44-45]. The Rosen model assumed a long column and a linear isotherm system.

$$L_{MTZ} \simeq 4\sqrt{uLR_{MT}} \quad \text{.....(C.171)}$$

where,

u; linear velocity (superficial velocity) [m/s]

L; length of a fiber sorbent and its module or bed depth of a packed bed [m]

R_{MT}; overall mass transfer resistance [s]

This equation could be derived from a concept that the chromatographic elution curve of CO_2 with NaY was simply approximated as a normal distribution and the leakage profile of CO_2 at breakthrough in the packed bed operation was assumed as the right-hand side of the normal distribution (Figure C-6). Three times of the reduced standard deviation of the residence time, σ_m/t_m, covers 99.7% of the breakthrough curve [46] and the L_{MTZ} was obtained with regard to the R_{MT};

$$\frac{L_{MTZ}}{L} = 3\frac{\sigma_m}{t_m} = 3\sqrt{\frac{2uR_{MT}}{L}} \simeq 4\sqrt{uLR_{MT}} \quad \text{.....(C.172)}$$

where,

t_m; mean residence time [s]

σ_m; standard deviation in residence time [s]

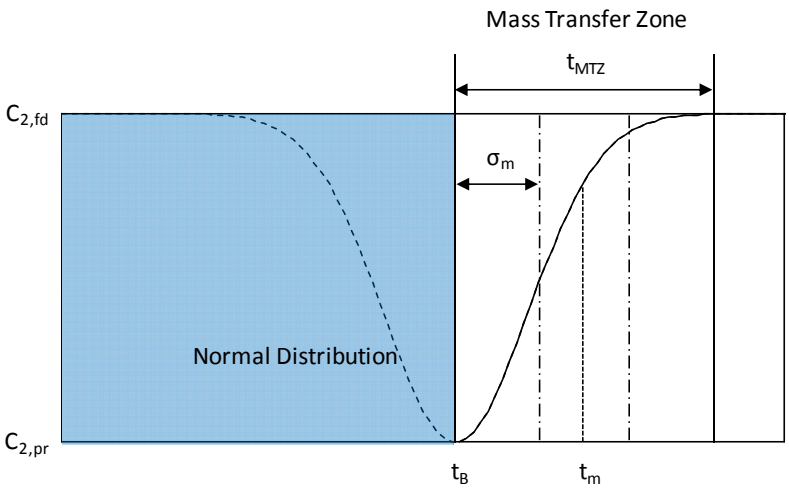

(a) Concentration Profile in Time Domain at Exit of Packed Bed (z = L)

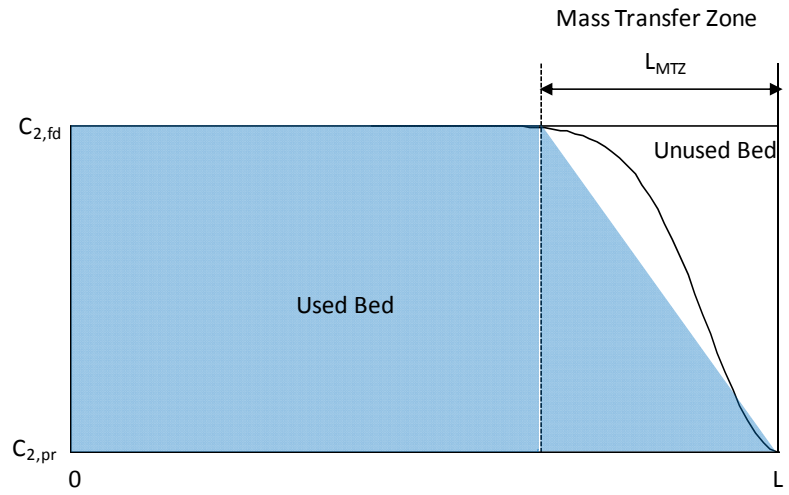

(b) Concentration Profile in Axial Direction at Breakthrough ($t = t_B$)

Figure C-6 Breakthrough Curve

From Equations (C.169) and (C.172), the relationship between the L_{MTZ} and the H was obtained;

$$L_{MTZ} = 3\sqrt{HL} \quad \text{.....(C.173)}$$

where,

H; height equivalent to a theoretical plate (HETP) [m]

L; length of a fiber sorbent and its module or bed depth of a packed bed [m]

To terminate the adsorption step with high purity of hydrogen as much as 99.99%, a half of the L_{MTZ} was assumed unavailable after the breakthrough in this modeling (Figure C-6), although breakthrough time, t_B [s], is determined typically at 5% leakage to the feed composition [47]. Utilization, U [-], was defined to express the amount of zeolite used in the adsorption step;

$$U = 1 - \frac{0.5 L_{MTZ}}{L} = 1 - 2\sqrt{\frac{R_{MT}}{\tau_u}} \quad \text{.....(C.174)}$$

where,

R_{MT}; overall mass transfer resistance [s]

τ_u; space time [s]

From Equation (C.174), the space time should be 4 times longer than the overall mass transfer resistance (of which unit is in time) in order to give positive U. Negative U means the mass transfer zone is longer than bed depth and leakage starts immediately after the adsorption step starts.

Operating capacity, $q_{V2,op}$ [mol/m^3], and the t_B were calculated by;

$$q_{V2,op} = U q_{V2,m} \quad \text{.....(C.175)}$$

$$t_B = \frac{q_{V2,op} L}{C_{2fd} u} = U K_{m,fd} \tau_u \quad \text{.....(C.176)}$$

where,

$q_{V2,m}$ (or $q_{V2,b}$); (volumetric) sorption capacity of a fiber sorbent module or a packed bed [mol/m^3]

C_{2fd}; feed concentration of Component 2 (CO_2) [mol/m^3]

$K_{m,fd}$ (or $K_{b,fd}$); dimensionless sorption equilibrium constant at feed conditions (Table C-1) [m^3-gas/m^3-module or bed]

For this modeling for the breakthrough, recovery was not considered as an entire PSA process which also must consider regeneration. Then, feed gas basis adsorbent productivity, $\eta_{p,fd}$ [kg-feed gas/kg-zeolite crystal/s], from Equation (B.48) was rewritten with $t_{cyc} = t_B$;

$$\eta_{p,fd} = \frac{\rho_g Q_{V,fd}}{\rho_c \phi_{c,m} V_m} \quad \text{.....(C.177)}$$

where,

ρ_g; density of mixed gas [kg/m^3]

$Q_{V,fd}$; volumetric flow rate of feed gas [m^3/s]

ρ_c; density of zeolite crystal [kg/m^3]

$\phi_{c,m}$ (or $\phi_{c,b}$); volume faction of zeolite crystals in a fiber sorbent or in a packed bed [-]

V_m; volume of a fiber sorbent module or a packed bed [m^3]

C.12. Temperature Increase – Adiabatic Case

The temperature increase due to heat of adsorption was assessed based on heat balance into the whole fiber sorbent module and the packed bed. In this simplified modeling, it was assumed that

heat transfer rate is very rapid to reach the equilibrium, and all physical property parameters were taken as constants.

Convective movement of thermal energy, Δh_g [J], was approximated;

$$\Delta h_g = \rho_{g,fd} c_{pg,fd} \left(T_{fd} - T_{pr} \right) Q_{V,fd} t_{II} \quad \text{(C.178)}$$

where,

subscript fd; at feed conditions (Table C-1)

ρ_g; density of mixed gas [kg/m^3]

c_{pg}; specific heat capacity of mixed gas [J/kg/K]

Q_V; volumetric flow rate of feed gas [m^3/s]

T_{fd}; temperature of feed gas [K]

T_{pr}; temperature of product gas [K]

t_{II}; time for Step II (Adsorption step) [s]

Note for this discussions, t_{II} = breakthrough time, t_B.

Accumulated thermal energy within a fiber sorbent module or a packed bed, Δh_s [J], including a stainless steel vessel (wall thickness, l_w = 1.5 mm) was;

$$\Delta h_s = \left\{ \left(\rho c_p \right)_m V_m + \rho_w c_{p,w} V_w \right\} \left(T_{fd} - T_{pr} \right) \quad \text{(C.179)}$$

$$V_w = \frac{\left(d_m + 2 l_w \right)^2}{4} L - V_m \quad \text{(C.180)}$$

where,

$(\rho c_p)_m$; apparent volumetric heat capacity of a fiber sorbent module or a packed bed [kg/m^3]

ρ_w; density of stainless steel [kg/m^3]

$c_{p,w}$; specific heat capacity of stainless steel [J/kg/K]

V_m; volume of a fiber sorbent module or a packed bed [m^3]

V_w; volume of a stainless steel vessel [m^3]

d_m; inner diameter of a stainless steel vessel [m]

L; length of a fiber sorbent and its module or bed depth of a packed bed [m]

Apparent volumetric heat capacity of a fiber sorbent module or a packed bed for each case in the comparison is summarized in Table C-16.

Table C-16 Apparent Volumetric Heat Capacity

	$(\rho c_p)_m$
Fiber Sorbent Module without Wax	$\rho_g \varepsilon_{mb} c_{pg} + \rho_c \phi_{c,m} c_{p,c} + \rho_{pm} \phi_{pm,m} c_{p,pm} + \rho_{ct} \phi_{ct,m} c_{p,ct} + \rho_s \varepsilon_{ms} c_{p,s}$.(C.181)
Fiber Sorbent Module with Wax	$\rho_g \varepsilon_{mb} c_{pg} + \rho_c \phi_{c,m} c_{p,c} + \rho_{pm} \phi_{pm,m} c_{p,pm} + \rho_{ct} \phi_{ct,m} c_{p,ct} + \rho_x \phi_x c_{p,x}$ ...(C.182)
Packed Bed	$\rho_g \varepsilon_b c_{pg} + \rho_c \phi_{c,b} c_{p,c} + \rho_{bd} \phi_{bd,b} c_{p,bd}$ .....(C.183)

ρ; density [kg/m^3], ε_{mb} and ε_{ms}; bore- and shell-side void fraction [-], ϕ; volume fraction [-], ε_b; void fraction of a packed bed
subscript c, pm, ct, s, x and bd; for zeolite crystals, polymer, impermeable (coated) layer, shell-side gas, paraffin wax and binder material

Generated heat due to heat of adsorption, Δh_{ads} [J], was;

$$\Delta h_{ads} = q_{V2,op} V_m \left(-\Delta H_{ads}\right) \quad \text{.....(C.184)}$$

where,

$q_{V2,op}$; (volumetric) operating capacity of a fiber sorbent module or a packed bed [mol/m^3]

$-\Delta H_{ads}$; heat of adsorption [J/mol]

Dissipated heat by fusion of paraffin wax, Δh_{fus} [J], was;

$$\Delta h_{fus} = \rho_x \phi_x V_m \left(-\Delta H_{fus}\right) \quad \text{(C.185)}$$

where,

ρ_x; density of paraffin wax [kg/m^3]

ϕ_x; volume fraction of paraffin wax (= ε_{ms}; shell-side void fraction of a fiber sorbent module) [-]

$-\Delta H_{fus}$; latent heat of adsorption [J/kg]

Heat balance for the fiber module became;

$$\Delta h_g + \Delta h_s + \Delta h_{ads} + \Delta h_{fus} = 0 \quad \text{(C.186)}$$

By applying the solver function of Microsoft® Office Excel® to solve Equation (C.179) for T_{pr} [K], the temperature increase, ΔT [K], was obtained;

$$\Delta T = T_{pr} - T_{fd} \quad \text{(C.187)}$$

For the packed bed, the dissipated heat in Equation (C.185) was not available ($\Delta h_{fus} = 0$). When PDMS was applied instead of paraffin wax for the thermal moderation, density and heat capacity data were changed accordingly and the latent heat of fusion was also neglected.

C.13. Results and Discussions

C.13.1. Base Case

Breakthrough time behavior for the base case (Table C-1) was discussed in Chapter 2, Section 2.5.

C.13.2. Effects of Key Parameters on the Breakthrough Time

In order to assess impact of several key parameters on the breakthrough behavior, one of the base conditions listed in Table C-1 was modified and compared with the base case.

C.13.2.1. Linear Velocity (Flow Rate)

Slower linear velocity (u = 20 cm/s) gave longer $t_{B,f}$ (Figure C-7) compared with the base case. Compared with the equivalent packed bed, the advantageous region, which was mentioned in the Chapter 2, Section 2.5, was observed as well as the base case, but the area was reduced. It indicates that the fiber sorbent module is advantageous when liner velocity or flow rate is high.

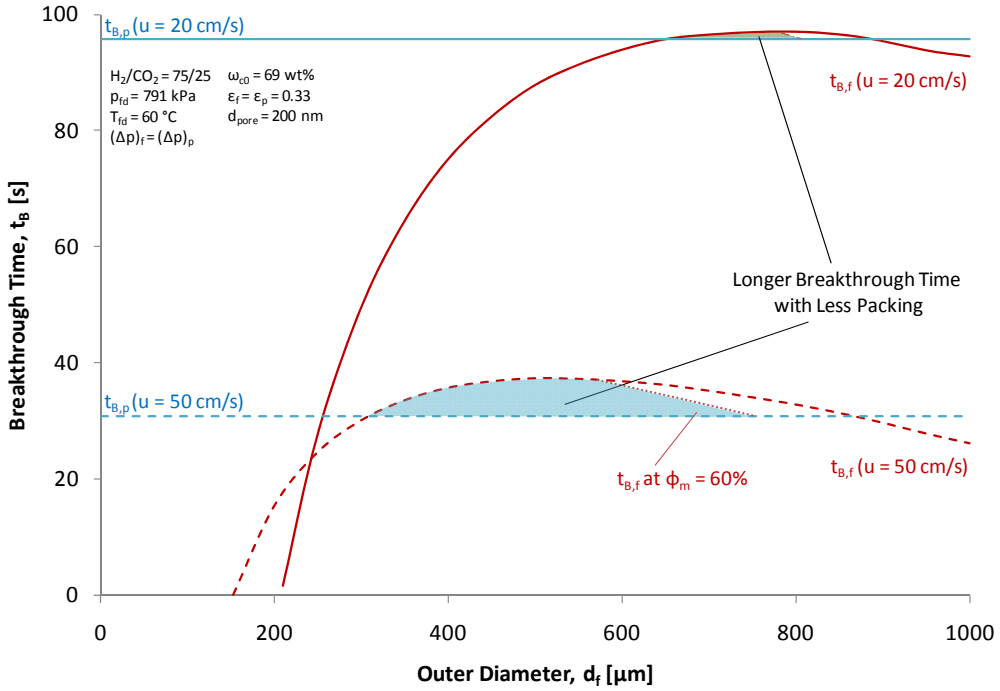

Figure C-7 Feed Linear Velocity Effect on Breakthrough Time

C.13.2.1. Feed Gas Conditions

Lower temperature, higher pressure and higher composition would give higher sorption capacity of the zeolite. The value of dimensionless sorption equilibrium constant of the zeolite, K_c, which was obtained from the sorption isotherm (Equation (2.10)), depends on the inlet molar concentration of CO_2 and temperature. Effect of feed gas conditions shown in Figure C-8 are corresponding to the K_c which are summarized in Table C-17, not simply on only one factor in the feed conditions which was changed. Higher K_c gave longer t_B. For example, lower feed pressure (lower sorption capacity) was anticipated shorter t_B, but gave longer t_B at maximum

point in Figure C-8 because of higher K_c. For all of the conditions applied here, there were the advantageous regions to show the longer $t_{B,f}$ with less packing compared to a packed bed.

Table C-17 Feed Gas Conditions and Sorption Capacities of Zeolite NaY

	p_{fd} [psig]	T_{fd} [°C]	y_{2fd} [-]	C_{2fd} [mol/m^3]	q_c [mol/kg]	K_c [m^3-gas/m^3-zeolite]
Base Case	100	60	0.25	71.4	4.63	91.4
Low T_{fd}	100	***35***	0.25	77.2	5.80	105.9
Low p_{fd}	***50***	60	0.25	40.3	3.78	132.3
High y_{2fd}	100	60	***0.50***	142.8	5.42	53.4

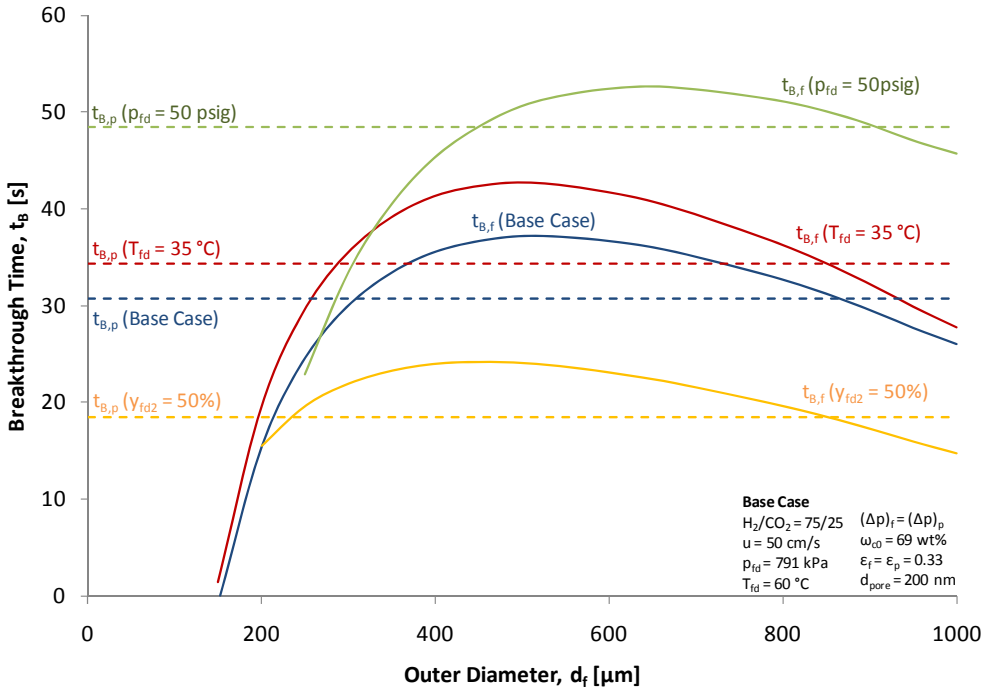

Figure C-8 Feed Gas Condition Effect on Breakthrough Time

C.13.2.2. Zeolite Loading

Higher zeolite loading (75 wt%) gave longer t_B compared with the base case (69 wt%) because of more sorption capacity of the fiber sorbent (Figure C-9). At the maximum of the t_B curve, the increase of t_B (8%) from the base case to the higher loading case was close to the increase of the zeolite loading. The comparison between the fiber sorbent module with less loading (69 wt%) and the packed bed with higher loading (75 wt%) showed 11% and 14% increase in the breakthrough time and adsorbent productivity, respectively. It indicated that dimensional and packing fraction conditions exist to achieve the same or longer t_B with the less loading by the fiber sorbent module.

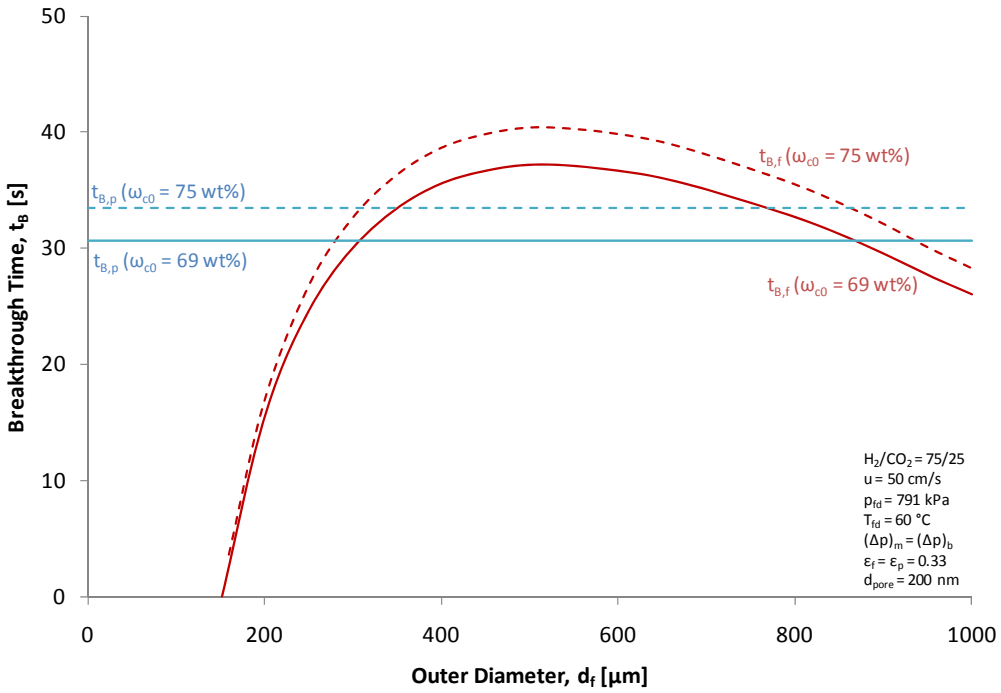

Figure C-9 Zeolite Loading Effect on Breakthrough Time

C.13.2.3. Pore Size and Porosity

Larger macropore size (500 nm) gave slightly longer breakthrough time due to faster pore diffusion (Figure C-10). For larger diameter, the effect of pore size was greater to result in the longer t_B.

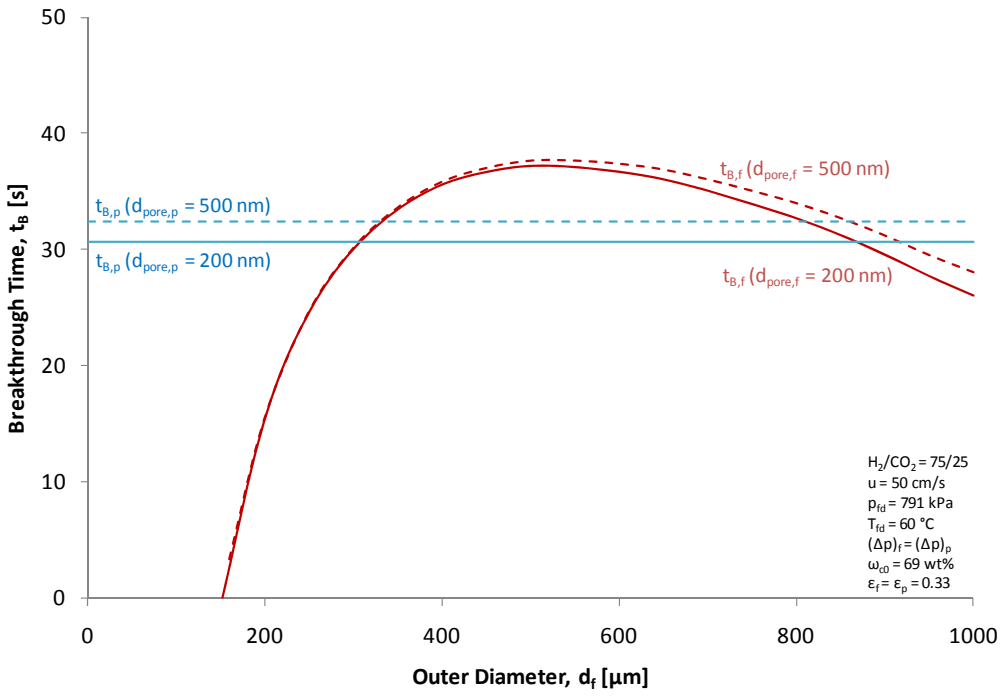

Figure C-10 Pore Size Effect on Breakthrough Time

Effect of porosity of the fiber sorbents depends on the degree of porosity compared with mass transfer resistance through the materials and sorption capacity. In Figure C-11, ε_f = 0.50 gave shorter t_B than the base case due to reduced sorption capacity in the fiber sorbent per volume. On the other hand, ε_f = 0.10 gave longer t_B than the base case for less than 400 µm in the outer diameter, d_f, and shorter t_B for larger than 400 µm in the d_f. Mass transfer resistance for ε_f = 0.10

was greater than that for the base case at any diameter. For the d_f < 400 μm, higher sorption capacity contributed to result in longer t_B, but larger mass transfer resistance decreased the t_B as the d_f became larger. For the packed bed, the same porosity of zeolite pellet (ε_p = 0.10) didn't make sense (negative t_B in the calculation due to longer mass transfer zone length), and ε_p = 0.50 gave the similar t_B to ε_p = 0.33.

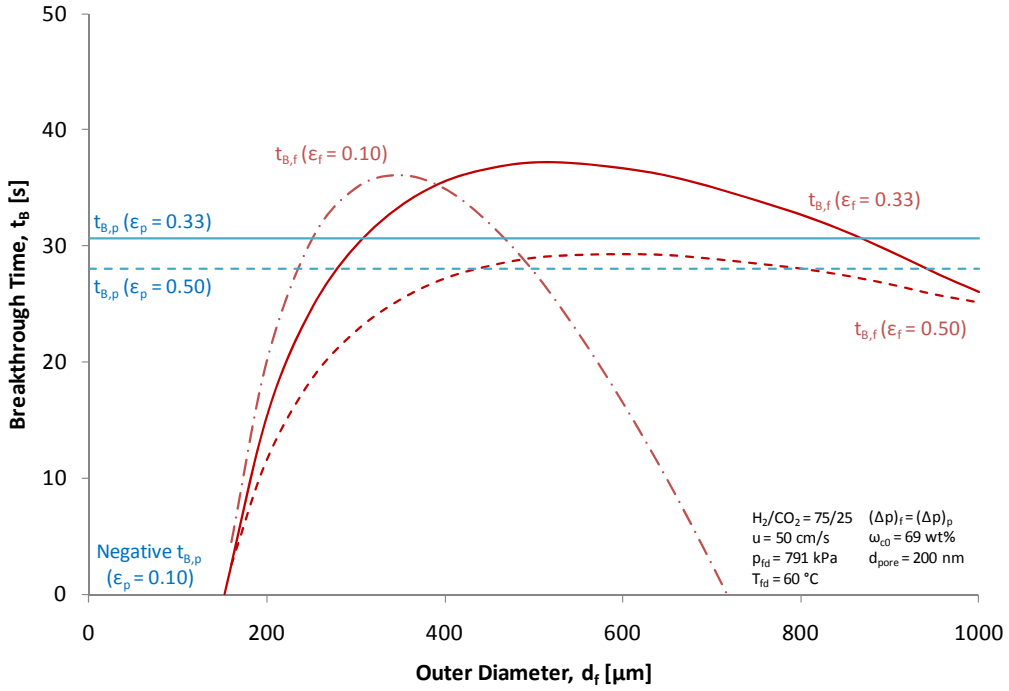

Figure C-11 Porosity Effect on Breakthrough Time

Corresponding to the base case in Figure 2-15, a ratio of external mass transfer resistance to overall mass transfer resistance with the change in the diameter was calculated and shown in Figure C-12. For the smaller diameter, external mass transfer was dominant. Therefore, porous structure (pore size and porosity) of the fiber sorbent is less significant compared with that of zeolite pellet, although the porous structure for the fiber sorbent is critical. On the other hand, as

the diameter became larger, intrafiber mass transfer became more comparable to the external mass transfer resistance due to thicker wall thickness. In this case, the porous structure contributes to the mass transfer resistance and larger pore size was effective. For the porosity, it concludes that an optimized porosity of the fiber sorbent exists depending on dimensions of fiber sorbents for a specific condition of zeolite loading and pore size. This is the similar discussion of the optimized design of wall thickness of the fiber sorbents with regard to packing and void fractions of the fiber sorbent modules in Chapter 2, Section 2.5. The more void space provides the faster mass transfer and the less sorption capacity.

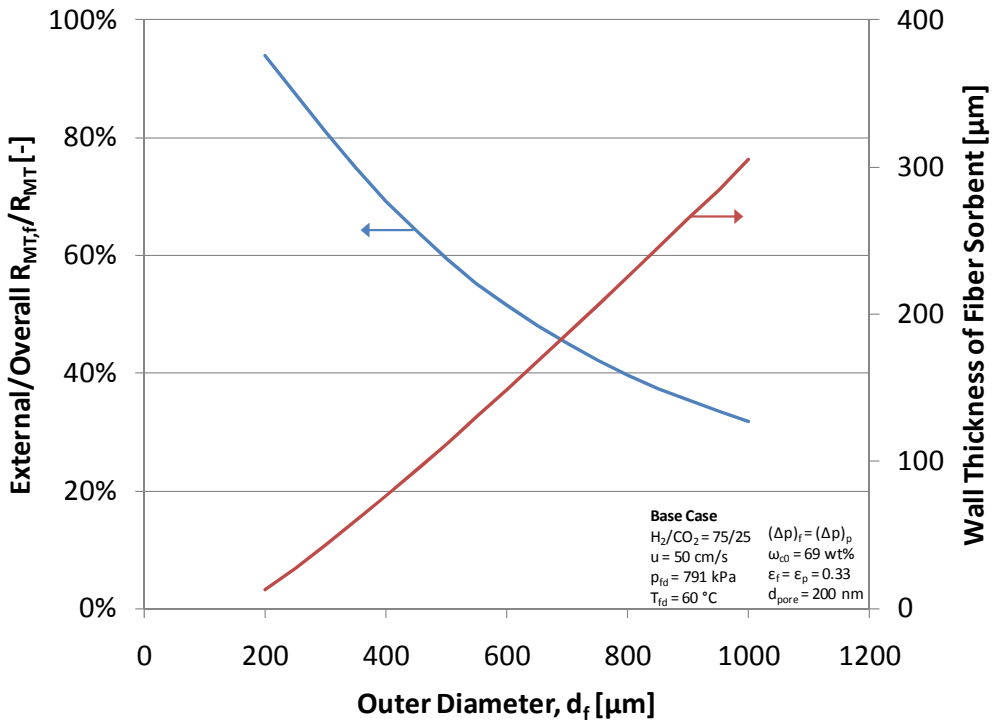

Figure C-12 Ratio of External to Overall Mass Transfer Resistance and Wall Thickness of Fiber Sorbent for the Base Case

C.13.3. Thermal Moderation

Under the reference conditions with adiabatic condition, temperature increase, ΔT, was predicted with three different situations. 1) No filler (gas), 2) PDMS and 3) paraffin wax. As increase of the $t_{B,f}$, the ΔT_f became larger. The maximum ΔT_f was not corresponded to the maximum $t_{B,f}$. This shift toward smaller d_f, especially in case of no filler, was due to the difference in the volumetric heat capacity between gas and solid portion in the module and lower apparent volumetric heat capacity contributed increase the temperature. The PDMS contributed to lower the temperature excursion due to the adsorption to provide additional heat capacity. The paraffin wax could eliminated temperature excursion for a certain range of the d_f. The comparison with the PDMS case implied that the contribution of the latent heat of fusion is more significant than the additional heat capacity in the shell side. The point asterisk (*) in Figure C-13 shows the optimized fiber sorbent to attain the maximum $t_{B,f}$ ($<t_{B,p}$) with less packing fraction and no temperature increase.

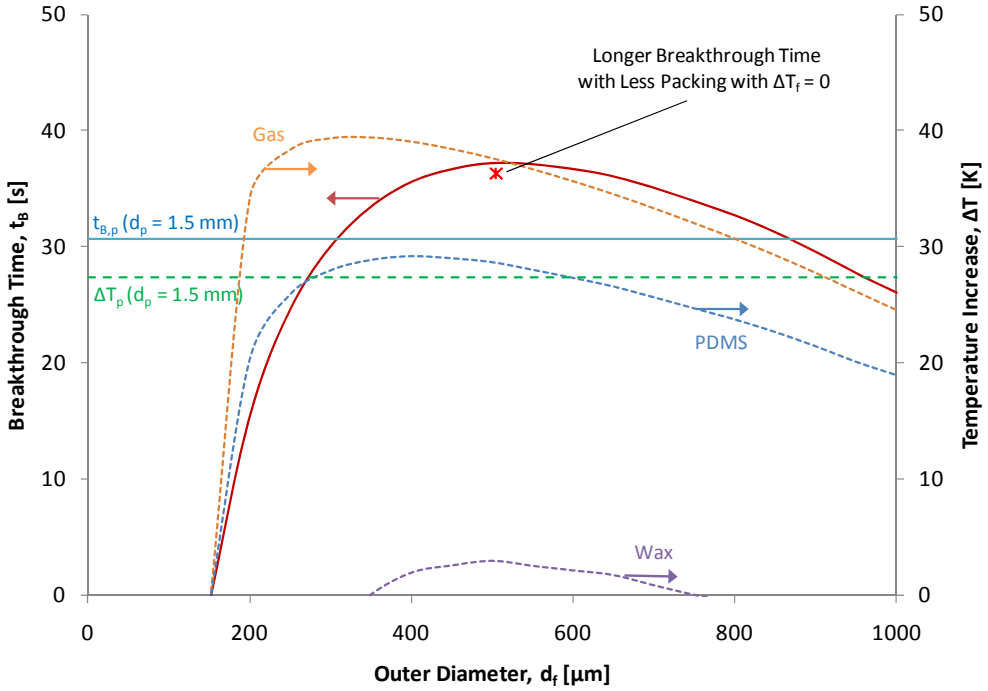

Figure C-13 Temperature Increase at Breakthrough Time

C.14. Conclusions

The simplified modeling of the fiber sorbent module to predict breakthrough behaviors in a comparison with an equivalent packed bed was beneficial to prove of the concept of a fiber sorbent and confirm the range of advantageous conditions over the packed bed. The controlling step in the overall mass transfer can be designed based on dimensions of the fiber sorbents and the external mass transfer contributes significantly more than the packed bed case. The sorption capacity of the module depends on the dimensions and porous structure of the fiber sorbents. The breakthrough time is determined by the balance between the mass transfer resistance and sorption capacity. In this study, it was found that less packing or less zeolite loading for the fiber sorbent module under several feed gas conditions could achieve the longer breakthrough time compared

with an equivalent packed bed. It concludes that the optimized design of the fiber sorbent is feasible for downsizing. In addition, thermal management by applying the shell-side void space to be filled with paraffin wax resulted in the potential to reduce the temperature increase due to heat of adsorption and to establish the pseudo-isothermal operation.

C.15. References

1. Chevron Technology Ventures LLC, *Personal Communications*. 2006.

2. Breck, D.W., *Zeolite Molecular Sieves: Structure, Chemistry, and Use*. 1974, New York: John Wiley & Sons.

3. LeVan, M.D., G. Carta, and C.M. Yon, *Adsorption and Ion Exchange*, in *Perry's Chemical Engineers' Handbook*, R.H. Perry, D.W. Green, and J.O. Maloney, Editors. 1997, McGraw-Hill: New York. p. 16-1-16-66.

4. Qiu, L.Y., et al., *Thermodynamic Investigations of Zeolites NaX and NaY.* Canadian Journal of Chemistry-Revue Canadienne De Chimie, 2006. **84**(2): p. 134-139.

5. Puleo, A.C., D.R. Paul, and S.S. Kelley, *The Effect of Degree of Acetylation on Gas Sorption and Transport Behavior in Cellulose-Acetate.* Journal of Membrane Science, 1989. **47**(3): p. 301-332.

6. MatWeb Material Property Database. *Eastman TENITE Acetate 105E1R26033 Clear, Trsp Cellulose Acetate*. 2010 [cited 2010 August 31]; Available from: http://www.matweb.com/.

7. Sasol Wax, *Sasolwax 6403 Safety Data Sheet*. 2008: Hamburg.

8. He, B. and F. Setterwall, *Technical Grade Paraffin Waxes as Phase Change Materials for Cool Thermal Storage and Cool Storage Systems Capital Cost Estimation.* Energy Conversion and Management, 2002. **43**(13): p. 1709-1723.

9. Livermore, C. and J. Voldman. *6.777J/2.751J Design and Fabrication of Microelectro-mechanical Devices*. 2004 [cited 2010 August 31]; Available from: http://web.mit.edu/6.777/www/matprops/pdms.htm.

10. Holman, J.P., *Heat Transfer*. SI Metric ed. 1989, New York: McGraw-Hill.

11. Sharma, A., S.D. Sharma, and D. Buddhi, *Accelerated Thermal Cycle Test of Acetamide, Stearic Acid and Paraffin Wax for Solar Thermal Latent Heat Storage Applications*. Energy Conversion and Management, 2002. **43**(14): p. 1923-1930.

12. Bird, R.B., W.E. Stewart, and E.N. Lightfoot, *Appendix E Tables for Prediction of Transport Properties*, in *Transport Phenomena*. 2002, John Wiley & Sons: New York. p. 863-866.

13. Smith, J.M., H.C. Van Ness, and M.M. Abbott, *Chapter 3 Volumetric Properties of Pure Fluids*, in *Introduction to Chemical Engineering Thermodynamics*. 2005, McGraw-Hill: Boston. p. 64-124.

14. Smith, J.M., H.C. Van Ness, and M.M. Abbott, *Chapter 11 Solution Thermodynamics: Theory*, in *Introduction to Chemical Engineering Thermodynamics*. 2005, McGraw-Hill: Boston. p. 378-429.

15. Bird, R.B., W.E. Stewart, and E.N. Lightfoot, *Chapter 1 Viscosity and the Mechanisms of Momentum Transport*, in *Transport Phenomena*. 2002, John Wiley & Sons: New York. p. 11-39.

16. Bird, R.B., W.E. Stewart, and E.N. Lightfoot, *Chapter 17 Diffusivity and the Mechanisms of Mass Transport*, in *Transport Phenomena*. 2002, John Wiley & Sons: New York. p. 513-542.

17. Kärger, J. and D.M. Ruthven, *Chapter 4 Diffusion Mechanisms*, in *Diffusion in Zeolites and Other Microporous Solids*. 1992, John Wiley & Sons: New York. p. 87-122.

18. Ruthven, D.M., *Chapter 5 Diffusion in Porous Media*, in *Principles of Adsorption and Adsorption Processes*. 1984, Wiley-Interscience Publication: New York. p. 124-165.

19. Hines, A.L. and R.N. Maddox, *Chapter 2 Diffusion Coefficients*, in *Mass Transfer: Fundamentals and Applications*. 1985, Prentice-Hall: Englewood Cliffs, N.J. p. 17-59.

20. Do, D.D., *Chapter 7 Fundamentals of Diffusion and Adsorption in Porous Media*, in *Adsorption Analysis: Equilibria and Kinetics*. 1998, Imperial College Press: London. p. 337-414.

21. Kärger, J. and D.M. Ruthven, *Chapter 11 Diffusion in Macro and Meso Pores*, in *Diffusion in Zeolites and Other Microporous Solids*. 1992, John Wiley & Sons: New York. p. 341-374.

22. Smith, J.M., H.C. Van Ness, and M.M. Abbott, *Chapter 4 Heat Effects*, in *Introduction to Chemical Engineering Thermodynamics*. 2005, McGraw-Hill: Boston. p. 125-158.

23. Smith, J.M., H.C. Van Ness, and M.M. Abbott, *Appendix C Heat Capacities and Property Changes of Formation*, in *Introduction to Chemical Engineering Thermodynamics*. 2005, McGraw-Hill: Boston. p. 683-687.

24. Bird, R.B., W.E. Stewart, and E.N. Lightfoot, *Chapter 9 Termal Conductivity and the Mechanisms of Energy Transport*, in *Transport Phenomena*. 2002, John Wiley & Sons: New York. p. 265-289.

25. Kärger, J., *Measurement of Diffusion in Zeolites - A Never Ending Challenge?* Adsorption, 2003. **9**(1): p. 29-35.

26. Pitale, K.K., et al., *Tracer Diffusion of Carbon-Dioxide and Methanol in Zeolite-Y and Zeolite-Zsm-5 Using C-14-Labeled Sorbates.* Current Science, 1988. **57**(7): p. 355-363.

27. Li, P. and F.H. Tezel, *Equilibrium and Kinetic Analysis of CO2-N2 Adsorption Separation by Concentration Pulse Chromatography.* Journal of Colloid and Interface Science, 2007. **313**(1): p. 12-17.

28. Plant, D., et al., *Diffusion of CO2 in NaY and NaX Faujasite Systems: Quasi-Elastic Neutron Scattering Experiments and Molecular Dynamics Simulations.* European Physical Journal-Special Topics, 2007. **141**: p. 127-132.

29. Kamiuto, K., A. Goubaru, and Ermalina, *Diffusion Coefficients of Carbon Dioxide within Type 13X Zeolite Particles.* Chemical Engineering Communications, 2006. **193**(5): p. 628-638.

30. Grenier, P., A. Malka-Edery, and V. Bourdin, *A Temperature Frequency Response Method for Adsorption Kinetics Measurements.* Adsorption, 1999. **5**(2): p. 135-143.

31. Onyestyak, G. and L.V.C. Rees, *Frequency Response Study of Adsorbate Mobilities of Different Character in Various Commercial Adsorbents.* Journal of Physical Chemistry B, 1999. **103**(35): p. 7469-7479.

32. Ahn, H., et al., *Diffusion Mechanism of Carbon Dioxide in Zeolite 4A and CaX Pellets.* Adsorption, 2004. **10**(2): p. 111-128.

33. McCabe, W.L., J.C. Smith, and P. Harriott, *Chapter 5 Incompressible Flow in Pipes and Channels*, in *Unit Operations of Chemical Engineering*. 2001, McGraw-Hill: Boston. p. 94-127.

34. McCabe, W.L., J.C. Smith, and P. Harriott, *Chapter 7 Flow Past Immersed Bodies*, in *Unit Operations of Chemical Engineering*. 2001, McGraw-Hill: Boston. p. 150-186.

35. McCabe, W.L., J.C. Smith, and P. Harriott, *Chapter 17 Principles of Diffusion and Mass Transfer Between Phases*, in *Unit Operations of Chemical Engineering*. 2001, McGraw-Hill: Boston. p. 511-545.

36. McCabe, W.L., J.C. Smith, and P. Harriott, *Chapter 12 Heat Transfer to Fluids Without Phase Change*, in *Unit Operations of Chemical Engineering*. 2001, McGraw-Hill: Boston. p. 511-545.

37. Wakao, N. and S. Kaguei, *Chapter 4 Particle-Fluid Mass Transfer Coefficients*, in *Heat and Mass Transfer in Packed Beds*. 1982, Gordon and Breach Science Publishers: New York. p. 138-160.

38. Patton, A., B.D. Crittenden, and S.P. Perera, *Use of the Linear Driving Force Approximation to Guide the Design of Monolithic Adsorbents.* Chemical Engineering Research & Design, 2004. **82**(A8): p. 999-1009.

39. Harlick, P.J.E. and F.H. Tezel, *Adsorption of Carbon Dioxide, Methane and Nitrogen: Pure and Binary Mixture Adsorption for ZSM-5 with SiO2/Al2O3 Ratio of 280.* Separation and Purification Technology, 2003. **33**(2): p. 199-210.

40. Kärger, J. and D.M. Ruthven, *Chapter 10 Chromatographic and Flow Methods of Measuring Intraparticle Diffusivity*, in *Diffusion in Zeolites and Other Microporous Solids*. 1992, John Wiley & Sons: New York. p. 289-337.

41. Ruthven, D.M., *Chapter 8 Dynamics of Adsorption Columns: Single-Transition Systems*, in *Principles of Adsorption and Adsorption Processes*. 1984, Wiley-Interscience Publication: New York. p. 220-273.

42. Hines, A.L. and R.N. Maddox, *Chapter 14 Adsorption*, in *Mass Transfer: Fundamentals and Applications*. 1985, Prentice-Hall: Englewood Cliffs, N.J. p. 456-500.

43. Yang, R.T., *Chapter 2 Adsorbents and Adsorption Isotherms*, in *Gas Separation by Adsorption Processes*. 1997, World Scientific: Singapore ; River Edge, N.J. p. 9-48.

44. Kawazoe, K., Y. Takeuchi, and S. Miyahara, *Adsorption and Ion Exchange*, in *Kagaku Kogaku Binran (Chemical Engineering Handbook of Japan)*, Kagaku Kogaku Kyokai (The Society of Chemical Engineers Japan), Editor. 1978, Maruzen: Tokyo. p. 870-871.

45. Suzuki, M., *Adsorption Engineering*. 1990, Tokyo, Amsterdam; New York: Kodansha; Elsevier.

46. Seborg, D.E., T.F. Edgar, and D.A. Mellichamp, *Chapter 21 Process Monitoring*, in *Process Dynamics and Control*. 2004, Wiley: Hoboken, NJ. p. 567-590.

47. McCabe, W.L., J.C. Smith, and P. Harriott, *Chapter 25 Fixed-Bed Separations*, in *Unit Operations of Chemical Engineering*. 2001, McGraw-Hill: Boston. p. 812-856.

APPENDIX D PEBA-BASED FIBER SORBENTS

D.1. Introduction

In order to pursue a range of potentially appropriate polymers for fiber sorbents, another polymer, poly(ether-*block*-amide) (PEBA), was also explored. The PEBA is a rubbery block copolymer of polyether (PE) and polyamide (PA) segments [1] (Figure D-1). Elastic property of the rubbery polymer was expected to contribute to more durable mechanical strength than glassy polymers. In terms of gas separations, some researchers have evaluated the polymer with flat sheet membranes because of high polar/non-polar selectivity [2]. The material is typically processed by melt. In conclusion, this material was not suitable for the fiber sorbents with zeolite NaY. This appendix provides some spinning results for the pure PEBA fibers and PEBA-NaY fiber sorbents and characterization.

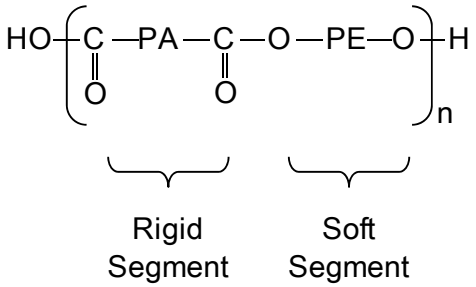

Figure D-1 Structure of PEBA [1]

D.2. Material

Poly(ether-*block*-amide) (PEBA) is, and is commercially available (PEBAX®, Arkema Inc.) [1]. Two grades of PEBAX® were provided kindly by Arkema as pellets. Major properties of the PEBA are listed in Table D-1.

Table D-1 Properties of PEBAX®

	Mn	T_G [°C]	T_m [°C]	PE	PE wt%	PA
MV1074 SA01 [2]	50,000	-55	158	PEO	55	PA12
MV3000 SA01	Unknown	Unknown	158	Unknown	Unknown	Unknown

PEO: poly(ethylene oxide), PA12: Nylon 12

The PE and PA moieties are soft and rigid segments, respectively. The nature of the hard segment has a large effect on the solvent resistance of the segmented block polymer [3]. Since the soft segments commonly used are soluble in common organic solvents, they will swell in these solvents and lose their integrity. On the other hand, the hard segments maintain the integrity of the swollen polymer. The semicrystalline amide hard segments used in the PEBA have lower solubility in many solvents. The TGA and DSC results of MV1074 are shown in Figure D-2. The T_G and T_m were close to the data disclosed by the manufacturer and the melting temperature which corresponds to the soft segment was 5.6 °C. This grade of PEBAX® was degraded above 300 °C.

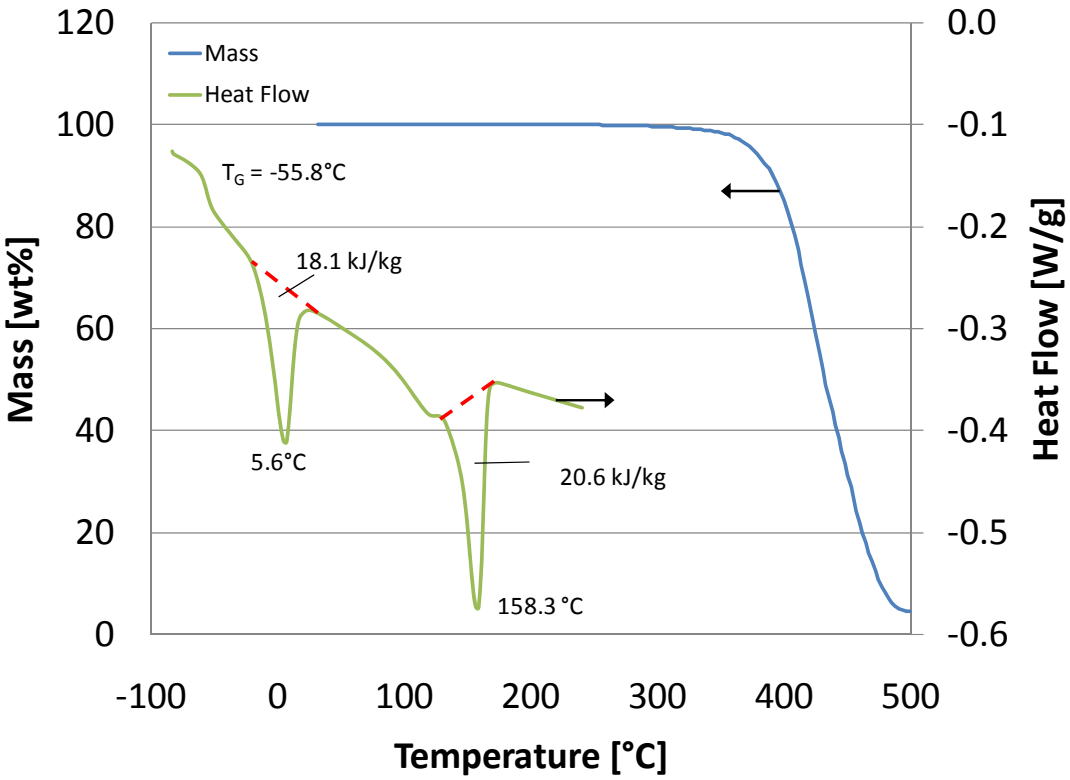

Figure D-2 TGA and DSC Curves of PEBAX® MV1074 SA

The PEBAX® polymers were insoluble in 1-Methyl-2-pyrrolidinone (*N*-Methyl-2-pyrrolidone, NMP, anhydrous grade, 99.5%, Sigma-Aldrich), acetone (≥99.5%, Sigma-Aldrich), tetrahydrofuran (THF, anhydrous and inhibitor-free grade, ≥ 99.9%, Sigma-Aldrich), N,N-Dimethylacetamide (DMAc, ≥99%, Sigma-Aldrich), toluene (anhydrous, 99.8%, Sigma-Aldrich), 2-propanol (IPA, anhydrous, 99.5%), Dichloromethane ($MeCl_2$, ≥ 99.9%, Sigma-Aldrich), 1-octanol (≥ 99.7%, Sigma-Aldrich), ethylene glycol (EG, anhydrous, 99.8%, Sigma-Aldrich) at room temperature (25 °C), and NMP and DMAc at 50 °C. To facilitate formation of the porous structure because of phase separation, polymer solution spinning is desired. The preparation and loading in the spinning apparatus of the PEBA dopes were technical challenges in addition to the spinning operational conditions.

Detailed information on the PEBAX® MV3000 was not disclosed by the manufacturer. The TGA and DSC results of the MV3000 are shown in Figure D-3. The T_G and T_m were similar to the MV1074, but there were two peaks for the melting of other components. It indicates there is a third component compared with the MV1074. A patent mentioned that the grade of PEBAX® contains acrylate resin [4].

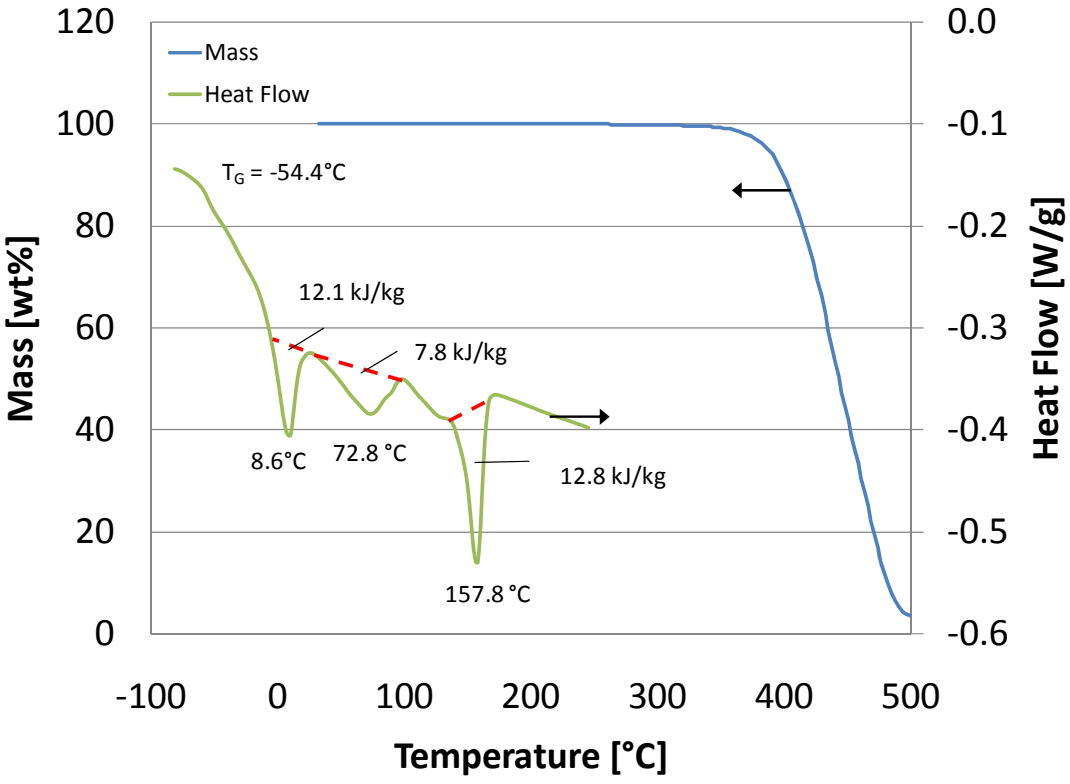

Figure D-3 TGA and DSC Curves of PEBAX® MV3000 SA

D.3. Experimental Methods

Since the PEBA was not dissolved in solvent easily and there was a limitation of available amount of PEBAX® resin, phase diagram for the PEBA solution with any solvent was not

created. However, the binary solution of PEBA and NMP could be prepared at 90 °C. The solution had low viscosity like water, but became gelled very quickly once the temperature was lowered. The spinning of pure PEBA fibers and NaY-PEBA fiber sorbents were executed by the same spinning apparatus described in Chapter 2, Section 2.2 and Chapter 3, Section 3.4. Spinning operational conditions are summarized in Table D-2 and some were quite different from pure cellulose acetate (CA) fibers and CA-NaY fiber sorbents described in Chapter 4. Dope and bore fluid flow rates were very high vs. that for pure CA fibers and CA-NaY fiber sorbents. Shallow quenching bath was adequate for the phase separation of the pure PEBA fibers and the PEBA-NaY fiber sorbents. Temperature of quenching bath had to be lower than room temperature. There were some challenges in obtaining long straight fiber due to; 1) entanglement in water bath, 2) stickiness to plastic or glass column wall in solvent exchange and 3) shrinkage after the solvent exchange. For solvent exchange, the apparatus was modified to avoid the issues as described in Chapter 3, Section 3.4. The pure PEBA fibers and the PEBA-NaY fiber sorbents were characterized by the same methods described in Chapter 3, Section 3.5.

Table D-2 Spinning Conditions for Pure PEBA Fibers and PEBA-NaY Fiber Sorbents

Dope	Composition	See Section D.4
	Pump Temperature	90 – 100 °C
	In-Line Temperature	25 – 90 °C
	Flow Rate	500 – 1,000 mL/h
Bore Fluid	Composition	Water = 100
	Temperature	Room Temperature
	Flow Rate	200 – 500 mL/h
Spinneret	Type	Pesek 1st Generation Spinneret
	Temperature	90 °C
Air Gap	Distance	1 – 5 cm
	Temperature	Room Temperature
	Humidity	42.0 – 47.0 %RH (Not Controllable)
	Air Flow	No
Quenching Bath	Media	Cold Tap Water
	Depth	30 cm
	Temperature	10 – 25 °C
Collection	Take-Up Rate	30 – 60 m/min
	Media	Tap Water
	Temperature	Room Temperature
Solvent Exchange	Non-Solvent	Water Methanol n-Hexane
Drying	Temperature	120 °C
	Pressure	Vacuum
	Time	1 hour

D.4. Results and Discussions

D.4.1. Pure PEBA Fibers

The binary solution of PEBA and NMP (PEBA:NMP = 10:90) was successfully spun with a hollow structure as shown in Figure D-4. An entirely dense structure was appeared.

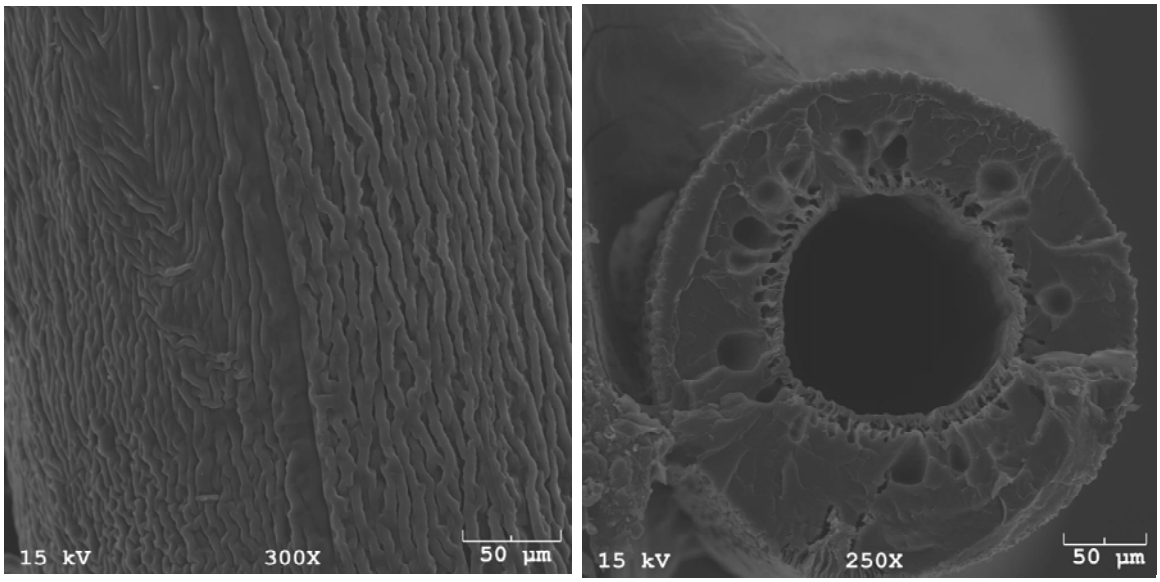

(a) Outer Surface (b) Cross Section

Figure D-4 Pure PEBA Hollow Fiber (PEBA:NMP = 10:90)

Another dope was modified with $LiNO_3$ addition for pore structure (PEBA:NMP:$LiNO_3$ = 10:85:5) and successfully spun with interconnected porous structure. However, there are still clearly dense portion in the morphology. The spinning conditions were not optimized yet to obtain the PEBA fibers enough to bundle them for a module.

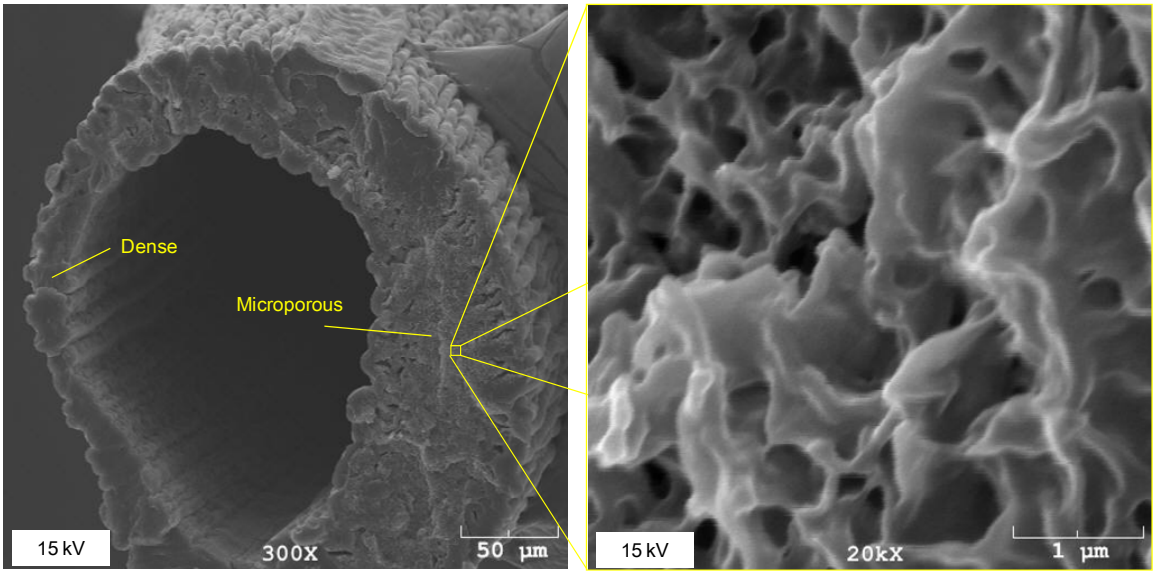

(a) Cross Section (b) Porous Structure

Figure D-5 Pure PEBA Hollow Fiber (PEBA:NMP:$LiNO_3$ = 10:85:5)

Another grade of PEBAX® (MV3000) could not be spun at all due to frequent fiber breaks, even if the same approaches used for the MV1074 was applied. The difficulties may be attributed to the nature of MV3000, but detailed composition is not disclosed by the manufacturer, so this is difficult to substantiate or pursue.

D.4.2. PEBA-NaY Fiber Sorbents

To prepare a dope of PEBA/NaY/NMP/$LiNO_3$, the $LiNO_3$ was dissolved in the NMP first followed by dispersion of the NaY with ultrasonication. And then, the PEBA pellets (MV1074) were added and stirred by the motor-driven mixer at 90 °C. The PEBA-NaY fiber sorbents were spun with Dope 1) PEBA:NaY:NMP:$LiNO_3$ = 10:10:75:5 [50% loading], Dope 2) 5:20:74:1 [80% loading] and Dope 3) 10:30:55:5 [75% loading]. The fiber sorbents with Dopes 2 and 3 could not be collected on the take-up drum, but hollow structure was kept for the SEM as shown

in Figure D-6 and Figure D-7. The fiber sorbent with Dope 2 disintegrated into pieces during the solvent exchange and the fiber sorbents with Dopes 1 and 3 also disintegrated into pieces several days after the drying. It appears that the optimal polymer composition in solution should be higher. At increased polymer solution composition and/or zeolite loading, however, viscosity of the solution increases like CA-NaY dope and bubbles in the dope seem to result in the easy break during spinning. Although degassing from the dope requires heating after the setting in the pump cylinder, another experimental technique such as in-situ mixing inside the pump cylinder need to be explored for the PEBA dope at higher temperature (90°C).

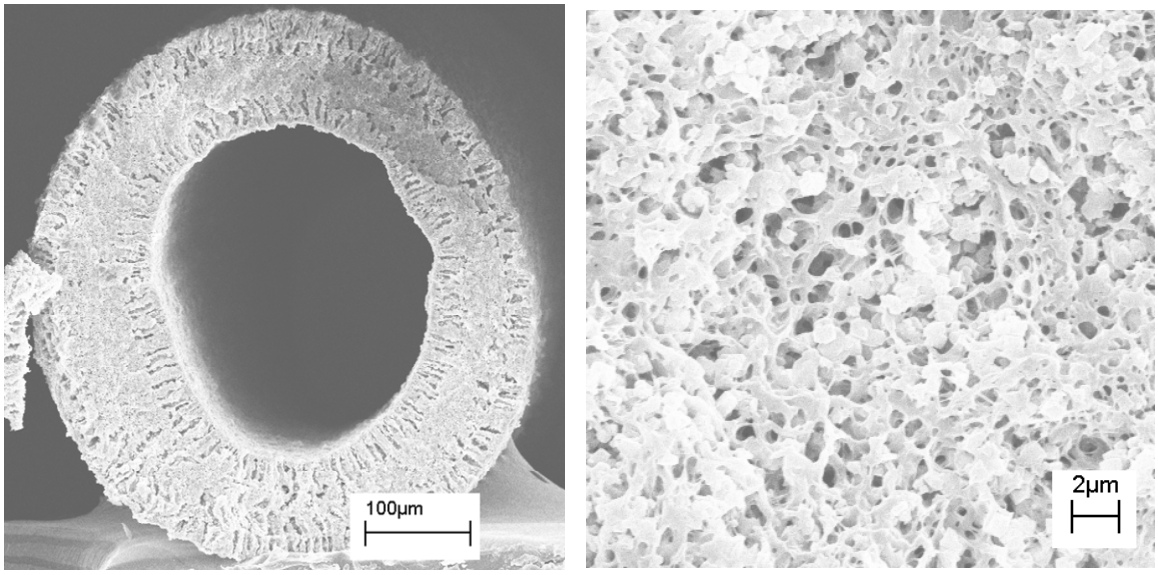

(a) Cross Section (b) Porous Structure

Figure D-6 PEBA-NaY Fiber Sorbent (50% Loading)

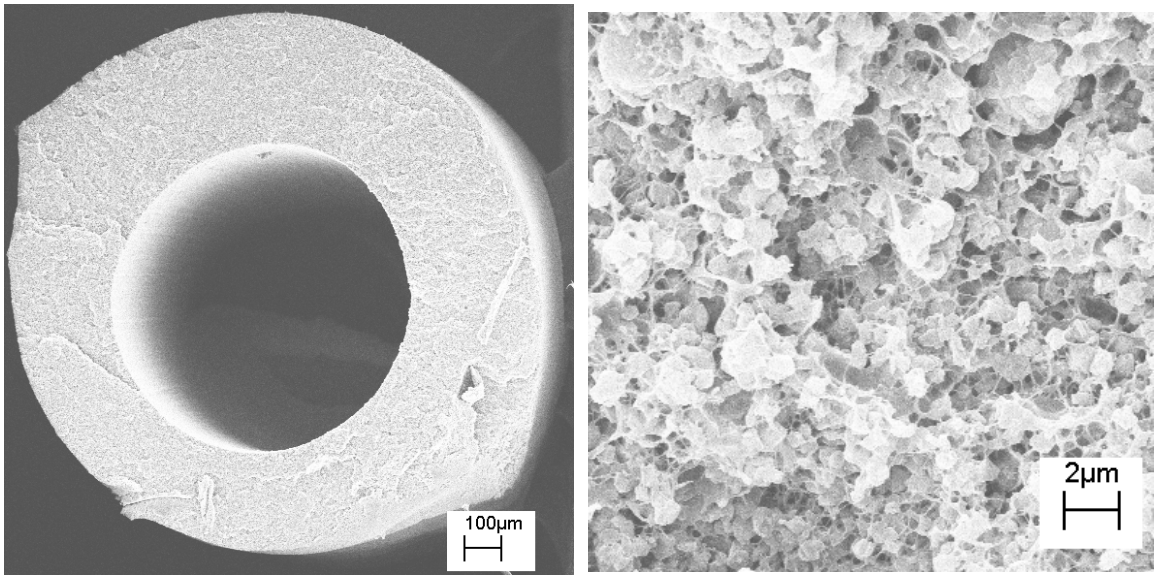

(a) Cross Section (b) Porous Structure

Figure D-7 PEBA-NaY Fiber Sorbent (75% Loading)

Sorption capacities of CO_2 to pure NaY, pure PEBA and PEBA-NaY fiber sorbent (75% loading) at 35 °C are shown in Figure D-8. The experimental sorption capacities of pure NaY and PEBA were close to reference data [2]. Sorption capacity of PEBA-NaY fiber sorbent was calculated based on the zeolite loading. The experimental sorption capacities of the PEBA-NaY fiber sorbent was significantly lower than the predicted values, which was 64% reduction. The NaY might be partially ion-exchanged into Li form during ultrasonication due to the $LiNO_3$ used as a viscosity modifier. Since zeolite LiY shows higher sorption capacity than the NaY [5], this is not a critical factor for the reduction in the sorption capacity.

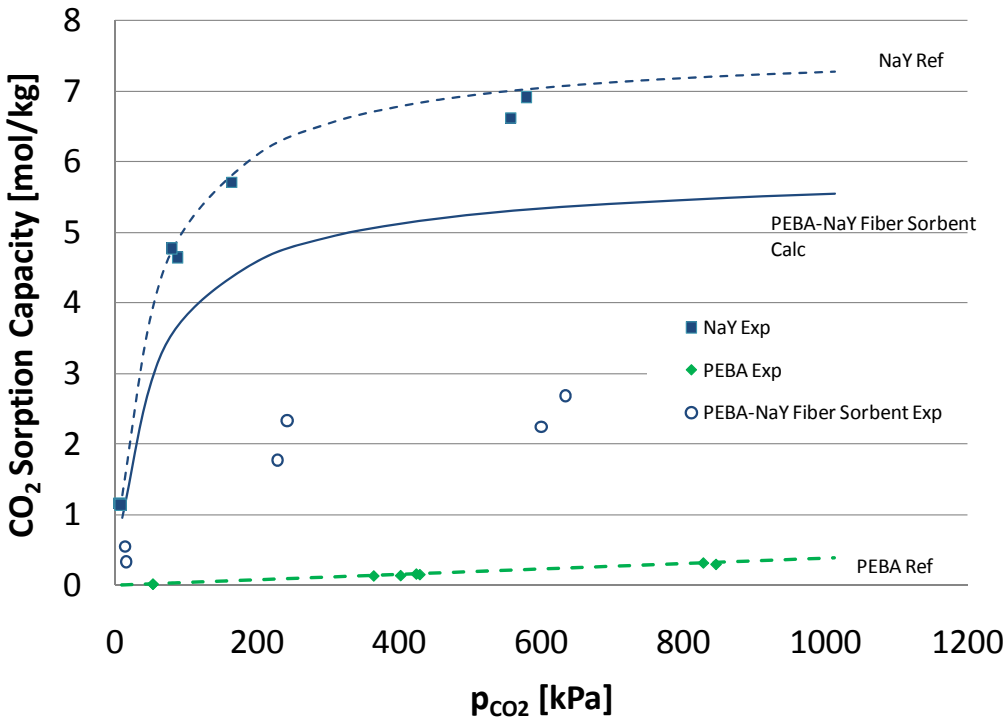

Figure D-8 Sorption Capacities of CO_2 to Pure NaY, Pure PEBA and PEBA-NaY Fiber Sorbent (75% Loading) at 35 °C

BET surface area of fiber sorbents were measured and compared with that of pure NaY in Table D-3. Corresponding to the reduction of the sorption capacity, the BET surface area for fiber sorbent was reduced by 29%. Horvath-Kawazoe differential pore volume plots for the NaY and PEBA-NaY fiber sorbent are shown in Figure D-9. For the PEBA-NaY fiber sorbent, pore volume at the zeolitic pore was reduced significantly.

Table D-3 BET Surface Area of Pure NaY and PEBA-NaY Fiber Sorbent

Sample	BET Surface Area m^2/g
Pure NaY	778.1
PEBA-NaY Fiber Sorbent (75% Loading)	
As Measured	407.1
Corrected by Loading Level	544.9

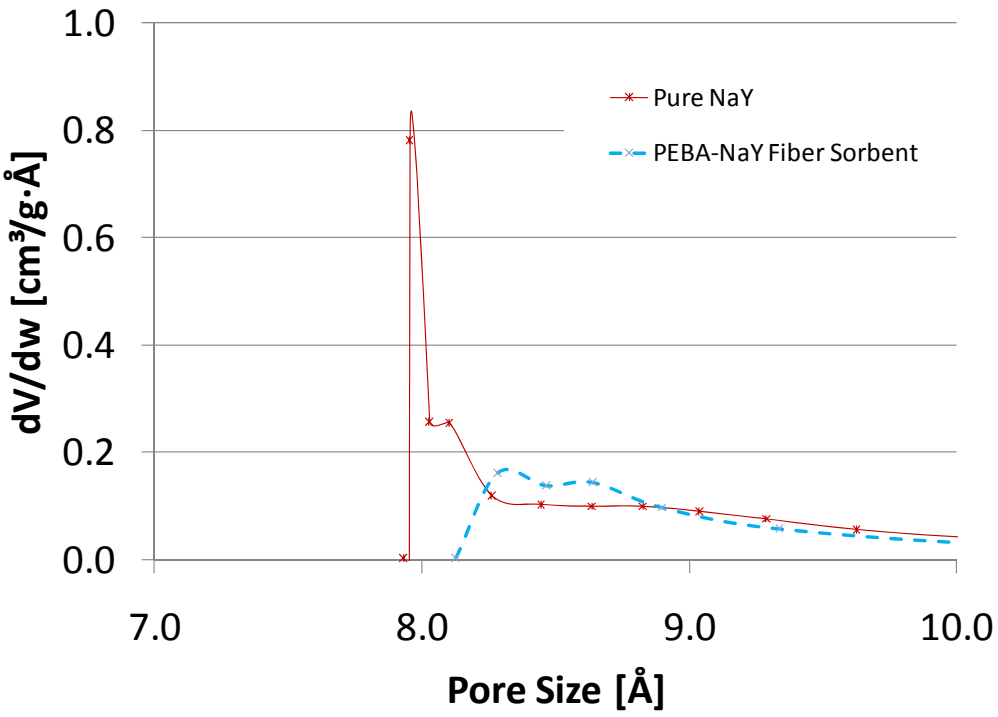

Figure D-9 Horvath-Kawazoe Differential Pore Volume Plots for Pure NaY and PEBA-NaY Fiber Sorbent (75% Loading)

Since the PEBA is synthesized through esterification, the polymer is susceptible to hydrolysis, which may reduce their properties lowering the polymer molecular weight and releases oligomers

due to decomposition. Impact on hydrolysis of lithium nitrate in the dopes, which is pore former, is not well-known incorporating with water used in the quenching bath at high temperature. Some oligomers might come out from the polymer matrix, and could penetrate into and plug off the zeolitic pores causing reduced sorption capacity. While TGA could potentially verify the presence of such oligomeric decomposition "debris", the general unattractiveness of this sticky and hard to process family of materials led to us to cease activities on it and to focus on cellulose acetate as described in the main body of the thesis.

A magnified SEM image for the PEBA-NaY interface is shown in Figure D-10. The surface of zeolite crystals might be covered by the PEBA and it also could result in blockage of zeolitic pores to the gas diffusion.

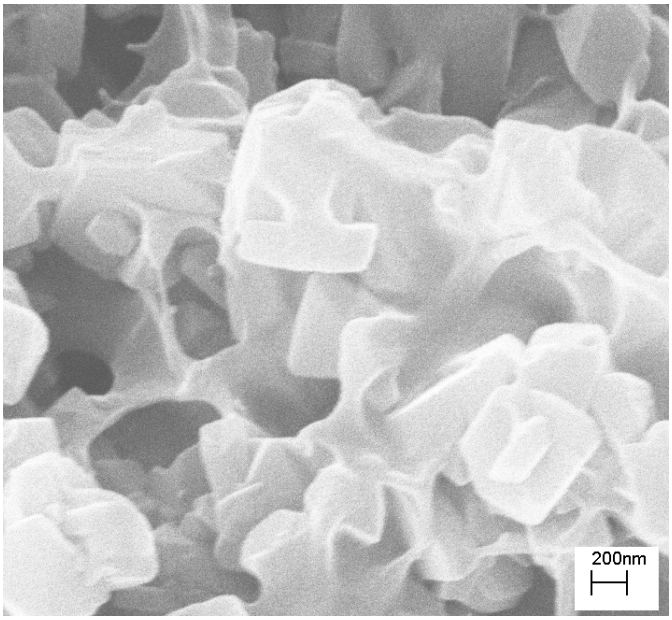

Figure D-10 Magnified SEM Image of PEBA-NaY Interface

D.5. Conclusions

The pure PEBA rubbery polymer was spun as hollow fibers with porous structure. In addition, the PEBA-NaY fiber sorbents were spun with the dispersed zeolite crystals with high loading. However, these spinning were quite difficult to produce long fibers enough to make modules for other tests. Especially the current dope composition were not optimized to hold the integrity of the fiber sorbents for a long time and to demonstrate the equivalent sorption capacity to pure NaY due to degradation. As of the samples which were produced, it was concluded that the PEBA was not appropriate for the fiber sorbents to be used under the stringent operational conditions such as the PSA processes for hydrogen recovery.

D.6. References

1. Arkema Inc., *Polyether Block Amides Technical Data*. 2003.

2. Bondar, V.I., B.D. Freeman, and I. Pinnau, *Gas Sorption and Characterization of Poly(Ether-b-Amide) Segmented Block Copolymers.* Journal of Polymer Science Part B-Polymer Physics, 1999. **37**(17): p. 2463-2475.

3. Nelb, R.G. and A.T. Chen, *Thermoplastic Elastomers Based on Polyamides*, in *Thermoplastic Elastomer*, G. Holden, H.R. Kricheldorf, and R.P. Quirk, Editors. 2004, Hanser: Munich, Germany. p. 217-246.

4. Kuratsuji, T., J. Maillet, and J. Yamamoto, *Water Vapor Permeable Plastic Film Comprising Inorganic Particles Coated with a Substance Having High Refractive Index*, in *U.S. Patent No.5,939,183*. 1999.

5. Kusakabe, K., et al., *Gas Permeation Properties of Ion-Exchanged Faujasite-Type Zeolite Membranes.* Aiche Journal, 1999. **45**(6): p. 1220-1226.

APPENDIX E CHARACTERIZATION OF ZEOLITE HY

E.1. Introduction

In order to pursue appropriate zeolites for fiber sorbents, another zeolite, zeolite HY, was also explored. The HY is a faujasite type as same as the NaY, but ionic form is in hydrogen form with higher Si/Al ratio (Table E-1). Since actual reformate gas contains a trace level water vapor, hydrophobic zeolite with high Si/Al was expected to higher resistance to the water vapor adsorption causing the reduction in sorption capacity of CO_2. In conclusion, this material was not suitable for the fiber sorbents for CO_2 removal. This appendix provides BET surface area of the HY and sorption capacity of CO_2 to the HY with a comparison to the NaY.

Table E-1 Commercial Zeolite Products [1]

Zeolite	Commercial Product	Structure	Ionic Form	Si/Al *
NaY	CBV-100	Faujasite	Na^+	2.6
HY	CBV780	Faujasite	H^+	40
ZSM-5	CBV-28014	MFI	NH_4^+	140

* Converted from SiO_2/Al_2O_3 Ratio

E.2. Materials

The HY, CBV-780, was obtained from Zeolyst International. Dry zeolite samples at 285 °C for an overnight.

E.3. Experimental Methods

BET surface area and sorption capacity of CO_2 were characterized by the same methods described in Chapter 3, Section 3.5.

E.4. Results and Discussions

E.4.1. BET Surface Area

The BET surface area of the HY was 19% higher than that of the NaY. However, Horvath-Kawazoe differential pore volume plots for the NaY and the HY shown in Figure E-1 indicated that zeolitic pore size of the HY is larger (11 Å) with wider distribution than that of the NaY (8 Å) even if both zeolites have the same faujasite structure with pore size of 7.4 Å.

Table E-2 BET Surface Area of the NaY and the HY

Sample	BET Surface Area m^2/g
NaY	778.1
HY	923.8

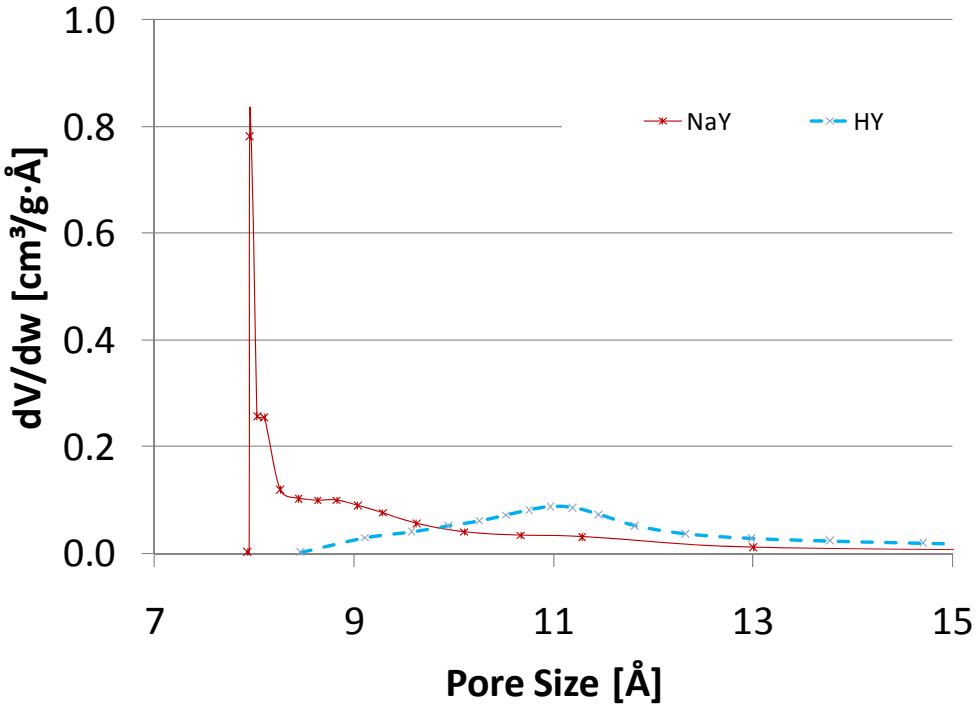

Figure E-1 Horvath-Kawazoe Differential Pore Volume Plots for the NaY and the HY

E.4.2. Sorption Capacity

The sorption capacity of CO_2 to the HY was significantly lower than that of the NaY, showing a 45% reduction (Figure E-2). This tendency was consistent with a literature data reported for other pressure and temperature range [2]. ZSM-5 in sodium form has lower capacity as well as that in hydrogen form [3], while the highest Si/Al ratio is achieved. The ammonium form was expected to have higher sorption capacity of CO_2 because of basicity [4]. However, the hydrogen-form zeolite can be derived from ammonium-form zeolite with heating in the air [5]. This indicates less chemical stability of the ammonium form under an oxidizing atmosphere. Structure and ionic forms are critical factors to select a zeolite for high sorption capacity of CO_2 used in fiber sorbents rather than the Si/Al ratio alone.

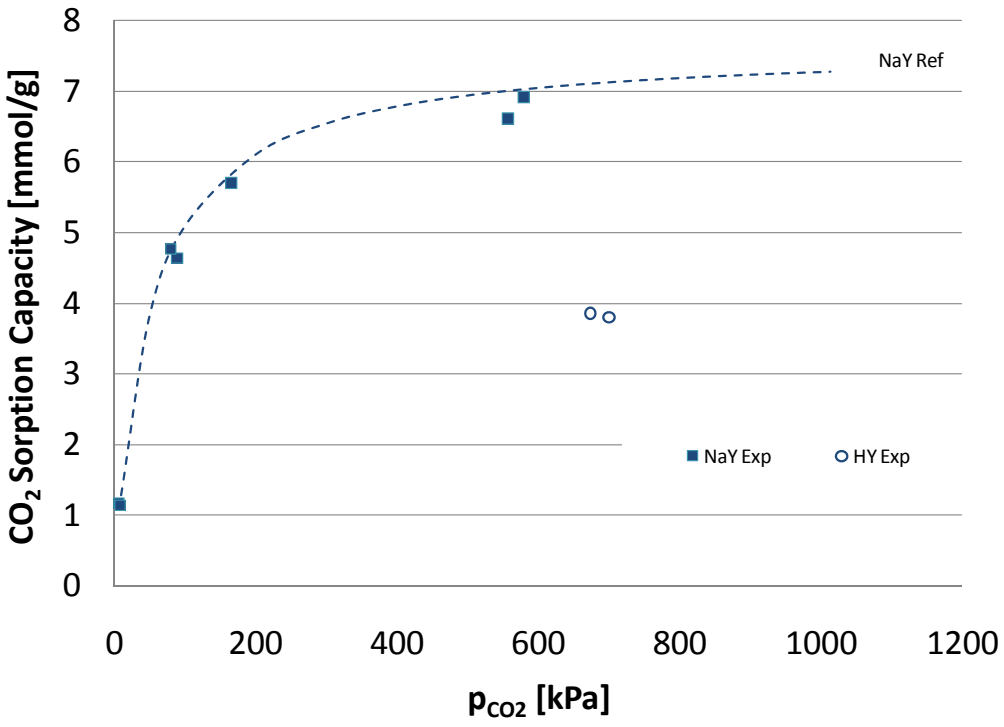

Figure E-2 Sorption Capacities of CO_2 to the NaY and the HY

E.5. Conclusions

Zeolite HY with high Si/Al was evaluated for the fiber sorbents used in hydrogen recovery. The BET surface area of the HY was greater than that of the NaY and was expected high sorption capacity, but the sorption capacity of CO_2 to the HY was significantly lower than that to the NaY. Although adsorption of water vapor is a practical issue, it requires more research to find or develop zeolites with high sorption capacity of CO_2 with less water vapor adsorption by exploring structure, ionic form and any modification to bare zeolite crystals. The commercially available NaY exhibits reasonably high sorption capacity as discussed in Chapter 4 under the typically operational conditions with dry gas basis at laboratory scale. For the present work, zeolite NaY was selected and used for fiber sorbents.

E.6. References

1. Zeolyst International. 2010 [cited 2010 August 31]; Available from: http://www.zeolyst.com.

2. Harlick, P.J.E. and F.H. Tezel, *An Experimental Adsorbent Screening Study for CO2 Removal from N2.* Microporous and Mesoporous Materials, 2004. **76**(1-3): p. 71-79.

3. Dunne, J.A., et al., *Calorimetric Heats of Adsorption and Adsorption Isotherms .2. O2, N2, Ar, CO2, CH4, C2H6, and SF6 on NaX, H-ZSM-5, and Na-ZSM-5 Zeolites.* Langmuir, 1996. **12**(24): p. 5896-5904.

4. Rastelli, H., C.C. Chao, and D.R. Garg, *Selective Adsorption of CO2 on Zeolites* in *U.S. Patent No.4,775,396*. 1988.

5. Shiralkar, V.P. and S.B. Kulkarni, *Sorption of Carbon-Dioxide in Cation Exchanged Y-Type Zeolites - Sorption Isotherms and State of Sorbed Molecule.* Zeolites, 1984. **4**(4): p. 329-336.

APPENDIX F HYDROPHOBIZATION OF ZEOLITE SURFACE

F.1. Introduction

A hydrophobic surface for the zeolite is preferred since it enables a strong adhesion between polymer and zeolite surface for mixed matrix membranes [1-2]. For fiber sorbents, more hydrophilic surface is preferred to yield a sieve-in-a-cage morphology that will allow gases to access the sieve efficiently. Grignard treatment to zeolites has been researched to create surface hydrophobicity [1-2], but it was designed for a small amount of zeolite to be used only for small amount of dope for film casting or a sheath layer of mixed matrix hollow fiber membranes. Another approach is hydrophobization with aliphatic alcohol (mainly methanol) for esterification of silanol groups on zeolite surfaces;

$$\equiv\text{Si-OH} + \text{R-OH} \rightarrow \text{Si-OR} + H_2O \quad \text{(F.1)}$$

This approach did not successfully produced a hydrophobic surface for mixed matrix membranes [1], but could yield a medium or large amount of dope with more than 50% zeolite loading for fiber sorbent spinning. I wanted to investigate effects of the hydrophobized zeolite particles on the morphology of fiber sorbents, but the method was not sufficient to change the morphology. This appendix provides the results of the hydrophobization of zeolite NaY and spun fiber sorbents.

F.2. Experimental Method

The original method of the hydrophobization was designed to process a small amount of zeolite for mixed matrix membranes [1]. For a batch, dried zeolite NaY of 25 g at 285 °C was heated with methanol (MeOH) of 250 g in a cleaned round-bottom flask as shown in Figure F-1. Methanol loading to the zeolite was 10 g-methanol/g-zeolite due to the limitation of the apparatus, while the method by Shu applied 20 g-methanol/g-zeolite [1]. Oil bath temperature was controlled at 105 ~ 110 °C, which was higher than boiling point of methanol (64.7 °C [3]), and maintained for 60 hours. The methanol vapor was cooled down through a condenser (Ace Glass) attached to the top of the flask and return to the flask. Both oil and mixture are stirred with magnetic stirrers at the same time on the hot plate (SNA1025B, Barnstead ThermoLyne). The top of the condenser is kept open and the heating process is operated under the ventilation. After the mixture was cooled down, separate the methanol from the treated zeolite with a centrifugal (IEC Multi, Thermo Electron Corp.). Because of the capacity of the centrifugal tubes, the mixture is divided into appropriate sizes and centrifugation is repeated for the entire amount. Additional methanol in a wash bottle was used for washing out the rest of the zeolites in the flask and the tubes to collect all of zeolites. Zeolite was dried at room temperature under residual methanol was evaporated. Combined with two batches, CA-NaY fiber sorbent dope was prepared following the dope preparation procedure described in Chapter 3, Section 3.3. The dried zeolite after the reaction might adsorb methanol and water (a by-product). Since the degradation temperature of the modified surface was unknown, the zeolite was used as dried with adsorbed methanol and water without vacuum drying at high temperature.

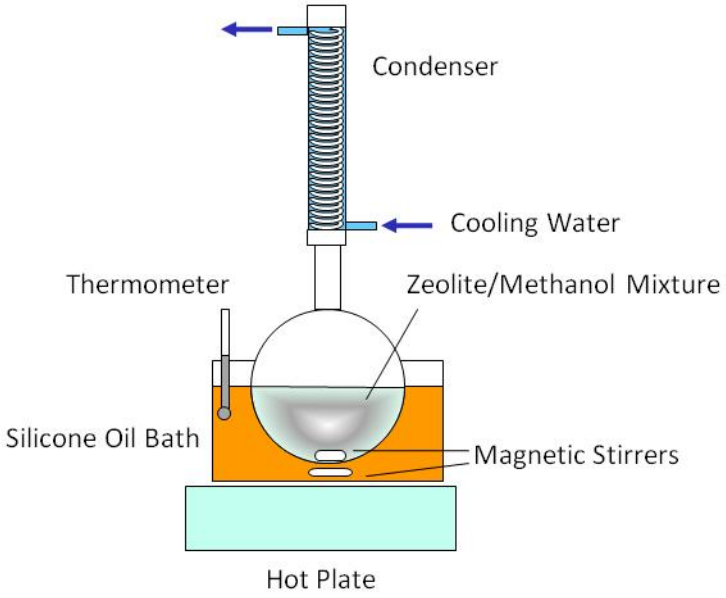

Figure F-1 Experimental Setup

F.3. Results and Discussions

Two batches (#3 and #6) of the surface modified NaY were analyzed by TGA with 10 K/min compared to the NaY with saturated with methanol and water vapor. Weight of the surface modified NaY samples were reduced stepwise at 510 – 580 °C as show in Figure F-2. This behavior was not observed with NaY with methanol and water vapor saturation. The rate of weight loss at 100 – 200 °C for the surface modified NaY was similar to that for the NaY with water vapor saturation as shown in Figure F-3. The rate of weight loss for the NaY with methanol saturation was lower than that for the NaY with the water vapor saturation. It indicates that water was produced as a result of the reaction and adsorbed to the NaY during the drying. The TGA results proved that the NaY was surely surface-modified per reaction (F.1).

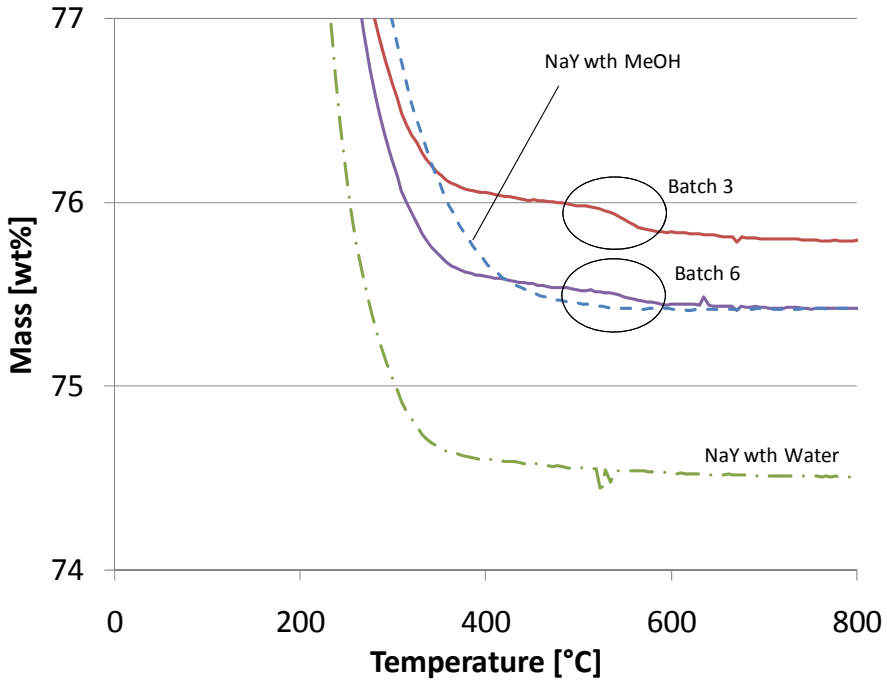

Figure F-2 TGA Curves (Weight Loss) of the Surface Modified NaY Compared with Raw NaY with Methanol and Water Vapor Saturation

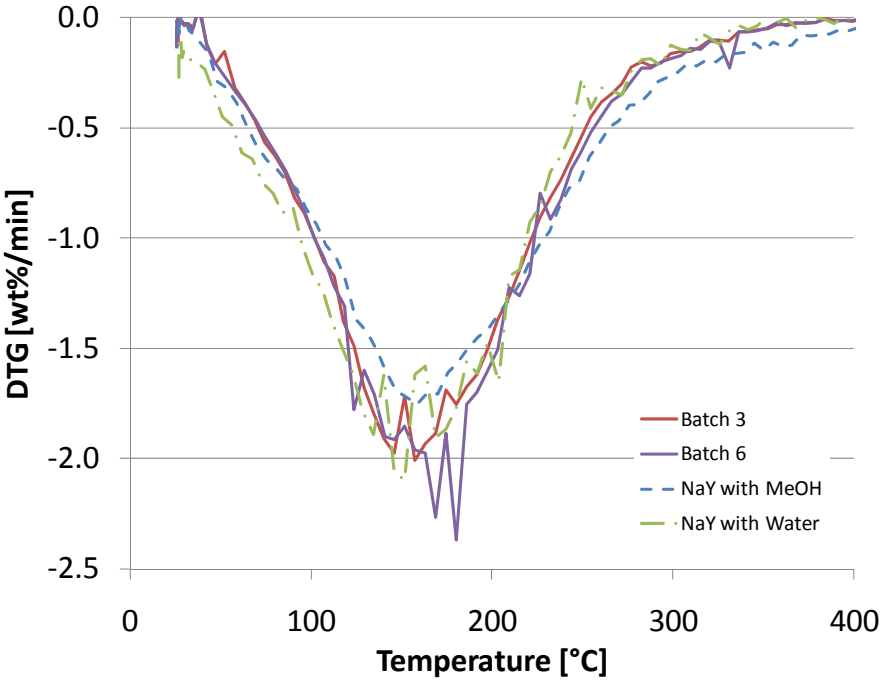

Figure F-3 TGA Curves (Differential Weight Loss) of the Surface Modified NaY Compared with Raw NaY with Methanol and Water Vapor Saturation

Several more batches of the surface modified NaY were prepared, and the CA-NaY fiber sorbent dopes (G-II 15% CA/76% Loading and G-I 25% CA/64% Loading) were spun in the same manner which is described in Chapter 3, Section 3.5 and Chapter 4, Section 4.3. The morphology of those fiber sorbents as shown Figure F-4 was similar to the fiber sorbent of CA-raw NaY and the sieve-in-a-cage morphology was observed. These results were consistent with Shu's results [1] and this surface hydrophobization approach was not appropriate enough to bond the polymer and zeolite surface tightly. As discussed in Chapter 4, Section 4.3, a dense polymer matrix was still observed for the surface modified NaY. Although the surface modification might not be at the desired level, other approaches such as Grignard treatment were not practical for the preparation of the required amount of zeolite for dopes of fiber sorbents. The fiber sorbent of G-II 15% CA/76% loading with the surface modified NaY showed less porous morphology than that for the raw NaY (Figure 4-16). The methanol behaves as another non-solvent to the CA in the dopes and the saturation with methanol of the NaY after the drying might impact on the phase separation process with regard to the dope composition shift. Phase diagram for the quaternary system of CA/NMP/water/MeOH was not investigated and involves more complication for the fiber sorbent dope with zeolite dispersion. Including the determination of drying conditions for the surface modified zeolite, it requires further efforts to investigate the phase separation mechanism beyond the scope of this research. The sieve-in-a-morphology is preferred for the fiber sorbents at least, which is different totally from the mixed matrix membranes. In terms of dense polymer matrix on the morphology, this surface hydrophobization approach did not show any significant difference between raw and modified NaY.

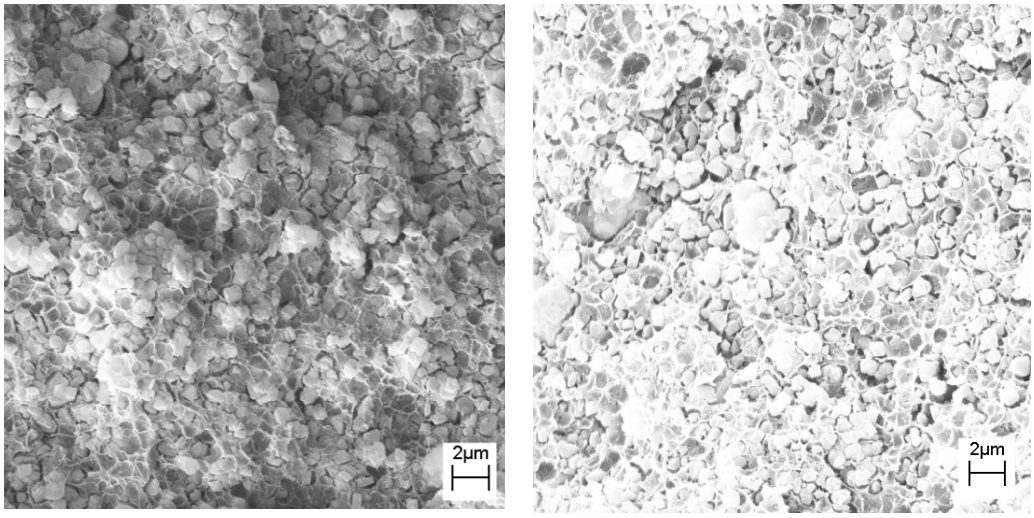

(a) G-II 15% CA/76% Loading (b) G-I 25% CA/64% Loading

Figure F-4 Morphology with Surface Modified Zeolite

F.4. Conclusions

Zeolite NaY was successfully hydrophoized with alcohol, but it was not sufficient to change the morphology of dense polymer matrix. Since the sieve-in-a-cage morphology works effectively for fiber sorbent, further investigation related to surface modification was not executed in this research.

F.5. References

1. Shu, S., *Engineering the performance of Mixed Matrix Membranes for Gas Separations*, in *Ph.D. Dissertation*. 2007, Georgia Institute of Technology.

2. Liu, J.Q., et al., *Butane Isomer Transport Properties of 6FDA-DAM and MFI-6FDA-DAM Mixed Matrix Membranes.* Journal of Membrane Science, 2009. **343**(1-2): p. 157-163.

3. Sigma-Aldrich Co. 2010 [cited 2010 August 31]; Available from: http://www.sigmaaldrich.com.

APPENDIX G DYNAMIC MODELING OF FIBER SORBENT MODULE IN PRESSURE SWING ADSORPTION PROCESSES INCLUDING NON-ISOTHERMAL HEAT TRANSFER EFFECTS

G.1. Introduction

This appendix provides code of dynamic modeling for fiber sorbent module and packed bed by gPROMS®. The code was designed to predict behaviors of both fiber sorbent modules and packed bed in the pressure swing adsorption process according to the equations described in Chapter 2, Section 2.7.

G.2. Key Notes

Equations used in the dynamic modeling to estimate physical and mass transport properties and sorption capacity were the same as described in Appendix C. Heat transfer was out of scope for the simplified model and the external heat transfer between gas and solid (the fiber sorbent including the impermeable layer and shell-side material) was considered. Assignment of parameters and variables are almost same defined in Appendix C, but explained in the code for each parameter and variable.

The code described below comprises of five segments; 'PROCESS adsorber', 'Task psa', 'Task cycles', 'Model fiber_sorbent_module' and 'Model packed_bed'. 'Model fiber_sorbent_module' and 'Model packed_bed' contain detailed calculation steps based on the equations in Chapter 2, Section 2.7. Select one model in 'PROCESS adsorber', 'Task psa' and 'Task cycles' accordingly.

Isothermal (iso = 0) and non-isothermal (iso = 1) conditions are selected in 'PROCESS adsorber'. For the fiber sorbent module, it is necessary to select a set of properties of a material used in the shell-side void space in 'PROCESS adsorber'.

Each step time is changeable in 'PROCESS adsorber'. For the breakthrough behaviors, step time except Step 2 is set as zero with appropriate initial conditions.

G.3. External Heat Transfer Coefficient

Similarly to external mass transfer mentioned in Appendix C, with the same concept of a flow through a pipe, heat transfer coefficient through external film for each fiber sorbent was predicted by [1];

$$Nu_f = 2.0Gz_{H0}^{1/3} = 1.845Gz_H^{1/3} \quad \text{.....(G.1)}$$

$$Nu_f = \frac{h_{f,f} d_{fb}}{D_{th}} \quad \text{.....(G.2)}$$

$$D_{th} = \frac{\kappa_g}{\rho_g c_{pg}} \quad \text{.....(G.3)}$$

$$Gz_{H0} = \frac{\pi d_{fb}^2 v}{4 D_{th} L} \quad \text{.....(G.4)}$$

$$Gz_M = \frac{d_{fb}^2 v}{D_{th} L} \quad \text{.....(G.5)}$$

where,

Nu_f; Nusselt number for a fiber sorbent [-]

Gz_{H0}; Graetz number for heat transfer (with $\pi/4$) [-]

D_{th}; thermal diffusivity in bulk gas [m^2/s]

κ_g; thermal conductivity of mixed gas [W/m/K]

ρ_g; density of mixed gas [kg/m^3]

c_{pg}; specific heat capacity of mixed gas [J/kg/K]

Gz_H; Graetz number for heat transfer (without $\pi/4$) [-]

$h_{f,f}$; external heat transfer coefficient for a fiber sorbent [$W/m^2/s$]

d_{fb}; inner (bore) diameter of a fiber sorbent [m]

v; interstitial velocity [m/s]

L; length of a fiber sorbent module [m]

Note that the Graetz number is defined with or without the $\pi/4$ factor depending on the reference [1].

For a packed bed, the convective heat transfer empirical equation has been proposed [2];

$$Nu_p = 2.0 + 1.1 Re_p^{0.6} Pr^{1/3} \quad \text{.....(G.6)}$$

$$Nu_p = \frac{h_{f,p} d_p}{D_{th}} \quad \text{.....(G.7)}$$

$$Re_p = \frac{\rho_g u d_p}{\mu_g} \quad \text{.....(G.8)}$$

$$Pr = \frac{c_{pg} \mu_g}{\kappa_g} \quad \text{.....(G.9)}$$

where,

Nu_p; Nusselt number for a packed bed [-]

Re_p; Reynolds number for a packed bed [-]

Sc; Prandtl number [-]

$k_{f,p}$; external heat transfer coefficient for a zeolite pellet [m/s]

d_p; diameter of a zeolite pellet [m]

u; linear velocity (superficial velocity) [m/s]

μ_g; viscosity of mixed gas [Pa·s]

G.4. Code

```
{
  gPROMS input file generated by gPROMS ModelBuilder 3.2.0
  Wed Oct 06 20:35:13 EDT 2010

  PSA -> file:/C:/Documents and Settings/My Documents/gPROMS/PSA.gPJ
}

DECLARE TYPE # PSA:notype
    notype = 0.5 : -1.000000000000000E+100 : 1.000000000000000E+100
END

MODEL fiber_sorbent_module # PSA:fiber_sorbent_module

# PARAMETER
# ParameterName AS INTEGER || REAL || LOGICAL < DEFAULT Value >
# ParameterName AS ARRAY ( Size < , ... > ) OF INTEGER || REAL || LOGICAL <
DEFAULT Value >
```

```
# ParameterName AS FOREIGN_OBJECT < "ForeignObjectClass" > < DEFAULT
"ForeignObjectValue" >

# ParameterName AS ORDERED_SET < DEFAULT [ "Name" < , ... > ] >

parameter

# ----- Defined in "Process adsorber" -----

pi, Rg                                                    as real

L, df, dfb, lct, wc0, dpore, ef, dm                       as real

nL, nf, iso                                               as integer

rhoc, cpc, kapc, dc, Hads, Dec                            as real

rhopm, cppm, kappm, rhoct, cpct, kapct                    as real

rhox, cpx, kapx, Tm, Hfus                                 as real

lw, rhow, cpw, kapw                                       as real

qcs0, Eqc, bc0, kpm, qpms, bpm                            as real

pH, pL, TH, TL, y2H, y2L                                  as real

Tstep, pstep, y2step, MVstep                    as array(4) of real

MW, sgLJ, ekLJ                                  as array(2) of real

cpmgc                                           as array(2,3) of real


# DISTRIBUTION_DOMAIN

# DomainName AS [ LowerBound : UpperBound ]

# DomainName AS ARRAY ( Size < , ... > ) OF [ LowerBound : UpperBound ]

distribution_domain

axial as [0:L]


# UNIT

# UnitName AS UnitModelName
```

```
# UnitName AS ARRAY ( Size || OrderedSet < , ... > ) OF UnitModelName



# PORT
# PortName AS ConnectionType
# PortName AS ARRAY ( Size || OrderedSet < , ... > ) OF ConnectionType



# VARIABLE
# VariableName AS VariableType
# VariableName AS ARRAY ( Size || OrderedSet < , ... > ) OF VariableType
# VariableName AS DISTRIBUTION ( DomainName < , ... > ) OF VariableType
variable
# ----- Defined in "Process adsorber" -----
lf, dfct, tauf, av                                      as notype
Sm, Vm, dmw, Smw, Sw, Vw, Vwm                           as notype
Vf, Vfb, Vct, Vfa, Vcta, Va                             as notype
phic0, phipm0                                           as notype
phif, phic, phipm, rhof                                 as notype
phicts, phifs, efs, phics, phipms, phis, rhos           as notype
wc, wpm, wct                                            as notype
ems, emb, phictm, phifm, phim, efm, phicm, phipmm, rhom  as notype
dp, ap, eb, phib                                        as notype
Qv, u0, t0                                              as notype
cpVmf0, cpVmp0, cpVmw, cpVms, Hadsm, Hadsb, Hfusm       as notype
```

```
# ----- Defined in This Code -----
mug12, MW12, Phi12, Phi21, Phi3, Phi4, Dg, omgD, Pr, Sc  as notype
MW3, sgLJ3, ekLJ3                                        as notype
DK, DMK, De                                              as notype
bc                                                       as notype
q0c, q0pm, q0V                                           as notype
Qmax                                                     as notype
af, ac                                                   as notype
Tmax, Ts                                                 as notype
cpVg, cpVf, cpVm, cpVmx                                  as notype
Red, GzM, Sh, GzH, Nu                                    as notype
kf, ks, kz                                               as notype
hf                                                       as notype
RMTf, RMTs, RMTcKe                                       as notype
MVs, v0                                                  as notype
tpd                                                      as notype
a_v, a_p, a_T, a_x1, a_x2, Hm1, Hm2                      as notype

kTe, rhog, cpmg, cpg, omgmu, mug, kapg, Dthg as array(3) of notype
ps, Cs, ys                                   as array(3) of notype

Tg, Tx        as distribution(axial) of notype
p, p1, p2     as distribution(axial) of notype
y1, y2        as distribution(axial) of notype
C1, C2, q2    as distribution(axial) of notype
bz, K, Kc, Ke as distribution(axial) of notype
```

```
RMT           as distribution(axial) of notype

H             as distribution(axial) of notype


# SELECTOR

# SelectorName AS ( Flag < , ... > ) < DEFAULT Flag >

# SelectorName AS ARRAY ( Size || OrderedSet < , ... > ) OF ( Flag < , ... > )
< DEFAULT Flag >

# SelectorName AS DISTRIBUTION ( DomainName < , ... > ) OF ( Flag < , ... > )
< DEFAULT Flag >

selector

mode as (step1, step2, step3, step4) default step1


# SET

# ParameterPath := Expression ;

# ParameterPath := [ Expression < , ... > ];

# ParameterPath := "<ForeignObjectClass::>ForeignObjectValue";

# ParameterPath := [ "Name" < , ... > ];

# DomainPath := [ BFDM || CFDM || FFDM || OCFEM , Order , NumOfElements ];


# Boundary condition equations

boundary


case mode of


  # Step 1: Pressurization

  when step1:
```

```
    # Feed End
    partial(Tg(0),axial) = 0;
    partial(p1(0),axial) = 0;
    partial(p2(0),axial) = 0;

    # Product End
    # --- Free End Setting ---
    partial(Tg(L),axial) = -(Tg(L)- Tstep(1))/(L/nL);
    partial(p1(L),axial) = -(p1(L)- (1-y2step(1))*pstep(1))/(L/nL);
    partial(p2(L),axial) = -(p2(L)- y2step(1)*pstep(1))/(L/nL);

    # --- Fixed End Setting ---
#    Tg(L) = Tstep(1);
#    p1(L) = (1-y2step(1))*pstep(1);
#    p2(L) = y2step(1)*pstep(1);

  # Step 2: Adsorption
  when step2:

    # Feed End
    # --- Free End Setting ---
    partial(Tg(0),axial) = -(Tstep(2)- Tg(0))/(L/nL);
    partial(p1(0),axial) = -((1-y2step(2))*pstep(2)- p1(0))/(L/nL);
    partial(p2(0),axial) = -(y2step(2)*pstep(2)- p2(0))/(L/nL);
```

```
    # --- Fixed End Setting ---
#    Tg(0) = Tstep(2);
#    p1(0) = (1-y2step(2))*pstep(2);
#    p2(0) = y2step(2)*pstep(2);

    # Product End
    partial(Tg(L),axial) = 0;
    partial(p1(L),axial) = 0;
    partial(p2(L),axial) = 0;

  # Step 3: Depressurization
  when step3:

    # Feed End
    partial(Tg(0),axial) = -(Tstep(3)- Tg(0))/(L/nL);
    partial(p1(0),axial) = -((1-y2step(3))*pstep(3)- p1(0))/(L/nL);
    partial(p2(0),axial) = -(y2step(3)*pstep(3)- p2(0))/(L/nL);

#    partial(Tg(0),axial) = 0;
#    partial(p1(0),axial) = 0;
#    partial(p2(0),axial) = 0;

    # Product End
    partial(Tg(L),axial) = 0;
    partial(p1(L),axial) = 0;
    partial(p2(L),axial) = 0;
```

```
  # Step 4: Purge
  when step4:

    # Feed End
    partial(Tg(0),axial) = 0;
    partial(p1(0),axial) = 0;
    partial(p2(0),axial) = 0;

    # Product End
    # --- Free End Setting ---
    partial(Tg(L),axial) = -(Tg(L)- Tstep(4))/(L/nL);
    partial(p1(L),axial) = -(p1(L)- (1-y2step(4))*pstep(4))/(L/nL);
    partial(p2(L),axial) = -(p2(L)- y2step(4)*pstep(4))/(L/nL);

    # --- Fixed End Setting ---
#    Tg(L) = Tstep(4);
#    p1(L) = (1-y2step(4))*pstep(4);
#    p2(L) = y2step(4)*pstep(4);

end

# TOPOLOGY
# Unit connection equations
```

```
# EQUATION
# Model equations
equation

#-------------------------------------------------------------------------
# Gas Conditions
#-------------------------------------------------------------------------
# Temperature and Pressure in Each Step
case mode of

  # Step 1: Pressurization
  when step1:
    Ts   = Tstep(1);
    ps(3)= pstep(1);
    ys(2)= y2step(1);
    MVs  = MVstep(1);

  # Step 2: Adsorption
  when step2:
    Ts   = Tstep(2);
    ps(3)= pstep(2);
    ys(2)= y2step(2);
    MVs  = MVstep(2);

  # Step 3: Depressurization
  when step3:
```

```
    Ts   = Tstep(3);
    ps(3)= pstep(3);
    ys(2)= y2step(3);
    MVs  = MVstep(3);

  # Step 4: Purge
  when step4:
    Ts   = Tstep(4);
    ps(3)= pstep(4);
    ys(2)= y2step(4);
    MVs  = MVstep(4);

end

# State
ys(3) = 1;
ys(1) = ys(3)-ys(2);            # Composisition of Component 1 [-]
ps(1) = ys(1)*ps(3);            # Partial Pressure of Component 1 [Pa]
ps(2) = ys(2)*ps(3);            # Partial Pressure of Component 2 [Pa]
Cs(1) = ps(1)/Rg/Ts;            # Concentration of Component 1 [mol/m3]
Cs(2) = ps(2)/Rg/Ts;            # Concentration of Component 2 [mol/m3]
Cs(3) = ps(3)/Rg/Ts;            # Total Concentration [mol/m3]

# Interstitial Velocity [m/s]
v0 = u0/emb;
```

```
# Properties
# MW    : Molar Weight [g/mol]
# sgLJ  : Lennard-Jones Collision Diameter [A]
# ekLJ  : Lennard-Jones Energy Parameter [K]
# rhog  : Density [kg/m3]
# cpmg  : Molar Heat Capacity of Single Gas / Rg [-]
# cpg   : Heat Capacity [J/kg/K]
# mug   : Viscosity [Pa*s]
# kapg  : Thermal Conductivity [W/m/K]
# Dthg  : Thermal Diffusivity [m2/s]
# Dg    : Binary Diffusivity [m2/s]
# kTe   : kT/e [-]
# omgmu : Collision Integral for Viscosity [-]
# Phi   : Parameters for Viscosity of Mixed Gas [-]
# omgD  : Collision Integral for Diffusivity [-]

# Pure Gas
for i:=1 to 2 do

rhog(i) = MW(i)*Cs(i)/1000;
cpmg(i) = cpmgc(i,1) + cpmgc(i,2)*Ts + cpmgc(i,3)/Ts/Ts;
cpg(i)  = cpmg(i)*Rg*MW(i)/1000;
kTe(i)  = Ts/ekLJ(i);
omgmu(i)= 1.16145/kTe(i)^0.14874 + 0.52487/exp(0.7732*kTe(i))
          + 2.16178/exp(2.43787*kTe(i));
mug(i)  = 2.6693e-6 * sqrt(MW(i)*Ts)/sgLJ(i)^2/omgmu(i);
```

```
kapg(i) = (cpmg(i) + 1.25)*Rg/MW(i)*1000*mug(i);
Dthg(i) = kapg(i)/rhog(i)/cpg(i);

end

# Mixed Gas
MW3     = ys(1)*MW(1) + ys(2)*MW(2);
rhog(3) = MW3*Cs(3)/1000;
cpmg(3) = ys(1)*cpmg(1)+ ys(2)*cpmg(2);
cpg(3)  = cpmg(3)*Rg/MW3*1000;
cpVg    = rhog(3)*cpg(3);
omgmu(3)= 0; # Dummy
mug12   = mug(1)/mug(2);
MW12    = MW(1) /MW(2);
Phi12   = (1+sqrt(  mug12)*(1/MW12)^0.25)^2/sqrt(8*(1+  MW12));
Phi21   = (1+sqrt(1/mug12)*(  MW12)^0.25)^2/sqrt(8*(1+1/MW12));
Phi3    = ys(1)/(ys(1) + ys(2)*Phi12);
Phi4    = ys(2)/(ys(1)*Phi21 + ys(2));
mug(3)  = Phi3*mug(1) + Phi4*mug(2);
kapg(3) = Phi3*kapg(1)+ Phi4*kapg(2);
Dthg(3) = kapg(3)/cpVg;
Pr      = cpg(3)*mug(3)/kapg(3);          # Prandtl Number [-]

# Binary Diffusivity
sgLJ3   = (sgLJ(1) + sgLJ(2))/2;
ekLJ3   = sqrt(ekLJ(1)*ekLJ(2));
```

```
kTe(3)  = Ts/ekLJ3;
omgD    = 1.06036/kTe(3)^0.1561 + 0.193/exp(0.47635*kTe(3))
         + 1.03587/exp(1.52996*kTe(3)) + 1.76474/exp(3.89411*kTe(3));
Dg      = 1.883e-2 * sqrt(Ts^3*(1/MW(1)+1/MW(2)))/ps(3)/sgLJ3^2/omgD;
# The original coefficent value was 1.8583e-7 for p in [atm]
Sc      = mug(3)/rhog(3)/Dg;                # Schmidt Number [-]

#-------------------------------------------------------------------------
# CO2 Sorption Capacity
#-------------------------------------------------------------------------
# Saturation Capacity for Bare Fiber Sorbent [mol/m3]
bc   = bc0*exp(Hads/Rg/Ts); # [1/Pa]
q0c  = qcs0*exp(Eqc/Rg/Ts)*bc*ps(2)/(1+bc*ps(2)); # [mol/kg]
q0pm = kpm*ps(2) + qpms*bpm*ps(2)/(1+bpm*ps(2));  # [mol/kg]
q0V  = phic*rhoc*q0c+ phipm*rhopm*q0pm;           # [mol/m3]

# Considering the amount in pores
#q0V  = ef*Cs(2) + phic*rhoc*q0c+ phipm*rhopm*q0pm; # [mol/m3]

# Net Maximum Generated Heat [J/m3]
Qmax = Hadsm*q0V - Hfusm;

# Volumetric Heat Capacity [J/m3/K]
cpVf  = efm*cpVg + cpVmf0; # [J/m3/K]
cpVmx = cpVf     + cpVms;  # [J/m3/K]
cpVm  = emb*cpVg + cpVmx;  # [J/m3/K]
```

```
# Maximum Temperature Rise [K]
Tmax = Qmax/cpVm;

#-------------------------------------------------------------------------
# Heat and Mass Transfer
#-------------------------------------------------------------------------
# External Mass Transfer
af   = av*phifm;                 # MT Area [m2/m3-module] (Bore-Side Feed)
Red  = rhog(3)*abs(v0)*dfb/mug(3);  # Reynolds Number [-]
GzM  = dfb^2*abs(v0)/L/Dg;       # Graetz Number for MT [-]
Sh   = 1.495*GzM^(1/3);          # Sherwood Number [-]
kf   = Sh*Dg/dfb;                # External MT Coefficient [m/s]
RMTf = 1/kf/af;                  # External MT Resistance [s]

# External Heat Transfer
GzH  = dfb^2*abs(v0)/L/Dthg(3);  # Graetz Number for HT [-]
Nu   = 1.845*GzH^(1/3);          # Nusselt Number [-]
hf   = Nu*kapg(3)/dfb;           # External HT Coefficient [W/m2/K]

# Intrafiber Mass Transfer
DK   = 1.534*dpore*sqrt(Ts/MW(2)*1000); # Knudsen Diffusivity [m2/s]
DMK  = 1/(1/Dg + 1/DK);          # For Series Diffusion of Bulk and Knudsen
De   = ef*DMK/tauf;              # Effective Diffusivity [m2/s]
ks = 8*lf/(4*lf^2-(0.5*(df^2+dfb^2)-
4/3*df*(df^2+df*dfb+dfb^2)/(df+dfb)+df^2))*De;
```

```
                                # Intrafiber MT Coefficient [m/s]
RMTs = 1/ks/af;                 # Intrafiber MT Resistance [s]

# Intracrystalline Mass Transfer
ac     = 6/dc*phic*phifm;       # MT Area for Zeolite Crystals [m2/m3-module]
kz     = 10*Dec/dc;             # Intracrystline MT Coefficient [m/s]
RMTcKe = 1/kz/ac;               # Part of Intracrystalline MT Resistance [s]

#-------------------------------------------------------------------------
# Coefficients for Governing Equations
#-------------------------------------------------------------------------
a_v  = 32*mug(3)/dfb/dfb;
a_p  = -phifm*Rg/emb;
a_T  = hf*af/emb;
a_x1 = Hadsm/cpVmx;
a_x2 = -hf*af/cpVmx;
Hm1  = cpVmx*Tm;
Hm2  = cpVmx*Tm + Hfusm;
# Assume that Imp Layer doesn't contribute to the mass balances.

#-------------------------------------------------------------------------
# Pressure Drop (Hagen-Poiseuille Equation)
#-------------------------------------------------------------------------
tpd = a_v*abs(v0)*L; #[Pa]

#-------------------------------------------------------------------------
```

```
# Governing Equations
#-------------------------------------------------------------------------
# C1  : Concentration of Component 1 in Gas Phase [mol/m3]
# C2  : Concentration of Component 2 in Gas Phase [mol/m3]
# q2  : Concentration of Component 2 in Fiber Sorbent Phase [mol/m3]
# p1  : Partial Pressure of Component 1 [Pa]
# p2  : Partial Pressure of Component 2 [Pa]
# p   : Total Pressure [Pa]
# y1  : Composition of Component 1 [-]
# y2  : Composition of Component 2 [-]
# Kc  : D-less Sorp Eq Constant for Zeolite Crystal [m3-gas/m3-material]
# K   : D-less Sorp Eq Constant for Fiber Sorbent [m3-gas/m3-material]
# Ke  : Effective D-less Sorp Eq Constant [m3-gas/m3-material]
# RMT : Overall Mass Transfer Resistance [s]

bz(0:L) = bc0*exp((Eqc+Hads)/Rg/abs(Tx(0:L)));
Kc(0:L) = phic*rhoc*Rg*Tg(0:L)*qcs0*bz(0:L)/(1+bz(0:L)*p2(0:L));
K(0:L)  = Kc(0:L) + Rg*Tg(0:L)*phipm*rhopm*(kpm+qpms*bpm/(1+bpm*p2(0:L)));
#K(0:L)  = ef + Kc(0:L) +
Rg*Tg(0:L)*phipm*rhopm*(kpm+qpms*bpm/(1+bpm*p2(0:L)));
Ke(0:L) = K(0:L)*K(0:L)/Kc(0:L);
RMT(0:L)= RMTf + RMTs + RMTcKe/Ke(0:L);

# Concentration of Component 2 in Fiber Sorbent Phase [mol/m3]
Tg(0:L)*RMT(0:L)*$q2(0:L)= p2(0:L)/Rg - q2(0:L)/K(0:L)*Tg(0:L);
```

```
# Partial Pressure of Component 1
$(p1(0|+:L|-)/Tg(0|+:L|-))=
 -v0*partial(p1(0|+:L|-)/Tg(0|+:L|-),axial);

# Partial Pressure of Component 2
$(p2(0|+:L|-)/Tg(0|+:L|-))=
 -v0*partial(p2(0|+:L|-)/Tg(0|+:L|-),axial)+ a_p*$q2(0|+:L|-);

# Temperature of Gas Phase --- Fixed rhog, cpg and hf ---
cpVg*$Tg(0|+:L|-)=
 -v0*cpVg*partial(Tg(0|+:L|-),axial)+ a_T*(Tx(0|+:L|-)-Tg(0|+:L|-));

# Temperature of Fiber Sorbent Phase
H(0:L) = cpVmx*Tx(0:L) + Hadsm*q2(0:L);

for z:=0 to L do
  if H(z) < Hm1 then
      $Tx(z) = a_x1*$q2(z) + a_x2*(Tx(z)-Tg(z));
  else
    if H(z) < Hm2 then
      $Tx(z) = a_x2*(Tx(z)-Tg(z));
    else
      $Tx(z) = a_x1*$q2(z) + a_x2*(Tx(z)-Tg(z));
    end
  end
end
```

```
p1(0:L) = C1(0:L)*Rg*Tg(0:L);

p2(0:L) = C2(0:L)*Rg*Tg(0:L);

p(0:L) = p1(0:L) + p2(0:L);

p(0:L)*y1(0:L) = p1(0:L);

p(0:L)*y2(0:L) = p2(0:L);


# ASSIGN

# VariablePath := Expression ;

# VariablePath := [ Expression < , ... > ];


# PRESET

# < RESTORE " >

# VariablePath := InitialValue ;

# VariablePath := InitialValue : LowerBound : UpperBound ;



# INITIALSELECTOR

# SelectorPath := FlagPath ;

# SelectorPath := [ FlagPath < , ... > ];



# INITIAL

# Equations


END # MODEL fiber_sorbent_module
```

```
TASK psa # PSA:psa

# PARAMETER
# ParameterName AS INTEGER || REAL || LOGICAL
# ParameterName AS INTEGER_EXPRESSION || REAL_EXPRESSION || LOGICAL_EXPRESSION
# ParameterName AS MODEL ModelName
parameter
ADS                as model fiber_sorbent_module
#ADS                as model packed_bed
ts1, ts2, ts3, ts4 as real

# VARIABLE
# VariableName AS INTEGER || REAL || LOGICAL



# SCHEDULE
# OperationSchedule
schedule
sequence

  # Step 1: Pressurization
  switch
    ADS.mode := ADS.step1;
  end
  continue for ts1
```

```
  # Step 2: Adsorption
  switch
    ADS.mode := ADS.step2;
  end
  continue for ts2

  # Step 3: Depressurization
  switch
    ADS.mode := ADS.step3;
  end
  continue for ts3

  # Step 4: Purge
  switch
    ADS.mode := ADS.step4;
  end
  continue for ts4

end
END # TASK psa

TASK cycles # PSA:cycles

# PARAMETER
# ParameterName AS INTEGER || REAL || LOGICAL
```

```
# ParameterName AS INTEGER_EXPRESSION || REAL_EXPRESSION || LOGICAL_EXPRESSION
# ParameterName AS MODEL ModelName
parameter
ADS                as model fiber_sorbent_module
#ADS                as model packed_bed
nc                 as integer
ts1, ts2, ts3, ts4 as real

# VARIABLE
# VariableName AS INTEGER || REAL || LOGICAL
variable
ni as integer # Cycle Number Counter

# SCHEDULE
# OperationSchedule
schedule
sequence
  ni := 1;
  while ni <= nc do
    sequence

      # Cycle
      psa(
        ADS is ADS,
        ts1 is ts1,
        ts2 is ts2,
```

```
        ts3 is ts3,
        ts4 is ts4
      )
      ni := ni + 1;
    end
  end
end


END # TASK cycles


PROCESS adsorber # PSA:adsorber


# PARAMETER
# ParameterName AS INTEGER || REAL || LOGICAL < DEFAULT Value >
# ParameterName AS ARRAY ( Size < , ... > ) OF INTEGER || REAL || LOGICAL <
DEFAULT Value >
# ParameterName AS FOREIGN_OBJECT < "ForeignObjectClass" > < DEFAULT
"ForeignObjectValue" >


# UNIT
# UnitName AS ModelName
# UnitName AS ARRAY ( Size < , ... > ) OF ModelName
unit
ADS  as fiber_sorbent_module
#ADS  as packed_bed
```

```
# MONITOR
# SYNTAX: VariablePathPattern ;



# SET
# ParameterPath := Expression ;
# ParameterPath := [ Expression < , ... > ];
# ParameterPath := "<ForeignObjectClass::>ForeignObjectValue";
# DomainPath := [ BFDM || CFDM || FFDM || OCFEM , Order , NumOfElements ];
set
within ADS do

#-------------------------------------------------------------------------
# Constant
#-------------------------------------------------------------------------
pi := 3.141592654;
Rg := 8.3142;              # Gas Constant [J/mol/K]

#-------------------------------------------------------------------------
# Pressure Conditions [Pa]
#-------------------------------------------------------------------------
pH := (100 + 14.69595)*6894.757;
pL := (14.69595)*6894.757;

#-------------------------------------------------------------------------
# Temperature Conditions [K]
```

```
#-------------------------------------------------------------------------

TH := 273.15 + 60;

TL := 273.15 + 25;


#-------------------------------------------------------------------------

# Composition Conditions [-]

#-------------------------------------------------------------------------

y2H := 0.25;

y2L := 1e-10;


#-------------------------------------------------------------------------

# PSA Process Parameters

#-------------------------------------------------------------------------

#Tstep  : Temperature [K]

#pstep  : Pressure [Pa]

#y2step : Composition of Component 2 [-]

#MVstep : Volumetric Flow Rate [MV/s]


#-------------------------------------------------------------------------

# Step 1: Pressurization Conditions

#-------------------------------------------------------------------------

Tstep(1) := TH;

pstep(1) := pH;

y2step(1):= y2L;

MVstep(1):= -2;
```

```
#-------------------------------------------------------------------------
# Step 2: Feed Gas Conditions
#-------------------------------------------------------------------------
Tstep(2) := TH;
pstep(2) := pH;
y2step(2):= y2H;
MVstep(2):= 0.5;

#-------------------------------------------------------------------------
# Step 3: Depressurization Conditions
#-------------------------------------------------------------------------
Tstep(3) := TH;
pstep(3) := pL;
y2step(3):= y2L;
MVstep(3):= -2;

#-------------------------------------------------------------------------
# Step 4: Purge Gas Conditions
#-------------------------------------------------------------------------
Tstep(4) := TH;
pstep(4) := pL;
y2step(4):= y2L;
MVstep(4):= -0.5;
# MVstep(4) must be negative (Opposite Direction)

#-------------------------------------------------------------------------
```

```
# Isothermal or Non-Isothermal Operation
#-------------------------------------------------------------------------
iso := 0;                # 0:Isothermal, 1:Non-Isothermal

#-------------------------------------------------------------------------
# Fiber Sorbent
#-------------------------------------------------------------------------
#L   := 0.25;              # Length [m] for Lab Experiment
L   := 1;                # Length [m] for Plant Module
df  := 505.0e-6;           # Outer Diameter [m]
dfb := 276.9e-6;           # Bore Diameter [m]
lct := 0e-6;            # Impermeable Layer Thickness [m]
wc0 := 0.69;             # Zeolite Loading by Weight [-]
#nf  := 8;                # Number of Fiber Sorbent [-] for Lab Experiment
nf  := 128760;            # Number of Fiber Sorbent [-] for Plant Module
# nf must be less than nfmax

# Porous Strucure
dpore := 200e-9;         # Pore Diameter [m]
ef    := 0.33;           # Porosity [-]

#-------------------------------------------------------------------------
# Module
#-------------------------------------------------------------------------
#dm  := 4.5e-3;           # Inner Diamter [m] for Lab Experiment
dm  := 0.2;              # Inner Diamter [m] for Plant Module
```

```
nL  := 200;              # Mesh Size

#axial:=[BFDM,1,100];

axial:=[CFDM,2,nL];

#axial:=[OCFEM,2,200];

# This setting gives very long time and ocsillaion in data


#-------------------------------------------------------------------------

# Materials (Isothermal Properties)

#-------------------------------------------------------------------------

# rho : Density [kg/m3]

# cp  : Heat Capacity [J/kg/K]

# kap : Thermal Conductivity [W/m/K]


# Zeolite Crystal : Zeolite NaY

rhoc := 1.408e3;

cpc  := 779;

kapc := 0.24;

dc   := 500e-9;          # Crystalline Diameter [m]

Hads := 2.286e4;         # Heat of Adsorption for CO2 [J/mol-CO2]
[Literature]

#Hads := 2.512e4;         # Heat of Adsorption for CO2 [J/mol-CO2]

Dec  := 1e-10;           # Effective Diffusivity of CO2 [m2/s]


# Polymer : Cellulose Acetate

rhopm := 1.32e3;

cppm  := 1465;
```

```
kappm := 0.25;

#///// Selection of Impermeable Layer /////
# Cellulose Acetate
rhoct := rhopm;
cpct  := cppm;
kapct := kappm;

#///// Selection of Material in Shell Side /////
# Paraffin Wax
#rhox := 0.8e3;
#cpx  := 2000;
#kapx := 0.24;
#Tm   := 273.15 + 60;      # Melting (Fusion) Point [K]
#Hfus := 1.89e5;           # Latent Heat of Fusion [J/kg]

# Gas [N2] in Shell Side
#rhox := 7.988;
#cpx  := 1028;
#kapx := 0.02696;
#Tm   := 273.15 + 60;
#Hfus := 0;

# Solid (Epoxy/PDMS) in Shell Side
rhox := 970;
cpx  := 1460;
```

```
kapx := 0.15;
Tm   := 273.15 + 60;
Hfus := 0;

#///// Vessel /////
# Steel
lw   := 1.5e-3;
rhow := 7.83e3;
cpw  := 465;
kapw := 54;

#-------------------------------------------------------------------------
# Feed Gas
#-------------------------------------------------------------------------
# Properties
# MW    : Molar Weight [g/mol]
# sgLJ  : Lennard-Jones Collision Diameter [A]
# ekLJ  : Lennard-Jones Energy Parameter [K]
# cpmg  : Coefficients fo cpmg

# Component 1 : H2
MW(1)    := 2.01588;
sgLJ(1)  := 2.915;
ekLJ(1)  := 38.0;
cpmgc(1,1):= 3.249;
cpmgc(1,2):= 0.422e-3;
```

```
cpmgc(1,3):= 0.083e5;

# Component 1 : He
#MW(1)    := 4.002602;
#sgLJ(1)  := 2.576;
#ekLJ(1)  := 10.22;
#cpmgc(1,1):= 2.5;
#cpmgc(1,2):= 0;
#cpmgc(1,3):= 0;

# Component 2 : CO2
MW(2)    := 44.0095;
sgLJ(2)  := 3.996;
ekLJ(2)  := 190.0;
cpmgc(2,1):= 5.457;
cpmgc(2,2):= 1.045e-3;
cpmgc(2,3):= -1.157e5;

# Default
#MW(3)    := 0;
#sgLJ(3)  := 0;
#ekLJ(3)  := 0;
#cpmg(1,1):= 0;
#cpmg(2,1):= 0;

#-------------------------------------------------------------------------
```

```
# CO2 Sorption Capacity
#-------------------------------------------------------------------------
# Langmuir Constants [Literature]
qcs0 := 3.791;    # [mol/kg]
Eqc  := 1.792e3;  # [J/mol]
bc0  := 2.647e-9; # [1/Pa]
kpm  := 5.279e-7;  # [mol/kg/Pa]
qpms := 0.4975;   # [mol/kg]
bpm  := 2.99e-6;  # [1/Pa]

## Langmuir Constants [Experimental]
#qcs0 := 3.061;
#Eqc  := 2.097e3;
#bc0  := 1.424e-9;
#kpm  := 5.28e-7;
#qpms := 0.4575;
#bpm  := 2.99e-6;

end

# EQUATION
# Equations
equation
within ADS do

#-------------------------------------------------------------------------
```

```
# Fiber Sorbent
#-------------------------------------------------------------------------
lf   = (df-dfb)/2;              # Annular Thickness of Fiber Sorbent [m]
dfct = df + 2*lct;              # Outer Diameter + Imp Layer [m]
tauf = 1/ef;                    # Tortuosity Factor [-]
av   = 4*dfb/(df^2-dfb^2);      # Internal Surface Area per Volume [m2/m3]

# Volume [m3]
Vf   = pi*df  ^2/4 * L;         # For Outer Diameter
Vfb  = pi*dfb ^2/4 * L;         # For Bore Diameter
Vct  = pi*dfct^2/4 * L;         # For Outer Diameter incld. Imp Layer
Vfa  = Vf  - Vfb;               # For Annulus of Fiber Sorbent
Vcta = Vct - Vf;                # For Annulus of Imp Layer
Va   = Vfa + Vcta;              # For Annulus of Fiber Sorbent + Imp Layer

# Volume Fraction (Solid Basis)
phic0  = wc0/rhoc / (wc0/rhoc + (1-wc0)/rhopm);  # For Zeolite
phipm0 = 1 - phic0;                              # For Polymer

# Volume Fraction (Bare Fiber Sorbent Basis)
phif  = 1 - ef;                 # For Solid
phic  = phif * phic0;           # For Zeolite
phipm = phif * phipm0;          # For Polymer
rhof  = phic*rhoc + phipm*rhopm; # Apparent Density [kg/m3]

# Volume Fraction (Coated Fiber Sorbent Basis)
```

```
phicts = Vcta / Va;              # For Imp Layer
phifs  = 1 - phicts;             # For Solid of Bare Fiber Sorbent
efs    = phifs * ef;             # For Porosity
phics  = phifs * phic;           # For Zeolite
phipms = phifs * phipm;          # For Polymer
phis   = phifs + phicts;         # For Solid of Coated Fiber Sorbent
rhos   = phics*rhoc + phipms*rhopm + phicts*rhoct; # Apparent Density [kg/m3]

# Weight Fraction (Coated Fiber Sorbent Basis)
wc   = phics*rhoc   / rhos;      # For Zeolite
wpm  = phipms*rhopm / rhos;      # For Polymer
wct  = phicts*rhoct / rhos;      # For Imp Layer

#-----------------------------------------------------------------------
# Module
#-----------------------------------------------------------------------
Sm  = pi * dm^2/4;               # Cross-Sectional Area of Module [m2]
Vm  = Sm * L;                    # Volume of Module [m3]
dmw = dm + 2*lw;                 # Outer Diameter + Wall [m]
Smw = pi * dmw^2/4;              # Cross-Sectional Area of Outer Dia + Wall
[m2]
Sw  = Smw - Sm;                  # Cross-Sectional Area of Wall [m2]
Vw  = Sw * L;                    # Volume of Wall [m3]
Vwm = Vw / Vm;                   # Volume Ratio of Wall to Module [-]

# Volume Fraction
```

```
ems    = 1- nf * Vct  / Vm;      # Shell-Side Void Fraction
emb    =    nf * Vfb  / Vm;      # Bore-Side Void Fraction
phictm =    nf * Vcta / Vm;      # For Imp Layer
phifm  =    nf * Vfa  / Vm;      # For Bare Fiber Sorbent
phim   = phictm + phifm;         # Fiber Packing Fraction
efm    = phifm * ef;             # For Pores
phicm  = phifm * phic;           # For Zeolite
phipmm = phifm * phipm;          # For Polymer
rhom   = phim  * rhos;           # Apparent Density [kg/m3]

#-------------------------------------------------------------------------
# Packed Bed / Zeolite Pellet
#-------------------------------------------------------------------------
dp   = 1.5e-3;                   # Pellet Size [m]
ap   = 6/dp;                     # External Surface Area per Volume [m2/m3]
eb   = 0.4;                      # Bed Void Fraction
phib = 1 - eb;                   # Packing Fraction

#-------------------------------------------------------------------------
# Flow Conditions
#-------------------------------------------------------------------------
Qv   = MVs*Vm;                   # Volumetric Flow Rate [m3/s]
u0   = Qv/Sm;                    # Linear Velocity [m/s]
t0   = L/u0;                     # Space Time [s]

#-------------------------------------------------------------------------
```

```
# Parameters
#------------------------------------------------------------------------
cpVmf0 = phicm*rhoc*cpc + phipmm*rhopm*cppm;         # [J/m3/k]
cpVmp0 = phic*phib*rhoc*cpc + phipm*phib*rhopm*cppm; # [J/m3/k]
cpVmw  = rhow*cpw*Vwm;                               # [J/m3/K]
cpVms  = phictm*rhoct*cpct + ems*rhox*cpx + cpVmw;   # [J/m3/K]
Hadsm  = phifm*Hads*iso;                             # [J/mol]
Hadsb  = phib*Hads*iso;                              # [J/mol]
Hfusm  = ems*rhox*Hfus;                              # [J/m3]

end

# ASSIGN
# VariablePath := Expression ;
# VariablePath := [ Expression < , ... > ];



# PRESET
# < RESTORE " >
# VariablePath := InitialValue ;
# VariablePath := InitialValue : LowerBound : UpperBound ;



# SELECTOR
# SelectorPath := FlagPath ;
# SelectorPath := [ FlagPath < , ... > ];
```

```
selector
within ADS do
  mode := step1;
end

# INITIAL
# Equations
# STEADY_STATE
initial
within ADS do
  Tg(0|+:L|-) = TH;
  Tx(0:L)     = TH;
  p1(0|+:L|-) = pH;
  p2(0|+:L|-) = 0;
  q2(0:L)     = 0;
end

# SOLUTIONPARAMETERS
solutionparameters
DASolver := "DASOLV" ["OutputLevel"       := 0 ;
#                     "AbsoluteTolerance" := 1E-8 ; #1E-5 ;
#                     "RelativeTolerance" := 1E-8 ; #1E-5 ;
#                     "EventTolerance"    := 1E-3 ; #1E-5 ;
#                     "EffectiveZero"     := 1E-3 ; #1E-5 ;
#                     "FDPerturbation"    := 1E-4 ; #1E-6 ;
                     "Diag"              := TRUE ;
```

```
#                       "LASolver" := "MA48" ;
#                       "InitialisationNLSolver" := "BDNLSOL"  ;
#                       "ReinitialisationNLSolver" := "SPARSE"
                      ];


# SCHEDULE
# OperationSchedule


  OutputLevel := 1


schedule
cycles(
  ADS is ADS,
  nc  is 1,     # Total Cycle Number
  ts1 is 0,     # Time for Step 1
  ts2 is 100,     # Time for Step 2
  ts3 is 0,     # Time for Step 3
  ts4 is 0      # Time for Step 4
)
END # PROCESS adsorber
```

G.5. References

1. McCabe, W.L., J.C. Smith, and P. Harriott, *Chapter 12 Heat Transfer to Fluids Without Phase Change*, in *Unit Operations of Chemical Engineering*. 2001, McGraw-Hill: Boston. p. 511-545.

2. Wakao, N. and S. Kaguei, *Chapter 8 Particle-Fluid Heat Transfer Coefficients*, in *Heat and Mass Transfer in Packed Beds*. 1982, Gordon and Breach Science Publishers: New York. p. 264-295.

APPENDIX H COMPETITVE SORPTION OF NMP AND WATER IN DRIED ZEOLITE NAY

H.1. Introduction

As discussed in Chapter 4, Section 4.3, dope composition change was considered based on the morphology and porous structure analyses. In this research, it was assumed that the hydrophilic zeolite NaY adsorbed only water selectively. However, the NMP was found to be adsorbed on the dried NaY when the NaY was dispersed in the NMP with ultrasonic power irradiation prior to mixing water. The details of the competitive sorption mechanism between NMP and water are still unknown. This appendix provides preliminary results of the competitive sorption study.

H.2. Materials

The NaY, NMP and water, which were used for dopes, were used.

H.3. Experimental Methods

The dried NaY was soaked in mixtures of NMP and water with different compositions in vials and retained for more than 1 week with rolling. For some samples, the NaY was contacted with NMP or water first, and the other component was added the next day. All of the zeolite crystals in the vials were settled down on a flat table. For convenience, the ratio of the NaY in the mixture of NaY and NMP was defined;

$$\Omega_{NaY} = \frac{\text{NaY[wt\%]}}{\text{NaY[wt\%]} + \text{NMP[wt\%]}} \quad \text{.....(H.1)}$$

NMP concentration in liquid phase was measured by UV absorption (DU 720, Beckman Coulter) with appropriate dilution in range of 5 – 15 ppm by weight. After the liquid phase was removed completely with pipettes, the wet solid phase was dried with the TGA described in Chapter 3 to measure the solid content. Void space was assumed as 26% for hexagonal closest packing of zeolite crystal in the settlement [1]. Weight of the liquid including that inside the void space was calculated subtracting the liquid contents obtained by the TGA from the total liquid, which was initially mixed. Applying the NMP concentration in the liquid phase, weight of NMP and water inside the NaY were calculated, respectively.

H.4. Results and Discussions

The results are summarized in Table H-1. At equilibrium, the liquid phase compositions changed due to "adsorption" of both NMP and water. The "adsorption" in this case implies three states; (1) on the external and internal surfaces of zeolite crystals and (2) in intracrystalline void of zeolite crystals. The amount of saturated water, which was assessed in Chapter 4, Section 4.3, to zeolite for the fiber sorbent dopes was 32 wt% increase to the dried NaY (Chapter 4, Section 4.3) and might account only for the state (1) since water vapor in gas phase were adsorbed on the zeolite surface. The molecular size (collision diameter), σ [Å], was estimated based on critical temperature and pressure [2] and given in Table H-2;

Table H-1 NMP and Water Loading at Equilibrium at 25 °C

Initial in Liquid Phase		Equilibrium in Liquid Phase	Equilibrium in Zeolite Phase		
NMP:Water [wt%:wt%]	Ω_{NaY} [wt%]	NMP [wt%]	NMP [wt%]	NMP [g/g-NaY]	Water [g/g-NaY]
50:50 N	11	46.7	90.1	1.12	0.12
50:50 N	23	50.6	47.5	0.59	0.65
50:50 W		49.4	53.8	0.67	0.58
50:50 M		49.2	53.6	0.67	0.58
50:50 N	40	53.3	45.3	0.57	0.68
50:50 W		53.7	44.6	0.56	0.69
50:50 M		52.0	47.2	0.59	0.66
70:30 N	17	67.8	79.2	0.99	0.26
	40	73.5	67.5	0.84	0.41
90:10 N	40	92.9	88.9	1.11	0.14

N; Zeolite was mixed with NMP first, and then water was added the next day.
W; Zeolite was mixed with water first, and then NMP was added the next day.
M; Zeolite was mixed with a mixture of NMP and water.

$$\sigma = 2.44\left(\frac{T_c}{p_c}\right)^{\frac{1}{3}} \quad \text{.....(H.2)}$$

where,

T_c; critical temperature [K]

p_c; critical pressure [atm]

Table H-2 Molecular Size

	T_c [K]	p_c [atm]	σ [Å]
NMP	721.7 [3]	44.6 [3]	6.17
Water	-	-	2.64 [4]

Zeolite 3A (pore size 2.9 Å [5]) can be used to adsorb water selectively from organic solvents when the molecular size of organic solvents is larger than the pore size of the 3A. On the other hand, zeolite NaY (pore size 7.4 Å [6]) allows both water and NMP to pass through the zeolitic pores. Therefore, in the liquid phase, the intracrystalline void space also contributed to retaining NMP and water inside the NaY. It is hard to distinguish to effects of surface adsorption and intracrystalline void separately. Because the small difference of size between zeolitic pore and NMP might give molecular sieving effect and result in the different composition from that in liquid phase.

The ratio of NaY to the mixture of NaY and NMP, Ω_{NaY}, was obtained as 40% as maximum used for the fiber sorbent dopes in Chapter 4, Section 4.3. As mentioned in Chapter 3, Section 3.4, dried zeolite was dispersed in NMP for the fiber sorbent dopes. For the samples which contacted with the NMP first listed in Table H-1, the amounts of adsorbed water increased as the Ω_{NaY} increased as shown in Figure H-1. On the other hand, amounts of adsorbed NMP decreased as shown in Figure H-2. As the initial composition of water decreased (or that of NMP increased), the amounts of adsorbed water decreased and that of NMP increased. It means that higher composition gave higher adsorption capacity. It also hypothesized that NMP molecules was stagnant inside intracrystalline voids due to size or occupied the adsorption sites and hindered the adsorption of water. Since the NaY is relatively hydrophilic, the effect of stagnation in the intracrystalline voids might be larger than the effect of surface adsorption.

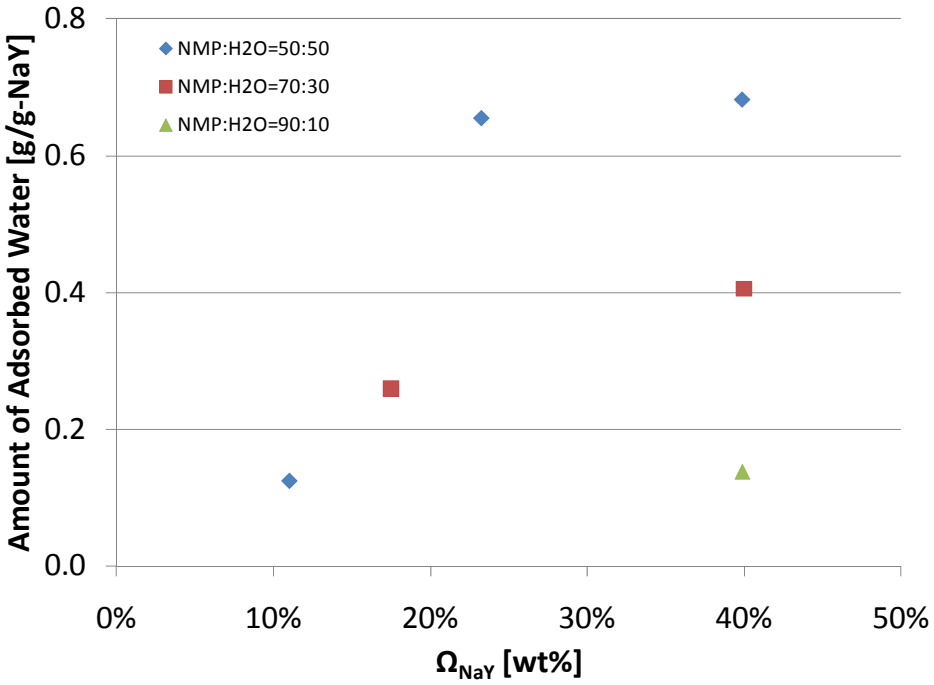

Figure H-1 Amount of Adsorbed Water vs. Ω_{NaY}

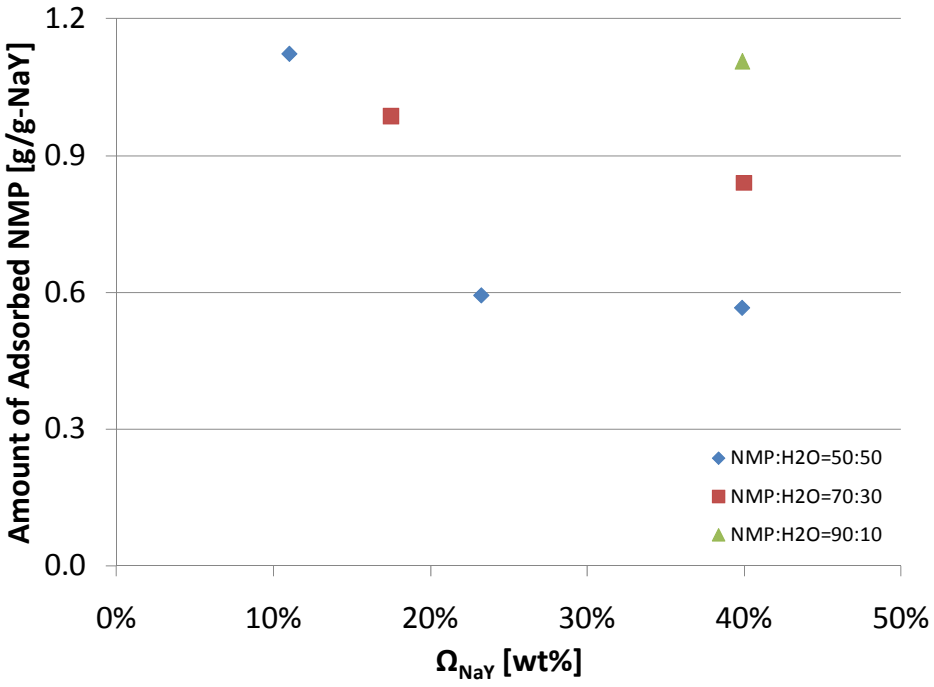

Figure H-2 Amount of Adsorbed NMP vs. Ω_{NaY}

Effect of the first contact with NMP or water varied depending on the ratio of NaY, Ω_{NaY}. For the cases of Ω_{NaY} = 23 and 40 wt%, the higher Ω_{NaY} resulted in similar amount of adsorbed water to one another. For the lower Ω_{NaY}, the amount of adsorbed water was reduced when the water or the binary mixture contacted first. Since the NaY is hydrophilic, the amount of adsorbed water was expected higher the NaY contacted with water first than when it contacted with NMP first. The results were not complied with the hypothesis. Further experimental data at different initial compositions is necessary

H.5. Conclusions

The competitive sorption mechanism is still unknown, but both NMP and water were adsorbed on the surface or in the intracrystalline voids of the zeolite crystals based on this preliminary works and it impacts on the dope composition change. Clarifying this phenomena helps to optimize fiber sorbent dope preparation further.

H.6. References

1. Jons, S., P. Ries, and C.J. McDonald, *Porous Latex Composite Membranes: Fabrication and Properties.* Journal of Membrane Science, 1999. **155**(1): p. 79-99.

2. Bird, R.B., W.E. Stewart, and E.N. Lightfoot, *Chapter 1 Viscosity and the Mechanisms of Momentum Transport*, in *Transport Phenomena*. 2002, John Wiley & Sons: New York. p. 11-39.

3. National Institute of Standards and Technology. *NIST Chemistry WebBook.* 2010 [cited 2010 August, 10]; Available from: http://webbook.nist.gov/chemistry/.

4. Hines, A.L. and R.N. Maddox, *Chapter 2 Diffusion Coefficients*, in *Mass Transfer: Fundamentals and Applications*. 1985, Prentice-Hall: Englewood Cliffs, N.J. p. 17-59.

5. Ruthven, D.M., *Chapter 1 Microporous Adsorbents*, in *Principles of Adsorption and Adsorption Processes*. 1984, Wiley-Interscience Publication: New York. p. 1-28.

6. International Zeolite Association. 2010 [cited 2010 August 20]; Available from: http://www.iza-online.org/.